LES Modelling of Non-premixed and Partially Premixed Turbulent Flames

S. K. Sadasivuni

A Doctoral Thesis

Submitted in partial fulfilment of the requirements for the award of
Doctor of Philosophy of Loughborough University

September 2009

In The Memory of My
Beloved Mother

Abstract

A large eddy simulation (LES) model has been developed and validated for turbulent non-premixed and partially premixed combustion systems. LES based combustion modelling strategy has the ability to capture the detailed structure of turbulent flames and account for the effects of radiation heat loss. Effects of radiation heat loss is modelled by employing an 'enthalpy-defect' based non-adiabatic flamelet model (NAFM) in conjunction with a steady non-adiabatic flamelet approach. The steady laminar flamelet model (SLFM) is used with multiple flamelet solutions through the development of pre-integrated look up tables.

The performance of the non-adiabatic model is assessed against experimental measurements of turbulent CH_4/H_2 bluff-body stabilized and swirl stabilized jet flames carried out by the University of Sydney combustion group. Significant enhancements in the predictions of mean thermal structure have been observed with both bluff body and swirl stabilized flames by the consideration of radiation heat loss through the non-adiabatic flamelet model. In particular, mass fractions of product species like CO_2 and H_2O have been improved with the consideration of radiation heat loss. From the Sydney University data the HM3e flame was also investigated with SLFM using multiple flamelet strategy and reasonably fair amount of success has been achieved.

In this work, unsteady flamelet/progress variable (UFPV) approach based combustion model which has the potential to describe both non-premixed and partially premixed combustion, has been developed and incorporated in an in-house LES code. The probability density function (PDF) for reaction progress variable and scalar dissipation rate is assumed to follow a delta distribution while mixture fraction takes the shape of a beta PDF. The performance of the developed model in predicting the thermal structure of a partially premixed lifted turbulent jet flame in vitiated co-flow has been evaluated. The UFPV model has been found to successfully predict the flame lift-off, in contrast SLFM results in a false attached flame. The mean lift-off

height is however over-predicted by UFPV-δ function model by ~20% for methane based flame and under-predicted by ~50% for hydrogen based flame. The form of the PDF for the reaction progress variable and inclusion of a scalar dissipation rate thus seems to have a strong influence on the predictions of gross characteristics of the flame. Inclusion of scalar dissipation rate in the calculations appears to be successful in predicting the flame extinction and re-ignition phenomena. The beta PDF distribution for the reaction progress variable would be a true prospect for extending the current simulation to predict the flame characteristics to a higher degree.

Acknowledgements

I wish to express my deep sense of gratitude to Professor W. Malalasekera for giving me an opportunity to pursue PhD under his guidance. His practical approach, kindness and helping nature made me realize a lot of things. I am grateful to him for his valuable comments, which had kept me on the right path throughout my course in the institute. The freedom and encouragement rendered to explore varied areas of research in computational combustion helped me to gain the knowledge and skills. I also thank him for the excellent world-class computing facilities provided to learn and carryout my research work.

I also wish to express my sincere thanks to my research co-supervisor, Dr. S. S. Ibrahim, for providing me the most useful discussions and has been immensely supportive and made every effort to carefully consider my ideas and interests to keep me on track.

I am grateful to all those people who have helped me in getting the things done at toughest times which I encountered during the course of this research. Dr. Ranga Dinesh from Cranfield University helped a great deal with LES. Dr. Matthias Ihme, Stanford University, provided valuable insight into the Unsteady Flamelet/Progress Variable approach. Dr. Ravikanti Murthy, Rolls Royce, UK, has been instrumental in the success behind the advanced flamelet modelling with the look-up-table concepts. Professor Heinz Pitsch, Stanford University, provided access and support to the FlameMaster code for flamelet calculations. Initial development of the large eddy simulation code has been greatly supported by Dr. Michael Kirkpatrick, Sydney University.

I would like to express my heartfelt thanks to Dr. Deiveegan, for extending all his support for the development of radiation code and its coupling with LES which has brought a great success.

I would like to take this opportunity to thank Mr. Madhavan Poyyapakkam, Alstom Power, Switzerland, for being a constant source of inspiration throughout my research work.

I convey my sincere thanks to my colleagues in the CFD research lab for their extended help. Dr. Sreenivas Rao Gubba and Mr. Abdul provided me with useful supportive information on combustion and other related topics.

Also I am grateful to Loughborough University for funding me with a research studentship and greatly acknowledged.

I would like to thank all the family members who have been a constant source of inspiration for my research work to carry ahead.

Finally, of all the above I thank my wife for being very supportive and patient enough to stand beside me to progress with my work in hard times. Lastly, I believe all the good luck that flourished for my success in all forms of life is due my little son.

Publications

S. K. Sadasivuni, W. Malalasekera and S. S. Ibrahim, "Unsteady Flamelet Progress/Variable Approach for Non-premixed Turbulent Lifted Flames", *6th International Seminar on Flame Structure*, Sep- 2008, Brussels, Belgium.

S. K. Sadasivuni, W. Malalasekera and S. S. Ibrahim, "Application of LES Based Steady Laminar Flamelet Model to Bluff Body Flames", *10th International Conference on Chemistry and its Role in Development*, Mar-2009, Egypt.

W. Malalasekera, M. Deiveegan, **S. K. Sadasivuni**, S. S. Ibrahim, "Evaluation of Turbulence/Radiation Effects using LES Combustion Simulation Data", *Proceedings of Eurotherm Seminar 83 - Computational Thermal Radiation in Participating Media III*, Apr-2009, Lisbon, Portugal.

S. K. Sadasivuni, W. Malalasekera and S. S. Ibrahim, "Validation of Unsteady Flamelet/Progress Variable Methodology for Non-premixed Turbulent Partially Premixed Flames", *4th European Combustion Meeting*, Apr-2009, Vienna, Austria.

S. K. Sadasivuni, W. Malalasekera and S. S. Ibrahim, "Unsteady Flamelet Progress/Variable Approach to Turbulent Partially Premixed Lifted Flames", To be submitted to Journal "*Combustion Science and Technology*".

S. K. Sadasivuni, W. Malalasekera and S. S. Ibrahim, "Coupled Radiation Calculations with Large Eddy Simulation for its Effect on Turbulence-Chemistry for Swirl Stabilized Flames", To be submitted to Journal "*Combustion and Flame*".

Contents

Chapter 1 Introduction 1

1.1 Background 1

1.2 Research Objectives 9

1.3 Organization of Thesis 11

Chapter 2 Literature Review 13

2.1 Steady Laminar Flamelet Model (SLFM) for turbulent non-premixed combustion 13

2.1.1 SLFM applied to RANS and LES 14

2.1.2 Effect of Transient Flamelet Modelling 21

2.2 Turbulent Partially-Premixed Combustion 26

2.3 Flamelet/Progress Variable (FPV) Approach 29

2.4 Unsteady Flamelet/Progress Variable (UFPV) Approach 30

2.5 Turbulence Radiation Interaction (TRI) 31

2.5.1 Non Adiabatic Flamelet Modelling in RANS 33

2.5.2 Non Adiabatic Flamelet Modelling in LES 35

2.6 Motivations For The Present Study 36

2.7 Closure 36

Chapter 3 Large Eddy Simulation - Turbulence Modelling 38

3.1 Introduction to LES 38

3.2 Spatial Filtering Technique 39

3.3 Filtered Governing Equations 40

3.3.1 Mass Conservation 40

3.3.2 Momentum Conservation 41

3.3.3 Species Conservation 41

3.3.4 Energy Conservation 43

3.4 Modelling Subgrid Scales Stresses 44

3.5 Closure 50

Chapter 4 Combustion Modelling 51

4.1 Mixture Fraction Space 52

4.1.1 Combustion and Chemistry 52

4.2 Steady Laminar Flamelet Model (SLFM) 53

4.2.1 Definition of Flamelet Equations 54

4.2.2 Probability Density Function 56

4.2.3 Flamelet Quenching 59

4.2.4 Limitations of SLFM 59

4.2.5 Advanced Flamelet Modelling 60

4.3 Non Adiabatic Flamelet Model (NAFM) 62

4.4 Flamelet/Progress Variable Approach 64

4.5 Unsteady Flamelet/Progress Variable Approach 66

4.5.1 Motivation 66

4.5.2 Formulation 67

4.6 Closure 70

Chapter 5 Coupling of Turbulence and Radiation 71

5.1 Introduction to TRI 72

5.2 Radiation Modelling 74

5.2.1 Discrete Transfer Radiation Model (DTM) 74

5.2.2 Gas Radiation Properties Model 79

5.3 Data Exchage Stratergy 80

5.4 Closure 81

Chapter 6 Numerical Approach 82

6.1 Finite Volume Method 82

6.2 Discretization of Governing Equations 83

6.3 Spatial Discretization 85

6.3.1 Unsteady Term 85

6.3.2 Convection Term 85

6.3.3 Diffusion Term 89

6.3.4 Source Term 90

6.3.5 Complete Equation 90

6.4 Time Advancement Scheme 91

6.4.1 Time Integration of Scalar Equations 91
6.4.2 Time Integration of Momentum Equations 92
6.5 Pressure Correction 94
6.6 Solution Procedure 95
6.6.1 Solution Procedure for General Reacting Flows 96
6.6.2 Steady Laminar Flamelet Model 98
6.6.3 Coupled LES Radiation Model - NAFM 99
6.6.4 UFPV-δ Function Model 100
6.7 Boundary conditions 101
6.7.1 Inlet Boundary Condition 102
6.7.2 Outflow Boundary Condition 103
6.7.3 Solid Boundary Condition 103
6.8 Closure 104

Chapter 7 PDF Calculations - Pre-processing Procedure 105

7.1 Flamelet Generation 106
7.1.1 Steady Adiabatic Flamelets 107
7.1.2 Steady Non-adiabatic Flamelets 110
7.1.3 Unsteady Adiabatic Flamelets 112
7.2 PDF Look-up Tables for SLFM 117
7.3 PDF Look-up Tables for NAFM 123
7.4 PDF Look-up Tables for UFPV-δ Model 125
7.5 Closure 130

Chapter 8 Modelling of Turbulent Non-premixed Bluff-body and Swirl Stabilized Flames 131

8.1 Experimental Details of Bluff-body Stabilized Flames 132
8.2 LES Modelling of HM1 & HM3 Flames 134
8.2.1 Computational Details & Boundary Conditions 136
8.2.2 Computational Grid 137
8.3 Results and Discussion 138
8.3.1 Flow Field and Mixing Predictions 139
8.3.2 Temperature and Major Species Predictions - HM1 Flame 141
8.3.3 Temperature and Major Species Predictions - HM3e Flame 144

8.3.4 Effect of Chemical Mechanism - HM1 Flame 151
8.3.5 Non-adiabatic Flamelet Modelling - HM1 Flame 153
8.4 Experimental Details of Swirl Stabilized Flames 163
8.5 LES Modelling of SMH1 Flame 165
8.5.1 Computational Details & Boundary Conditions 165
8.5.2 Computational Grid 166
8.6 Results and Discussion -NAFM 167
8.6.1 Flow Field Predictions 168
8.6.2 Mixing, Temperature and Major Species Predictions - SMH1 Flame 171
8.6.3 Effect of Number of Rays Fired 178
8.7 Effect of Chemical Mechanism 179
8.8 Closure 181

Chapter 9 Partially Premixed Combustion - UFPV Approach 182

9.1 Experimental Details of the Burner 183
9.2 Computational Set up for LES 185
9.3 Results and Discussion 186
9.3.1 Performance of SLFM & UFPV Models - CH_4/Air Flame 187
9.3.2 Performance of UFPV Model - H_2/N_2 Flame 193
9.4 Closure 204

Chapter 10 Conclusions and Future Work 205

10.1 Conclusions 206
10.2 Recommendations for Future Work 208

References 210

List of Figures

1.1 Representation of DNS, LES and RANS with Kolmogorov energy spectrum, Energy E(κ) related to a wave-number, κ.……..3

1.2 Block diagram of the research work performed ……11

4.1 Surface of stoichiometric mixture for a turbulent jet diffusion flame…….55

4.2 Solution space of laminar unsteady flamelet equations for CH_4/Air flame (Berkeley lifted flame) Fuel CH_4-Air (25%-75%) at 323 K and Oxidizer (vitiated co-flow) at 1355 K……61

4.3 Unsteady flamelet solution space for H_2/N_2 flame. Dotted values resemble the unsteady flamelet solutions at various scalar dissipation rates……61

4.4 Definition of flamelet parameter for scalar dissipation rate of $0.1s^{-1}$ for Berkeley lifted flame……...……66

5.1: Schematic diagram of data exchange between radiation (DTM) and LES codes 81

6.1 Staggered grid and node placement in two dimensions ……83

6.2: Finite volume cell and its neighbours in three dimensions ……..…..85

6.3: A Finite volume cell and its neighbours in the *xy*- plane ……..87

7.1: Steady flamelet solutions generated for HM1, HM3 and SMH1 diffusion flames. Profiles corresponding to fully burning state and extinguished state are represented with increasing value in scalar dissipation rate, χ_{st}……109

7.2: Enthalpy defect implementation on temperature profile for SMH1/HM1 flame……...111

7.3: Variation of extinction limit with enthalpy defect for CH_4-H_2 conditions...…...112

7.4: Unsteady flamelet solutions for fully burning, partially extinguished and fully extinguished states. Flamelets generated for the Berkeley CH_4-Air lifted jet flame conditions. These solutions are used for UFPV based turbulent flame calculations. (—–) fully burning and fully extinguished states; (-------) partially extinguished state at 0.1 s^{-1}……..114

7.5: Unsteady flamelet solution space for H_2/N_2 flame. Dotted values resemble the unsteady flamelet solutions at various scalar dissipation rates ……..…115

7.6: Unsteady flamelet solutions for fully burning, partially extinguished and fully extinguished states. Flamelets generated for the Berkeley H_2-N_2 lifted jet flame conditions. These solutions are used for UFPV based turbulent flame calculations. (–) fully burning and fully extinguished states; (-.-.-.-) partially extinguished state at 0.0001s^{-1}…….....116

7.7: Steady adiabatic flamelet profiles at equilibrium condition generated for methane-hydrogen (SMH & HM) flames. Dots with vertical lines show alternative grid points along mixture fraction space. …….....118

8.1: Schematic of bluff-body burner with measurement locations. (Courtesy: www.aeromech.usyd.edu.au/thermofluids).....133

8.2: Details of computational grid and domain with boundary conditions specified. ……138

8.3: Streamlines of time averaged velocity fields from the simulation with temperature contours behind ……..……140

8.4: Radial profiles of mean mixture fraction at various axial lengths of HM1 flame. Predictions obtained from LES calculations with SLFM involving GRI 2.11 mechanism …….141

8.5: Radial profiles of mean temperature at various axial lengths of HM1 flame. Predictions obtained from LES calculations with SLFM ……..142

8.6: Radial profiles of mean mass fraction of CO_2 at various axial lengths of HM1 flame. Predictions obtained from LES calculations with SLFM …..…….143

8.7: Radial profiles of mean mass fraction of H_2O at various axial lengths of HM1 flame. Predictions obtained from LES calculations with SLFM ….……..144

8.8: Radial profiles of mean mixture fraction at various axial lengths of HM3e flame. Predictions obtained from LES calculations with SLFM involving GRI 2.11 mechanism……..145

8.9: Radial profiles of mean temperature at various axial lengths of HM3e flame. Predictions obtained from LES calculations with SLFM ……..146

8.10: Radial profiles of mean mass fraction of CO_2 at various axial lengths of HM3e flame. Predictions obtained from LES calculations with SLFM ……...148

8.11: Radial profiles of mean mass fraction of H_2O at various axial lengths of HM3e flame. Predictions obtained from LES calculations with SLFM ……...149

8.12: Radial profiles of mean mass fraction of CO at various axial lengths of HM3e flame. Predictions obtained from LES calculations with SLFM….……...149

8.13: Experimental scattered data for temperature with mixture fraction at various axial locations along the HM3e flame……150

8.14: Computational scattered data for temperature with mixture fraction at various axial locations along the HM3e flame. ……..……150

8.15: Radial profiles of mean temperature at various axial lengths of HM1 flame. Predictions obtained from LES calculations with SLFM for different chemical mechanisms used ……...151

8.16: Radial profiles of mean mass fraction of CO_2 at various axial lengths of HM1 flame. Predictions obtained from LES calculations with SLFM for different chemical mechanisms used ……..…….152

8.17: Radial profiles of mean mass fraction of H_2O at various axial lengths of HM1 flame. Predictions obtained from LES calculations with SLFM for different chemical mechanisms used ……...153

8.18: Radial profiles of mean mixture fraction at various axial lengths of HM1 flame. Predictions obtained from LES calculations with SLFM involving GRI 2.11 mechanism …….154

8.19: Radial profiles of mean temperature at various axial lengths of HM1 flame. Predictions obtained from LES calculations with SLFM involving GRI 2.11 mechanism …….……...155

8.20: Radial profiles of mean mass fraction of CO_2 at various axial lengths of HM1 flame. LES with SLFM tested for two different grid configurations……...…….156

8.21: Radial profiles of mean mass fraction of H_2O at various axial lengths of HM1 flame. LES with SLFM tested for two different grid configurations ……157

8.22: Radial profiles of mean temperature at various axial lengths of HM1 flame for comparison of SLFM and NAFM combustion models ...……..157

8.23: Radial profiles of mean temperature at various axial lengths of HM1 flame. LES with SLFM and NAFM tested for effect of radiation ...……158

8.24: Radial profiles of mean mass fraction of CO_2 at various axial lengths of HM1 flame. LES with SLFM and NAFM tested for effect of radiation …….……..159

8.25: Radial profiles of mean mass fraction of H_2O at various axial lengths of HM1 flame. LES with SLFM and NAFM tested for effect of radiation …..……160

8.26: Contour plots of temperature highlighting the flame shapes with two different cases: (1) without radiation and (2) with radiation ……..……..161

8.27: Instantaneous temperature contours at the mid-plane for the NAFM case …..162

8.28: Schematic of experimental test facility for the SMH1 Flame (Courtesy: www.aeromech.usyd.edu.au/thermofluids) ….…….164

8.29: Computational details of SMH1 flame …….……166

8.30: Stream traces of axial velocity plotted against temperature at the centre plane……...167

8.31: Radial plots for axial velocity at different axial locations……....169

8.32: Radial plots for RMS of axial velocity at different axial locations ……169

8.33: Radial plots for RMS of axial velocity at different axial locations ….……170

8.34: Radial plots for RMS of swirl velocity at different axial locations ……170

8.35: Radial plots for mixture fraction at different axial locations …...……171

8.36: Radial plots of mixture fraction variance at different axial locations …..……173

8.37: Radial plots of temperature at different axial locations …...……173

8.38: Comparison of mean temperature plot at centre plane (a) Without radiation (left) (b) With radiation (right)……175

8.39: Instantaneous temperature comparisons at the centre plane (a) Without radiation (b) With radiation……...175

8.40: Radial plots for mean mass fraction of H_2O at different axial locations ……..177

8.41: Radial plots for mean mass fraction of CO_2 at different axial locations ……..178

8.42: Radial plots for mean temperature at different axial locations – comparison for different chemical mechanisms……..180

8.43: Radial plots for mean CO_2 mass fraction at different axial locations – comparison for different chemical mechanisms …..……..180

8.44: Radial plots for mean H_2O mass fraction at different axial locations – comparison for different chemical mechanisms…….181

9.1: Schematic of the burner geometry
(Source: http://www.me.berkeley.edu/cal/VCB/Data/).....183

9.2: Details of computational grid and domain with boundary conditions specified – Berkeley Flame ……..186

9.3: Radial plots of mixture fraction at various axial locations along the burner axis for CH_4/Air Flame ……..……...188

9.4: Temperature contours plot for comparison of SLFM and UFPV (a) UFPV (b) SLFM for CH_4/Air flame ……..……188

9.5: Radial plots of temperature at various axial locations along the burner axis for CH_4/Air Flame ……..189

9.6: Scattered temperature data plotted against mixture fraction at specific axial locations ……190

9.7: Radial plots of mean mass fraction of H_2O at various axial locations along the burner axis for CH_4/Air Flame ….……191

9.8: Mass fraction of CO_2 contours plot for comparison of SLFM and UFPV (a) UFPV (b) SLFM ……...192

9.9: Radial plots of mean mass fraction of CO_2 at two axial locations along the burner axis for CH_4/Air Flame ….……..…...193

9.10: Radial plots of mean mass fraction of CO at two axial locations along the burner axis for CH_4/Air Flame …….…….....193

9.11: Radial plots of mixture fraction at various axial locations along the burner axis for H_2/N_2 Flame …….194

9.12: Radial plots of temperature at various axial locations along the burner axis for H_2/N_2 Flame ……..……195

9.13: Temperature contour plot for the observation of lift-off at the centre plane for H_2-N_2 flame……...……196

9.14: Contour plot of averaged OH mass fraction (ppm) for the observation of lift-off at the centre plane for H_2-N_2 flame……...197

9.15: Contour plot of instantaneous OH mass fraction (ppm) for the observation of lift-off at the centre plane for H_2-N_2 flame ……...197

9.16: Contour plot of averaged OH mass fraction (ppm) for the observation of lift-off at the centre plane for H_2-N_2 flame with 200ppm iso-contour line ……..198

9.17: Experimental scattered data for temperature with mixture fraction at different axial locations along the burner …….…….……...199

9.18: Numerical calculated scattered data for temperature with mixture fraction at different axial locations along the burner ……..200

9.19: Variation in the instantaneous filtered temperature (K) distribution with respect to time– H_2/N_2 Flame ...…….203

List of Tables

1.1: Turbulent combustion models (*Source:* Turbulent Combustion, N Peters, Cambridge University Press, 2000)……..…….…….5

8.1: Details of bluff body flames under study and their condition…….134

9.1: Details of the two lifted flame configurations – Berkeley flames...……...……184

Nomenclature

Roman Letters

C	Reaction Progress variable
Co	Courant Number
C_p	Specific heat at constant pressure
C_s	Smagorinsky coefficient
f	Mixture fraction
f_{st}	Stoichiometric mixture fraction
f_e	Mass fraction of element
h	Mixture enthalpy
k	Turbulent kinetic energy
l	Turbulent length scale
p	Pressure
$P(\ )$	Probability density function
Pe	Peclet number
Pr	Prandtl number
R_o	Universal gas constant
Re	Reynolds number
Sc	Schmidt number
T	Temperature
t	Time
u_k	Cartesian velocity components
W_i	Molecular weight of species
x_k	Cartesian direction components
Y_i	Mass fraction of species
I_b	Black body intensity
p_w	Partial pressure of water vapour
p_c	Partial pressure of carbon dioxide
N_θ	Number of polar directions
N_ϕ	Number of azimuthal directions

Greek Letters

Γ	Diffusive transport coefficient
Γ ( )	Gamma function
δ	Delta function
γ	Time scale ratio
τ	Stress tensor
β	Beta function
λ	Flamelet parameter
δ_{ij}	Kronecker delta
κ	Wave number
$\tilde{\upsilon}$	Dynamic viscosity (laminar)
$\widetilde{\upsilon_t}$	Dynamic eddy viscosity (turbulent)
ρ	Density
ζ	Enthalpy defect
ϕ	Scalar variable
χ	Scalar (mixture fraction) dissipation rate
$\overline{\Delta}$	Grid filter width

Greek Letters Used for Radiation

μ	Cosine of the polar angle
θ	Polar angle
τ	Optical depth
ϕ	Azimuthal angle
ω	Single scattering albedo
ε_w	Wall emissivity
ε_g	Global emissivity

Diacritical Marks

$\tilde{\phi}$	Favre filtered or Favre averaged value of ϕ
$\tilde{\phi}''$	Fluctuations about the Favre filtered or averaged value of ϕ

Subscripts and Superscripts

e	Element
fuel	Fuel
in	Inlet
k	Cartesian directions
norm	Normalized
oxid	Oxidiser
prod	Product
st	Stoichiometric
eq	Equilibrium
q	Quenching limit
slfe	Steady laminar flamelet equations
t	turbulent

Abbreviations

CFD	Computational Fluid Dynamics
RANS	Reynolds Averaged Navier Stokes
DNS	Direct Numerical Simulation
LES	Large eddy simulation
CMC	Conditional Moment Closure
EPFM	Eulerian Particle Flamelet model
PDF	Probability density function
RMS	Root mean square
TDMA	Tri-diagonal matrix algorithm
SLFM	Steady laminar flamelet model
FPV	Flamelet/progress variable
UFPV	Unsteady flamelet/progress variable
NAFM	Non adiabatic flamelet model
DTM	Discrete Transfer Method
DOM	Discrete Ordinate Method
SGS	Subgrid scale
FPDF	Filtered probability density function
HED	High enthalpy defect

NO	Nitric Oxide
CSEM	Conserved scalar equilibrium model
LEM	Linear eddy model
DLN	Dry low NO_x
LEPDF	Large eddy probability density function
LELFM	Large eddy laminar flamelet model
RFRP	Recursive filter refinement procedure
FDF	Filtered density function
TLFM	Transient laminar flamelet model
LFM	Lagrangian flamelet model
RIF	Representative interactive flamelet
DI	Direct injection
EFM	Eulerian flamelet model
LFD	Laminar flamelet decomposition
SMLD	Statistically most likely distribution

Chapter 1

Introduction

1.1 Background

The increasing demand of mankind for a better and enhanced life is forcing the technology towards the global warming. The basic needs are fulfilled from automobiles, electric power generation, petroleum industry and many more. The aftermath of utilizing these facilities have a great effect on the environment. The increasing emissions lead to many health hazards and increasing global temperatures every year. Therefore, there is a need for better science to lower the emissions and increase the efficiency of the engines. In order to achieve this intense research has started decades ago for enhanced design changes in almost all the energy producing equipments. A major part of the pollutants are the products of combustion that are released into the atmosphere through various sources. One of the main sources is the automobile sector which includes internal combustion engines. On the upper atmosphere, aero-engine gas turbine emissions are depleting the ozone layer, thus resulting in various hazards. Also the power sector related processes are increasing the emission levels. Emissions are the result of hydrocarbon combustion process taking place in any energy producing equipment. Therefore, an in-depth understanding of the combustion physics became vital to reduce the emissions.

Any design change on the real specimen to study its effects would lead to increased costs and time. Computational Fluid Dynamics (CFD) came into existence as a solution. Numerical methods in fluid flow gave path to a new generation for flow visualization. CFD is found to be an alternate tool for expensive experimental methods for implementation of design changes. Despite the fact that modelling combustion with CFD has its own setbacks, recent modelling in combustion CFD provides an alternative to experimental processes. Therefore, CFD is considered as a potential tool to predict and replicate the flow physics for its use to reduce the design cycle time and cost involved with experiments.

Numerical simulation involves solving general fluid flow equations using finite volume or finite element techniques. The three basic conceptual alternatives for numerical simulation of turbulence are Reynolds Averaged Navier Stokes (RANS) methodology, Large Eddy Simulation (LES) and Direct Numerical Simulation (DNS). The three methods can be represented in the well-known Kolmogorov energy spectrum as shown in Fig.1. The spectrum shows the distribution of the energy among the various scales of a turbulent flow in wave-number space (i.e., large scales represented by small wave-numbers and small scales by large wave-numbers). Most of the energy is initially contained in the large scales of the energy-containing range, which is then transferred in a cascading process via the inertial sub-range to the scales of the dissipation range, where the energy is eventually dissipated.

Among the above, DNS provides the highest accuracy as it aims at complete resolution of all scales in any turbulent combusting flow. Hence, theoretically there would be no unresolved scales left. But the drawback involved is the utilization of high computational resources and time to solve the time dependent exact solution of Navier Stokes equations involving the broad range of length and time scales appearing in the turbulent flow. Therefore, DNS is applicable to only simple geometries with low Reynolds number flows. DNS is therefore regarded as an unfeasible solution for industry based systems such as gas turbine combustors as they involve with high Reynolds number flows with complex geometries. On the contrary, RANS based simulation involves modelling and solves time averaged quantities of the flow which reduces the computational time drastically. Therefore, RANS based calculations form the eventual solution for industry to produce quick turn around of results which can include all the geometric complexities. The turbulence closure for the RANS based simulations uses either the k-ε or the Reynolds stress model. But the accuracy provided by RANS is not sufficient for complex turbulent flows. Therefore, at one end, the adequate computational capacity is not enough for execution of DNS, while on the other end, inaccurate calculations of RANS gives a promising alternative for LES. The strategy of LES consists of resolving the large flow structures and modelling the effect of the small flow structures on the large structures. In contrast to the use of Reynolds averaging in RANS, spatial filtering is employed in LES to separate the resolved large scales from the unresolved small scales. A detailed description of LES and its advantages is discussed later in this chapter.

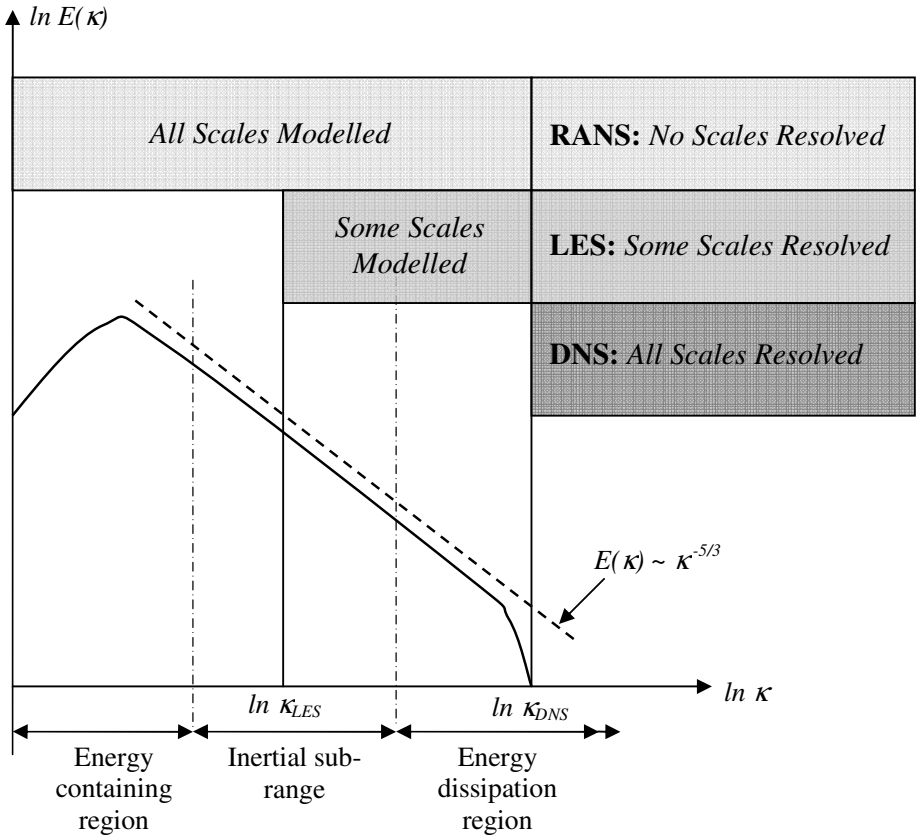

Figure 1.1 Representation of DNS, LES and RANS with Kolmogorov energy spectrum, Energy E(κ) related to a wave-number, κ

Turbulent combustion systems can be categorized under three different streams based on the state of mixing of fuel and oxidiser: premixed, partially premixed and non-premixed combustion. Large amount of work is done in premixed and non-premixed combustion modelling in the past three decades (Pitsch *et al*. (1996), Pierce and Moin (1998), Poinsot and Veynante (2001), Cook *et al.* (2007), Malalasekera *et al.* (2008), Kempf *et al.* (2008)). Recently, partially premixed mode of combustion is attracting the gas turbine combustor industry as most of the industrial combustors and furnaces are prone to partial premixing rather than premixed or non-premixed modes. All the three modes of combustion have a common phenomena in between which involve the strong coupling among the chemical reactions, molecular transport and fluid dynamics. Non-premixed combustion ideally takes place at stoichiometric conditions leading to high peak temperatures and therefore higher NO_x emissions. While in premixed combustion, fuel and oxidizer are thoroughly mixed prior to reaching the reaction zone also called as flame front. In contrast to the non-premixed combustion

the position of the reaction zone is not defined by the diffusion of reactants, but by balancing the local convective velocity of the reactants with the rate of consumption of the reactants which corresponds to flame speed. Premixed combustion can take place at equivalence ratio other than one and therefore the excess air in the mixture helps in reducing the maximum temperatures in the reaction zone. Hence the thermal NO_x production can be controlled in this mode of combustion. Partially premixed combustion is characterized by its degree of unmixedness and helps to achieve reduction in the maximum flame temperatures keeping the flame stable. Therefore, flame propagation, lowering emissions and flame stability issues can be handled with this mode of combustion.

Modelling of turbulent non-premixed flames can be subdivided into two groups in terms of the assumption used in chemistry and transport phenomenon. The two major assumptions in the chemistry model studies are infinitely fast chemistry assumption and finite rate chemistry assumption. Conserved Scalar Equilibrium Model (CSEM) is the most popularly used combustion model with infinitely fast chemistry for non-premixed flames. Bray-Moss-Libby Model (Bray and Moss, 1977; Libby and Bray, 1981) is used in the premixed category for infinitely fast chemistry. The combustion models widely used that are based on the finite rate chemistry are flamelet models, PDF transport model and Conditional Moment Closure (CMC) model. Table .1 shows a summary of main combustion models. CSEM is the combination of equilibrium model with presumed PDF approach with infinitely fast chemistry for non-premixed combustion. This chemistry model is simplest and most effectively used in the past but was not able to predict the emissions correctly. In the finite rate chemistry models, PDF and LEM are the most advanced models used in both premixed and non-premixed modes. However, the major drawback lies in the computational time required as it involves high number of chemical reaction mechanisms in its solution. CMC and flamelet model for non-premixed combustion have proven to be best ongoing models in research, but CMC model was not considered again for application in the industry due to its high computational time required to calculate chemistry. Therefore, the only model that includes detailed chemistry and allows for numerical separation of turbulence and chemistry calculations in order to reduce the computational time and gives increased accuracy in the predictions is the flamelet

modelling approach. The present research is thus focused on advanced flamelet modelling for non-premixed flames based on mixture fraction.

Table.1.1 Turbulent combustion models (*Source:* Turbulent Combustion, N Peters, Cambridge University Press, 2000)

<table>
<tr><th></th><th>Premixed Combustion</th><th>Non-premixed Combustion</th></tr>
<tr><td>Infinitely Fast Chemistry</td><td>Bray-Moss-Libby Model
Coherent Flame Model</td><td>Conserved-Scalar Equilibrium Model (CSEM)</td></tr>
<tr><td rowspan="4">Finite Rate Chemistry</td><td rowspan="2">Flamelet Model Based on the G-Equation, (Peters, 1986)</td><td>Flamelet Model Based on Mixture Fraction, (Peters, 1984)</td></tr>
<tr><td>Conditional Moment Closure (CMC), (Klimenko, 1990) (Bilger, 1993)</td></tr>
<tr><td colspan="2">PDF Transport Equation Model, (Pope, 1985)</td></tr>
<tr><td colspan="2">Linear Eddy Model (LEM), (Kerstein,1992)</td></tr>
</table>

Flamelet model treats turbulent and combustion separately. This model assumes a turbulent diffusion flame to be an ensemble of locally stretched laminar flamelets. The flamelets maintain the structure even though they are strained and stretched by the turbulent flow field. Non-premixed combustion process takes place at very high Reynolds number which indicates smaller Kolmogorov length scales (varies approximately as $Re^{-3/4}$) and flamelet approach can be applied even if the local flame thickness is smaller than the Kolmogorov length scale and therefore proved to be the ultimate choice for combustion model. In this approach, species concentrations are determined from the laminar flamelet solution. Detailed kinetics can be captured by including finite rate effects in the flamelet model. This makes the chemical reaction mechanism to decouple effectively with the turbulence model. A flamelet model is therefore, required to build further to be able to get the predicting capabilities for extreme finite rate chemistry with extinction and re-ignition physics. Also with the advancements in Dry Low NO_x (DLN) combustion systems emerging in the industry with effect from the stringent emission norms, there is a need for better combustion chamber design and thus better combustion model to validate these design changes. Laminar flamelet model is therefore considered as one of the successful combustion

models to be improvised for extending and enhancing its capabilities to capture these emissions for a better design of the combustors. Also the inclusion of the physical phenomena like radiation coupled with turbulence with flamelet model would be advantageous.

Progress variable approach of Pierce and Moin (2004) with flamelet theory incorporated, has spurred the modelling approach for non-premixed flames. This methodology also termed as Flamelet/Progress Variable (FPV) approach have been found to excel and overcome the drawbacks of the flamelet model. Although the inclusion of progress variable equation in the solution procedure increases the computational time, its predicting capabilities for the partially premixed flames have given a new dimension for the FPV approach. Recently, FPV approach has been applied with both the turbulence models like RANS and LES and found to predict well for partially premixed lifted flames (Ravikanti, 2008). Inclusion of transient flamelets in the FPV approach for the consideration of scalar dissipation rate fluctuations to build an improved flamelet model to predict the local extinction and re-ignition phenomena is the current research interest. This modelling strategy is termed as Unsteady Flamelet Progress Variable (UFPV) approach. Most recently UFPV has been attempted with success for the emission predictions (Ihme and Pitsch, 2005). This new approach towards the modelling of partially premixed combustion is yet to be explored.

RANS based modelling has been so far the most commonly used tool for turbulence calculations involving combustion processes due to its lower computational time involved. But in the recent years, interest has grown in applying LES to reactive flows due to immense increase in available computational power. LES has started as a research tool three decades ago but currently is in the implementation stage for all CFD analysis both in academia and industry. Deardorf (1974) was the first to implement LES on three dimensional turbulent channel flows. Since then LES was under various applications and improvisations, undergone considerable progress with engineering oriented problems with its unsteady solution behaviour from simple flow configurations to complex turbulent flames, Piomelli (1999), Poinsot and Veynante (2001). In the recent past, LES is applied in the problems dealing with thermo-acoustic instabilities in the combustors. LES resolves the large scale turbulent motions

which contain the majority of turbulent kinetic energy and control the dynamics of turbulence while small scales or the subgrid scales are restricted to modelling. RANS on the other end engross in modelling of all scales. In LES, the model coefficients for the sub-grid scale models can be determined by employing dynamic model (Germano *et al.* 1991) embedded in the solution, which is independent of filter size. These features give LES a better chance to display its advantages with regard to the accuracy and predictability of turbulence compared to RANS. But in the LES of reacting flows, chemical reactions take place at the smallest scales and thus resolving large scale motions cannot be applied to chemical source terms. Therefore, the modelling of source term is needed similar to RANS based calculations. Considering the merits and de-merits, LES still have the advantage of calculating intense mixing process and advanced predicting capabilities with improved accuracy when compared with RANS.

Having gained reasonable success with RANS based flamelet modelling LES with flamelet theory is the current research issue for modelling turbulent non-premixed combustion. Application of flamelet model to LES has drawn significant research interest and still an ongoing process for advanced modelling strategies (Cook & Riley, 1998; Pitsch & Steiner, 2000; Pitsch, 2002; Mahesh *et al.,* 2004; Raman & Pitsch, 2005; Malalasekera *et al.*, 2008). As mentioned earlier, UFPV approach is the advanced flamelet modelling option (Pitsch & Ihme, 2005) for partially premixed combusting flames. Therefore, considering the detailed chemistry with finite rate effects to its extreme limits to capture the flame extinction and re-ignition physics, the UFPV approach with LES turbulence model proves to be a promising numerical tool for lifted flames of partially premixed category.

Within the complexities involved with combustion modelling like turbulence/chemistry interactions, chemical kinetics, coupling of flow turbulence and heat transfer, radiation is often neglected in numerical simulations of many combusting flows. This is mainly due to the high computational effort needed to model radiation and the complexities involved in coupling with turbulence and chemistry. However, some of the main reasons that enforce for the consideration of thermal radiation in any combusting flame are (i) radiative heat transfer rates vary strongly with temperature differences (to the fourth or higher power) and (ii) the radiation properties of combustion gases exhibit strong and irregular variations with

wave-number (Modest, 2003). Therefore, inclusion of radiation effects in combustion models is an important aspect to achieve high standards of accuracy in predictions. Not only radiation coupled turbulence combustion models predict correct wall heat transfer but also computes the right flame physics. Radiation is the primary mechanism of heat transfer in flames that contain large volumes of small solid particles. These solid particles occur either naturally (soot, pulverized coal) or introduced to enhance the heat transfer characteristics (metal oxides in natural gas flames) (Sivathanu and Gore, 1993). Radiation fluctuations provide valuable information concerning turbulence/radiation interactions in flames. These fluctuations in-practice affects the temperature variations and absorption coefficients which contribute to combustion instabilities leading to flame extinction and re-ignition effects. The time varying behavior of LES turbulence model is well suited for coupling with radiation fluctuations involved in any practical flame.

At high temperatures, heat transfer takes place by thermal radiation process rather than convective transfer process (Edwards and Balakrishnan, 1973). Most of the combustion related equipments deal with high temperature flows. Therefore, radiation heat transfer plays a vital role in turbulence combustion modelling. This also involves many practical situations like building configurations, complex furnaces, pulse combustion systems and others. In turbulent reacting flows, the turbulent fluctuations of the flow field cause fluctuations of species concentrations and temperature which in-turn influences the radiation field. The combined effects of fluctuating radiation properties and temperature increase the fluctuations in radiative fluxes reasonably higher than the estimates based on mean properties. Therefore, in all numerical simulations, fluctuations in radiation field interact with the fluctuations of flow field. This necessitates the need for an appropriate model for turbulence radiation interaction (TRI) (Li and Modest, 2003). Sufficient experimental and numerical evidence suggests that TRI has a significant influence due to the above mentioned fluctuations of species and temperature which involves with the non-linear relationship among temperature, radiative properties and radiation intensity (Coelho *et al.,* 2003). Hence in order to predict radiative heat transfer accurately in many practical turbulent flows, it is necessary to couple the radiation calculation with turbulence calculations.

Recently, effects of TRI has been studied for both premixed and non-premixed flames related to industrial combustors and laboratory-scale flames with all the turbulence models like RANS, DNS and LES, Xu *et al.,* (2006), Wu *et al.,* (2007), Deshmukh *et al.,* (2008), Goncalves dos Santos *et al.* (2008). But most of the work involved only simple chemistry and stressed for implementation of detailed finite rate chemistry in their TRI studies. RANS based radiation models are based on mean of cell predictions for the radiation calculations. On the other hand, LES can be utilized for unsteady calculations of radiation where the quantities are calculated exactly instead of mean values. Large eddy simulation is coupled with the radiative heat transfer with the data exchange process in a most portable, flexible and versatile way (Goncalves *et al.*, 2008). The two independent solvers are linked through a specialized framework and are coupled in a required manner for the exchange and calculation of data. Motivated by the influence of radiation on combustion related turbulent flows, the present research is focused on direct coupling of radiation model with LES based turbulence calculations applied specifically to non-premixed flames mainly bearing in mind the current and future needs of gas turbine industry.

Along with the turbulence-radiation studies for non-premixed flames, the current research also focuses on the development of advanced combustion models like UFPV for flame statistics of partially premixed lifted flames.

1.2 Research Objectives

The specific objectives of the current research are to:

1. Develop and validate the predictive capability of Unsteady Flamelet/Progress Variable (UFPV) combustion model for LES based turbulent partially premixed combusting flames.
2. Conduct detailed investigation on turbulence coupled radiation calculations with Non-Adiabatic Flamelet Model (NAFM) and its effect on the flame structure for swirl and bluff body based non-premixed flames using LES.

The current research is focused to conduct advanced unsteady flamelet modelling strategy with a developed in-house FORTRAN based LES numerical code. As per the motivation from TRI (Turbulence Radiation Interaction) studies, research is

conducted to couple a FORTRAN based radiation code with the above mentioned LES code. After the achievement of the aforementioned topics under research, it is expected that this would not only contribute to improve our knowledge in the predictive capability of the advanced combustion models such as UFPV but also will enhance the sophistication of the in-house LES code coupled with radiation and combustion modelling facility to all categories of turbulent combusting and radiating flames.

In order to attain the objectives of this research the following sub-tasks have been laid out (also represented in block diagram if Fig. 1.2 in a simplest form):

1. Incorporation of steady laminar flamelet model (SLFM) and unsteady flamelet/progress variable (UFPV) approach based models in the in-house LES code with the capability of conducting calculations through a computationally efficient look-up-table strategy.

   1.1 Generation of steady and unsteady adiabatic flamelets using the FlameMaster code.
   1.2 Development of pre-processing tools for generating pre-integrated look-up-tables for SLFM and UFPV.

2. Development and incorporation of LES based modelling for turbulent non-premixed bluff-body and swirl stabilized flames with steady flamelet model for SLFM studies. Later the incorporation of non-adiabatic flamelet model for LES radiation studies with the introduction of enthalpy defect concept in the in-house LES code through lookup table formulation.

   2.1 Generation of steady adiabatic flamelets using the FlameMaster code and conversion to non-adiabatic flamelet solution.
   2.2 Generation of pre-processing tools for generating pre-integrated look-up-tables with both adiabatic for SLFM studies and non-adiabatic flamelet solution with the inclusion of enthalpy defect for coupled turbulence-radiation studies.
   2.3 Incorporation of enthalpy equation in the LES code to calculate the enthalpy defect in order to couple the radiation code for the studies involving turbulence.

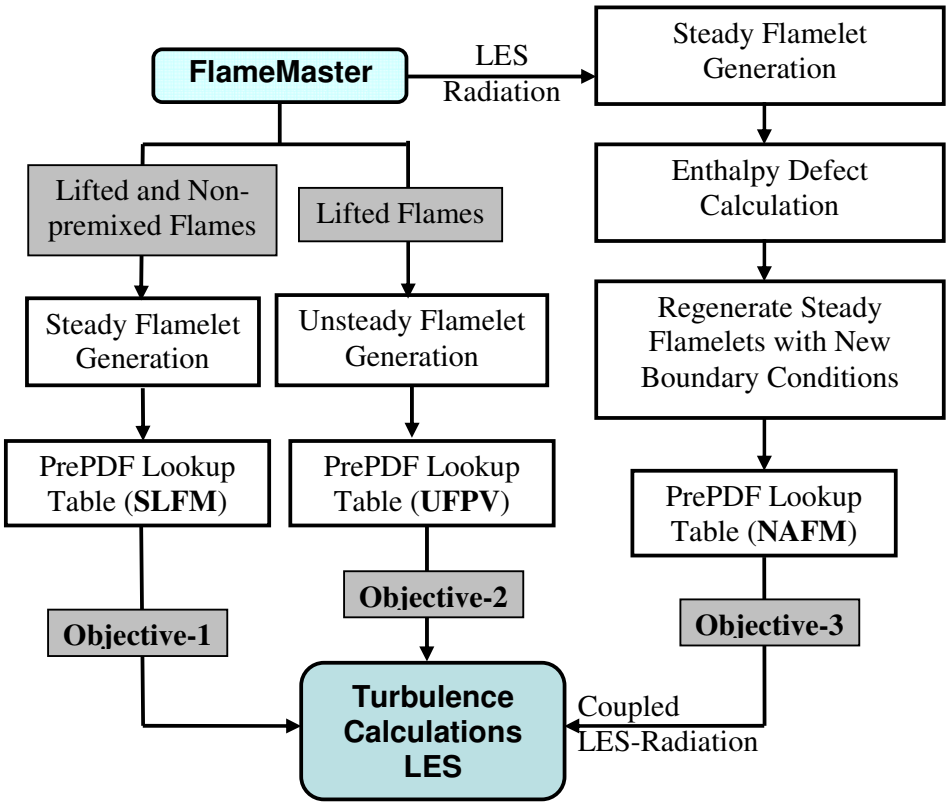

Figure 1.2 Block diagram of the research work performed

1.3 Organization of Thesis

The present chapter discussed the background for the research objectives and motivation obtained from the previous studies. The remaining part of the thesis has been organized as below:

Chapter 2: Literature in the area of flamelet based modelling of turbulent non-premixed and partially premixed combustion is reviewed. Also, literature in the field of turbulence radiation interactions in the context of both RANS and LES is presented.

Chapter 3: The LES approach of modelling turbulence with the solution technique involved in solving the governing equations is presented. LES formulation with the description of filtering technique, models employed for the closure of subgrid stress and models for closure of subgrid scalar fluxes is discussed in detail.

Chapter 4: Combustion models used in the LES based modelling is presented. Application of steady laminar flamelet model, non-adiabatic flamelet model and unsteady flamelet progress variable model in the LES calculations is discussed

Chapter 5: Radiation models used in the LES-TRI calculations are presented in this chapter. A detail description of TRI and its coupling with LES involving the data exchange procedure are discussed.

Chapter 6: The numerical approach adopted in the in-house LES code is presented. A detailed description of the solution procedures of LES combustion calculations with the different combustion and radiation models is presented.

Chapter 7: The pre-processing work involving the calculations for the generation of pre-integrated look-up-tables for LES is presented. A detailed working procedure for the pre-processing tools developed for the different steady flamelet model, non-adiabatic flamelet model and the UFPV approach based models is presented.

Chapter 8: Results and discussion pertaining to the LES based modelling of turbulent non-premixed bluff-body and swirl stabilized flames using the steady flamelet model and non-adiabatic flamelet model in conjunction for the effect of radiation on turbulence is presented in this chapter.

Chapter 9: Results and discussion related to LES based modelling of turbulent partially premixed lifted jet flames with steady flamelet model and the unsteady flamelet/progress variable approach based models is presented.

Chapter 10: Conclusions from the present studies and scope for the future work is described in this chapter.

Chapter 2

Literature Review

This chapter reviews the literature that has contributed towards the development of flamelet models in RANS and LES modelling techniques for turbulent non-premixed and partially premixed flames. Literature related to the development and progress of TRI and the importance of radiation in turbulence combustion is also presented and discussed. Section 2.1 presents the research work involving flamelet models for turbulent non-premixed flames followed by the work on flamelet models specifically developed for partially premixed flames in section 2.2. Work related to the development of the flamelet progress variable are discussed in section 2.3 followed by literature discussions on UFPV which motivated the present research involving development of combustion model for partially premixed turbulent lifted flames in section 2.4. Finally, work related to radiation and TRI involving the effects and importance of TRI in practical combustion systems is discussed in section 2.5.

2.1 Steady Laminar Flamelet Model (SLFM) for Turbulent Non-premixed Combustion

Non-premixed combustion research is focused on diffusion principle where diffusion is the rate controlling parameter. Laminar flamelet modelling was introduced by Peters (1984) which is also known as steady or stretched laminar flamelet model (SLFM). SLFM is based on a concepts developed by Williams (1975) which defines turbulent diffusion flame brush as an ensemble of discrete, steady laminar stretched flames, called “flamelets”. Each and every individual flamelet is assumed to have the same structure as laminar flames obtained by calculations. These laminar flamelets are embedded in a turbulent flame by the introduction of statistical PDF methods. Peters (1983, 1984) have validated the theory of existence of laminar flamelets in turbulent flames in a systematic way through numerical approach. Also, Robert and Moss (1981) and Drake (1986) have conducted experimental studies to verify the existence of laminar flamelets in turbulent diffusion flames. The parameter that guides

the stretch in the flamelets is scalar dissipation rate and all the thermo-chemical properties of any single flamelet is expressed as a function of conserved scalar "mixture fraction" and scalar dissipation rate. Thus, the flamelet model describes the turbulent flame structure as the thermo-chemical flame brush with statistical distribution of mixture fraction and scalar dissipation rate. The main advantage of using flamelet model is that realistic chemical kinetics effects can be incorporated into turbulent flames. Having explained the simplicity of the flamelet model, it is limited to combustion modelling with relatively fast chemistry. The flame is assumed to respond instantaneously to the aerodynamic strain and therefore the model was found to be incapable of predicting deep non-equilibrium effects such as extinction, re-ignition and slow chemistry processes like NO_x formation. This incapability of flamelet model was improvised with the introduction of flamelets into turbulent flame by considering their joint probability density function (PDF). The evaluation of the PDF is simplified by assuming statistical independence of the parameters and presuming the shape of the PDF for mixture fraction to follow a β function and that of scalar dissipation to follow log-normal distribution in most cases. Scalar dissipation rate distribution can also take the shape of delta PDF depending on the problem statement and time. Thus the incorporation of detailed chemistry was possible with PDF approach with laminar flamelet model which offers tremendous computational savings by separating the turbulent flow calculations from chemistry calculations.

2.1.1SLFM applied to RANS and LES

This section initially discusses the research works performed on SLFM related to RANS turbulence model and then later with LES. Development of laminar flamelet model was performed by Liew *et al.* (1984) for modelling turbulent methane/air jet diffusion flames. The effect of the stretch was found to be very minimal in the entire flow field. However, the model was successful in predicting the observed oxygen penetration through burning zone due to local quenching. But the predictions with O_2 and CO concentrations were distracted and lead to the conclusion that amendments are required in the model to account for the post flamelet process where probable partial mixing of reactants occurs. Overall, the potential of their model in the implications for practical combustors can be judged from the results. Rogg *et al* (1986) extended the model to take into account partial premixedness of diffusion

flamelets. The results depicted reasonable O_2 concentration predictions to data but there was no improvement in CO predictions. Haworth *et al.* (1988a) studied the application of SLFM on turbulent jet diffusion flames with $CO/H_2/N_2$ –air mixtures. Monte Carlo solution algorithm with a two-scalar stretched laminar flamelet chemistry approach was used. Their predictions were compared with experiments and found that laminar flamelet approach was reasonably well predicting the fuel rich regions of the flow, but yielded an overly rapid approach to chemical equilibrium in the downstream of the jet. The importance of flamelet model towards the coupling between chemical reaction and molecular diffusion was clearly specified. Lentini (1994) also applied SLFM to $CO/H_2/N_2$ turbulent jet diffusion flame and found that model's prediction capability with respect to super equilibrium concentration of OH radical was superior to that of equilibrium model. Based on the results, Lentini (1994) also showed that SLFM predicted an overly rapid approach to chemical equilibrium. Consideration of time varying behavior of scalar dissipation rate could resolve this issue, Haworth *et al.* (1988b). In another study by Lentini (1994), SLFM was applied to methane/air jet flames originally studied by Liew *et al.* (1984) showed that inclusion of all the flamelets from extinction to equilibrium and also with extinguished or mixing flamelet limit, improves the predictive capabilities of reactive scalars like CO which were over-predicted in the previous studies of Liew *et al.* (1984). SLFM was later applied to study the turbulent jet diffusion flame involving chloromethane-air mixture by Lentini and Puri (1995). The SLFM proved to be in good agreement than near-equilibrium model. Inclusion of finite rate chemistry enabled significant improvement in the predictions of species associated with slow chemical kinetics like CO. However, SLFM in this case had resulted in large discrepancies in the comparisons with experiments.

Hossain (1999) carried out a similar study based on the flamelet model to a relatively complicated reacting flame structures for bluff body stabilized flames. The study included the application of SLFM with inclusion of all the flamelets from extinction to equilibrium similar to the studies of Lentini (1994). The results included the performance of SLFM in $CO/H_2/N_2$ and CH_4/H_2 bluff-body stabilized flames of Correa and Gulati (1992) and Dally *et al.* (1998a, 1998b) respectively. The model capability on various blow-off limits was studied based on the inclusion of finite rate effects. The results showed a promising predictive capability of SLFM for the above

mentioned flames operating away from the blow-off limits. But the model was unable to predict the extinction near to blow-off (70-90 %) as observed in the experiments. Therefore, the use of transient flamelets was one of the proposed studies to consider and capture the extinction phenomena in such combusting flames. A similar study for the capability of SLFM to predict the experimentally observed local flame extinction and re-ignition has been performed by Ferreira (1996) on methane-air jet diffusion flames of Masri *et al.* (1988). Later Ferreira (2001) showed that inclusion of unsteady effects in the flamelet equations of Peters (1984) for partially premixed region resulted in better flame behavior when applied to piloted methane-air flame. Partial premixed state was considered by a simple model based on a single reaction progress variable.

Hossain and Malalasekera (2005) used SLFM to study the flame structures of bluff body non-premixed flames operated at different inlet axial velocities. Results showed reasonably good agreement for temperature and other major species mass fractions. However, their studies failed to predict the local extinction effect at the necking zone of the flame. Hossain and Malalasekera (2007) also conducted studies for the performance of different combustion models on bluff body flames of Dally *et al.* (1998b). Combustion models like laminar flamelet model, equilibrium chemistry model, constrained equilibrium chemistry model and flame sheet models were studied and based on the predictions, laminar flamelet model was found to outperform considering the advanced chemistry calculations. Hossain *et al.* (2001), in a different study for the effects of radiation on bluff body combusting flames, used flamelet model coupled with radiation. However, this did not focus on the flame extinction and self ignition phenomena. Apart from RANS and LES based SLFM modelling, recently, Liu *et al.* (2006) conducted a comparative study of laminar diffusion flamelet model with 2D direct numerical simulation for an axisymmetric co-flow laminar ethylene-air diffusion flame. Significant differences were found with the temperature and other species predictions with the above models. The Flamelet model failed to predict a distinct feature of the co-flow flame structure and the occurrence of the peak concentrations of the CO_2 and H_2O at different locations. It was found to predict a rapid approach to equilibrium in the downstream region of the flame in contradiction with the other model. Neglecting multidimensional convection and diffusion process and inadequate use of boundary conditions for local flamelets in the

downstream region was reported to be the main reasons for the above drawbacks of flamelet model. Flamelet model is thus advised to be used with caution for multidimensional diffusion flames. Recently, Claramunt et al (2006) investigated the application of the laminar flamelet concept to the multidimensional numerical simulation of non-premixed laminar flames. The performance of steady and unsteady flamelets was analyzed.

Research has been carried out intensely with SLFM for NO modelling. The first ever use of flamelet model to simulate nitric oxide was carried out by Vranos *et al.* (1992). Their studies include the flamelet model for turbulent methane/hydrogen jet flames for the prediction of NO levels. Large discrepancies were found with the measured and numerically calculated values of NO. The most possible cause was depicted as the over-prediction in differential diffusion effects of hydrogen and other hydrocarbon species. Other reasons like transient effects and flame interactions were also highlighted. Sanders *et al.* (1997) also carried out a similar study using flamelet model for NO formation in turbulent hydrogen jet diffusion flames and suggested that the discrepancies in over-prediction in NO levels would have been caused as a result of differential diffusion effects. Previous to the above, a numerical analysis of turbulent non-premixed hydrogen-air flames was carried out by Schlatter *et al.* (1996) to predict the NO formation with laminar flamelet model as one of the models. Suggestions were made that the chemical processes must be modeled with concepts of progress variable.

The Flamelet model together with the PDF approach was tested by Chen and Chang (1996) for turbulent methane-hydrogen jet non-premixed flame. Similar to the above mentioned studies, the argument continued with the drawbacks of flamelet model in their studies as well. Modelling of NO formation using flamelet model resulted in pointing out the various effects like transients, flame interaction, preferential diffusion and radiative heat loss as the major sources. Their research reported that radiative heat loss was an important process in the prediction of NO levels especially in the far field of the jet flame where the residence time of the flamelet is high enough for effects of radiation to become significant. Also the failure with the flamelet model for the NO predictions was highlighted when compared with PDF model. In continuation with the use of flamelet model for NO predictions, Heyl and Bockhorn (2001) conducted

numerical modelling of a laminar axisymmetric CH_4/air diffusion flame. Results showed that insufficient resolution of the flamelet library in the low scalar dissipation rate region has an impact on the predictions of temperature and other species. Reasonably good predictions were noticed with temperature and all major species mass fractions except for NO and OH. The influence of the shape of the PDF for scalar dissipation rate on the species like OH and NO has been reported to be the reason behind. Prior to the above study, Chou *et al.* (1998) conducted a detailed flamelet approach towards modelling of NO formation in laminar Bunsen flames. Inclusion of detailed chemistry with a range of scalar dissipation rates was incorporated in the flamelet library along with the radiation modelling for the heat loss on NO formation. Comparisons were observed to be fairly reasonable with the experiments with the flamelet model but advised to improve the radiation model.

SLFM based NO modelling of bluff body stabilized CH_4/H_2 flame through a mean NO transport equation based approach was conducted by Hossain and Malalasekera (2003). Their studies showed the effect of differential diffusion effects and found that unity Lewis number flamelet were predicting better rather than with the inclusion of differential diffusion effects However, Hossain and Malalasekera (2003) showed their results with large underprediction on modelling works of NO. This was attributed to the simplified NO chemistry which accounted for only thermal NO and therefore the need for accounting all possible NO production sources was highlighted. Ravikanti *et al.* (2008) conducted flamelet based NO_x radiation integrated studies for turbulent non-premixed flames with the Reynolds stress model. Radiation was coupled with flamelet with the introduction of enthalpy defect concept. Flamelet model in adiabatic form was extended to non-adiabatic to account the radiation heat loss along with the effects of NO_x formation. An over-prediction in NO_x using different models involving adiabatic and non-adiabatic flamelet models was observed. However, non-adiabatic model with multiple flamelet library data proved to be the best among them with marginal improvement. More recently, Ravikanti (2009) also studied the effect of chemical mechanism from laminar flamelet based modelling for turbulent bluff body flames. GRI Mech-2.11 was found to predict more close to the experimental values for NO_x with an over-prediction in the computational results. However, from the above two studies of Ravikanti *et al.* (2008, 2009) it can be concluded that non-adiabatic flamelet model (enthalpy defect concept) with multiple flamelets with GRI

Mech-2.11 found to be the optimum flamelet modelling approach for NO_x based calculations.

Based on the reasonable success of the flamelet model on RANS based simulations, LES was also a popular choice for many researchers for the validation of flamelet model in its preliminary and advanced stages. Cook *et al.* (1997) performed the first ever studies on the sub grid scale combustion model (the so called flamelet model in LES). Their studies include the application of a presumed shape beta PDF formulation called the Large Eddy Probability Density Function (LEPDF), for the mixture fraction and the flamelet profiles were obtained from a single step reaction. The concept of LEPDF was proposed in their previous work (Cook and Riley, 1994) by the filtered mixture fraction and its subgrid variance which was obtained from an algebraic model equation based on scale similarity assumption. This model was found to be reasonably accurate compared to DNS data of homogeneous, isotropic decaying turbulence. Cook *et al.* (1997) used flamelet theory in conjunction with an assumed Large Eddy Probability Density Function (LEPDF) to derive a model for the filtered chemical species in an incompressible, isothermal flow with a single step reaction. This model was named as Large Eddy Laminar Flamelet Model (LELFM). Following their previous work, Cook and Riley (1998) performed a priori testing of this model by varying the activation energy of the one-step model and obtained better agreement with DNS data than models using equilibrium chemistry.

A method for predicting filtered chemical species concentrations and filtered reaction rates in LES of non-premixed, non-isothermal, turbulent reacting flows has been demonstrated to be quite accurate for higher Damkohler numbers by De Bruyn Kops *et al.* (1998). This subgrid model was based on flamelet theory and used presumed forms for both the dissipation rate and subgrid scale probability density function of the conserved scalar. The model was found to accurately reproduce the spatial average of the filtered species obtained from DNS data.

Pierce and Moin (1998) further extended the work of Cook *et al.* (1997) to include the effects of swirl and chemical heat release which required the use of variable-density transport equations. These studies were successful in predicting velocity and conserved scalar mixing fields in complex combustor flows but they did not consider

the effects of finite-rate chemistry or the general issue of chemistry modelling in LES. Using the dynamic model, they conducted LES of a swirling, confined, coaxial jet flame and obtained convincing comparisons with experimental data. Branley and Jones (1999) employed the dynamic model of Pierce and Moin (1998) and conducted LES of swirling methane flame with a single flamelet profile. Their results showed good qualitative agreement with the measurements.

A Recursive Filter Refinement Procedure (RFRP) for large eddy simulations of bluff body stabilized non-premixed flames was carried out by Raman and Pitsch (2005). This new strategy for LES grid generation with RFRP has been used to generate optimized clustering for variable density combustion simulations. Methane/hydrogen fuel based bluff body stabilized experimental configuration has been simulated with the combustion chemistry using a pre-computed, laminar flamelet model-based lookup table. A beta function was used for the sub-filter mixture fraction filtered density function (FDF). This simulation procedure was used along with the steady flamelet model for subgrid scale combustion and the dynamic model of Pierce and Moin (1998) for turbulent CH_4/H_2 bluff-body stabilized flames and excellent match with experimental data was obtained. Kempf *et al.* (2005) conducted LES of piloted methane/air jet flame using a steady flamelet model with multiple flamelet libraries involving detailed chemistry. The subgrid mixture fraction variance was modeled using the approach of Forkel (1999) while the filtered scalar dissipation rate was obtained from the model suggested by Girimaji and Zhou (1996) and De Bruyn Kops *et al*. (1998). Their calculations showed that for the selected partially premixed fuel, steady flamelet approach sufficiently describes the major species except for CO which is over-predicted in the fuel rich region. Following the previous work, Kempf *et al.* (2006) conducted LES of CH_4/H_2 bluff-body stabilized flames of Dally *et al.* (1998a) and obtained encouraging results for temperature and major species but they reported significant errors in the computed NO concentration. Application of LES to turbulent CH_4/H_2 unconfined swirling flames was studied by Ranga-Dinesh *et al*. (2006) employing a single flamelet based steady flamelet model. Their work adopted the scale similarity model of Cook and Riley (1994) to model the subgrid variance of mixture fraction and employed the localized dynamic procedure of Piomelli and Liu (1995) to calculate the turbulent eddy viscosity. They showed reasonably good results for temperature and major species. However, the model failed to capture the vortex

breakdown downstream of the flame. More recently Malalasekera *et al.* (2008) demonstrated that LES with flamelet modelling predicts better flame structure for swirl based flames. Results conclude a strong modelling capability of SLFM but also the discrepancies in the comparisons at some locations along the flame suggest that a better combustion model related to flamelet modelling is needed. The steady laminar flamelet model was used in two different LES codes from two different research groups for simulation of swirl stabilized turbulent flames for both non-reacting and reacting cases, Kempf *et al.* (2008). Their results highlight good agreement with the recirculation structures and vortex breakdown. However, the predictions for reacting flow was less satisfactory. Failure in the accurate predictions of temperature and other major species allowed for an improvement in SLFM combustion model to incorporate the transient effects as one of the solutions. Importance of transient effects in the flamelet solution and its background research works is explained in the next section related to RANS and LES.

2.1.2Effect of Transient Flamelet Modelling

The first half of this section deals with the research involved in RANS based transient flamelet modelling and remaining half discusses the LES based transient SLFM. The drawbacks of single flamelet model of SLFM in the flame predictions could be overcome with consideration of unsteady effects in the model. The solution of the flamelet equations of Peters (1984) in general omits the time dependent term in most of the SLFM models and thereby results in steady laminar flamelets. This involves the dependency of any scalar which is parameterized in terms of scalar dissipation rate and stoichiometric mixture fraction. The omission of time variable decreases the variations in scalar dissipation rate. In general all turbulent combusting flames have high to moderate fluctuations in scalar dissipation rate which needs to be accounted for. Therefore, consideration of time variable in the calculation of flamelets attracted the researchers to include the unsteady term in the flamelet equations. The importance of time dependent flame structures in laminar flamelet models for turbulent jet diffusion flames was first shown by Haworth *et al*. (1988b). They introduced an ad-hoc modification to the laminar flamelet model through an equivalent strain analysis and obtained improved agreement with data for $CO/H_2/N_2$ jet flame. Unsteady flamelets were employed by Mauss *et al.* (1990) to simulate flamelet extinction and

re-ignition effects in a steady turbulent jet diffusion flame. A Lagrangian time was introduced to account for history effects in the flamelet structure. Unsteady effects caused by localized extinction in steady jet diffusion flames were studied by Ferreira (1996). The study developed a transient laminar flamelet model (TLFM) which used a transient flamelet library parameterized by mixture fraction, scalar dissipation rate, reaction progress variable and flamelet residence time similar to the Lagrangian time. TLFM was shown to produce the extent of local extinction and re-ignition behavior observed in the experimental study of Masri *et al*. (1988).

Pitsch *et al.* (1998) developed an unsteady flamelet approach and validated with experiments for a turbulent jet diffusion flame. The unsteady flamelet was solved interactively with CFD solver and transient effects were discussed in relevant time scales. Flame structure was reported to be undisturbed with the inclusion of transient flamelets and radiation was said to have minimal effect on the flamelets. However, the study also suggested that transient effects were needed to slow production process of NO. A qualitative comparison of results with experiments showed that steady flamelet model performed well with temperature and other species like OH but failed to reproduce the NO formation. An important observation from their work was consideration of radiation through a radiation source term in steady flamelet equations which lead to deterioration in predictions since the omission of time dependant term lead to inaccurate capturing of effect of radiation heat loss which is a slow physical phenomenon. However, the same when considered with unsteady flamelet equations improved the predictions for NO. Pitsch (2000) extended the above Lagrangian Flamelet Model (LFM) to account for differential diffusion effects in steady turbulent $CH_4/H_2/N_2$-air diffusion flame and found reasonably good agreement with data. Three different chemical mechanisms were tested and found to prove identical in the predictions. Results suggested that a differential diffusion effects were influential even they were considered only close to the nozzle and switched to unity Lewis number downstream of the potential core. Flamelet modelling was used to predict the local extinction and re-ignition in turbulent non-premixed combustion by accounting a flamelet formulation for transport along mixture fraction iso-surfaces by Pitsch *et al.* (2003). A new transport term in the flamelet equations was modeled by stochastic mixing approach. The time scales appearing in the model is considered with the effect of changes in the scalar dissipation rate. A new “re-ignition parameter” was defined

and modified equations were solved with Monte Carlo calculations. Results showed that re-ignition parameter modified the steady state solution by increasing the scalar dissipation rate at the lower turning point of the S-shaped curve thereby allowing re-ignition to the burning state at higher scalar dissipation rates. Earlier to this study, Kim *et al.* (2001) conducted flamelet modelling with both steady and unsteady calculations on turbulent non-premixed $CO/H_2/N_2$ jet flames for the NO_x formulation in specific. Unsteady flamelet model with Lagrangian approach correctly predicted the experimental data for conditional mean scalar structure and unconditional means as well as the full NO_x chemistry. Failure in steady flamelet approach has been mentioned with the potential error involved with the optically thin radiation model; full NO chemistry model and the error with differential diffusion. Very recently, Delhaye *et al.* (2008) conducted detailed simulations for a series of steady and unsteady non-premixed flames with a specific type of unsteady flamelet simulation where flamelets were subjected to temporally varying strain rates.

Application of flamelet model to unsteady turbulent flows like internal combustion engines was also carried out and therefore the importance of flamelet model in these types of engines should be discussed. Unsteady flamelet models have been applied to diesel engines in the past. Pitsch *et al.* (1996) proposed a new concept called "Representative Interactive flamelet" (RIF) where unsteady 1D flamelet calculations were interactively coupled with the CFD code. The flamelet parameters that govern the unsteady evolution of the flamelets were extracted from the solution of the CFD code by statistically averaging over a representative domain. This model was applied to an n-heptane fueled diesel engine and was found to be capable of describing auto-ignition, following the burnout of the partially premixed phase, and the transition to diffusive burning. NO_x data was found to be in good agreement, while soot was under-predicted. In this RIF model only one interactive flamelet was considered representative of entire domain and the spatial variation of scalar dissipation rate was ignored. Barths *et al.* (1998) extended the RIF model to multiple flamelets which accounted for the spatial dependence of scalar dissipation rate. The RIF model was used in the above studies for Diesel engine combustion processes with not more than two consecutive injections into the combustion chamber. Felsch *et al.* (2009) recently studied the extension of RIF model for any number of injection events with the extended flamelet model. Recently, Cook *et al.* (2007) developed an enthalpy-flamelet

based model of auto-ignition with thermal in-homogeneities applicable to compression ignition engines.

The approach of Eulerian Particle Flamelet Model (EPFM) includes numerical tracer particles each representing a flamelet history is introduced into the turbulent flow field. An unsteady convection-diffusion equation is solved in CFD code for each tracer particle to find probability of local occurrence of flamelet. The current flamelet solution is then weighted with these local probabilities to obtain scalar concentrations. This model was applied to turbulent non-premixed DI diesel engine combustion by Barths *et al*. (1998) and Barths *et al*. (2000). They found a significant improvement in the prediction of partially premixed burning phase and subsequent pollutant formation, NO_x and Soot. The EPFM has also been applied to steady turbulent non-premixed combustion in a gas turbine combustor by Barths *et al* (1998a). One of the main advantages of EPFM over Lagrangian model is it's applicability to both parabolic as well as elliptical flows. In the Lagrangian flamelet model the flamelet time is computed by integration of the inverse of the streamwise velocity at the stoichiometric radial position along the streamwise direction which limits its application to strictly parabolic flows.

Coelho and Peters (2001a) simulated the piloted methane/air jet flame with EPFM. Unsteady calculations were performed in post processing stage using Eulerian transport equations for passive scalars to describe temporal evolution of the scalar dissipation rate. Predictions with EPFM were shown to have significantly better agreement for NO compared to those with SLFM. Coelho and Peters (2001b) applied EPFM to a combustor with high air preheating and strong internal exhaust gas recirculation. Good agreement to data for NO_x emissions was achieved. Riesmeier *et al*. (2004) applied EPFM to kerosene fueled diffusion flame gas turbine combustor and encouraging predictions for exhaust emissions, NO_x and soot were achieved. Odedra and Malalasekera (2007) applied EPFM to complex turbulent non-premixed bluff body flames. Both the steady and unsteady flamelet models were tested. Results showed that unsteady effects were negligible for almost all major species including OH. But EPFM proved to be efficient in capturing NO formation. Different chemical mechanisms were also tested and GRI Mech-2.11 with EPFM showed encouraging results for NO formulation. Very recently, Kim and Kim (2008) applied EPFM

approach to turbulent non-premixed $CO/H_2/N_2$ fuel jet with different nozzle diameters mainly to judge the predictive capability of NO_x formation. A new approach towards the modelling of the conditional scalar dissipation rate based on a least square fit through a mass weighted spatial distribution in order to get the correct estimate of averaged conditional scalar was proposed. A better agreement with experiments has been reported with the new approach of EPFM.

Application of LES based transient flamelet modelling was studied for the first time by Pitsch and Steiner (2000). The Lagrangian flamelet model of Pitsch *et al.* (1998) was applied for the study of LES of partially premixed methane/air diffusion flame (Sandia flame D) with the dynamic model of Pierce and Moin (1998) for the subgrid variance of mixture fraction. The unsteady flamelet equations were coupled with the LES solution to provide the filtered density and other filtered reactive scalar quantities. The scalar dissipation rate required to solve flamelet equations was determined from a method proposed by Bushe and Steiner (1999). Inclusion of complete chemistry with unsteady effects helped to reproduce the NO formation predictions close to experiments.

The LFM model was reformulated to account for the local inhomogeneities of the scalar dissipation rate and to demonstrate their effect by Pitsch (2002). He conducted an advanced subgrid scale flamelet combustion model where flamelet equations were rewritten in Eulerian form with complete coupling with LES to enable the solution for resolved fluctuations of the scalar dissipation rate. This new model was written in Eulerian coordinates and hence given the name Eulerian Flamelet Model (EFM).This model was used for the study of LES piloted methane/air jet diffusion flames. Significant improvements in the CO predictions have been reported in comparison to the Lagrangian flamelet model based calculations of Pitsch and Steiner (2000) and steady flamelet model calculations of Kempf (2005). Recently, Ferraris and Wen (2008) used the Laminar Flamelet Decomposition (LFD) approach for conditional source term estimation applied to LES of Sandia flame D. An unsteady flamelet formulation was used with unity Lewis number assumption. Failure to predict local extinction and re-ignition effects were reported with steady laminar flamelets.

The above literature review shows the importance of transient flamelets that encourages the present research to consider the unsteady term in solving the flamelet equations for better representation of flame structure.

2.2 Turbulent Partially Premixed Combustion

Partial premixed mode of combustion is achieved when fuel and oxidizer enter the combustion zone (non-premixed) but get influenced with the turbulent flow structure resulting in mixing to its desired quality in the immediate region of the fuel and air inlet thereby naming it as partially premixed before combustion zone. Lifted flames studied in the present work is categorized with partial premixing nature due to combustion products at higher temperature are introduced in the oxidizer stream. Whereas, the geometric features originally developed for non-premixed combustion, in which combustion occurs in a stratified medium upon ignition in the zone thereafter. This mode of combustion is also referred to as partially premixed combustion. Modern gas turbine combustion systems originally manufactured for non-premixed mode of combustion is prone to partial premixing due to geometric features are the best example for this kind. Partial premixed mode has advantage over non-premixed and premixed modes. Non-premixed combustion regime has the drawback of attaining high temperatures which effects the emission formation like NO. On the other end, lean premixed combustion is prone to generate combustion instabilities with high pressure fluctuations. Most of the modern day gas turbine combustors are subjected to partial premixed mode. The two common features that are concern for this mode of combustion are flame stabilization and lift-off.

Flame stabilization was studied experimentally by Vanquickenborne and Van Tigglen (1966) with respect to lifted turbulent diffusion flames. They concluded that stabilization was obtained only based on the location of stoichiometric composition similar to turbulent premixed flame front where the turbulent burning velocity balances with the gas flow velocity. A similar argument was provided by Eickhoff *et al*. (1986), Kalghatgi (1981, 1984) and Lee *et al.* (1997). Other theories proposed the stabilization mechanism based on (i) the quenching of laminar non-premixed flamelets, Peters and Williams (1983), (ii) large scale motion generated in jets, Brodwell *et al.* (1984); Dahm and Dibble (1988); Miake-Lye and Hammer (1988);

Pitts (1988,1990), (iii) distributed reaction zone, Schefer *et al.* (1990) and (iv) reactedness and mixedness, Bradley *et al.* (1990). For lifted flames, the flame stability and blowout of lifted flames have been investigated by Savas and Gollahalli (1986). Apart from these studies, the concept of "*tribrachial*" or triple flamelets on flame liftoff and the importance of Schmidt number of fuel on mixing process with air have been demonstrated by Chung and Lee (1991). Liñán (1994) and Veynante *et al*. (1994) have shown theoretically that in a laminar flow lifted flames are stabilized by a triple flame configuration. Domingo and Vervisch (1996) showed that the triple flame was more robust than a diffusion flame. With the wide variety of conclusions from the above researchers on stabilization of liftoff height for turbulent lifted partially premixed flames, it is rather difficult to focus on one specified theory to model combustion for the prediction of lifted flames.

A flamelet model was proposed by Bradley *et al.* (1990) called a reactedness-mixedness model for non-premixed flames. This model employs premixed laminar flamelets rather than the conventional diffusion flamelets and allows for a degree of premixing before combustion occurs. The lift-off height was determined as the location of onset of heat release rate. The predicted lift-off heights compared favorably with the experimental data of Kalghatgi (1984). This model was later improved by Bradley *et al*. (1998a, 1998b) by allowing for flame extinction at both positive and negative strain rate. The model was found to not only predict the lift-off heights of Donnerhack and Peters (1984) but also the blow-off velocity as a function of nozzle diameter as reported by Kalghatgi (1981). Sanders and Lamers (1994) formulated a model based on diffusion flamelet extinction. The stretch on the flame was accounted by a strain rate rather than scalar dissipation rate. This model reproduced approximately the correct slope of linear dependence of lift-off heights on exit velocities in turbulent natural gas lifted diffusion flames.

Müller *et al*. (1994) developed a model for partial premixed turbulent combustion using the G-equation approach similar to that adopted by the premixed laminar flamelet model of Peters (1986). The G-equation formulation used for flame propagation differs from the level-set approach of Peters (1986) in that the laminar burning velocity was taken as a function of scalar dissipation rate as well as mixture fraction. For the turbulent burning velocity, Müller *et al*. (1994) proposed a model

containing three terms: a term for premixed flame propagation, a term accounting for partial premixing, and a flamelet quenching term. By including the three terms, they claimed to have accounted for both the premixed flame propagation and diffusion flamelet extinction theories. Müller *et al.* (1994) claimed that the premixed flame propagation term controls the upstream flamelet propagation while the modelling of the flamelet quenching term controls the lift-off height. However, it was later concluded that the diffusion flamelet extinction was not the mechanism that has been modeled. Henceforth, Peters (1999) modified the formulation and based it entirely on the premixed flame propagation mechanism.

The partially premixed flamelet model of Peters (1999) combines the flamelet models for non-premixed and premixed combustion. The level-set, G equation, approach was used to calculate the location and geometry of the premixed flame front while mixing was accounted by mixture fraction. The dependence of scalar field on mixture fraction was accounted by a diffusion flamelet structure. The turbulent partially premixed burning velocity was based on the premixed flame propagation but takes into account the partial premixing via a conditional turbulent burning velocity based on mixture fraction. This model was successfully applied to turbulent methane and propane jet flames by Chen *et al.* (2000) and it was shown that the mean structure of the lifted flame was similar to that of a laminar triple flame and the lift-off heights were found to be in good agreement with measurements. Later, the extension of the partially premixed flamelet model of Peters (1999) to LES has been carried out by Duchamp de Lageneste and Pitsch (2001). They carried out LES studies of turbulent Bunsen burner flames as well as turbulent partially premixed combustion in a dump combustor. Their research showed the ability of their approach to handle both premixed as well as partially premixed combustion. Successful application of the above model to LES of turbulent lifted methane/air flames was performed by Pitsch and Duchamp de Lageneste (2001). Lyons *et al.* (2007) conducted a detailed understanding of turbulent lifted hydrocarbon jet flames and the conditions under which they are stabilized. Stabilization mechanisms with respect to laminar lifted flame are discussed. Theory behind types of turbulent lifted flames were also presented. Experiments supporting the importance of variety of effects, including partial premixing, edge flames, local extinction, streamline divergence and large scale structures were presently in detail.

The present research is different from the above studies as the partially premixed combustion is attempted to be modeled namely with UFPV approach which is primarily developed for turbulent non-premixed combustion. However, the use of scalars like mixture fraction and progress variable formulation with the unsteady flamelet solution suits more towards the partially premixed mode. Therefore, the test case chosen for the simulation of partially premixed combustion is that of a turbulent lifted methane-air jet flame where the fuel is premixed (Cabra *et al*., 2005). This flame has an additional feature where the fuel jet is surrounded by high temperature vitiated co-flow. This is a new flame stabilization mechanism in the form of auto-ignition in addition to the premixed flame front propagation. The present research aims mainly at the ability of the UFPV model to capture the gross characteristics of the lifted flame applied with LES.

2.3 Flamelet/Progress Variable (FPV) Approach

This model was originally developed and implemented on mainly LES based numerical calculations by Pierce (2001) and Pierce and Moin (2004). The fundamental concept behind the model is from typical SLFM based flamelet theory but differs in the approach of its modelling. The FPV approach uses a reaction progress variable instead of a scalar dissipation rate to parameterize the flamelet library. In order to involve the local extinction and re-ignition flame physics, this method potentially gives the advantage over the SLFM. In SLFM, with scalar dissipation rate as a parameter, only the steady state solutions lying below the extinction limit and the fully extinguished state are considered in the generation of flamelet library. Therefore, consideration of partially extinguished states is not possible since they result in a non-unique parameterization of the flamelets. But with the FPV approach, adopting reaction progress variable addresses the above mentioned problem and thus the full range of steady state solutions can be considered in the library. Apart from the advantages of FPV, LES requires to solve the transport equation for progress variable along with mixture fraction. The definition of progress variable is undoubtedly the question which is under research. But it has been considered as the sum of product mass fractions by many in the past. The closure for the model has to be provided with the joint PDF of mixture fraction and reaction progress variable. Pierce and Moin (2004) studied this model on confined coaxial jet

swirling non-premixed flame, where they employed a delta (δ) function for the filtered PDF of reaction progress variable. They showed significant improvement in the flame stabilization region with the FPV approach in comparison to SLFM.

A priori tests using DNS data for turbulent non-premixed combustion in isotropic turbulence was carried out by Ihme *et al.* (2005) with the concern for improvement of the FPV model. Their study concentrated on the model for the presumed filtered PDF for reaction progress variable. The beta (β) function was proposed as a possible improvement for the FPDF of reaction progress variable and a closure model for the reactive scalar variance has been provided. They also showed that the steady state assumption of the flamelet solutions especially during re-ignition at low scalar dissipation rates is inaccurate. Ihme and Pitsch (2005) extended the use of FPV model with an unsteady flamelet formulation. They employed the unsteady FPV model in LES of turbulent confined swirling flames previously studied by Pierce (2001) and obtained notable improvement in the distribution of CO mass fraction. Later, Ihme and Pitsch (2008) developed the new model for reactive scalar FPDF with the application of statistically most like distribution (SMLD). FPV approach was tested for the first time on lifted flames with both FPDF for reaction progress variable taking the form of beta (β) and delta (δ) functions by Ravikanti (2008). Numerical validation of RANS and LES based FPV model was carried out with the experiments conducted by Cabra *et al.* (2005). Both the turbulence models were found to predict reasonable lift off height but the prediction of flame extinction and re-ignition characteristics was found to fail with FPV approach. Therefore, the present work aims to include the unsteady effects in the FPV approach to predict the lifted flame better.

2.4 Unsteady Flamelet/Progress Variable (UFPV) Approach

Partially premixed flames are better predicted with the inclusion of unsteady effects in the flamelet solution with the model's potential to predict local extinction and re-ignition phenomena and especially the flame lift-off. Therefore, unsteady flamelet progress variable (UFPV) model, which combines the unsteady flamelet formulation with the progress variable approach, has been used to predict emissions like CO mass fraction by Ihme and Pitsch (2005) with reasonable success. With this confidence, the

present study considers the unsteady flamelet approach with the variations in scalar dissipation rate coupled with the progress variable approach. Here the model is used mainly to predict the lift-off height and flame properties of partially premixed flames. With the beta PDF for progress variable, the inclusion of scalar dissipation rate and beta PDF for mixture fraction in the lookup table considerably increases the computational space and time. In our work presented here, as a preliminary step towards developing the unsteady flamelet progress variable (UFPV) approach, a delta PDF for reaction progress variable is selected to keep the computational cost manageable and UFPV model is applied to predict lifted flames. The objective of the present work is to validate the UFPV combustion model for partially premixed lifted flames and test the model with two different fuel compositions namely CH_4/Air and H_2/N_2 where experimental data is available. In the current work, UFPV model employed in LES framework to study the accuracy with which the model can envisage the partially premixed mode of combustion without the benefits of resolution of large scale motion provided by LES. The details of the FPV and UFPV modelling strategies are presented in Chapter 4.

2.5 Turbulence Radiation Interaction (TRI)

In the recent past, effect of radiation is felt to be an important issue in turbulence involved thermo-chemistry related problems. Radiation plays an important role in predicting the flow field with temperature and other major species distribution. However, radiation requires considerable resources for the solving of the radiative transfer equation (RTE). Solving this equation directly along with other equations makes the simulation process time consuming for medium to complex geometries. The alternative solution of coupling the radiation with LES when it requires is the optimum way to implement radiation in turbulence chemistry calculations. Solving radiation itself is quite a cumbersome procedure when it is applied to complex flame structures such as swirl or bluff body flames.

Importance of radiation and its effect on combustion gases was studied by Edwards and Balakrishna (1973) who concluded that heat transfer takes place by thermal radiation process rather than convective process when gases are at high temperatures. Based on the importance of radiation on gases, Cox (1977) suggested that turbulent

flames fluctuate in temperature and emissivity and studied their effect on radiation heat transfer. Following these research findings, Kabashnikov and Kmit (1979) found that local values of temperature and concentrations of radiative components fluctuate irregularly about their average values in any turbulent flow. They attempted to examine the influence of turbulent fluctuations on the transfer of monochromatic thermal radiation. Kabashnikov and Myasnikov (1985) used different approaches to account for the mean thermal radiation in turbulent flows and found that accounting the turbulent fluctuations substantially increased radiation. Thus the interaction of radiation with turbulence was the research topic under high priority. Song and Viskanta (1987) studied the TRI effects in order to provide better fundamental understanding of temporal aspects of radiative transfer applicable to combustion systems. Importance of radiation heat transfer to any combustion system was highlighted by Viskanta and Mengue (1987) who argued that an adequate treatment of thermal radiation heat transfer is very much essential to mathematical models of any combustion process and to the design of combustion systems.

TRI effects were then started to be examined for non-premixed flames, Kounalakis *et al.* (1988). It was found that intensity of radiation fluctuations of 20-110% provided a direct evidence of TRI in such flames. Having observed the significance of TRI, Gore *et al.* (1992) conducted a detailed study on coupled radiation-structure analysis for turbulent non-premixed strongly radiating acetylene/air flames. Using the concepts of TRI, Adams and Smith (1995) tried to develop a three dimensional combustion model which couples turbulent flow statistics with chemical reactions and radiative heat transfer to evaluate the effect of soot and turbulence radiation coupling on radiative transfer in an industrial scale furnace. Discrete ordinate method (DOM) was used in their radiation intensity field calculations. A new approach based on formulation of equations for statistical moments was presented for modelling turbulence radiation interaction by Johannes *et al*. (1995) where it was used for confined combustion systems.

TRI has been studied on confined diffusion flames by Hartick *et al.* (1996) where chemistry was coupled with two dimensional PDF of mixture fraction and heat release rate. Importance of TRI in turbulent diffusion jet flames has been quantified by Li and Modest (2003). They strongly concluded that TRI effects account for about 1/3rd of

the total drop in flame peak temperatures caused by radiative heat transfer. Importance of complete absorption coefficient-Planck function correlation was also discussed. Not only pertaining with reacting flows, Mazumdar and Modest (1999) performed detailed studies on effect of TRI on non-reacting flows of combustion products like CO_2 and H_2O. They have interestingly concluded that for most of the situations of practical interest, TRI effects are indeed negligible on the wall heat loads. Malalasekera *et al.* (2002) have reviewed some of the currently available radiative heat transfer calculation techniques suitable for both complex and simple CFD applicable geometries which could be used to include TRI effects.

Based on the above research developments in the field of radiation and its effect on turbulence, it is indeed necessary to incorporate radiation in turbulence calculations for all types of flames ranging from medium to high luminosity. But the chance of implementing RTE in any general turbulence model would be expensive in terms of time and computational resources when they are applied to complex combustion systems. In a different approach to tackle radiation, non-adiabatic flamelet model came into existence. The sections below highlight some of the basic research that was carried out in the development and utilization of NAFM applied to both RANS and LES based turbulent flows.

2.5.1Non Adiabatic Flamelet Modelling in RANS

Accounting for the effects of radiation heat loss on the thermo-chemical structure of the flame through a radiation source term in the flamelet equations is the simplest method. Bray and Peters (1994) suggested that it is more appropriate to consider the effect of emission and absorption over a wide range of length scales present in a turbulent flame. They introduced a parameter called ‘enthalpy defect’ (difference between the adiabatic and actual enthalpy) to provide the coupling between the non-adiabatic turbulent flow and the flamelet structure. The flamelet library is then parameterized by mixture fraction, scalar dissipation rate and additionally the enthalpy defect. Based on this concept, Marracino and Lentini (1997) developed a non-adiabatic flamelet model to study the effects of radiation in turbulent methane/air jet flames. Considering an optically thin medium assumption for the gas phase radiation, they obtained noticeable improvement in mean temperature predictions.

This non-adiabatic flame model was extended by Giordano and Lentini (2001) to account for turbulence-radiation interaction. Hossain *et al*. (2001) extended SLFM to a non-adiabatic model using the enthalpy defect concept and the methodology of Marracino and Lentini (1997). Calculations based on the DTM have been used for radiation source term calculations. They validated the model for turbulent CH_4/H_2 bluff-body flames and found marked improvements in OH radical concentrations. However, no notable improvement in temperature or major species was reported. Enthalpy defect based non-adiabatic flamelet modelling has also been reported by Ma *et al*. (2002) who extended the premixed flamelets based mixedness-reactedness flamelet model of Bradley *et al*. (1990) to account for thermal radiation in laboratory scale and large scale natural gas flames. Reasonable improvements in the mean temperature have been reported with the non-adiabatic model.

Coelho *et al*. (2003) developed a non-adiabatic approach based on steady flamelet model for studying the spectral radiative effects and turbulence/radiation interaction in turbulent jet diffusion flames. This approach employs steady flamelet equations and ignores the effect of radiative heat transfer on flamelet chemical composition. Effect of radiation heat loss on flamelet temperature was however accounted through an implicit equation which was a function of temperature, conditional averaged scalar dissipation rate and radiation heat loss factor which was obtained from calculations based on Discrete Ordinates Method. Later Coelho (2004) employed this approach to study the different methods of accounting for turbulence-radiation interaction in turbulent jet diffusion flames. Recently Xu *et al*. (2006) developed a non-adiabatic form of Lagrangian flamelet model. In this model, the effects of thermal radiation on thermo-chemical structure of the flame were accounted through a radiation source term in unsteady flamelet equations which was obtained from CFD using detailed radiation calculations based on finite volume correlated *k* method. They applied this model to methane/air Sandia D jet flame and showed promising improvements for temperature and other major species.

2.5.2Non Adiabatic Flamelet Modelling in LES

Turbulence radiation interaction studies pertaining to direct numerical simulation (DNS) have been intense in the recent past rather than using LES. DNS applied for

premixed combustion was performed to study the effect of TRI on combustion systems, Wu *et al.* (2005). However, their studies include very simple geometry with Monte Carlo method for the solution of radiative transfer equation. Soon after Wu *et al*. (2007) developed advanced high-order photon Monte Carlo method for radiative transfer using DNS. The compatibility of this method with high fidelity DNS for chemically reacting flows was tested. Deshmukh *et al.* (2008) have also used DNS to study TRI effects in a one dimensional non-premixed system. Here too photon Monte Carlo method was implemented to solve the RTE which was coupled with the flow solver. Research has been very scant with the utilization of LES as the turbulence model to test any complex configuration with radiation. Most of the LES turbulent flows ignore radiation because partly due to the additional complexity and computational requirements inherent to radiative transfer calculations and partly due to the flames studied are laboratory based. Very recently Coelho (2009) attempted to solve the filtered RTE to incorporate TRI using LES. SANDIA flame D was considered with a semi-casual stochastic model used to generate a time-series of turbulent scalar fluctuations along the optical paths. A few modelling studies based on LES to account radiative heat transfer were performed but none of them has considered the TRI effects. One such coupled calculation on LES with radiative heat transfer on turbulent combusting flames were studied by Goncalves dos Santos *et al.* (2008). Two independent codes working on LES and radiation were coupled in a systematic manner in order to exchange data when ever needed through a specialized language. Radiation code received the temperature and mass fraction field from the combustion code and returned the radiation source terms. This code was found to be very versatile, portable and flexible to use. Due to the complexities involved with flames like swirl and bluff body configurations, the present study is focused on the coupling of turbulence with radiation. Therefore, similar to the strategy of Goncalves dos Santos *et al.* (2008) present work tries to implement the coupling of radiation (DTM ray tracing method) with LES with a simple data exchange process with the inclusion of enthalpy defect concept. Complete details of coupling of LES and DTM can be found in Chapter 5.

The non-adiabatic flamelet model carried out in this thesis extends the work carried by Ravikanti (2008) who has applied NAFM on RANS based calculations. NAFM is now applied to LES as an attempt to judge the effect of radiation on turbulence as

LES always has the advantage over RANS based simulations. Steady non-adiabatic flamelets have been developed for integration with the non-adiabatic flamelet model. The non-adiabatic model in this work employs a detailed chemical kinetic mechanism of GRI 2.11. Developments with regard to the computational efficiency of the model have also been carried out where the CFD calculations with the non-adiabatic model run on a look-up-table strategy. Further details about the non-adiabatic model are given in section 4.3.

2.6 Motivations For The Present Study

Two most important physical criteria involved in any combustion system have been considered for improvements in combustion modelling. One such intricate problem is predicting the lifted flames and other complicated issue is the inclusion of radiation effects to study the importance of radiation in any highly fluctuating turbulent flames.

1. UFPV modelling is undertaken as the task for developing the combustion model for the first time for turbulent lifted flames which are supposed to be partially premixed in nature. This code was developed and tested for Cabra flame (Cabra *et al.* (2005)) with two different fuel compositions and flame conditions.
2. Although it is known that TRI would be the most complex process in studying the effect of radiation on turbulence, an attempt is made to couple LES and DTM radiative code first of its kind to learn the importance of radiation on turbulent flames in a more simplistic procedure than solving for filtered RTE in LES. Enthalpy defect as a parameter defines the inclusion of radiative properties and other scalars like temperature and species mass fractions are calculated in the coupling procedure for LES with DTM. This code is tested with two different flames (swirl and bluff body flames) to report the effect of inclusion of radiation.

2.7 Closure

This chapter dealt with the literature related to the flamelet modelling at the first instance. Detailed review of the work performed in the past regarding the SLFM and transient based solutions from unsteady flamelets was discussed. Development of

FPV and UFPV combustion models were presented with a complete review of the past work done on these models. Importance of TRI and its aftermath were discussed. An approach to handle coupling of LES with DTM, based on the past studies on enthalpy defect in the form of NAFM strategy was concluded as one of the research targets. Detailed review on NAFM applied to both RANS and LES was presented.

Chapter 3

Large Eddy Simulation - Turbulence Modelling

3.1 Introduction to LES

In LES, the scales of turbulence are separated into large scales and small scales or sub-grid scales (SGS). The scale selection that LES works is a separation between large and small scales, Ferziger (1977), Lesieur and Metais (1996), Mason (1994), Rogallo and Moin (1984). In order to define these two categories, a reference or cutoff length has been determined. Those scales that are of a characteristic size greater than the cutoff length are called large or resolved scales and others are called as small or subgrid scales. The large scales are completely resolved and hence directly computed while the influence of small scales on the large scales is modelled with appropriate SGS mathematical models. LES therefore employs '*filtering*' of the instantaneous governing equations such that they provide description of the space and time dependence of the resolved large scales. Since chemical reactions occur at the smallest scales, there is no resolved portion of chemical source term in LES and hence combustion needs to be modelled similar to RANS. Since LES can predict the turbulent mixing which is key to chemical conversion, more accurately than RANS, it is capable of bringing improvements to predictions of turbulent reacting flows.

During the last three decades, this technique has developed considerably while developing underline theories, new models and more efficient numerical schemes, Piomelli (1999). The first LES calculation on turbulent channel flow has been carried out by Deardorff (1970). Since then LES has been applied to variety of flow problems from simple turbulent channel flow to complex aircraft gas turbine combustors. The turbulent flow is usually dominated by large scale structures (large eddies), which depend strongly on the boundaries and nature of the flow and responsible for most of the transport of mass, momentum and in flows involving mixtures of gases, species concentrations etc. At the same time, the small scales formed by the interaction of the

large scales whose main function is to dissipate fluctuations of transported quantities which affect the mean characteristics of the flow only slightly. These small scales are more universal in nature and therefore more amenable to modelling than the large scales. This strong observation leads to find an approach, whereby scales which cannot be represented on the numerical grid are removed from the description of the turbulence in the simulation leaving only the large energy containing eddies whose evaluation is calculated directly. This approach is referred to as the so called *large eddy simulation (LES).*

3.2 Spatial Filtering Technique

The governing equations are subjected to spatial filtering to differentiate the solution space into resolved and unresolved scales. Scales are separated by applying a scale high-pass filter, i.e. low-pass in frequency to the exact solution. This filtering is represented mathematically in physical space as a convolution product. The resolved part $\overline{f}(x, y, z, t)$ of the space time variable $f(x, y, z, t)$ is defined formally by the relation, Leonard (1974):

$$\overline{f}(x,y,z,t) = \int_{-\infty}^{+\infty}\int_{-\infty}^{+\infty}\int_{-\infty}^{+\infty} G(x-x', y-y', z-z')\, f(x,y,z,t)\, dx\, dy\, dz \qquad (3.1)$$

where G is the convolution kernel which is the characteristic of the filter used and is associated with the cutoff scales in space and time, $\overline{\Delta}$ and $\overline{\tau_c}$ respectively. The difference between the filtered field (resolved field) $\overline{f}(x,y,z,t)$ and the original field $f(x, y, z, t)$ is described as small unresolved scale $f'(x,y,z,t)$:

$$f(x,y,z,t) - \overline{f}(x,y,z,t) = f'(x,y,z,t) \qquad (3.2)$$

The three convolution filters ordinarily used for performing the spatial scale separation are the Fourier cut-off filter, the Gaussian filter and the box filter. Each filter has a length scale $\overline{\Delta}$ associated with it and is taken to be intermediate between the Kolmogorov length scale and the integral length scale. Eddies of size larger than $\overline{\Delta}$ are classified as large eddies while the ones smaller than $\overline{\Delta}$ are classified as the small eddies which need to be modelled. In the present LES, a box filter has been adopted, as this filter fits naturally into a finite volume discretization. The process of

finite volume discretization of the continuous governing equations is equivalent to applying a box filter of width $\overline{\Delta}$.

Box or Top Hat Filter

This filter fits naturally into a finite volume discretization. The process of rewriting the continuous equations in discrete form using a finite volume formulation is equivalent to applying a box filter of width to the equations.

$$\overline{\Delta} = 2(\Delta x \Delta y \Delta z)^{1/3} \tag{3.3}$$

where $\Delta x, \Delta y$ and Δz refer to the width of the finite volume in the three coordinate directions and $\overline{\Delta}$ is the characteristic width of the filter. A typical top-hat filter (rectangular filter) of the three widths Δ_i can be defined as:

$$G(x_i - x_i^{'}) = \begin{cases} \prod_{i=1}^{3} \frac{1}{\Delta_i} & if \quad |x_i^{'}| \le \frac{\Delta_i}{2} \\ 0 & otherwise \end{cases} \tag{3.4}$$

3.3 Filtered Governing Equations

The filtered governing equations are obtained by applying the spatial filtering operator. The filtering operator removes the small scales (below than the filter width) that cannot be resolved by the numerical method and appear through a subgrid scale (SGS) model.

3.3.1 Mass Conservation

The Favre filtered equation for conservation of mass is represented as:

$$\frac{\partial \overline{\rho}}{\partial t} + \frac{\partial \overline{\rho} \tilde{u}_i}{\partial x_j} = 0 \tag{3.5}$$

3.3.2Momentum Conservation

The Favre filtered equation for conservation of momentum or Navier-Stokes equations gives to:

$$\frac{\partial \bar{\rho}\tilde{u}_i}{\partial t}+\frac{\partial \bar{\rho}\widetilde{u_i u_j}}{\partial x_j}=-\frac{\partial \bar{P}}{\partial x_i}+\frac{\partial}{\partial x_j}\left[\bar{\rho}\left(\upsilon\frac{\partial \tilde{u}_j}{\partial x_i}+\upsilon\frac{\partial \tilde{u}_i}{\partial x_j}\right)-\frac{2}{3}\bar{\rho}\upsilon\frac{\partial \tilde{u}_k}{\partial x_k}\delta_{ij}\right]+\bar{\rho}g_i \tag{3.6}$$

The diffusion term is given by the following expression

$$\upsilon\frac{\widetilde{\partial u_j}}{\partial x_i}=\tilde{\upsilon}\frac{\widetilde{\partial u_j}}{\partial x_i} \tag{3.7}$$

The filtered momentum equation includes unknown terms. Because of the nonlinearity of the convective terms in filtered Navier-Stokes equations, the Favre filtering introduces an unknown term $\widetilde{u_i u_j}$ leaving the equations unclosed.

This non-linear correlation $\widetilde{u_i u_j}$ can be decomposed into resolved part $\tilde{u}_i\tilde{u}_j$ and a residual stress τ_{ij}^{SGS}

$$\widetilde{u_i u_j}=\tilde{u}_i\tilde{u}_j+\tau_{ij}^{SGS} \tag{3.8}$$

The residual stress τ_{ij}^{SGS} also known as sub-grid stress represents the shear stress of the small scale (unresolved) turbulent motion. Therefore, the filtered momentum equation can be re-written as follows

$$\frac{\partial \bar{\rho}\tilde{u}_i}{\partial t}+\frac{\partial \bar{\rho}\tilde{u}_i\tilde{u}_j}{\partial x_j}=-\frac{\partial \bar{P}}{\partial x_i}+\frac{\partial}{\partial x_j}\left[\bar{\rho}\upsilon\left(\frac{\partial \tilde{u}_j}{\partial x_i}+\frac{\partial \tilde{u}_i}{\partial x_j}\right)-\frac{2}{3}\bar{\rho}\upsilon\frac{\partial \tilde{u}_k}{\partial x_k}\delta_{ij}-\bar{\rho}\tau_{ij}^{SGS}\right]+\bar{\rho}g_i \tag{3.9}$$

The additional sub-grid stress τ_{ij} term has to be modeled in order to represent the sub-grid contribution on resolved velocity field.

3.3.3Species Conservation

The Favre filtered transport equation for mixture fraction is obtained by applying the filter as

$$\frac{\partial \overline{\rho}\tilde{f}}{\partial t}+\frac{\partial\left(\overline{\rho}\widetilde{fu_j}\right)}{\partial x_j}=\frac{\partial}{\partial x_j}\left(\tilde{\Gamma}\frac{\partial \tilde{f}}{\partial x_j}\right) \tag{3.10}$$

The convection term in this case $\overline{\rho}\widetilde{fu_j}$ has the non-linear relation and therefore needs to be decomposed into resolved part $\tilde{f}\,\tilde{u}_j$ and subgrid part F_j^{SGS} which contribute the small unresolved flux of turbulent motion:

$$\widetilde{fu_j}=\tilde{f}\;\tilde{u}_j+F_j^{SGS} \tag{3.11}$$

Substituting equation (3.11) into (3.10) the Favre filtered transport equation for the mixture fraction is obtained as:

$$\frac{\partial \overline{\rho}\tilde{f}}{\partial t}+\frac{\partial\left(\overline{\rho}\tilde{f}\;\tilde{u}_j\right)}{\partial x_j}=\frac{\partial}{\partial x_j}\left(\tilde{\Gamma}\frac{\partial \tilde{f}}{\partial x_j}+F_j^{SGS}\right) \tag{3.12}$$

All the above filtered governing equations subjected to the implicit grid filter for mass (Eq. 3.5), momentum (Eq. 3.9) and mixture fraction (Eq. 3.12), form a set of coupled partial differential equations which can be numerically solved. The instantaneous subgrid fluctuations τ_{ij}^{SGS} and F_j^{SGS} are modeled through the known resolved field and added to close the equations.

In order to close the filtered mixture fraction equation (3.12), the unknown term F_j^{SGS} has to be modelled. Again the turbulent term is incorporated into mixing like additional diffusion and hence F_j^{SGS} is modeled by using eddy diffusivity approach, which is similar to eddy viscosity approach. To model the term F_j^{SGS}, turbulent diffusivity Γ_t is used along with the gradient of the filtered mixture fraction $\frac{\partial \tilde{f}}{\partial x_j}$:

$$F_j^{SGS}=\Gamma_t\frac{\partial \tilde{f}}{\partial x_j} \tag{3.13}$$

Substituting this into the filtered mixture fraction equation (3.12) and rewriting the right hand side gives as follows:

$$\frac{\partial}{\partial x_j}\left(\left(\tilde{\Gamma}+\Gamma_t\right)\frac{\partial \tilde{f}}{\partial x_j}\right) \tag{3.14}$$

The diffusion coefficients $\tilde{\Gamma}$ and Γ_t can be written in terms of the laminar viscosity $\tilde{\upsilon}$ and the dynamic viscosity υ_t and are only scaled by the Schmidt number σ. The Schmidt number defines the ratio of momentum transport due to viscosity to mixture fraction transport due to diffusion and is written as:

$$\sigma = \frac{\upsilon / \rho}{\Gamma} \approx \frac{\tilde{\upsilon} / \overline{\rho}}{\tilde{\Gamma}} \tag{3.15}$$

and also,

$$\sigma_t = \frac{\upsilon_t / \overline{\rho}}{\Gamma_t} \tag{3.16}$$

Substituting the above into (3.12), the filtered equation for the mixture fraction becomes

$$\frac{\partial \overline{\rho} \tilde{f}}{\partial t} + \frac{\partial \left(\overline{\rho} \tilde{f} \ \tilde{u}_j \right)}{\partial x_j} = \frac{\partial}{\partial x_j} \left(\frac{1}{\overline{\rho}} \left(\frac{\tilde{\upsilon}}{\sigma} + \frac{\upsilon_t}{\sigma_t} \right) \frac{\partial \tilde{f}}{\partial x_j} \right) \tag{3.17}$$

3.3.4Energy Conservation

Numerical simulations involving radiation coupling with the non-adiabatic flamelet modelling with the concept of enthalpy defect, ζ needs the enthalpy equation to be solved in LES along with all the above. The filtered enthalpy equation can be written as follows

$$\frac{\partial \overline{\rho} \tilde{h}}{\partial t} + \frac{\partial}{\partial x_j} \left(\overline{\rho} \tilde{u}_j \tilde{h} \right) = \frac{\partial}{\partial x_j} \left[\frac{1}{\overline{\rho}} \left(\frac{\tilde{\upsilon}}{\mathrm{Pr}} + \frac{\upsilon_t}{\mathrm{Pr}_t} \right) \frac{\partial \tilde{h}}{\partial x_j} \right] + \dot{Q}_{rad} \tag{3.18}$$

In the above equations ρ is the density, u_i is the velocity component in x_i direction, p is the pressure, f is the mixture fraction, h is the enthalpy, υ_t is the dynamic viscosity, $\tilde{\upsilon}$ is laminar viscosity, σ is the laminar Schmidt number, σ_t is the turbulent Schmidt number, Pr is the laminar Prandtl number and $\mathrm{Pr_t}$ is the turbulent Prandtl number. An over-bar in the above equations describes the application of the spatial filter while the tilde denotes Favre filtered quantities. The laminar Schmidt number is set to 0.7 and the turbulent Schmidt number for mixture fraction is set to 0.4. Similarly, laminar Prandtl number is set to 0.7 and the turbulent Prandtl number for enthalpy is set to 0.4.

The reason for selecting the Schmidt numbers less than 1.0 is to have a stabilized code as observed from the past research experience (Ravikanti (2008), Ranga-Dinesh (2007), Kirkpatrick (2002)). The term $\dot{Q}_{rad}$ is the radiation source which is calculated from the discrete transfer (DT) method radiation code and is given as the input for source in the above enthalpy equation. The details of DT method and coupling strategy are explained clearly in Chapter 5.

3.4 Modelling Subgrid Scale Stresses

To close the system of filtered equations like the filtered momentum equations which govern the evolution of the resolved scale motion, a parameterization is needed for the subgrid terms. This results in the subgrid scale contribution on the momentum equation τ_{ij}^{SGS} which is not solved on the filtered governing equations. Therefore, subgrid scales must be modeled as a function of known resolved values. Also the prime requirement of SGS model is to ensure that the energy cascade is from large scales to small scales. The cascading procedure is considered as an average process. Locally and instantaneously the transfer of energy can be much larger or much smaller than the average. Energy cascade can also occur in the opposite direction (i.e. from smaller scales to larger scales) known as backscattering (Piomelli *et al.*, 1996). Therefore, SGS model should also be accounted for this local instantaneous transfer.

Leonard's Residual Stress Decomposition

The subgrid stress can be expressed by substituting a decomposition of the velocity field of the form as shown below into equation (3.8)

$$u_i = \tilde{u}_i + u_i' \tag{3.19}$$

Where, u_i' is the subgrid scale velocity. The subgrid stresses is decomposed into three parts, Leonard (1974):

$$\tau_{ij}^{SGS} = \widetilde{u_i u_j} - \tilde{u}_i \tilde{u}_j = L_{ij} + C_{ij} + R_{ij} \tag{3.20}$$

Where,

$$L_{ij} = \widetilde{\tilde{u}_i \tilde{u}_j} - \tilde{u}_i \tilde{u}_j \tag{3.21}$$

$$C_{ij} = \widetilde{\tilde{u}_i u'_j} + \widetilde{\tilde{u}_j u'_i} \tag{3.22}$$

and $R_{ij} = \widetilde{u'_i u'_j}$ (3.23)

L_{ij} is termed as the Leonard stress, C_{ij} is called as the cross stress and R_{ij} is the subgrid scale Reynolds stress. The Leonard stress represents interactions between resolved scales that result in subgrid scale contributions. The cross term represents interactions between resolved and unresolved scales, whereas the subgrid scale Reynolds stress represents interaction between small unresolved scales. The representation of turbulent stresses through the use of simplified linear models based on the eddy viscosity approach is well known among the turbulence modelers. The classical model of this group was introduced by Smagorinsky (1963). From an historical point of view, the progenitor of all subgrid scale stress models is the so called Smagorinsky model. The introduction of dynamic modelling concept Germano *et al.* (1991) has spurred significant progress in the subgrid scale modelling in non-equilibrium flows. In this dynamic model the coefficient(s) of the model are determined as the calculation progresses, based on the energy content of the smallest resolved scales rather than input *a priori* as standard Smagorinsky model.

Concept of Eddy Viscosity Model

Almost all subgrid scale models used in the present day research are eddy viscosity models that parameterize the SGS stress in terms of an eddy viscosity by assuming that the anisotropic part of the SGS stress tensor τ_{ij} is proportional to the large scale rate tensor S_{ij}:

$$\tau_{ij}^{SGS} - \frac{2}{3}\delta_{ij}\tau_{kk}^{SGS} = -\upsilon_t\left(\frac{\partial \tilde{u}_j}{\partial x_i} + \frac{\partial \tilde{u}_i}{\partial x_j}\right) \tag{3.24}$$

Since small scales have more universal and homogeneous behavior than the large scales, we can summarize that simple algebraic models can describe the accurate physics of turbulence. The eddy viscosity υ_t is calculated algebraically to avoid solving an additional equation. Finally, since the SGS stresses only account for a fraction of total stresses, modelling errors should not affect the overall accuracy of the results as in the standard turbulence modelling approach.

In eddy viscosity approach the SGS stress term τ_{ij} is modeled by adding a turbulent viscosity term υ_t to the molecular viscosity υ, resulting in an effective viscosity as

$$\upsilon_{eff} = \upsilon + \upsilon_t \tag{3.25}$$

Substituting the effective viscosity υ_{eff} in the filtered Navier-Stokes equation yields,

$$\frac{\partial \bar{\rho}\tilde{u}_i}{\partial t} + \frac{\partial \bar{\rho}\tilde{u}_i\tilde{u}_j}{\partial x_j} = -\frac{\partial \bar{P}}{\partial x_i} + \frac{\partial}{\partial x_j}\left[\bar{\rho}\upsilon_{eff}\left(\frac{\partial \tilde{u}_j}{\partial x_i} + \frac{\partial \tilde{u}_i}{\partial x_j}\right) - \frac{2}{3}\bar{\rho}\upsilon_{eff}\frac{\partial \tilde{u}_k}{\partial x_k}\delta_{ij}\right] - \frac{1}{3}\frac{\partial}{\partial x_i}\bar{\rho}\tau_{kk} + \bar{\rho}g_i \tag{3.26}$$

Where as for incompressible flows, the isotropic part of the SGS stress tensor τ_{kk} is absorbed into the pressure:

$$\bar{p} = \bar{P} - \frac{1}{3}\bar{\rho}\tau_{kk} \tag{3.27}$$

Substituting equation (3.27) in (3.26) the filtered momentum equations becomes

$$\frac{\partial \bar{\rho}\tilde{u}_i}{\partial t} + \frac{\partial \bar{\rho}\tilde{u}_i\tilde{u}_j}{\partial x_j} = -\frac{\partial \bar{p}}{\partial x_i} + \frac{\partial}{\partial x_j}\left[\bar{\rho}\upsilon_{eff}\left(\frac{\partial \tilde{u}_j}{\partial x_i} + \frac{\partial \tilde{u}_i}{\partial x_j}\right) - \frac{2}{3}\bar{\rho}\upsilon_{eff}\frac{\partial \tilde{u}_k}{\partial x_k}\delta_{ij}\right] + \bar{\rho}g_i \tag{3.28}$$

Smagorinsky Model

Effective viscosity υ_{eff} is designed based on the calculation of eddy viscosity υ_t. The Smagorinsky model is based on the equilibrium hypothesis, according to which small scales of motion have shorter time scales than the large energy carrying eddies. Thus it can be assumed that small scales adjust more rapidly to perturbations than the large scales and recover equilibrium nearly instantaneously. Energy is generated at the large scale level and transmitted to small scales, where the viscous dissipation takes place. The equilibrium hypothesis based Smagorinsky model is described in the following section.

By dimensional analysis eddy viscosity is the product of length scale *l*, and the velocity scale q_{sgs}. For unresolved scales the most active term is the cutoff which in the natural length scale in LES modelling is the filter width that determines the size of

the smallest structure in the flow and is proportional to the grid size, Piomelli and Chasnov (1996)

$$\upsilon_t \sim l q_{sgs} \tag{3.29}$$

The viscous dissipation term in equilibrium condition is given as

$$-\tau_{ij}\frac{1}{2}\left(\frac{\partial \tilde{u}_j}{\partial x_i}+\frac{\partial \tilde{u}_i}{\partial x_j}\right)=\varepsilon \tag{3.30}$$

So we obtain,

$$q_{sgs} \sim l \left|\frac{1}{2}\left(\frac{\partial \tilde{u}_j}{\partial x_i}+\frac{\partial \tilde{u}_i}{\partial x_j}\right)\right| \tag{3.31}$$

Assuming $l \sim \Delta$ for the grid size, the eddy viscosity can be written as

$$\upsilon_t = (C_s\Delta)^2\left|\frac{1}{2}\left(\frac{\partial \tilde{u}_j}{\partial x_i}+\frac{\partial \tilde{u}_i}{\partial x_j}\right)\right| \tag{3.32}$$

or

$$\upsilon_t = (C_s\Delta)^2\left|\tilde{S}\right| \tag{3.33}$$

where $\left|\tilde{S}\right| = \sqrt{2\tilde{S}_{ij}\tilde{S}_{ij}}$.

and

$$S_{ij} = \frac{1}{2}\left(\frac{\partial \tilde{u}_j}{\partial x_i}+\frac{\partial \tilde{u}_i}{\partial x_j}\right) \tag{3.34}$$

Dynamic Procedure

The classical Smagorinsky model has a significant number of problems. The model coefficient C_s is not a constant value. It is flow dependent, with different values typically in the range $C_s = 0.05 - 0.25$. Lilly (1967) suggested that the $C_s \sim 0.17$ for homogeneous isotropic turbulence with a filter cutoff in the inertial sub-range based on equilibrium argument. Piomelli and Chasnov (1996) found $C_s = 0.065$ to be the optimal for a turbulent channel flow. Transitional and shear flows require a different value of C_s. Piomelli and Chasnov (1996) showed that transitional flows that contain

large regions in which energy flows in the reverse direction, namely from the subgrid scales to the resolved scales termed as backscatter process cannot be represented in the classical Smagorinsky model.

To surmount the above problem Germano *et al.* (1991) presented a procedure to calculate the Smagorinsky model coefficient dynamically using local instantaneous flow conditions. In this method, the model coefficients are computed dynamically as the calculation progresses (rather than imposed a priori) based on the energy content of the smallest resolved scale. The procedure involves the application of two filters. In addition to the grid filter, which defines the resolved and subgrid scales, a test filter (denoted by a caret) is used, whose width $\hat{\Delta}$ is larger than the grid filter width Δ. Along with the grid scale filtering, the test filter defines the new set of stresses leading to a test level subgrid stress tensor known as the subtest scale stresses.

$$T_{ij} = \bar{\rho}\left(\widehat{\widetilde{u_i u_j}} - \hat{\tilde{u}}_i \hat{\tilde{u}}_j\right) \tag{3.35}$$

Also Leonard stress term is modified as

$$L_{ij} = \bar{\rho}\left(\widehat{\tilde{u}_i \tilde{u}_j} - \hat{\tilde{u}}_i \hat{\tilde{u}}_j\right) \tag{3.36}$$

L_{ij} represents the contribution of the smallest resolved scales to the Reynolds stresses which can be computed from the resolved velocity and is related to the SGS stresses, τ_{ij} by the identity, Germano *et al.* (1991)

$$L_{ij} = T_{ij} - \hat{\tau}_{ij} \tag{3.37}$$

The subgrid and subtest scale stresses are then parameterized by eddy viscosity approach

$$\tau_{ij} - \frac{\delta_{ij}}{3}\tau_{kk} = -2C\Delta^2 \left|\tilde{S}\right| \tilde{S}_{ij} = -2C\beta_{ij} \tag{3.38}$$

$$T_{ij} - \frac{\delta_{ij}}{3}T_{kk} = -2C\hat{\Delta}^2 \left|\hat{\tilde{S}}\right| \hat{\tilde{S}}_{ij} = -2C\alpha_{ij} \tag{3.39}$$

where

$$\hat{\tilde{S}}_{ij} = \frac{1}{2}\left(\frac{\partial \hat{\tilde{u}}_i}{\partial x_j} + \frac{\partial \hat{\tilde{u}}_j}{\partial x_i} \right) \text{ and } \left| \hat{\tilde{S}} \right| = \sqrt{2 \hat{\tilde{S}}_{ij} \hat{\tilde{S}}_{ij}} \tag{3.40}$$

Substituting (3.38) and (3.39) into (3.37) yields

$$L_{ij}^{mod} = -2C^2 \widehat{\overline{\Delta}^2} \left| \hat{\tilde{S}} \right| \hat{\tilde{S}}_{ij} + 2\widehat{C^2 \overline{\Delta}^2 \left| \tilde{S} \right| \tilde{S}_{ij}} \tag{3.41}$$

Ideally, C can be chosen such that

$$L_{ij} - L_{ij}^{mod} = 0 \tag{3.42}$$

But since the Eq. 3.42 is a tensor equation, it can only be satisfied in some average sense. Lilly (1991) proposed the minimization of the root mean square of the left-hand-side which yields:

$$C^2(x, y, z, t) = -\frac{L_{ij} M_{ij} - 1/3 L_{kk} M_{ll}}{2\overline{\Delta}^2 \left(M_{ij} M_{ij} - 1/3 M_{kk} M_{ll} \right)} \tag{3.43}$$

Where $M_{ij} = \alpha^2 \hat{\overline{\rho}} \left| \hat{\tilde{S}} \right| \hat{\tilde{S}}_{ij} - \overline{\rho} \widehat{\left| \tilde{S} \right| \tilde{S}_{ij}}$ and $\alpha = \frac{\hat{\overline{\Delta}}}{\overline{\Delta}}$ is the ratio of test filter to grid filter.

For an incompressible flow, Eq. 3.43 simplifies to

$$C^2(x, y, z, t) = -\frac{L_{ij} M_{ij}}{2\overline{\Delta}^2 M_{ij} M_{ij}} \tag{3.44}$$

Thus, with the dynamic procedure, the Smagorinsky co-efficient can be dynamically calculated at every spatial grid point and time step with only α as the only input to the model. The dynamic procedure ensures correct behaviour near wall without any damping functions by automatically reducing the value of the co-efficient near to the wall. However, the values of model co-efficient tend to fluctuate considerably in space and time thus requiring some form of averaging to maintain stability of the numerical simulation. Typically, L_{ij} and M_{ij} are averaged in spatially homogeneous directions in space. However, this requires the flow to have at least one homogeneous direction. An interesting feature of this Germano *et al.* (1991) model is that it can calculate negative values for the model coefficient, which is inconsistent with the Smagorinsky model. The negative Smagorinsky coefficient leads to negative eddy viscosity υ_t, which then results in negative effective viscosity υ_{eff}. This destabilizes the numerical schemes and results in counter gradient species diffusion if a gradient

flux approach is used for species transport. Various methods have been developed to avoid negative peaks in the Germano *et al.* (1991) procedure. Kempf (2003) gives a more detailed picture of the above. But the present work uses an alternatively less expensive method known as localized dynamic procedure of Piomelli and Liu (1995), which involves finding an approximate solution to the integral equation by using the value of C at the previous time step to give a first approximation C^*. This method offers the advantage of smoothing in space without any homogeneous direction required and hence is adopted in the present LES code.

3.5 Closure

This chapter highlighted the concepts of LES and its development for the present research work. The basic theory behind the filtering technique and its application to governing equations of mass, momentum, scalar (mixture fraction and progress variable in the present case) and enthalpy was discussed. Closure of SGS terms were also focussed with Smagorinsky model and Dynamic procedure of Germano *et al.* (1991). Chapter 4 deals with the combustion modelling related to SLFM, NAFM and UFPV approach.

Chapter 4

Combustion Modelling

Solving the transport equations for all the species involved in any fuel and oxidiser with the set of chemical reaction mechanism makes a huge task. Considering the computational time and resources, the most efficient way to simulate the non-premixed turbulent combustion process is by conserved scalar mixture fraction methodology. Also when coupled with a reaction variable like the *"reaction progress variable"* suits for the simulation of partially premixed flames. Progress variable approach for partially premixed flames with flamelet model has proved to predict better with the LES rather than RANS (Ravikanti, 2008).

With diffusion as the rate controlling parameter, non-premixed combustion is also referred to as diffusion combustion. The pioneering work of Burke and Schumann (1928) is based on the fast chemistry assumption. Application of this model to non-premixed combustion has received recognition to predict the flame global properties. Consideration of the conservation of element mass fraction of all species results in a balanced equation which will be free from the chemical source term. This eliminates the need to evaluate mean reaction rate. With the assumption of unity Lewis number, equal diffusivity and adiabatic conditions, the enthalpy equation of any process takes a form identical to that of element mass fraction. These conserved scalars can be related to a single normalized conserved scalar called the *mixture fraction*.

In the present chapter, the role of mixture fraction in non-premixed combustion is discussed in section 4.1 as a preface to the classical steady laminar flamelet model which is discussed in section 4.2. Details of the non-adiabatic flamelet model (NAFM) with the advanced formulation for non-premixed combustion to account the radiation heat losses are discussed in section 4.3. Introduction to flamelet progress variable approach and its formulation is presented in section 4.4. Finally, the unsteady flamelet/progress variable approach which is the current research topic is discussed in section 4.5.

4.1 Mixture Fraction Space

Under the assumption of unity Lewis number, equal diffusivity and adiabatic conditions, the conserved scalars such as the element mass fraction of species can be related to single normalized conserved scalar, the mixture fraction, and the problem can be reduced to the solution of a single transport equation for the mixture fraction. All the species mass fractions and temperature can then be calculated from mixture fraction concentrations using functional relationships. This forms the basis of the conserved scalar approach. This approach is introduced through the main formulation of flame-sheet model which is the simplest of the conserved scalar models. The conserved scalar approach and its formulations have been extensively discussed by Williams (1985).

With the inclusion of differential diffusion the mixture fraction becomes sensitive to the particular element on which the definition is based. The element mass fraction no longer has a linear dependence with flame position (Drake and Blint, 1988). To overcome this problem, Bilger (1988) suggested a definition for mixture fraction which is based on a linear combination of elemental mass fractions of C, H and O:

$$f = \frac{2(f_C - f_{C,2})/W_C + (f_H - f_{H,2})/2f_H - (f_O - f_{O,2})/W_O}{2(f_{C,1} - f_{C,2})/W_C + (f_{H,1} - f_{H,2})/2f_H - (f_{O,1} - f_{O,2})/W_O} \qquad (4.1)$$

where, subscripts 1 and 2 denote fuel and air streams and W represents the molecular weight. This formulation preserves the stoichiometric value of the mixture fraction, independent of the effects of differential molecular diffusion. This definition of mixture fraction has been widely adopted (Dally, 1998a; Pitsch and Peters, 1998; Hossain, 1999; Barlow *et al.*, 2000; Liu *et al.*, 2005) and is therefore employed in the present study.

4.1.1 Combustion and Chemistry

The basic models that are used to relate the chemical state and mixture fraction are based on the general assumption of 'fast' chemistry, the condition that chemical kinetics are infinitely fast in comparison to other processes in the flow. One of the well known models is the Burke-Schumann limit or Flame sheet model, where the chemistry is described by a single step irreversible reaction and the reactive scalar

variables are determined directly from the given reaction stoichiometric conditions, with no reaction rate or chemical equilibrium information required. The Flame Sheet model requires minimal calculation effort but is limited to the prediction of only major species of the single step reaction. It provides no information on intermediate species or dissociation effects thereby often resulting in an over-prediction in flame temperatures. Equilibrium chemistry model assumes that the chemistry is fast enough for the chemical equilibrium to always exist at molecular level. The reactive scalar variables are expressed as a function of mixture fraction using the minimization of Gibbs free energy. This model offers the advantage of predicting intermediate species even without the knowledge of detailed chemical kinetic rate data. In each of these models, the reactive scalar variables are expressed only as function of mixture fraction:

$$\phi = \phi(f), \phi = \rho, T, Y_i \tag{4.2}$$

In turbulent reacting flows, the instantaneous relationship between the mixture fraction and the reactive scalars is non-linear due to fluctuations. Hence the mean scalar variables cannot be obtained by the above relations by simple substitution of a mean mixture fraction $\tilde{f}$ instead of *f*. To overcome this problem, a presumed shape probability density function *P(f)* is introduced and the mean reactive scalar variables in the turbulent field are obtained from:

$$\tilde{\phi} = \int_0^1 \phi(f) P(f) df \tag{4.3}$$

Fast chemistry/Equilibrium chemistry models are limited to situations where chemical kinetics does not play a significant role. However, they provide basis for the development of more capable models.

4.2 Steady Laminar Flamelet Model (SLFM)

Flame-sheet model considers single step irreversible reaction with infinitely fast chemistry and therefore the reactants cannot co-exist and the reaction occurs in an infinitely thin zone. The thermo chemical state is a function of only the mixture fraction. In this model the fluctuations of variables like temperature and species mass fraction are taken into account by incorporating a probability density function (PDF) to calculate the mean quantities. In the PDF approach, which resembles the turbulence

modelling technique where the average value of a thermo-chemical scalar variable is obtained by weighting the instantaneous value with a probability density function for mixture fraction *f*. But this model is not capable of predicting intermediate species. Equilibrium model overcomes this problem but fails in accounting finite rate effects. Partial equilibrium models predict well to an extent by implementing reduced reaction mechanisms. Finally, the laminar flamelet model was found to deal with non-equilibrium effects with detailed chemistry and is considered as an extension of conserved scalar approach.

The SLFM replaces the equilibrium states of the thermo-chemistry by the set of solution space consisting of steady one-dimensional diffusion-reaction equations called as the flamelet equations. SLFM is considered as a turbulent flame which is an ensemble of large laminar diffusion flamelets. Flamelets are thin reactive-diffusive layers embedded within an otherwise non-reacting turbulent flow field. For a fixed level of stretching, all the thermo-chemical properties of flamelets are function of conserved scalar i.e., the mixture fraction. Hence a flamelet is a function of mixture fraction and scalar dissipation rate. These parameters are statistically distributed in turbulent flows. To predict non-equilibrium effects in turbulent diffusion flames, introduction of these flamelets into turbulent flow is performed by considering their joint probability density function. Flamelet modelling has the advantage of separating the numerical effort associated with the resolution of small chemical time and length scales from CFD computations of turbulent flow field.

4.2.1Definition of Flamelet Equations

Peters (1984) was the first to derive the flamelet equations for describing the reactive-diffusive structure in the vicinity of flame surface as a function of mixture fraction. A co-ordinate transformation, applied at the flame surface is introduced as a first step. This is illustrated in Fig. 4.1 for a two feed turbulent jet diffusion flame.

The field equation for the mixture fraction that determines the flame surface location is given by:

$$\frac{\partial}{\partial t}(\rho f)+\frac{\partial}{\partial x_k}(\rho u_k f)=\frac{\partial}{\partial x_k}\left[\rho\Gamma\frac{\partial f}{\partial x_k}\right] \tag{4.4}$$

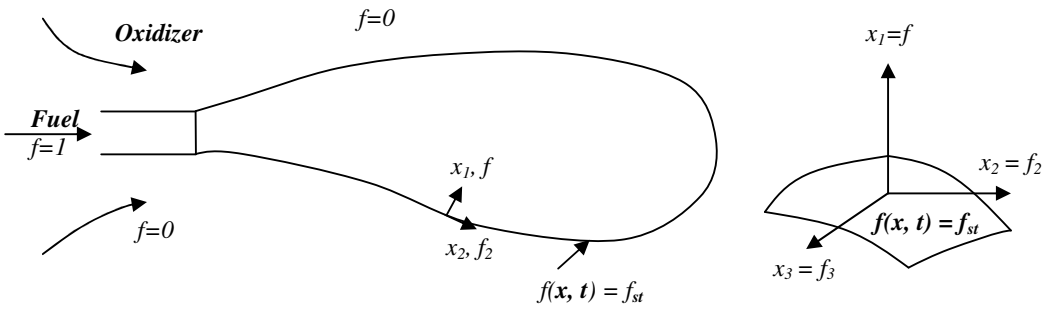

Figure 4.1 Surface of stoichiometric mixture for a turbulent jet diffusion flame

Solution to the above equation provides information about the mixture fraction f as a function of space (x) and time (t). Combustion essentially takes place in the vicinity of the stoichiometric surface ($f=f_{st}$) if the local mixture fraction gradient is sufficiently high, Peters (1984). This thin layer with the surrounding inert mixing region is termed as ***laminar diffusion flamelet***. An orthogonal coordinate system is attached to this stoichiometric surface (Fig 4.1-right hand diagram) in such a way that f is normal to surface while the other two coordinates lie tangential to the surface as shown. Transformation from coordinate system (x_1, x_2, x_3, t) to (f, f_2, f_3, τ) is implemented in balance equations for species and temperature and the modified equations after simplifications are used for the solution domain.

With the basic assumption that the reactive scalars in the tangential directions to be negligible when compared in the normal or f direction, the equations are simplified further and represented for unity Lewis number as below

$$\rho\frac{\partial Y_i}{\partial t}=\rho\frac{\chi}{2}\left(\frac{\partial^2 Y_i}{\partial f^2}\right)+\dot{\omega}_i \tag{4.5}$$

$$\rho\frac{\partial T}{\partial t}-\rho\frac{\chi}{2}\left(\frac{\partial^2 T}{\partial f^2}\right)-\rho\frac{\chi}{2C_p}\left(\frac{\partial T}{\partial f}\frac{\partial C_p}{\partial f}\right)-\sum_{i=1}^{N}\rho\frac{\chi}{2}\frac{C_{pi}}{C_p}\left(\frac{\partial Y_i}{\partial f}\frac{\partial T}{\partial f}\right)+\frac{1}{C_p}\sum_{i=1}^{N}h_i\dot{\omega}_i+\frac{Q_{rad}}{C_p}=0 \tag{4.6}$$

where, ρ is the density, T is the temperature, C_p is the specific heat at constant pressure, $\dot{\omega}$ is the reaction rate, h is the enthalpy, Q_{rad} is the radiative source per unit volume and the subscript i refers to the i^{th} chemical species. The symbol χ in the above equations is the instantaneous scalar dissipation rate and represents the influence of flow field on local flame structure.

The value of χ in the above two equations is given by the expression below,

$$\chi = 2D\left(\frac{\partial f}{\partial x_k}\right)^2 \tag{4.7}$$

The scalar dissipation rate accounts for non-equilibrium effects caused by both convection and diffusion (Bray and Peters, 1994). The above equations (4.5) and (4.6) describe the one dimensional flamelet structure in mixture fraction space. In above equations, curvature effects are neglected i.e. spatial gradients tangential to flame front are considered negligible compared to the one normal to surface. A functional dependence of scalar dissipation rate on mixture fraction is modelled according to Peters (1984) by considering laminar counter flow diffusion flame configuration to solve the above mentioned equations.

4.2.2Probability Density Function

In order to control the non-linear fluctuations between the instantaneous mixture fraction and scalars a presumed probability density function *P(f)* is introduced and the mean scalar variables in a turbulent field can be expressed as

$$\tilde{\phi} = \int_0^1 \phi(f)\, P(f)\, df \tag{4.8}$$

The shape of the probability density function for the mixture fraction in the present work is assumed to be β-PDF function (Jones and Whitelaw, 1982). The β-PDF is given in terms of mean mixture fraction and mixture fraction variance. The latter two are obtained from the solution of their respective transport equations. Mean mixture fraction and its corresponding variance transport equation are given as:

$$\frac{\partial}{\partial t}\left(\rho\tilde{f}\right) + \frac{\partial}{\partial x_k}\left(\rho u_k \tilde{f}\right) = \frac{\partial}{\partial x_k}\left[\frac{\mu_t}{Sc_{\tilde{f}t}}\frac{\partial \tilde{f}}{\partial x_k}\right] \tag{4.9}$$

$$\frac{\partial}{\partial t}\left(\rho\widetilde{f''^2}\right) + \frac{\partial}{\partial x_k}\left(\rho u_k \widetilde{f''^2}\right) = \frac{\partial}{\partial x_k}\left(\frac{\mu_t}{Sc_{\widetilde{f''^2}t}}\frac{\partial \widetilde{f''^2}}{\partial x_k}\right) + 2\frac{\mu_t}{Sc_{\widetilde{f''^2}t}}\left(\frac{\partial \widetilde{f''^2}}{\partial x_k}\right)^2 - \bar{\rho}\tilde{\chi} \tag{4.10}$$

A transport equation (4.9) for filtered mixture fraction is solved and the subgrid variance is modelled in LES. Such an approach has been established for LES after significant testing carried out by several works in the past (Cook and Riley, 1994;

Branley and Jones, 2001; Pierce and Moin, 1998). Cook and Riley (1994) suggested the following model based on a scale similarity hypothesis.

$$\widetilde{f''^2} = C_z\left(\widehat{\tilde{f}^2} - \hat{\tilde{f}}^2\right) \tag{4.11}$$

The filter operator with the cap in the above equation indicates the test filtering operator by dynamic procedure. The value of the constant $C_z = 1.0$ is considered to be a reasonable assumption. The hypothesis behind scale similarity is that the largest unresolved scales have a structure similar to the smallest resolved scalars. Laminar flamelet modelling includes all the scalar variables as function of mixture fraction and scalar dissipation rate. Mean values of these scalar variables are given by the following expression:

$$\tilde{\phi} = \int_0^\infty \int_0^1 \phi(f;\chi_{st})\, P(f)\, P(\chi_{st})\, df\, d\chi_{st} \tag{4.12}$$

Flamelet calculations provide the scalar profiles as a function of mixture fraction and scalar dissipation rate. In turbulent flow field these parameters are statistically distributed. In order to predict non-equilibrium effects in turbulent diffusion flames, it is therefore necessary to predict the joint probability distribution function of f and χ. In the present study, the joint PDF is modeled by assuming statistical independence between f and χ_{st} and presuming the shape of their marginal PDF as

$$\tilde{P}(f,\chi_{st}) = \tilde{P}(f)\,\tilde{P}(\chi_{st}) \tag{4.13}$$

The shape of the mixture fraction equation is assumed to be β-PDF distribution and that of scalar dissipation rate χ is assumed to delta function in the present study.

$$\widetilde{P}(f) = \frac{f^{a-1}(1-f)^{b-1}}{\int_0^1 f^{a-1}(1-f)^{b-1}\,df} = \frac{\Gamma(a+b)\, f^{a-1}(1-f)^{b-1}}{\Gamma(a)\ \Gamma(b)} \tag{4.14}$$

where, the coefficients a and b are functions of mean mixture fraction and its variance.

$$a = \tilde{f}\left[\frac{\tilde{f}\left(1-\tilde{f}\right)}{\widetilde{f''^2}} - 1\right] \tag{4.15}$$

$$b = \left(1-\tilde{f}\right)\left[\frac{\tilde{f}\left(1-\tilde{f}\right)}{\widetilde{f''^2}}-1\right] \tag{4.16}$$

The marginal PDF for scalar dissipation rate is assumed to follow a log-normal distribution in case of NAFM approach towards radiation coupled LES calculations. The presumption of log-normal distribution for scalar dissipation rate has been experimentally found to be valid by Effelsberg and Peters (1988).

$$\tilde{P}\left(\chi_{st}\right) = \frac{1}{\chi_{st}\sigma\sqrt{2\pi}} exp\left[-\frac{1}{2\sigma^2}\left(ln\chi_{st}-\mu\right)^2\right] \tag{4.17}$$

where the parameters μ and σ are related to the first and second moments of χ by

$$\tilde{\chi} = exp\left(\mu+\frac{\sigma^2}{2}\right) \tag{4.18}$$

$$\widetilde{\chi''^2} = \tilde{\chi}^2\, exp\left(\sigma^2-1\right) \tag{4.19}$$

Therefore, $\tilde{P}\left(\chi_{st}\right)$ can be evaluated from the knowledge of $\tilde{\chi}$ and σ. For the present study a value of σ=2.0 has been chosen after experimental results by Sreenivasan *et al.* (1977).

Cook and Riley (1998) suggested that filtered scalar dissipation rate can be derived using the effective viscosity and filtered mixture fraction gradient. The model equation is given by

$$\tilde{\chi} = 2\left(\frac{\nu}{Sc}+\frac{\nu_T}{Sc_T}\right)\left(\frac{\partial\tilde{f}}{\partial x_k}\frac{\partial\tilde{f}}{\partial x_k}\right) \tag{4.20}$$

The effective viscosity is obtained from a localized dynamic procedure while the laminar and turbulent Schmidt numbers take the values of 0.7 and 0.4 respectively. Current LES calculations adopt the above model for filtered scalar dissipation rate calculations. The scalar dissipation rate and the strain rate are the two parameters which directly represent the flow dependent effects in the laminar flamelet calculations. Scalar dissipation rate can be expressed in terms of the strain rate, a_s and mixture fraction f as below:

$$\chi_{st} = \frac{a_s}{\pi}\exp\left\{-2\left[erfc^{-1}\left(2f_{st}\right)\right]^2\right\} \tag{4.21}$$

Here χ_{st} is the stoichiometric scalar dissipation rate and $erfc^{-1}$is the inverse of the complementary error function.

4.2.3Flamelet Quenching

The scalar dissipation rate is used to describe local extinction according to the flamelet concept. As the scalar dissipation rate is increased, the stretch on the flamelet is increased and at a particular limit the heat loss from the reaction zone balances the heat generation from chemical reaction. This is the quenching limit, χ_q and is obtained from the flamelet calculations. Beyond this limit, the flamelet extinguishes. The fraction of burnable flamelets in the turbulent flame may then be calculated as probability of $\chi < \chi_q$:

$$P_b = \frac{1}{2} + \frac{1}{2}\left(erf\left(\frac{\ln\chi_q/\tilde{\chi} + 1/2\sigma^2}{\sqrt{2}\sigma}\right)\right) \tag{4.22}$$

The value of P_b lies between zero and unity depending on the extent of non-equilibrium in the turbulent flame. For a zero mean scalar dissipation rate corresponding to equilibrium condition P_b is unity. As the scalar dissipation rate increases the chemistry shifts away from equilibrium, probability of occurrence of flamelets decreases and P_b becomes less than unity. Flamelet after quenching is assumed to follow pure mixing state.

4.2.4Limitations of SLFM

The incapability of SLFM to handle local extinction and to predict NO_x emissions is a concern for its application towards turbulent flames. The assumption of considering steady-state solutions of the flamelet equations has been advocated by Peters (1984) with the view that away from extinction, the changes in scalar dissipation rate are slow enough for the flamelet structure to be considered as in steady state. However, this assumption becomes invalid for the slow chemistry of NO_x and the complex physical phenomena of radiation. Pitsch *et al.* (1998) have shown that considering the radiation heat loss through the source term in the steady flamelet equations results in large discrepancies in the reactive scalars. Considering solutions of unsteady flamelet

equations and therefore resorting to a transient flamelet modelling has been advocated by them to resolve the issues with both radiation and NO_x. However, from a practical application perspective, employing a transient flamelet modelling is significantly more expensive than the steady flamelet modelling especially when CFD calculations are coupled with flamelet calculations.

Hence in the present work, attempts have been made to extend the steady flamelet model to a LES based non-adiabatic formulation which while using steady flamelets, is able to consider the effect of radiation heat loss through enthalpy defect concept. The current work also focuses on implementing unsteady flamelet calculations for modelling partially premixed lifted flames.

4.2.5Advanced Flamelet Modelling

With the restricted utilization of SLFM, combustion modelling is required to develop by considering the flame instabilities. Figure 4.2 shows the maximum flamelet temperature as a function of the stoichiometric scalar dissipation rate. The inverse S-shaped curve includes three major portions.

1. Stable burning branch
2. Partially extinguished unstable branch
3. Fully extinguished limit

The upper branch describes the fully burning solutions and the lower branch the non-burning state. The intermediate branch comes from solutions of the steady flamelet equations, but the solutions are unstable. In the steady flamelet model, we use only the upper branch of the curve. Even though the lower branch also describes physical solutions to the equations, incorporating these solutions in the model leads to large jumps in temperature and density for dissipation rates around the extinction limit and also results in numerical instabilities.

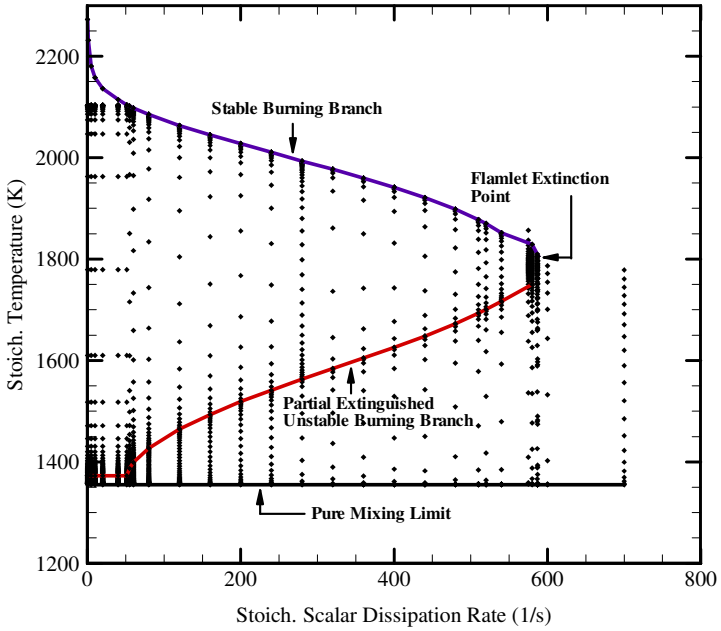

Figure 4.2 Solution space of laminar unsteady flamelet equations for CH_4/Air flame (Berkeley lifted flame) Fuel CH_4-Air (25%-75%) at 323 K and Oxidizer (vitiated co-flow) at 1355 K.

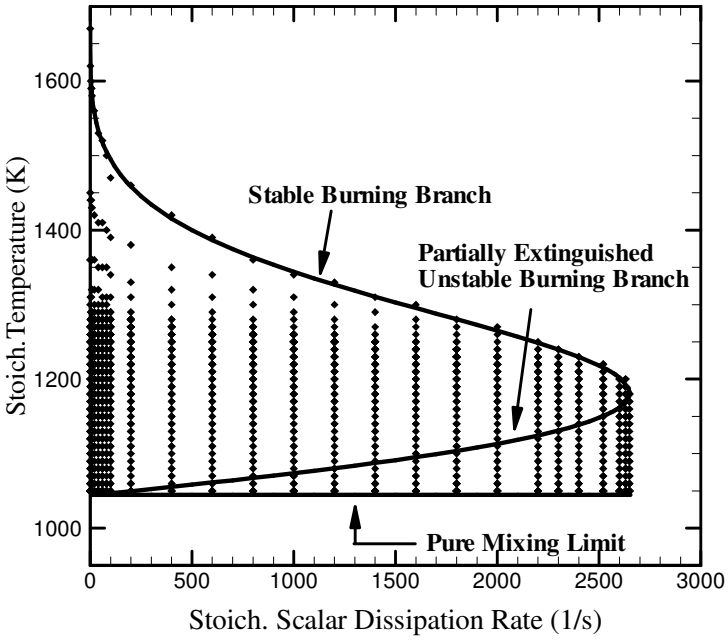

Figure 4.3 Unsteady flamelet solution space for H_2/N_2 flame. Dotted (*) points resemble the unsteady flamelet solutions at various scalar dissipation rates

The point of maximum flame temperature at scalar dissipation rate near to zero represents to the state of chemical equilibrium. An increase in the scalar dissipation rate corresponds to an increase in the mixing of the reactants. Thus, on the stable burning branch, the maximum flame temperature decreases with increase in the scalar dissipation rate due to the dilution of the product concentrations with the increased concentration of reactants. As the quenching point is reached, the flame temperature drops to a level where Arrhenius rate factors in the chemical kinetics begin to limit the reaction rates and thereby results in the complete extinction of the flamelet from thereon. Along unstable branch, dissipation rate decreases with decreasing flame temperature to keep the mixing in balance with the lower reaction rates. On the lower branch of completely extinguished states, the effect of chemical kinetics is negligible and the chemical states are independent of dissipation rate. All the chemical states on the lower branch thus point to pure mixing of the reactants.

4.3 Non Adiabatic Flamelet Model (NAFM)

The laminar flamelet model of Peters (1984) describes the thermo-chemical structure of a laminar flamelet in terms of a conserved scalar given by mixture fraction (*f*) and scalar dissipation rate (χ_{st}) which is conditioned on stoichiometric mixture fraction is used in the present study. But for the case of non-adiabatic flamelet model, flamelet structure will have the effect from radiative heat loss which should be accounted for. Bray and Peters (1994) and Ravikanti *et al.* (2008) have suggested solving a transport equation for enthalpy with radiation source term with the introduction of a new parameter called "enthalpy defect" (ζ) to couple the flamelet structure with non-adiabatic flow. Enthalpy defect ζ is defined as the difference between the actual enthalpy $\tilde{h}$ and adiabatic enthalpy $\tilde{h}_{ad}$ which can be directly related to the mean mixture fraction:

$$\zeta = \tilde{h} - \tilde{h}_{ad} = \tilde{h} - \left(h_1 + \tilde{f} \left(h_2 - h_1 \right) \right) \tag{4.23}$$

In the above expression, h_2 and h_1 represent the enthalpy of fuel and air streams respectively. Enthalpy defect provides a measure of the local non-adiabatic conditions in the turbulent flame. By imposing enthalpy defect as an additional parameter onto the flamelet solution, coupling between the non-adiabatic conditions in the turbulent flame and the thermo-chemical structure of the flamelet is achieved. As the effect of

radiation on flamelet structure is not handled through a source term, steady flamelet equations can be used to obtain the thermo-chemical structure of the flame. Therefore, any scalar variable (ϕ) in the non-adiabatic flamelet model is a function of mixture fraction *f*, stoichiometric scalar dissipation rate χ_{st} and the enthalpy defect ζ.

$$\tilde{\phi} = \tilde{\phi}\left(f; \chi_{st}; \zeta\right) \tag{4.24}$$

Turbulent mean value of a scalar ϕ can then be obtained by integrating the instantaneous values with joint PDF of the three parameters *f*, χ_{st} and ζ.

$$\tilde{\phi} = \int_{\zeta_{min}}^{\zeta_{max}} \int_0^\infty \int_0^1 \phi\left(f; \chi_{st}; \zeta\right) \tilde{P}\left(f, \chi_{st}, \zeta; x, t\right) df\, d\chi_{st} d\zeta \tag{4.25}$$

A statistical independence between the three parameters (*f*, χ_{st} and ζ) has been assumed and a presumed PDF approach has been adopted. The PDF for mixture fraction is assumed to follow β function distribution, PDF for scalar dissipation rate assumed to follow log-normal distribution and a δ function has been assumed for enthalpy defect. Bray and Peters (1994) argued that fluctuations in enthalpy are mainly due to mixture fraction variations and therefore strengthens our selection of δ function for enthalpy defect and β function distribution for mixture fraction. Therefore, any filtered scalar can be represented in the integral form which is represented as

$$\tilde{\phi} = \int_{\zeta_{min}}^{\zeta_{max}} \int_0^\infty \int_0^1 \phi\left(f; \chi_{st}; \zeta\right) \tilde{P}\left(f\right) \tilde{P}\left(\chi_{st}\right) \delta\left(\zeta - \tilde{\zeta}\right) df\, d\chi_{st} d\zeta \tag{4.26}$$

The present simulation studies include density as a function of mixture fraction alone. But all other scalars like temperature and major species are assumed to take the above integral form with a function of mixture fraction, scalar dissipation rate and enthalpy defect. This non-adiabatic version of steady laminar flamelet model (SLFM) has been referred as NAFM (non-adiabatic flamelet model with multiple scalar dissipation rates) in the present study. The present model involves the variation in non-adiabatic structure with respect to scalar dissipation rate for each enthalpy defect. Hossain *et al.* (2001) contributed to the development of this model considering only a single flamelet per enthalpy defect. Such a simplification drastically reduces the flamelet generation effort as well as pre-integration effort. However, the present work aims at

incorporation of all flamelet solutions for each enthalpy defect in order to include the scalar dissipation rate fluctuations.

4.4 Flamelet/Progress Variable Approach

The FPV model first developed by Pierce and Moin (2004) was specifically for LES to address flame lift-off and re-ignition issues. All filtered scalar quantities are evaluated from a flamelet library and a presumed joint filtered PDF (FPDF). This is similar to the steady flamelet model, but the two quantities that are used to parameterize the flamelet solutions are the mixture fraction f and a reaction progress parameter λ, which is related to the reaction progress variable C. Also the presumed joint FPDF that is used in the model has to be formulated for these two quantities. This flamelet parameter replaces the scalar dissipation rate. But when the fluctuations in the scalar dissipation rate are considered, the problem becomes more complicated. A transport equation is solved for the filtered reaction progress variable. The reaction progress variable can be defined in different ways. The present case study is involved with CH_4/Air partially premixed flame in vitiated co-flow. The vitiated co-flow in this flame, which also acts as the oxidizer, has significant levels of H_2O and H_2. Therefore, in order to keep the definition of progress variable as simple as possible, the mass fractions of CO_2 and CO are considered. The progress variable is thus given by:

$$C = Yco_2 + Yco \tag{4.27}$$

The definition of flamelet parameter is considered as the maximum value of the progress variable from each flamelet (C_{max}) as depicted in Fig. 4.4. Each flamelet has its own flamelet parameter and therefore it is independent of mixture fraction. Thus easing the task of integration with individual PDF shapes considered for mixture fraction and flamelet parameter to be solved. Therefore, any filtered values of the reactive scalars $\tilde{\phi}$ in large eddy simulation can be obtained as

$$\tilde{\phi} = \int_0^1 \int_{\lambda_{min}}^{\lambda_{max}} \phi(f;\lambda)\, \tilde{P}(f,\lambda;x,t)\, d\lambda\, df \tag{4.28}$$

But the Favre filtered joint PDF in the above expression is independent of its parameters, can be written as

$$\tilde{P}(f,\lambda;x,t)=\tilde{P}(f)\tilde{P}(\lambda) \tag{4.29}$$

Early works of Pierce and Moin (2004) and Pitsch and Ihme (2005) involving the marginal FPDF of flamelet parameter was assumed to be a δ-function PDF. Ihme *et al.* (2005) have proved to predict better with the β-function PDF for the same flamelet parameter under DNS calculations. The present study uses a δ-function PDF for flamelet parameter considering the computational cost involved with the inclusion of scalar dissipation rate fluctuations where the scalar dissipation rate is assumed to follow a δ-function PDF. This forms the basis for modelling of Unsteady Flamelet/Progress Variable (UFPV) approach.

Flamelet parameter space is converted to progress variable space, thereby converting any scalar $\tilde{\phi}$ in-terms of mean mixture fraction, mixture fraction variance and mean progress variable.

$$\tilde{\phi}=\tilde{\phi}\left(\tilde{f},\widetilde{f''^2},\tilde{C}\right) \tag{4.30}$$

The transport equation for the reaction progress variable can be derived from the definition of C which has the assumption of unity Lewis numbers for the species involved in its filtered form is given as

$$\frac{\partial}{\partial t}\left(\bar{\rho}\tilde{C}\right)+\frac{\partial}{\partial x_k}\left(\bar{\rho}\tilde{u}_k\tilde{C}\right)=\frac{\partial}{\partial x_k}\left(\left(\frac{\mu}{Sc}+\frac{\mu_t}{Sc_t}\right)\frac{\partial\tilde{C}}{\partial x_k}\right)+\bar{\rho}\tilde{\dot{\omega}}_c \tag{4.31}$$

Here the filtered reaction source term $\tilde{\dot{\omega}}_c$ is calculated from the chemical states predicted by the steady flamelet equations which is the summation of the production rates of product species involved in progress variable definition i.e., CO_2 and CO. The laminar and turbulent Schmidt numbers in the above equation takes a value of 0.7 and 0.4 respectively. The progress variable from the steady laminar flamelet solution can therefore be expressed as

$$\tilde{C}_{slfe}=\int_0^1\int_{\lambda_{min}}^{\lambda_{max}}C(f;\lambda)\beta\left(f;\tilde{f},\widetilde{f''^2}\right)\delta\left(\lambda-\tilde{\lambda}\right)d\lambda df \tag{4.32}$$

$\tilde{C}_{slfe}$ is the value of the progress variable obtained from the solution of steady laminar flamelet equations. The methodology adopted in the present study is taken from the work carried out by Ravikanti (2008) for the constraint equation which satisfies

$$\tilde{C} = \tilde{C}_{slfe} \tag{4.33}$$

This eliminates the need for direct computation of the filtered flamelet parameter $\tilde{\lambda}$ in turbulence modelling. The re-mapping or re-interpolation technique employed in the present thesis originally developed by Ravikanti (2008)

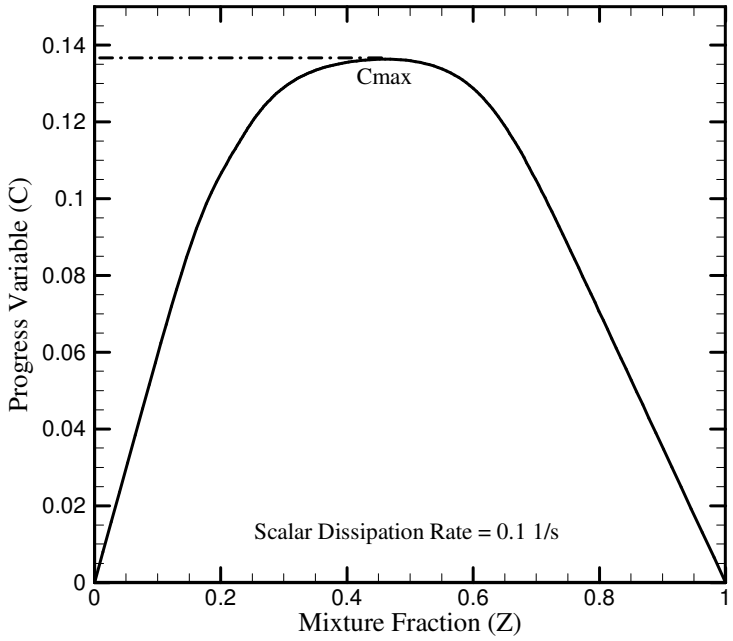

Figure 4.4 Definition of flamelet parameter for scalar dissipation rate of $0.1s^{-1}$ for Berkeley lifted flame.

4.5 Unsteady Flamelet/Progress Variable Approach

4.5.1 Motivation

The UFPV approach derives motivation from some of the fundamental problems with the steady flamelet model for non-premixed combustion (SLFM) and flamelet progress variable (FPV) approach in addressing the most complex features of flame extinction and re-ignition. Partially premixed flames are better predicted with the inclusion of unsteady effects in the flamelet solution. Therefore, unsteady flamelet

progress variable (UFPV) model, which combines the unsteady flamelet formulation with the progress variable approach, has been used to predict emissions like CO mass fraction by Ihme and Pitsch (2005) with reasonable success. With this confidence, the present study considers the unsteady flamelet approach with the variations in scalar dissipation rate coupled with the progress variable approach.

Here the model is used mainly to predict the lift-off height and flame properties of partially premixed flames. With the beta PDF for progress variable, the inclusion of scalar dissipation rate and beta PDF for mixture fraction in the lookup table considerably increases the computational space and time. In the work presented here, as a preliminary step towards developing the unsteady flamelet progress variable (UFPV) approach, a delta PDF for reaction progress variable is selected to keep the computational cost manageable and UFPV model is applied to predict lifted flames. The objective of the present work is to validate the UFPV combustion model for partially premixed lifted flames and test the model with two different fuel compositions CH_4/Air and H_2/N_2 where experimental data is available.

4.5.2Formulation

An unsteady flamelet/progress variable model was developed and formulated as an extension of the steady flamelet/progress variable model, Ihme and Pitsch (2005). A large number of unsteady laminar flamelet simulations are performed for the various scalar dissipation rates and the solutions are recorded as function of time. The flamelet library is generated later which provides the filtered quantities of all scalars as a function of the filtered mixture fraction, the mixture fraction variance, the filtered reaction progress variable and the filtered scalar dissipation rate. UFPV was applied to co-axial burner for testing emission predictions (Ihme and Pitsch, 2005) in the past, but is applied to partially premixed lifted flames for the first time in the current research. Theory behind this model is explained below. This model is yet to be tested for any lifted non-premixed flames.

The transient solution of the flamelets is expected to predict the flame extinction and re-ignition phenomena in turbulent flows. The instantaneous drastic change in the scalar dissipation rate cannot be neglected for the turbulent flow which might not

follow the instantaneous change in the temperature. In UFPV approach, flamelet parameter and scalar dissipation rate are independent parameters along with the mixture fraction for the construction of flamelet library. Therefore, each scalar dissipation rate has an individual distribution of flamelet parameter and mixture fraction. The flamelet library is constructed with all the extinguished and re-igniting flamelets. Figure 4.2 shows the vertical dots that represent the unsteady flamelet solution, which are calculated with respect to time for different scalar dissipation rates from equilibrium to extinction. The flamelet library consists of all scalars which are dependent on mean mixture fraction, mixture fraction variance, progress variable and scalar dissipation rate. The flamelet library is produced from the flamelet generation methodology adopted by Pitsch and Fedotov (2001) where the rate of change in temperature is positive on the left of S-shaped curve (Fig. 4.2) and negative on the right side. Here, in the present case we considered the flamelets till extinction. Therefore, we are focused on the left side of the S-shaped curve including the extinction limit. Flamelet calculations are performed using the steady state solutions on the unstable branch of the S-shaped curve as initial conditions. The value of the scalar dissipation rate is assumed to be slightly lower than that of steady state for the unsteady calculations. Because of the unstable nature of the middle branch, the maximum temperature from the flamelet solution tries to increase and reach the stable branch. Similarly the unsteady solution below the middle branch is obtained with a slight increase in the scalar dissipation rate as the initial solution. The vertical dots in Fig. 4.2 and Fig. 4.3 represent the unsteady solution space which is later converted to a pre-integrated PDF table. The variable parameter here is time which is eliminated in UFPV approach, similar to elimination of scalar dissipation rate in FPV approach with the flamelet parameter λ. Thus the flamelet solution is now parameterized with mixture fraction *f,* flamelet parameter λ and stoichiometric scalar dissipation rate χ_{st}. The flamelet space for any scalar can be expressed as

$$\phi = \phi(f, \lambda, \chi_{st}) \tag{4.34}$$

The flamelet parameter and scalar dissipation rate are independent of mixture fraction and the three parameters are assumed to be independent of each other and thus the joint PDF can be expressed as

$$\tilde{P}(f, \lambda, \chi_{st}) = \tilde{P}(f)\tilde{P}(\lambda)\tilde{P}(\chi_{st}) \tag{4.35}$$

Similar to FPV approach, the distribution of mixture fraction is assumed to be beta PDF and a delta PDF distribution for flamelet parameter. The scalar dissipation rate is assumed to follow a delta PDF distribution. Hence the above equation can be represented as

$$\tilde{P}(f,\lambda,\chi_{st}) = \beta\left(f;\tilde{f},\widetilde{f''^2}\right)\delta\left(\lambda-\lambda^*\right)\delta\left(\chi_{st}-\chi_{st}^*\right) \qquad (4.36)$$

The complexity of solving the property variables of the delta function, λ^* and χ^* is eliminated by replacing the value of flamelet parameter λ by progress variable $\tilde{C}$ and stoichiometric scalar dissipation rate χ_{st} by mean scalar dissipation rate $\tilde{\chi}$, Pitsch and Ihme (2005).

The LES model solves the equations of conserved scalar and progress variable to obtain the mean values of mixture fraction $\tilde{f}$, its variance $\widetilde{f''^2}$, progress variable $\tilde{C}$ and scalar dissipation rate $\tilde{\chi}$. Flamelet parameter is normalized to vary from 0 to 1. The re-mapping technique of Ravikanti (2008) is used here for conversion of flamelet parameter to progress variable. The mean progress variable obtained from the LES is made equal to the progress variable calculated from the pre-integration PDF table as the only constraint. We thus obtain the filtered scalars as a function of $\tilde{f}, \widetilde{f''^2}, \tilde{C}$ and $\tilde{\chi}$. These four parameters are obtained as the mean values from LES which are interpolated for obtaining the mean scalars from the PDF lookup table. The variables such as the density, temperature and other species will be a function of the above mentioned quantities and thus,

$$\tilde{\rho} = \tilde{\rho}\left(\tilde{f},\widetilde{f''^2},\tilde{C},\tilde{\chi}\right)$$

$$\tilde{T} = \tilde{T}\left(\tilde{f},\widetilde{f''^2},\tilde{C},\tilde{\chi}\right)$$

$$\tilde{Y}_i = \tilde{Y}_i\left(\tilde{f},\widetilde{f''^2},\tilde{C},\tilde{\chi}\right)$$

$$\tilde{\dot{\omega}}_c = \tilde{\dot{\omega}}_c\left(\tilde{f},\widetilde{f''^2},\tilde{C},\tilde{\chi}\right) \qquad \ldots\ldots (4.37)$$

During the LES calculations, the variables are read from the lookup table for every time step. Density and progress variable source term $\tilde{\omega}_c$ are read for all inner iterations in order to solve the transport equation for progress variable from the lookup table. This makes the computational time increase by a small amount but the solution covers the entire flamelets in order to capture the re-ignition and extinction phenomena.

4.6 Closure

The basic concepts of combustion modelling were discussed in the present chapter. Conserved scalar approach also called the mixture fraction approach was presented in brief following the theory behind the steady laminar flamelet model. Advanced flamelet theory with flamelet progress variable approach and unsteady flamelet progress variable methodology was discussed when applied to partial premixed turbulent lifted flames. Also the coupling of combustion-radiation modelling, well known as non-adiabatic flamelet model for reviewing the effects of radiation heat losses was presented.

Chapter 5

Coupling of Turbulence and Radiation

Radiation is often neglected in the turbulence reacting flow simulations applied to both automotive and gas turbine industry. The main reason for such neglecting it is the amount of effort needed to model radiation and the time involved in the overall solution procedure. However, in the recent past, effect of radiation is considered to be an important parameter in turbulence involved thermo-chemistry related problems. Radiation plays an important role in predicting the flow field with temperature distribution. Emissions are directly related to the temperature and heat release in any advanced gas turbine combustor and all other energy producing equipments. Therefore, better prediction in temperatures lead to better results in emissions such as NO_x and CO. Inclusion of radiation in turbulence chemistry flows, have shown to predict accurate temperature patterns, lower than those considered without radiation effects in general. Hence radiation calculations cannot be neglected for the proper flow and emissions prediction applied to any combusting related design.

Turbulence and radiation interaction is considered as a two way process. Turbulent fluctuations affect the radiation fluxes and in a similar manner radiation may in turn influence turbulence fluctuations. Most of the work on TRI has been performed to study the influence of turbulence on radiation. In the present work, turbulence is coupled with radiation to consider the non-linearity functional relationship of temperature and species concentration with the radiative flux. The radiative properties of the medium like the absorption coefficient depend on the temperature and species concentrations. A systematic approach for data exchange process between LES and radiation is performed and discussed later in this chapter.

Combustion and radiation are two different complex phenomena. In contrast to combustion process, radiation involves in long distance interaction phenomena and therefore was so far considered to be difficult for implementing radiation along with combustion chemistry. But the present day computer resources help to incorporate radiation in turbulence chemistry related problems through various radiation techniques such as DOM, DTM and Monte Carlo methods in solving the radiative transfer equation (RTE). Inclusion of radiation in RANS is disadvantageous as this turbulence model cannot provide the instantaneous values for scalars like temperature, mole fraction of CO_2 and H_2O. DNS and LES thus become the favourites for study of interaction between turbulence and radiation. Due to cost and time constraints, DNS remains expensive and is limited to simple flow configurations with relatively small Reynolds numbers. Hence, LES emerges as the preferred tool to inspect TRI effects in complex flow structures.

5.1 Introduction to TRI

Inclusion of radiation effects in combustion models is very important to achieve good accuracy in combustion modelling and estimation of correct wall heat transfer in the design equipment. Combustion and radiation are two different phenomena which need to couple with turbulence. The three giant physical processes are attempted to combine for better flow physics in the present work. Solving radiation alone involves considerable modelling effort. Approaches like Discrete Ordinate method (DOM) (Coelho *et al.,* 2003), Monte Carlo simulations (Tesse *et al.*, 2004) and Discrete Transfer method (DTM) (Coelho, 2004) ray tracing techniques are commonly used for radiation calculations. These methods are considered to be very expensive in terms of computational cost and time. But with the appropriate coupling strategy, these methods can prove very beneficial in the near future with the drastic growth in computer power. Radiative power is considered to be highly non-linear and varies at the first order as the fourth power of the local instantaneous temperature and thus requires information on local spatial correlations which can be obtained from large eddy simulation (LES) turbulence model. This problem of turbulence radiation interaction (TRI) has been addressed in the past and most recently by several authors (Coelho

(2003), Giordano and Lentini (2001), Li and Modest (2003), Wang *et al.* (2005)). SANDIA flame (Flame D) was most commonly used in studying the TRI effects and validation (Coelho (2003), Coelho (2004)). Direct numerical simulation (DNS) and LES gives the advantage to access the instantaneous spatial distribution of temperature and species which is the key input to radiation models. However, DNS will remain out of reach for practical industrial combustion systems for a long time as its application is limited to small configurations. TRI effects are best suited with LES for accounting the instantaneous spatial distribution. The subgrid scale contribution towards radiation may be eliminated or modeled. Solving the full filtered equation of RTE is a challenging task to be performed in LES. In a different approach, coupled LES of turbulent combustion and radiative heat transfer was performed by Goncalves dos Santos *et al.* (2005). A data exchange process within two different codes (radiation and LES) was performed to study the effects of radiation on turbulent combustion. A similar strategy is used in the present work with application of non-adiabatic flamelet model (NAFM). The details of this approach were depicted in Chapter 4.

Fluctuations in temperature and absorption coefficients result in radiation fluctuations which affect and contribute to combustion instabilities, extinction and re-ignition effects in all practical combusting situations. Radiation fluctuations have been studied and recognized to be an important issue in a number of studies (Tan and Foster, 1978), (Kounalakis *et al.*, 1988), (Porscht, 1975), (Koch *et al.*, 1975), (Sivathanu *et al.*, 1990), (Hartick *et al.*, (1995), (Sivathanu and Gore, 1993), (Cox, 1977), (Faith *et al.*, 1989), (Gore and Faith, 1986). Radiant intensity is found to increase by 24% with turbulent fluctuations in flames channeled under a corridor ceiling by Cox (1977) based on his theoretical studies. Experimental and theoretical work of Faeth *et al.* (1989), Gore and Faeth (1986) and Kounalakis *et al.* (1988) have shown that fluctuation of radiation intensity can be 100% of the mean values. Nelson (1988) showed that temperature fluctuations are dominating in TRI effects and Kiritzstien and Saufiani (1993) demonstrated the effect of turbulent fluctuations on radiation intensity. However, they found that concentration effects have minimal effect on radiation. A reasonable amount of work was carried out by Coelho (2007) on

TRI studies. Modelling TRI without transient data was performed by using PDF equations and Monte Carlo techniques by Mazumder and Modest (1999) for methane-air diffusion flames and showed that inclusion of absorption coefficient-temperature correlation increase radiative heat flux by 40-45%. Using DNS coupled with Monte Carlo approach for non-premixed flame situations, Modest and co-workers showed the important contributions from temperature self correlation, absorption coefficient-Planck function correlation and absorption coefficient-intensity correlation. Coelho (2007) using simulated flame conditions showed that turbulent fluctuations contribute to decrease in flame temperatures when compared with cases involving no radiation fluctuations.

The present study attempts to solve the non-adiabatic flamelet model for the inclusion of radiation effects with the introduction of ***enthalpy defect*** concept. The method involves the data exchange process, where the radiation source is calculated from the ray tracing discrete transfer (DT) method. This source is utilized in solving the enthalpy equation in LES. LES in return provides the instantaneous temperature, mole fractions of CO_2 and H_2O to radiation code which are required to calculate the absorption coefficient and all other parameters like radiation source and intensity. Therefore, the radiation data and statistics presented here are a coupled calculation which provides important parameters to identify TRI effects through a proper data transfer procedure.

In the following sections we describe the details of radiation methodology, details of data exchange process for coupling turbulence and radiation and finally the role of radiation on turbulence chemistry.

5.2 Radiation Modelling

Discrete transfer radiative methodology is employed in the present work out of the various techniques available. The sections below highlight the details of this method with the coupling procedure for the data exchange process.

5.2.1 Discrete Transfer Radiation Model (DTM)

The governing equation for describing radiation intensity field in an absorbing, emitting and scattering medium is the Radiative Transfer Equation (RTE) (Siegel

and Howell, 2001) which is of the integro-differential type. The radiative transfer equation is given by

$$\mu\frac{dI(\tau,\mu,\phi)}{d\tau} = -I(\tau,\mu,\phi) + (1-\omega)\, I_B[T] + \frac{\omega}{4\pi}\int_{\mu'=-1}^{1}\int_{\phi'=0}^{2\pi} I(\tau,\mu',\phi')\,\Phi(\mu',\phi';\mu,\phi)\, d\mu'\, d\phi'$$

(5.1)

where μ is the cosine of the polar angle θ, ϕ is the azimuthal angle, $I(\tau,\mu,\phi)$ is the intensity along direction μ, ϕ at optical depth τ measured perpendicular to the surface of the medium, I_B is the spectral black body intensity at temperature T, ω is the single scattering albedo and $\Phi(\mu',\phi';\mu,\phi)$ is the scattering phase function. The governing radiative transfer equation is of integro-differential nature which makes the analysis difficult and computationally expensive. The discrete transfer method (DTM) of Lockwood and Shah (1979, 1981) is one of the widely used methods to solve radiative transfer problems with participating medium.

The discrete transfer method is based on solving radiative transfer equation (RTE) for some representative rays fired from the boundaries. Rays are fired from surface elements into a finite number of solid angles that cover the radiating hemisphere about each element and the main assumption of the DTM is that the intensity through solid angle is approximated by a single ray. The number of rays and directions are chosen in advance. In the DT method RTE is solved for each ray from one solid boundary to another solid boundary in the geometry. Rays fired from solid surface boundaries and traced through the volume. The calculation of radiation source term is based on the distance traveled in each control volume. At the boundaries, radiative heat transfer boundary conditions are used to determine the intensity of rays fired from that surface area. As the correct initial intensities are unknown at the start of the calculation the procedure become iterative until correct radiative intensities are resolved. If ray intersection data is saved either in memory or as a file, ray tracing is not required after the 1st iteration, available ray data can be readily used making the process very efficient.

The following steps are followed in DTM calculations.

1. Read mesh file
2. Indexing
3. Calculate wall cell parameters
4. Calculate cell geometry parameters
5. Read input radiative transfer parameters
6. Conduct ray tracing and search procedure
7. Calculate radiative heat transfer outputs (wall fluxes/source terms)
8. Write results to a file.

The three-dimensional radiation space is sub divided into hexahedral control volumes. The information read from the mesh file include (i) the number of control volumes, (ii) position of nodes and (iii) cell flags. This information is stored in arrays for further usage. When cell numbers, vertex coordinates, connectivity and information regarding wall surfaces are known, following geometrical parameters are pre-calculated and stored for the use in the DT method: cell face centers of the wall faces (DT rays are fired from these positions), cell face normal of all faces of cells, cell face areas, cell volumes. These quantities are used in the DT method and in the ray tracing algorithm.

For the radiative transfer simulation several input parameters (to characterize the wall and the medium) are needed. The parameters defined are: gas temperature distribution of the medium, absorption coefficient distribution of medium, temperature and emissivity of walls, number of rays and firing directions, control parameters like type of problem (temperature or source specified), symmetry and planner. The absorption coefficient is calculated from LES data using transient temperature and mole fractions of CO_2 and H_2O. For this the Mixed Grey Gas Model (Truelove, 1976) is used in the present study.

The number of polar N_θ and azimuthal N_ϕ directions is chosen. From this the total number of rays fired per hemisphere is calculated as

$$nrays = N_\theta \times N_\phi \tag{5.2}$$

The major computational effort in the discrete transfer method is to trace the ray through the hexahedral volumes in the discretised radiation space. The information returned by the ray tracing algorithm to discrete transfer method is the path segment lengths in each cell cut by the ray. This procedure of shooting the rays and the tracing of the rays are repeated for all the wall cells. For a wall cell, rays are traced from the interior boundary along directions prescribed by the type of angular discretization used in the formulation. The face centre of the wall cell is fixed as an origin. The problem is then reduced to recursively finding the nearest element intersected by the ray, until a boundary surface is struck. The algorithm searches each triangle for an intersection point. An effective search strategy that minimizes the number of triangle element that must be checked for an intersection is used (Henson, 1999, Henson and Malalasekera, 1997). The detail about ray tracing is not discussed here in the interest of brevity.

As a ray traverses successive cells, its origin is updated to position of the last intersection in the previous cell. For each hexahedral cell crossed, all twelve of its bounding triangular elements must be checked for an intersection, excluding that containing new origin. The total length of the ray path can be calculated by adding all the segment length.

The shooting and tracing gives the knowledge about the distance traveled by the ray δl and number of segments (N_{seg}) for each ray. A ray is traced in each direction through the radiation space until it strikes another surface, say at P. Then, starting from P, the ray is followed back to its origin (point O), while solving for the intensity distribution along its path with the recurrence relation:

$$I_{n+1} = I_n \exp(-\beta .\delta l) + S\left[1-\exp(-\beta .\delta l)\right];\ 1 \le n \le (N_{seg}-1) \qquad (5.3)$$

where I_n is intensity of the ray at the entry of the control volume, I_{n+1} is the intensity of the ray at the exit of the control volume, β is the extinction coefficient (absorption coefficient + scattering coefficient), δl is the distance traveled by the ray and S is the source function. The source function and extinction coefficient assumed to be constant over the interval δl. This procedure is repeated for all rays leaving the given wall cell. The intensities calculated from

Eq. (5.3) are assumed to be constant over each finite solid angle $\delta\Omega$, such that the incident radiative heat flux at P is obtained as:

$$q_i(r_p) = \sum_{k=1}^{N_{rays}} I_{i,k} \cos\theta_k \sin\theta_k \sin d\theta_k \, d\phi_k \tag{5.4}$$

This incident flux, together the temperature and surface emissivity, are assumed to be constant over the entire element S_e. Then the outgoing intensity is everywhere $I_o = q_o/\pi$, where the emitted flux has been defined as

$$q_o = (1-\varepsilon_w) q_i + \varepsilon_w \sigma T_w^4 \tag{5.5}$$

where, ε_w is wall emissivity. Hence, for those rays originating from surface elements that strike S_e, an initial intensity I_o is used in the recurrence relation (Eq. 5.6). Since q_o depends on the value of q_i, an iterative solution is required, unless all the surfaces are black. The net surface heat flux over of the surface elements is then found from Eq. (5.6), i.e. restating the equation:

$$q_s = q_o - q_i \tag{5.6}$$

In the above expression o and i represents outgoing and incoming respectively. An equation is also required for the divergence of radiative heat flux $\nabla \cdot q_r$ in each volume element. Each ray considered as a beam of radiative energy, such that the heat source associated with its passage through a volume *n* from the definition, is:

$$Q_{gn} = (I_{n+1} - I_n) \; A_n \; \cos\theta_n \; \sin\theta_n \; \sin d\theta \; d\phi \tag{5.7}$$

Here A_n is the area of the surface element from which the ray was emitted and it is again assumed that the intensity is constant over the finite solid angle. When the beam of energy associated with a ray only partially intersects a volume the actual source is a fraction of that in Eq. (5.7). However, complex source sharing calculations are avoided by simply lumping all of the energy Q_g into only those volume element cut by the central ray path $\hat{s}$, saving considerable computational effort, without a significant loss in accuracy. Summing the individual source contributions from all the (N_{rays}) rays passing through a volume element, and

then dividing this value by its volume, V_n gives the divergence of radiative heat flux as:

$$\nabla \cdot q_r = \sum_{n=1}^{N_{cells}} \frac{Q_{g\,n}}{V_n} \tag{5.8}$$

Note here that flux divergence is assumed to be constant over each volume element as are other radiative properties. Finally, solution of the Eq. (5.8) requires a value for the source function S. The source function for absorbing only problems is simply $S = I_b$, where I_b is black body intensity of the medium. The heat sources at various points of the medium and heat flux at various walls are calculated. The net surface heat flux is calculated by Eq. (5.6)

For the divergent of heat flux or gas emissive power as mentioned earlier is calculated from Eq. 5.8 where the source contribution at a cell is calculated as

$$Q_{g\,n} = \left(I_{n+1} - I_n\right) A_n \cos\theta_n \sin\theta_n \sin d\theta\, d\phi \tag{5.9}$$

5.2.2Gas Radiation Properties Model

In the present model, the products of combustion like CO_2 and water vapor H_2O have been considered as the participating gases, which absorb and emit radiation depending on local mixture temperatures. The emissivity of the gases is calculated using the weighted sum of gray gases model (WSGGM). This model is summarized below for the sake of completeness. In a mixture with two participating gases, namely CO_2 and H_2O, the global emissivity of the participating non gray gas mixture is represented by (Hottel and Sarofim 1967):

$$\varepsilon_g = \sum_n a_{g,n}(T)\left[1 - \exp\left(-k_{g,n}\left(p_w + p_c\right)L\right)\right] \tag{5.10}$$

where the summation *n* is over the gases of the assumed mixture; p_w and p_c is the partial pressure of water vapor and carbon dioxide and *L* is the mean radiation path length. The influence of temperature is introduced by the weighting co-efficient:

$$a_{g,n} = b_{1,n} + b_{2,n}T \tag{5.11}$$

These coefficients have been fitted to the gas mixture total emmitance evaluated from the spectral data by Truelove (1976). The value of k_g required for the calculations is then obtained from the 'pseudo gray' approximation:

$$\varepsilon_g = 1 - \exp\left(-k_g L\right) \tag{5.12}$$

where L is the path length. For a cubic cell path, length can be taken as

$$L = \sqrt{\Delta x^2 + \Delta y^2 + \Delta z^2} \tag{5.13}$$

where Δx, Δy and Δz are cell dimensions.

5.3 Data Exchange Strategy

The coupling of LES and radiation is performed through a systematic approach taking care of the computational time involved in radiation calculations. LES solves for continuity, momentum, mixture fraction and enthalpy equations. For solving the enthalpy equation in its filtered form, it requires a radiative source term as input. Solution of RTE through DTM ray tracing mechanism provides the source at every nodal point in the domain for every time step. In order to solve the radiative equation, we need the temperature and mole fractions of CO_2 and H_2O as input parameters. In the present simulation we assume that CO_2 and H_2O are the vital emitting gases which contribute to the absorption coefficient. The mean values of mixture fraction, mixture fraction variance, mean scalar dissipation rate and mean enthalpy defect are calculated from LES calculations. The definition of enthalpy defect and its theory was presented in Chapter 4. From the mean values obtained by LES, a four dimensional interpolation is performed for the calculation of temperature, density, mole and mass fractions of CO_2 and H_2O from the pre-integrated lookup tables. The results from this interpolation forms the mean values for the input to radiation code (temperature, mole fractions of CO_2 and H_2O). The radiation code thus calculates and provides the source term for solving enthalpy equation. This loop continues for every time step and thus source term is updated every time step and enthalpy equation is thus solved in this manner. The complete coupling strategy is depicted in Fig. 5.1 which is represented in the form of a flow diagram. In order to reduce the computational time involved in the above process for any medium to high intensity flames, radiation is called into calculations for approximately every

0.18 ms. The simulation with the above criteria was tested in order to save the time involved in the coupled LES radiation cases and compared with the cases involving the radiation calculations performed every time step and no significant difference was found in more expensive calculations.

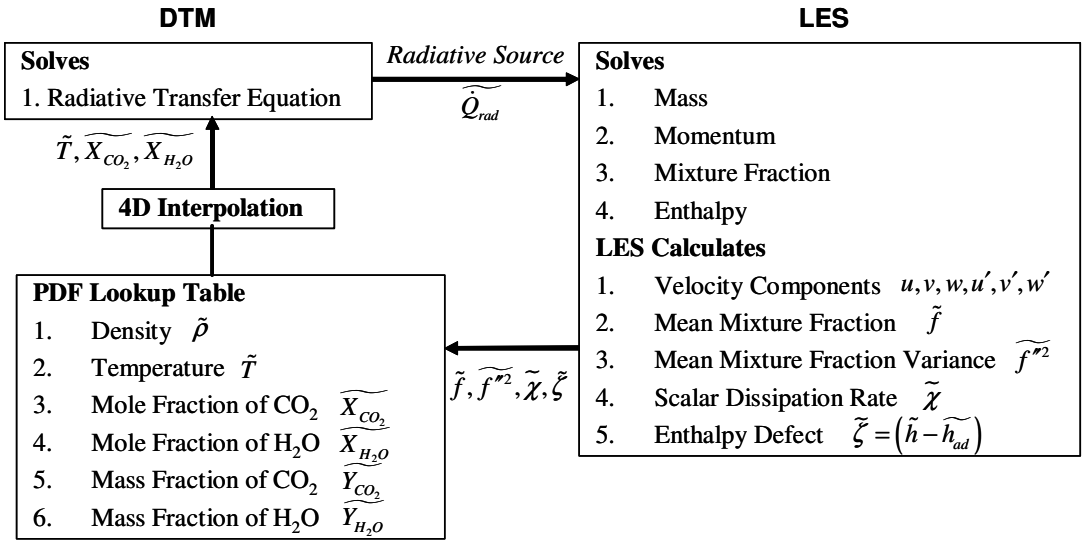

Figure 5.1 Schematic of the flow of data between radiation (DTM) and LES codes.

5.4 Closure

A brief introduction to the radiation model used in the present work was presented in this chapter. Discrete transfer radiative method was explained with the gas radiative properties model used in the present study. A complete description of the data exchange strategy between radiation and LES codes was also presented. This chapter provided the coupling methodology between radiation and turbulence.

Chapter 6

Numerical Scheme

The numerical techniques for the LES method containing the spatial discretization schemes and the procedures used to integrate the fluid flow equations in time and boundary conditions are discussed in this chapter. The spatial and time discretization schemes in the present LES code PUFFIN were originally developed by Kirkpatrick (2002) and Kirkpatrick *et al.* (2003). The spatial discretization is based on a control volume formulation on a staggered, non-uniform, Cartesian grid capable of handling three dimensional flows. Advanced discretization schemes and solvers are utilized in the present LES code in order to reduce the computational time and cost involved.

6.1 Finite Volume Method

Finite volume method involves the discretization of the domain space into discrete number of cells or finite volumes. Each computational cell is incorporated with the governing equations leading to a system of algebraic equations. The solution to these equations is an approximation to the solution of continuous equations at a set of discrete points or nodes. There is one node in each cell and the solution found for each node is considered representative of the solution within the cell. The numerical discretization is based on a staggered Cartesian grid and defines the boundaries of the rectangular finite volumes as depicted in Fig. 6.1.

In the Fig. 6.1 circles represent the scalar nodes, horizontal arrows are nodes with u velocity component and vertical arrows symbolize the nodes of the v velocity component. Extension to the third dimension uses the same structure in z-direction with addition of the w velocity component. Pressure and mixture fraction are calculated at the scalar nodes while the solution for the velocity components is found at the velocity nodes. Velocity nodes are placed at the centroid of the scalar cell faces. The spatial discretization schemes for momentum and mixture fraction transport equations are discussed in the following sections. Staggering of the velocity nodes

avoids physically non-realistic predictions for oscillating pressure fields. As velocities are generated at scalar cell faces, interpolation of velocities for scalar transport computations can be avoided.

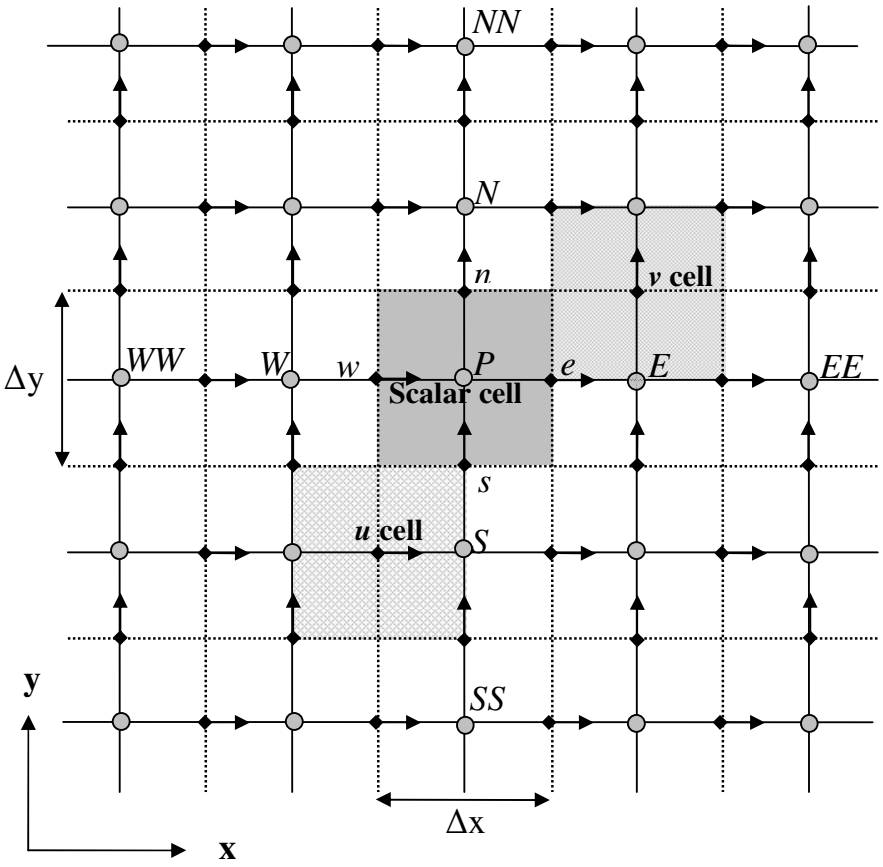

Figure 6.1 Staggered grid and node placement in two dimensions.

6.2 Discretization of Governing Equations

The generic transport equation for any generic variable $\tilde{\phi}$ is given by:

$$\frac{\partial}{\partial t}\left(\bar{\rho}\tilde{\phi}\right)+\frac{\partial}{\partial x_k}\left(\bar{\rho}\tilde{u}_k\tilde{\phi}\right)=\frac{\partial}{\partial x_k}\left(\Gamma_\phi\frac{\partial\tilde{\phi}}{\partial x_k}\right)+\tilde{S}_\phi \qquad (6.1)$$

where Γ represents kinematic diffusion coefficient and $\tilde{S}_\phi$ represents a source/sink term. Integrating Equation 6.1 over the volume V bounded by a surface S and using the Gauss Divergence Theorem to convert volume integrals into surface integrals yields the integral form of the equation:

$$\frac{\partial}{\partial t}\int_V \bar{\rho}\tilde{\phi}\,dV + \int_S \bar{\rho}\tilde{u}_k\tilde{\phi}\,dS_k = \int_S \Gamma_\phi \frac{\partial \tilde{\phi}}{\partial x_k}\,dS_k + \int_V \tilde{S}_\phi\,dV \qquad (6.2)$$

The differential surface area vector dS_k has a magnitude equal to the area of the segment of surface and direction corresponding to the direction of the outward normal to the segment. The first term on the LHS of the equation 6.2 represents an unsteady term, second term depicts the advection term whereas the first term on RHS represents diffusion term and the second shows the source term. Spatial discretization involves approximating the volume and surface integrals in this equation and applying this approximation to each volumetric cell to obtain a set of simultaneous linear algebraic equations in $\tilde{\phi}$.

An example of a scalar cell P in Fig 6.1 for which the integrals are to be calculated and its neighbors (indicated by E, W, N, S) and one level away from neighbors (indicated by EE, WW, NN and SS) have been shown in two dimensional space. Extension of this structure to a typical three dimensional cell and its neighbors is shown in Figure 6.2. The central node *P* refers to the cell for which the integrals are to be calculated and surrounded by its northern (*N*), eastern (*E*), southern (*S*), western (*W*), up (*U*) and down (*D*) neighbors. The surfaces separating two cells are denoted as A_n, A_e, A_s, A_w, A_u and A_d, the associated fluxes are F_n, F_e, F_s, F_w, F_u and F_d. East (*E*), North (*N*) and up (*U*) correspond to positive *x, y* and *z* directions, respectively which is also denoted as x_1, x_2 and x_3 in index notation and also similarly west (*W*), south (*S*) and down (*D*) to the negative *x, y* and *z* directions. Small letters *e, n* etc. refer to the points at the centroid of the respective cell faces.

In the following sections, *nb* is used as a generic subscript for neighbor cell and *f* is a generic subscript for a quantity evaluated at a cell face. To reduce the complexity of the notation, the fluxes are given for a particular face such as the east or the north face. All results can be applied in a similar manner to other faces as well.

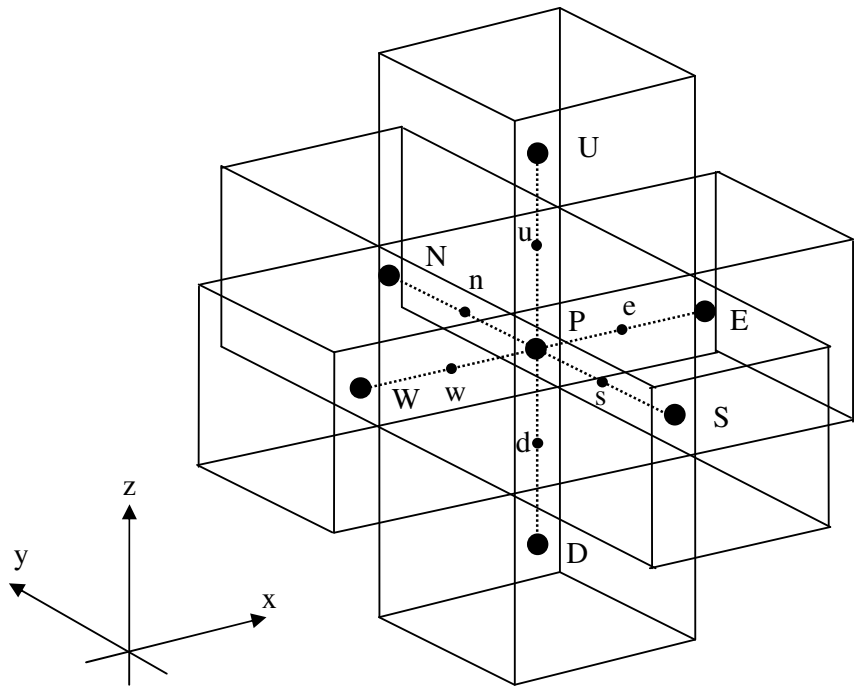

Figure 6.2 Finite volume cell and its neighbors in three dimensions

6.3 Spatial Discretization

6.3.1 Unsteady Term

The unsteady term of the general transport equation is advanced using a central difference approximation for the time derivative $n + \frac{1}{2}$ which gives

$$\frac{\partial}{\partial t}\int_V \bar{\rho}\tilde{\phi}\, dV \approx \frac{(\rho\phi)^{n+1} - (\rho\phi)^n}{\Delta t}\Delta V \tag{6.3}$$

where the superscript n stands for the time level, which indicates the values that are taken at the start of the current time step, while $n + 1$ indicates the end of the time step.

6.3.2 Advection Term

The convective flux across a cell face is given by

$$F_{adv} = \left(\bar{\rho}\tilde{u}_{\perp}\Delta A\tilde{\phi}\right)_f \tag{6.4}$$

where $\tilde{u}_{\perp}$ represents the velocity normal to the face (the advecting velocity) and ΔA is the area of the face. For the east face the above expression will be represented as

$$F_{adv_e} = \left(\overline{\rho}\tilde{u}\Delta A\right)_e \tilde{\phi}_e \tag{6.5}$$

Interpolation to find the value of $\tilde{\phi}_e$ at the centre of the face uses a linear profile,

$$\tilde{\phi}_e = (1-\theta)\tilde{\phi}_p + \theta\tilde{\phi}_E \tag{6.6}$$

where the weighting factor θ for the interpolation is

$$\theta = \frac{\Delta x_e}{\Delta x_E} \tag{6.7}$$

Δx_e and Δx_E are the distances from the node *P* to the face centroid *e* and the east neighbor node *E* as shown in the two-dimensional view of a cell and its neighbors in Figure 6.3.

As a staggered grid is used, it is required to find the convective velocity u_e at the face and the density ρ_e at the face depending on whether the variable $\tilde{\phi}$ is a scalar or velocity component. When $\tilde{\phi}$ is a scalar, the convective velocity is computed directly as the *u* velocity component is established at the cell face centroid. However, density must be interpolated using Equation 6.6 which gives the relation as

$$\tilde{\rho}_e = (1-\theta)\tilde{\rho}_P + \theta\tilde{\rho}_E \tag{6.8}$$

Whereas if $\tilde{\phi}$ is a velocity component, linear interpolation is required to find the convective velocity while ρ is readily available. Finally the resulting formulation for the convection fluxes can be described using a second order central difference scheme:

$$F_{adv_e} = (\rho\, u\, \Delta A)_e \left[(1-\theta)\,\phi_P + \theta\,\phi_E\right] = C_e\left[(1-\theta)\phi_P + \theta\phi_E\right] \tag{6.9}$$

This linear interpolation numerical scheme used to calculate the variables at cell faces of the finite volumes is equivalent to a second order central difference scheme in finite difference formulation. The most desirable advantage of this scheme is it is simple to implement, computationally efficient and second order in accuracy. This

scheme is desirable for LES since numerical damping acts as an extra un-quantified contribution to the eddy viscosity and contaminates the effects of the subgrid scale model. However, this scheme tends to give solutions containing non-physical oscillations or 'wiggles' in areas of the field containing high gradients. These wiggles are the result of dispersive error terms inherent in the second order central difference discretization. Increasing grid refinement in these areas is the only solution to this problem.

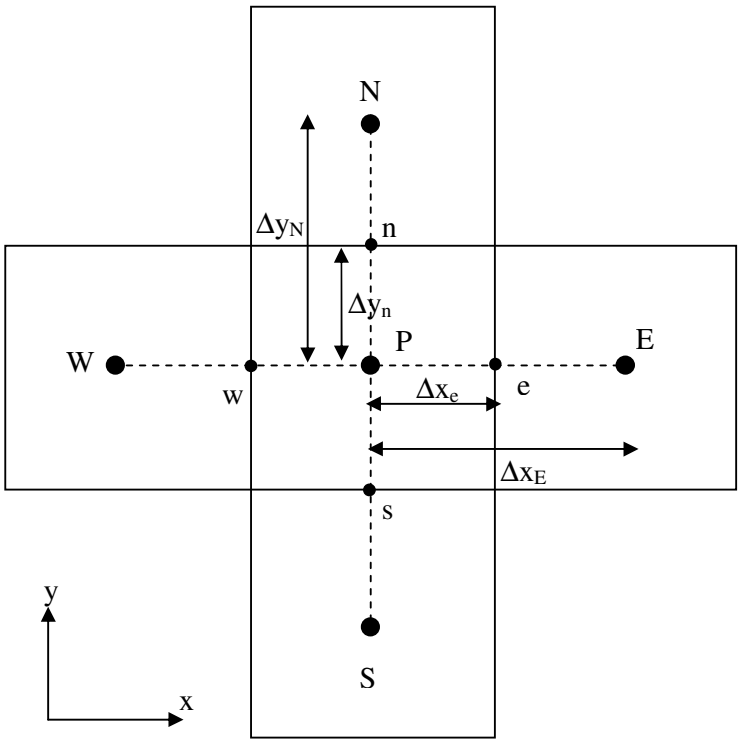

Figure 6.3 A Finite volume cell and its neighbors in the *xy*- plane

The convection terms in the scalar equations are particularly problematic due to the large gradients which often occur in the scalar fields. Because scalars are often coupled with the velocity field through density, wiggles which result from use of the central difference for the scalar convection terms cause problems with the numerical stability of the overall solution. Hence this scheme is hardly suited for scalar transport, especially when they have to remain bounded. For example, mixture fraction is limited to a range from 0 to 1. From this scheme, wiggles may lead to unphysical results such as predictions of mixture fraction outside the range 0 and 1, which do not yield a chemical state. For this reason, the convection term for the scalar

equation is discretised using non-centered schemes, QUICK of Leonard (1979) or SHARP Leonard (1987).

A third order upwind numerical scheme called QUICK is used to reduce numerical oscillations by introducing a fourth order dissipation. Quadratic interpolation is used to find the value ϕ at the centre of the cell faces. The value of ϕ for the east face can be represented as:

$$\tilde{\phi}_e = \left[(1-\theta)\tilde{\phi}_p + \theta\tilde{\phi}_E \right] - \frac{1}{8} CRV \times \Delta x_E{}^2 \tag{6.10}$$

The upwind biased curvature term is defined as

$$CRV = \left[\frac{\tilde{\phi}_p - 2\tilde{\phi}_E + \tilde{\phi}_{EE}}{\Delta x_E{}^2} \right] \quad u < 0 \tag{6.11}$$

$$CRV = \left[\frac{\tilde{\phi}_E - 2\tilde{\phi}_P + \tilde{\phi}_W}{\Delta x_E{}^2} \right] \quad u > 0 \tag{6.12}$$

The double subscript *EE* refers to the cell east of the eastern neighbour. The first term in the equation (6.10) is the value of ϕ at the cell face calculated using linear interpolation. The second term in the equation is an upwind biased curvature term which makes the overall interpolation quadratic. The weighting factor θ is calculated from equation 6.7. The linear interpolation term accounts for the non-uniform grid through the weighting factor θ, while the curvature terms have no grid weighting included. Castro and Jones (1987) have shown that the uniform grid formula for QUICK gives negligible errors for grid expansion ratios $r_x = \Delta x_{i+1} / \Delta x_i$ between 0.8 and 1.25. Substituting equation (6.10) into equation (6.5) gives the convective flux of ϕ across the east face as

$$F_e = (\bar{\rho}\tilde{u}\Delta A)_e \left[\left((1-\theta)\tilde{\phi}_p + \theta\tilde{\phi}_E \right) - \frac{1}{8} CRV \times \Delta x_E{}^2 \right]$$

$$= C_e \left[\left((1-\theta)\tilde{\phi}_p + \theta\tilde{\phi}_E \right) + S_{QUICK} \right] \tag{6.13}$$

where, $S_{QUICK} = -\frac{1}{8} CRV\left(\Delta x_E^2\right)$. The source term S_{QUICK} indicates the curvature of the field. The term S_{QUICK} is included as part of the source term S_ϕ in the code. QUICK

scheme however does not remove the wiggles completely. In order to solve this problem we use another scheme called SHARP, Leonard (1987), which is a modification to QUICK. SHARP introduces second order diffusion where local conditions are such that oscillations will not occur, thereby ensuring that the solution remains monotonic. An outline of this scheme can be found in Leonard (1987). The summation of the convective fluxes across all faces can be described as a discrete convection operator,

$$\int_S \bar{\rho}\tilde{u}_k\tilde{\phi}\, dS_k \approx \sum C_f \left[\left(\left(1-\theta_f\right)\tilde{\phi}_p + \theta_f \tilde{\phi}_{nb} \right) + \sum S_{QUICK_f} \right] \tag{6.14}$$

To give a second order time advancement scheme the value of this term must be evaluated at the midpoint of each time step. This is achieved by applying the operator at a number of time levels and taking a weighted mean.

6.3.3Diffusion Term

The diffusion term for ϕ across a cell face is given by

$$F_{diff} = \left(\Gamma_\phi \Delta A \frac{\partial \tilde{\phi}}{\partial x_k} \right)_f \tag{6.15}$$

where n is the direction normal to the face, Γ is the kinematic diffusion coefficient and ΔA the area of the face. The flux at the centre of the east cell face is then computed from the values at the two neighboring points and their distance from central difference approximation,

$$F_{diff_e} = \left(\Gamma_\phi \Delta A\right)_e \left(\frac{\partial \tilde{\phi}}{\partial x} \right)_e = \left(\Gamma_\phi \Delta A\right)_e \left(\frac{\tilde{\phi}_E - \tilde{\phi}_P}{\Delta x_E} \right) \tag{6.16}$$

The diffusion coefficient at the centre of the face Γ_e is calculated by linear interpolations same as density calculation in the convective fluxes. Finally the summation of the diffusive fluxes across all faces can be described as a discrete diffusion operator,

$$\int_S \Gamma_\phi \frac{\partial \tilde{\phi}}{\partial x_k} dS_k \approx \sum D_f \left(\tilde{\phi}_{nb} - \tilde{\phi}_P \right) \tag{6.17}$$

The discrete diffusion operator does not suffer from numerical instability as observed in advection operator and therefore used in this form for all variables.

6.3.4Source Term

Source terms differ from each of the transport equations for each variable. In momentum equations, the effect of the pressure gradient and the gravitational force act as source terms. A reaction progress variable is associated with a chemical source term. For enthalpy in the non-adiabatic flows, radiation heat exchange is treated as a source term. In spatial integration, source terms are usually treated in similar manner. They are calculated by evaluating the function representing the source term S_ϕ at the node and multiplying by the volume of the cell given as

$$\int_V \tilde{S}_\phi \, dV \approx \tilde{S}_{\phi p} \Delta V \tag{6.18}$$

Gradients are calculated using second order central differences while interpolations use a linear profile similar to that used for the convective and diffusive fluxes. Generally source term can be described as a combination of an implicit and explicit component.

$$\tilde{S}_{\phi p} \Delta V = \tilde{S}_{imp} \tilde{\phi}_p + \tilde{S}_{exp} \tag{6.19}$$

The terms "implicit" and "explicit" refers to the manner in which the components of the source term are integrated in time. The implicit component is integrated using an implicit time stepping scheme, while integration of the explicit component uses explicit scheme.

6.3.5Complete Equation

The resulting discretised transport equation for a general variable ϕ is

$$\begin{aligned} \frac{\left(\overline{\rho}\tilde{\phi}\right)^{n+1} - \left(\overline{\rho}\tilde{\phi}\right)^{n}}{\Delta t} \Delta V = & \left\{ \sum \left(\overline{\rho}\tilde{u} \Delta A \right)_f \left[\left(1-\theta_f\right) \tilde{\phi}_P + \theta_f \tilde{\phi}_{nb} \right] \right\}^{(n-2,n-1,n,n+1)} \\ & + \left\{ \sum \left(\frac{\left(\Gamma \Delta A\right)_e}{\Delta x_E} \right) \left(\tilde{\phi}_{nb} - \tilde{\phi}_P \right) \right\}^{(n-1,n,n+1)} \\ & + \left\{ \tilde{S}_{imp} \tilde{\phi}_P \right\}^{(n-1,n,n+1)} + \left\{ \tilde{S}_{\exp} \right\}^{(n-2,n-1,n,n+1)} \end{aligned} \tag{6.20}$$

Here the curly brackets *{ }* with superscripts ($n - 2$, $n - 1$, n, $n + 1$) represent a weighted average of the term evaluated at the listed time intervals, which gives an estimate of the term at the (n+ ½) time level. The weightings for each time level

depend on the time-advancement scheme as discussed in the next section. By collecting coefficients the equation becomes as

$$\begin{aligned} a_P^{n+1}\tilde{\phi}_P^{\,n+1} &= \sum_{nb}\left(a_{nb}^{\;n+1}\tilde{\phi}_{nb}^{\;n+1}\right)+S_{imp}\tilde{\phi}_P^{\,n+1}+S_{exp}^{n+1} \\ &+\left[\sum_{nb}\left(a_{nb}^{\;n}\tilde{\phi}_{nb}^{\;n}\right)-a_P^n\tilde{\phi}_P^n+S_{imp}\tilde{\phi}_P^{\,n}+S_{exp}^n\right] \\ &+\left[\sum_{nb}\left(a_{nb}^{n-1}\tilde{\phi}_{nb}^{n-1}\right)-a_P^{n-1}\tilde{\phi}_P^{n-1}+S_{imp}\tilde{\phi}_P^{\,n-1}+S_{exp}^{n-1}\right] \\ &+\left[\sum_{nb}\left(a_{nb}^{n-2}\tilde{\phi}_{nb}^{n-2}\right)-a_P^{n-2}\tilde{\phi}_P^{n-2}+S_{exp}^{n-2}\right] \end{aligned} \tag{6.21}$$

Where the coefficients corresponding to the node a_P and its neighbors a_{nb} are formed from the connective and diffusive fluxes contributions.

6.4 Time Advancement Scheme

The methods in which the partial differential equations are integrated with respect to time are discussed in the following sections. The time integration schemes for the scalar and momentum equations are described which are applied to the system of governing equations.

6.4.1 Time Integration of Scalar Equations

The time integration of scalar equation is performed using the Crank-Nicolson scheme. The time dependent conservation equation integrated in time using Crank-Nicolson scheme is written

$$\begin{aligned} \frac{\left(\bar{\rho}\tilde{\phi}\right)^{n+1}-\left(\bar{\rho}\tilde{\phi}\right)^{n}}{\Delta t}\Delta V &= -\frac{1}{2}\left[H^{n+1}\left(\tilde{\phi}^{n+1}\right)+H^{n}\left(\tilde{\phi}^{n}\right)\right] \\ &+\frac{1}{2}\left[L^{n+1}\left(\tilde{\phi}^{n+1}\right)+L^{n}\left(\tilde{\phi}^{n}\right)\right] \\ &+\frac{1}{2}\left[S_{imp}^{n+1}\tilde{\phi}^{n+1}+S_{imp}^{n}\left(\tilde{\phi}^{n}\right)\right] \\ &+\frac{1}{2}\left[S_{exp}^{n+1}\tilde{\phi}^{n+1}+S_{exp}^{n}\left(\tilde{\phi}^{n}\right)\right] \end{aligned} \tag{6.22}$$

Here H is the discrete convection operator

$$H\left(\tilde{\phi}\right)=\sum\left(\rho u\Delta A\right)_f\left[\left(\left(1-\theta_f\right)\tilde{\phi}_p+\theta_f\tilde{\phi}_{nb}\right)\right] \tag{6.23}$$

L is the discrete diffusion operator

$$L\left(\tilde{\phi}\right)=\sum\frac{\left(\Gamma\Delta A\right)_e}{\Delta x_E}\left(\tilde{\phi}_{nb}-\tilde{\phi}_P\right) \tag{6.24}$$

and $S_{imp}\phi$ and $S_{\exp}$ the discrete implicit and explicit source terms. (S_{imp} is a coefficient of ϕ rather than a function of ϕ). A second order accurate scheme in time is used to evaluate each term at the n and n+1 time levels and uses linear interpolation to estimate their value at n + 1/2. At least two iterations of scalar equation per time step are required due to the contributions of terms containing $\tilde{\phi}^{n+1}$ to the explicit source term which result from the use of the QUICK and SHARP spatial discretization schemes. The number of outer iterations for the entire time advancement scheme per time step is heavily dependent on the density variation which needs more number of iterations than expected for large variations to maintain the stability of the solution.
The criterion for Crank-Nicolson scheme to remain non-oscillatory is given by

$$\Delta t\le\frac{\left(\Delta x\right)^2}{\Gamma} \tag{6.25}$$

While this criterion poses a rather stringent limitation on the improvement that could be achieved on spatial accuracy, it results from an error term in the Taylor series expansion which contains the second derivative in space $\partial^2\tilde{\phi}/\left(\partial x\right)^2$. Typically, this term remains relatively small in most flow problems and the scheme remains stable for considerably larger time steps.

6.4.2Time Integration of Momentum Equations

Time integration of the momentum equations is performed by either Crank-Nicolson scheme or the second and third order hybrid Adams schemes. In these hybrid schemes, Adams-Bashforth method is used for the advection terms and Adams-Moulton method for the diffusive terms. The momentum equation for velocities are integrated by using Crank-Nicolson scheme as

$$\begin{aligned}\frac{\bar{\rho}^{n+1}\tilde{u}^{*}-\left(\bar{\rho}\tilde{u}\right)^{n}}{\Delta t}\Delta V=&-\frac{1}{2}\left[H^{n+1}\left(\tilde{u}^{*}\right)+H^{n}\left(\tilde{u}^{n}\right)\right]\\&+\frac{1}{2}\left[L^{n+1}\left(\tilde{u}^{*}\right)+L^{n}\left(\tilde{u}^{n}\right)\right]\\&+\frac{1}{2}\left[S_{imp}^{n+1}\tilde{u}^{*}+S_{imp}^{n}\left(\tilde{u}^{n}\right)\right]\\&+\frac{1}{2}\left[S_{exp}^{n+1}\tilde{u}^{n+1}+S_{exp}^{n}\left(\tilde{u}^{n}\right)\right]\\&-Gp^{n-1/2}\end{aligned}\qquad(6.26)$$

The above equation is similar to the Crank-Nicolson scheme used for the scalar equation. However, an additional term added as a pressure gradient term $Gp^{n-1/2}$, which considers $n-1/2$ time level concerning the pressure correction scheme. The velocity obtained before pressure correction step at $n + 1$ time level is specified with superscript u^{*}. As the advection terms in the momentum equations are non-linear, they are treated from explicit time advancement scheme as Crank-Nicolson required iterations to retain second order accuracy. In the code, second and third order hybrid schemes are used such that advection terms are treated explicitly using an Adam-Basforth scheme while diffusion terms are treated implicitly using Adams-Moulton. The additional terms such as gravitational terms are treated explicitly with Adams-Bashforth. The second order Adams-Bashforth/ Adams-Moulton scheme for the momentum equations is represented as

$$\begin{aligned}\frac{\bar{\rho}^{n+1}\tilde{u}^{*}-\left(\bar{\rho}\tilde{u}\right)^{n}}{\Delta t}\Delta V=&-\frac{1}{2}\left[3H^{n+1}\left(\tilde{u}^{n}\right)-H^{n-1}\left(\tilde{u}^{n-1}\right)\right]\\&+\frac{1}{2}\left[L^{n+1}\left(\tilde{u}^{*}\right)+L^{n}\left(\tilde{u}^{n}\right)\right]\\&+\frac{1}{2}\left[S_{imp}^{n+1}\tilde{u}^{*}+S_{imp}^{n}\left(\tilde{u}^{n}\right)\right]\\&+\frac{1}{2}\left[3S_{exp}^{n+1}\tilde{u}^{n}-S_{exp}^{n-1}\left(\tilde{u}^{n-1}\right)\right]\\&-Gp^{n-1/2}\end{aligned}\qquad(6.27)$$

and similarly the third order Adams-Basforth/ Adams-Moulton scheme is given as

$$\begin{aligned}\frac{\bar{\rho}^{n+1}\tilde{u}^{*}-\left(\bar{\rho}\tilde{u}\right)^{n}}{\Delta t}\Delta V=&-\frac{1}{12}\left[23H^{n}\left(\tilde{u}^{n}\right)-16H^{n-1}\left(\tilde{u}^{n-1}\right)+5H^{n-2}\left(\tilde{u}^{n-2}\right)\right]\\&+\frac{1}{12}\left[5L^{n+1}\left(\tilde{u}^{*}\right)+8L^{n}\left(\tilde{u}^{n}\right)-L^{n-1}\left(\tilde{u}^{n-1}\right)\right]\\&+\frac{1}{12}\left[5S_{imp}^{n+1}\tilde{u}^{*}+8S_{imp}^{n}\left(\tilde{u}^{n}\right)-S_{imp}^{n-1}\left(\tilde{u}^{n-1}\right)\right]\\&+\frac{1}{12}\left[23S_{exp}^{n}\tilde{u}^{n}-16S_{exp}^{n-1}\left(\tilde{u}^{n-1}\right)+5S_{exp}^{n-2}\left(\tilde{u}^{n-2}\right)\right]\\&-Gp^{n-1/2}\end{aligned}\qquad(6.28)$$

The non-linear advection terms and explicit source terms are calculated at previous time steps where all necessary details are known from these schemes. Hence these schemes do not require any iteration as Crank-Nicolson to maintain the accuracy. However, when the density and viscosity fluctuate significantly, iteration of the overall solution procedure is required to include the correct value of density in the unsteady term and viscosity in the diffusion term at the $n + 1$ time step.

The advection transport terms has the time step which is proportional to the characteristics convection time $\Delta x_i / u_i$ which is usually described with respect to a non dimensional number called Courant number, $C = u_i \Delta t / \Delta x_i < 1.0$. For diffusion term the maximum usable time step is proportional to the characteristic diffusion time $\Delta x_i^2 / \mu$. However, the Adams methods require some initial treatment where no information about previous time steps is available. Therefore, the Crank-Nicolson is used for the initial time steps to enable the calculation of the $n-1$ and $n-2$ source terms for the Adams schemes.

6.5 Pressure Correction

The fractional step method based on pressure correction scheme introduced by VanKan (1986) and Bell and Colella (1989) is used for calculation of pressure correction. This version of the fractional step method was found to be the fastest of the methods tested by Armfield and Street (2002). In this scheme, first the momentum equations for three velocity components are integrated to find an approximate solution for the velocity field u^*. Mass conservation is then enforced through a pressure correction step in which the approximate velocity field is projected onto a subspace of divergence free velocity fields. The projection is achieved by solving a Poisson

equation for the pressure correction p' in which the source term is the mass conservation error in each cell,

$$\Delta t \frac{\delta^2 p'}{\left(\delta x_i\right)^2} = -\left[\frac{\overline{\rho}^{n+1} - \overline{\rho}^{n}}{\Delta t} + \frac{\delta\left(\overline{\rho}^{n+1} u_i^*\right)}{\delta x_i}\right] \tag{6.29}$$

The pressure correction is then used to correct the velocity field,

$$u_i^{n+1} = u_i^* - \Delta t \frac{\delta p'}{\delta x_i} \tag{6.30}$$

and the pressure field is given as

$$p^{n+1/2} = p^{n-1/2} + p' \tag{6.31}$$

The pressure correction equation is discretised in space in a similar manner to the discretization of the transport equations of momentum presented earlier. For incompressible flows, the integration of equation (6.29) over a finite volume cell and applying the Gauss divergence theorem gives

$$\Delta t \sum\left(\Delta A \frac{\delta p'}{\delta x_i}\right)_f = -\left[\frac{\overline{\rho}^{n+1} - \overline{\rho}^{n}}{\Delta t}\Delta V + \sum\left(\overline{\rho}^{n+1} u_i^* \Delta A\right)_f\right] \tag{6.32}$$

Where summation is performed over each of the faces of area ΔA, and ΔV is the volume of the cell. A second order central difference scheme is used to calculate the gradients $\delta p'/\delta x_i$. It is important to use the same discretization for the pressure gradient in the momentum equation and the pressure correction in the pressure correction equation. This minimizes the projection error and ensures convergence if an iterative scheme is used. Details of time advancement schemes used in depth can be found in Kirkpatrick (2002), Kirkpatrick *et al.* (2003).

6.6 Solution Procedure

The system of linear equations obtained from the numerical discretization is solved using a linear equations solver. The present work includes the ***Bi-Conjugate Gradient Stabilized*** (BiCGStab) solver with a ***Modified Strongly Implicit*** (MSI) pre-conditioner to solve the momentum and scalar equations, which is more efficient for the large variations in cell size. The BiCGStab solver is also used for the pressure correction equation. Convergence of the solvers is measured using the L_2 norm of the

residual (L_2 norm is a vector norm that is commonly encountered in vector algebra and vector operations such as dot product). The residual was set to be less than 10^{-10} for the solution of the momentum and scalar equations, which typically requires one or two sweeps of the solver to obtain convergence.

At each time step a number of iterations of the pressure/velocity correction step are generally required to ensure adequate conservation of mass. The pressure correction equation is solved every iteration until either the residual is reduced to ten percent of its original value or the BiCGStab solver has performed seven sweeps. Each sweep of the solver includes two sweeps of the pre-conditioner. The solution is then used to correct the pressure and velocity field and the divergence of the corrected velocity field is calculated. The process is repeated until the L_2 norm of the divergence error is less that a pre-set value. The minimum attainable divergence error is typically reached after six or eight projections.

6.6.1Solution Procedure for General Reacting flows

The overall solution procedure for each time step follows an approach that has been implemented by Ranga Dinesh (2007) in the context of a single flamelet based steady flamelet combustion for any incompressible reacting flow in the present in-house LES code. In the present work, the combustion modelling capability in LES has been enhanced by incorporating a comprehensive steady flamelet model which can handle multiple flamelets or the variation in scalar dissipation rate and advanced flamelet models, namely the Unsteady Flamelet/Progress Variable (UFPV) approach based UFPV δ function model. The solution procedure remains the same as the approach employed by Ranga Dinesh (2007) as the current models used in the present study are completely flamelet based. However, the solution procedure changes very marginally according to the adopted advanced combustion models and these are discussed in detail in the subsequent sections.

An iterative time advancement scheme for variable density calculation similar to the algorithm proposed by Pierce (2001) is used in the present calculations. For incompressible variable density flow, both the velocity and density fields must be corrected to ensure conservation of mass. An iterative method is required as density

depends on mixture fraction (in flamelet calculation). The iteration procedure employed in the present study is described below. In the following, the superscript n refers to solution values that are known from the previous time level, the superscript k refers to the iteration cycle between the solutions at time step n and $n + 1$, the superscript 0 indicates the initial guess for the first iteration when $k = 0$.

Step 1. Choose the initial guesses or predictors for the values of the variables at the next time level. Here a simple choice is adopted by choosing the solution values at the current time level:

$$u_k^0 = u_k^n, \quad \phi_k^0 = \phi_k^n, \quad \text{etc.}$$

Step 2. Solve the scalar transport equation (s) to obtain provisional scalar values. This facilitates better estimation of the density early in the iteration process. Solving the scalar transport gives predictor for ϕ^{k+1} and current density predictor gives the value $\hat{\phi}$

$$\hat{\phi} = \frac{(\rho\phi)^{k+1}}{\rho^k} \tag{6.34}$$

Step 3. Calculate density from the provisional scalar values according to the strategy appropriate to the adopted combustion model. This step varies for all the three models used in the present work i.e. SLFM, NAFM and UFPV approach.

Step 4. Re-update the scalars based on the new density to preserve primary scalar conservation:

$$\phi^{k+1} = \frac{(\rho\phi)^{k+1}}{\rho^{k+1}} \tag{6.36}$$

Step 5. Solve the momentum equations

Step 6. Solve the pressure correction equation

Step 7. Correct the pressure and velocity fields

Step 8. Check the mass conservation error and repeat steps 6 and 7 as required.

This completes one iteration cycle within a time step. Typically, 6-8 iterations of this procedure is required to obtain satisfactory convergence at the end of each time step. Two more steps need to be executed after this:

Step 9. Calculate eddy viscosity.

Step 10. Calculate the temperature and species mass fractions

These steps complete one cycle for a time step. Time step is varied to ensure that the Courant number given by $Co = \Delta t u_i / \Delta x_i$ remains approximately constant. In general, the solutions are advanced with a time step corresponding to a Courant number in the range $Co = 0.2 - 0.8$.

Density Under-Relaxation

The above scheme requires the code to under-relaxation the density in time. Therefore, the density ρ^{n+1} computed from the flamelet library is no longer applied to the CFD-code, but rather it is under-relaxed and taken a value of $\overline{\rho}_r^{n+1}$ as depicted below

$$\overline{\rho}_r^{n+1} = \alpha \overline{\rho}^{n+1} + (1-\alpha)\,\overline{\rho}_r^{n+1} \tag{6.37}$$

Here α is a real number whose value is $0 < \alpha < 1$ and the relaxation factor used in this study is 0.25. This is required to establish stability in the initial stages.

6.6.2Steady Laminar Flamelet Model

Steps 2, 3, 4 and 10 of the above solution procedure are dictated by the employed combustion model. The steady laminar flamelet model (SLFM) for combustion implemented in the present study has the following procedure:

Steps 2&4: Calculation of scalar transport equations

2.1: Solve for the filtered mixture fraction equation.

2.2: Compute the sub-grid variance of mixture fraction from its model equation and subsequently calculate the normalized subgrid-variance.

2.3: Compute the filtered scalar dissipation rate from its model equation

Step 3: Calculation of density

3.1: Compute the sub-grid variance of mixture fraction from its model equation and subsequently calculate the normalized subgrid-variance.

3.2: Compute the filtered scalar dissipation rate from its model equation

3.3: Read the pre-integrated 3D look-up-table specific to SLFM for ordered values of filtered density. While using single flamelet solution for the flames, density is

calculated by undergoing the PDF integration inside the LES solution procedure. A single flamelet file is provided as an input for the density PDF calculations. In this case step3 can terminate here. For implementation of multiple flamelet solution a PrePDF is generated and therefore follows the next step.

3.4: From the known value of filtered mixture fraction, its normalized variance and filtered scalar dissipation rate, obtain filtered density from the look-up-table using the 3D interpolation technique (Ravikanti, 2008).

Step 10: Calculation of temperature and species concentrations

10.1: Read the pre-integrated 3D look-up-table specific to SLFM for ordered values of filtered temperature and species mass fractions.

10.2: From the known filtered mixture fraction, its normalized variance and filtered scalar dissipation rate, obtain filtered temperature and species mass fractions from the look-up-table using the 3D interpolation technique.

6.6.3Coupled LES Radiation Model - NAFM

For the combustion coupled with radiation calculations (NAFM) implemented in the present work of LES code, the following working procedure is used:

Steps 2&4: Calculation of scalar transport equations

2.1: Solve for the filtered mixture fraction and filtered enthalpy equation. Enthalpy equation requires the source term that needs to be provided from the radiation calculations. Radiation involves the Discrete Transfer (DT) method which is obtained from **Step 11**. To start the solution, an initial guess value for radiation source is provided. But as the solution progresses, this source term is updated based on the DT method with temperature and mole fractions of CO_2 and H_2O.

2.2: Compute the sub-grid variance of mixture fraction from its model equation and subsequently calculate the normalized subgrid-variance.

2.3: Calculate the mean scalar dissipation rate and enthalpy defect.

Step 3: Calculation of density

3.1: Compute the sub-grid variance of mixture fraction from its model equation and subsequently calculate the normalized subgrid-variance.

3.2: Calculate density from the PDF integration.

Step 10: Calculation of temperature and species concentrations

10.1: Read the pre-integrated 4D look-up-table specific to steady non-adiabatic flamelet model for ordered values of mean temperature and species mass fractions.

10.2: From the known values of mean mixture fraction, its normalized variance, mean scalar dissipation rate and enthalpy defect, obtain mean temperature and species mass and mole fractions from the look-up-table using the 4D interpolation technique (Ravikanti, 2008).

Step 11: Calculation of radiation source term from DT method

11.1: Read the filtered values of temperature and mole fractions of CO_2 and H_2O from the above step.

11.2: Using Discrete Transfer radiation model, solve for the radiation transfer equation (RTE) to obtain the source term. This source is provided as the input for solving enthalpy equation in **Step 2.1**.

6.6.4UFPV-δ Function Model

In the present study, UFPV-δ function model was tested for partially premixed lifted flames with the foremost objective of capturing the experimentally observed temperature distribution and species mass fractions. The working procedure for UFPV-δ function model is thus as follows:

Steps 2&4: Calculation of scalar transport equations

2.1: Solve for the filtered mixture fraction equation.

2.2: Compute the sub-grid variance of mixture fraction from its model equation and subsequently calculate the normalized subgrid-variance.

2.3: Compute the filtered scalar dissipation rate from its model equation

2.4: Read the pre-integrated 4D look-up-table (discussed in Chapter 7) specific to UFPV δ function model for ordered values of filtered reaction progress variable source term.

2.5: From the values of filtered mixture fraction and its normalized variance computed from **steps 2.1** and **2.2**, filtered scalar dissipation rate from **step 2.3** and filtered reaction progress variable obtained from previous time step or iteration,

compute filtered progress variable source term from the look-up-table using the 4D interpolation technique.

2.6: Solve the transport equation for filtered progress variable using the filtered chemical source term obtained from **step 2.5**.

Step 3: Calculation of density

3.1: Compute the sub-grid variance of mixture fraction from its model equation and subsequently calculate the normalized subgrid-variance.

3.3: Read the pre-integrated 4D look-up-table specific to UFPV δ function for ordered values of filtered density. From the known values of filtered mixture fraction, its normalized variance, filtered scalar dissipation rate and the filtered reaction progress variable obtained from **step 2.6**, obtain filtered density from the look-up-table using the 4D interpolation technique.

Step 10: Calculation of temperature and species concentrations

10.1: Read the pre-integrated 4D look-up-table specific to UFPV for ordered values of filtered temperature and species mass fractions like CO_2, H_2O and CO in the present case.

10.2: From the known values of filtered mixture fraction, its normalized variance, filtered scalar dissipation rate and the filtered reaction progress variable obtain filtered temperature and species mass fractions from the look-up-table using the 4D interpolation technique.

Generation of the look-up-tables for the above different models implemented in LES has been discussed in Chapter 7.

6.7 Boundary Conditions

Appropriate boundary conditions are the prerequisite for an accurate reproduction of physical CFD domain and its flow condition. Initial and boundary conditions are equally needed for solving all the partial differential equations. Along with these conditions, turbulence conditions are given for the solution. Turbulence has to be prescribed at the inflow in order to simulate turbulence. In all simulations the flow is impulsively started at $t = 0$, when the simulation is started. Pressure impulsively starts the flow as inlet conditions are applied, initially producing a potential flow.

Turbulence from the inlet gradually fills the domain, eventually forming a fully developed flow field. For solving all isothermal flows, the boundary conditions must be supplied for five dependent variables: ρ, u_i and p. Whereas for all reacting flows, boundary conditions for other scalars such as mixture fraction, subgrid variance, scalar dissipation rate, enthalpy and progress variable has to be supplied. The boundary condition for density can be specified from mixture fraction as density is dependent on mixture fraction. Continuity requires that mass conservation be satisfied over the complete domain at all times, and the boundary conditions for the velocity field must therefore ensure that

$$\int_{\Omega} \frac{\partial \rho}{\partial t} dV + \int_{S} \rho u_i n_i dS = 0 \tag{6.38}$$

Dirichlet and Neumann boundary conditions are applied for the variables in the present solution. In Dirichlet condition, the value on the boundary $\partial \Delta V$ of any scalar variable ϕ of the computational domain ΔV is given by:

$$\phi = \phi_{\partial} \tag{6.39}$$

In Neumann boundary condition, the gradients $\partial \phi / \partial x_j$ in surface normal direction n_j *are* given by c_{∂}:

$$\frac{\partial \phi}{\partial x_j} n_j = c_{\partial} \tag{6.40}$$

6.7.1Inlet Boundary Condition

The instantaneous inflow boundary conditions have been generated by using mean velocity profiles with random fluctuations. The mean velocity distributions were specified using power law velocity profile as shown

$$\langle U \rangle = C_0 U_{bulk} \left(1 - \frac{|y|}{\delta} \right)^{1/7} \tag{6.41}$$

where U_{bulk} is the bulk velocity, y is the radial distance from the jet centre-line and δ = 1.01× R_j, with the fuel jet radius R_j. The coefficient C_0 has the value ranging from 1.218 to 1.6 depending on the grid distribution in the fuel inlet region to ensure correct mass flow rate at the inlet, Masri *et al.* (2000). The fluctuations are generated from a Gaussian distribution such that the inflow has the correct level of turbulent

kinetic energy obtained from the experimental measurements, Branley and Jones (2001). The instantaneous inflow velocity u_i is then computed as

$$u_i(x_i,t) = \langle U_i \rangle + \theta(x_i,t)\langle u_i' \rangle_{rms} \tag{6.42}$$

where U_i is the mean velocity obtained from equation 6.41, $\langle u_k' \rangle_{rms}$ is the root mean square of turbulent fluctuations obtained from experimental measurements at the inflow and $\theta(x_i, t)$ is a random number from a Gaussian distribution.

6.7.2Outflow Boundary Condition

The outflow boundary conditions can be either a zero normal gradient condition or a convective outlet boundary condition. A zero gradient condition at an outlet boundary is given by the formula

$$\frac{\partial \phi}{\partial n} = 0 \tag{6.43}$$

The gradient in the above equation is taken normal to the outflow boundary. Another form of outlet boundary condition known as a mass conserving convective outlet boundary condition given by

$$\frac{\partial \tilde{\phi}}{\partial t} + U_b \frac{\partial \tilde{\phi}}{\partial n} = 0 \tag{6.44}$$

where U_b is the bulk velocity across the boundary and n is the coordinate in the direction of outward at the outlet boundary. The zero normal gradient condition assumes a zero gradient for all flow variables except pressure in a direction normal to the outlet place. Such a condition is appropriate when the flow is fully developed at the outlet and devoid of any flow reversal. Hence, zero normal gradient condition often demands a lengthy computational domain and subsequently more number of grid points which is not desirable from the perspective of LES calculation time. Therefore, the present LES work includes convective outlet boundary condition.

6.7.3Solid Boundary Condition

A solid wall boundary is to set the normal and tangential velocity components to zero. These conditions correspond to the impermeability condition and the no-slip condition respectively which are given as

$$u_i(x,t) = 0 \tag{6.45}$$

On the contrary, slip boundary condition is defined by treating boundaries as frictionless surfaces. The flow adjacent to the boundary is allowed to move in the direction parallel to the boundary by enforcing a zero gradient condition normal to the surface as

$$\frac{\partial u_i}{\partial n} = 0 \tag{6.46}$$

For the turbulent boundary layers it is necessary to use an approximate boundary condition or wall functions in order to apply the correct shear force to the fluid. The wall function adopted in this study is that of Werner and Wengle (1991) which uses a power-law approximation to the log-law. For unconfined flows, artificial confinement is usually adopted to avoid the problem of numerical instability due to reverse flow at open boundaries. Thus, artificial wall boundaries which do not exist in practice are placed in the computational domain. The placement of these walls is such that the computational domain is restricted to an affordable size yet the walls are far enough to have any influence on the flame structure. These artificial walls are treated with a free-slip condition which represents a friction less surface. With the free-slip condition, the fluid flow in the direction tangential to the wall exists while the flow in the normal direction is zero. Hence the normal component of velocity and the gradients of tangential components of velocity are set to zero at the wall. For pressure and all the scalars, the gradients in the wall normal direction are set to zero near the wall boundaries in the domain. A detailed theory on wall boundary conditions used in the present LES code can be obtained from Kirkpatrick (2002).

6.8 Closure

This chapter discussed the numerical approach with finite volume technique employed in the present LES code. The methods used for the discretization of the governing equations were highlighted. Time and space discretization were discussed along with the solution procedure involved in each of the combustion model used in the LES code. Finally the boundary conditions used for inlet, outlet and wall were discussed in detail.

Chapter 7

PDF Calculations – Pre-processing Procedure

Modelling combustion along with turbulence by solving all the scalar equations along with other governing equations of flow is a complex and time consuming process. Turbulence calculations are therefore coupled with combustion modelling with the concept of look-up tables which are calculated before hand. In order to optimize the time involved in the turbulence-chemistry calculations in LES, look-up tables are found to be the best in terms of computational time involved in combustion calculations. This concept was proved to be efficient with flamelet modelling. Flamelet solution from either steady or unsteady calculations is fed through a proper integration technique to develop a pre-integrated look-up table. The present work includes the generation of flamelets in both steady and unsteady regime based on the model used. For example, for SLFM model development of steady flamelet solution is performed while for UFPV model generation of unsteady flamelet profiles is carried out. These flamelets contain the dependence of mixture fraction with temperature and all other mass and mole fractions of the species taking part in the chemical mechanism. This set of data is made to undergo the integration process to evolve the table of data which is feed directly into the LES calculations. Therefore, generation of flamelets and integration form the pre-processing stage and is thus independent of actual LES calculations.

The steady flamelets generated in the present study can be broadly categorised as adiabatic and non-adiabatic, based on their process of generation. Within each category, flamelets can be classified as non-premixed and partially premixed based on their structure. The present chapter describes the procedure for generation of flamelets (section 7.1). Both steady and unsteady flamelet generation technique is discussed in this section. Using the above set of flamelet solution for the development of look-up tables specific to each of the combustion model (SLFM, NAFM and UFPV) is

discussed later in the sections. Each of the models is performed with different approach towards the integration process as the dependence of any scalar varies from model to model. Details of different PDF distributions are depicted in Chapter 4, section 4.2.2. Both beta and log normal distributions were clearly explained in section 4.2.2. Once the look-up tables are generated, this data is read accordingly when required in the LES code for the calculations of density, temperature and all major species predictions.

7.1 Flamelet Generation

In the present research work, flamelet libraries are generated using the code called FlameMaster originally developed by Pitsch (1998). Generation of the steady or unsteady flamelets forms the initial step for developing the PDF look-up tables. The process of generating flamelets involves obtaining solutions for the flamelet equations (Eqs.4.5 & 4.6) after enforcement of appropriate assumptions and inputs. The inputs required are (1) the boundary conditions for fuel and oxidizer streams and (2) chemical kinetic mechanism along with the thermodynamic data. Since the assumption of unity Lewis number and equal diffusivity is made in the derivation of the flamelet equations, the assumption is inherently enforced for all the calculations. However, assumptions regarding the radiation heat loss need to be explicitly specified. All the steady flamelet solutions are obtained without the radiation source term in the flamelet equations. The steady non-adiabatic flamelets also do not consider the radiation source term but employ an enthalpy defect approach which is discussed later in this section.

The GRI 2.11 (Bowman *et al.*, 2007) mechanism is used in the present study for describing the methane-air combustion which provides a detailed account of the elementary reactions participating in the carbon-hydrogen-oxygen chemistry. The mechanism comprises of 277 elementary reactions with 49 species out of which 102 reactions and 17 species pertaining to the NO_x chemistry. GRI 3.0 is also tested and compared with GRI 2.11 in the present work for bluff body and swirl flames. GRI 3.0 consists of 325 elementary reactions with 53 species. Hydrogen fueled flame is also tested for lifted flame category under UFPV modelling. The chemical mechanism used for this particular flame was obtained from Peters and Rogg (1993) with 19

reactions and 9 species. Both SLFM and NAFM involve the steady state calculations from the flamelet equations while UFPV deals with unsteady state calculations.

7.1.1Steady Adiabatic Flamelets

Generation of steady adiabatic flamelets involves solving for the flamelet equations without the time derivative term and the radiation source term:

$$\rho\frac{\chi}{2}\left(\frac{\partial^2 Y_i}{\partial f^2}\right)+\dot{\omega}_i=0 \tag{7.1}$$

$$\rho\frac{\chi}{2}\left(\frac{\partial^2 T}{\partial f^2}\right)+\rho\frac{\chi}{2C_p}\left(\frac{\partial T}{\partial f}\frac{\partial C_p}{\partial f}\right)+\sum_{i=1}^{N}\rho\frac{\chi}{2}\frac{C_{pi}}{C_p}\left(\frac{\partial Y_i}{\partial f}\frac{\partial T}{\partial f}\right)=\frac{1}{C_p}\sum_{i=1}^{N}h_i\dot{\omega}_i \tag{7.2}$$

Solving these equations lead to solution obtained for the specific fuel air conditions depending on the flame configuration. For example Fig. 4.2 represents Berkeley CH_4-Air lifted flame with the S-shaped curve. The stoichiometric temperature resulting from each flamelet solution is depicted through the solid line which consists of three different branches namely the top stable burning branch, middle unstable branch of partially extinguished states and the bottom branch of completely extinguished states.

The solutions along the fully burning branch are obtained by progressively increasing the stretch rate represented by the stoichiometric scalar dissipation χ_{st} from its value at equilibrium (χ_{st}=0) to the quenching limit $\chi_{st,q}$. The quenching limit is dictated by the composition and temperature of fuel and oxidizer streams in the turbulent flame. The flamelet structure upon complete extinction corresponds to that of inert mixing of the reactants and remains unaffected for all $\chi_{st} > \chi_{st,q}$. The middle branch of unstable partially extinguished states represents the transition from fully burning to complete extinction. Generation of flamelet solutions for the middle branch involve choosing a solution corresponding to χ_{st} slightly less than $\chi_{st,q}$ and then using this value as initial solution for a simulation towards smaller values of stoichiometric scalar dissipation rate. With the steady flamelet model SLFM, flamelets are parameterized by scalar dissipation rate and to ensure a unique parameterization, the unstable middle branch is ignored. Therefore, the task of flamelets generation for SLFM based turbulent flame calculations is made simpler by performing the calculations for flamelet profiles

related to fully burning branch and completely extinguished state alone. The present research work involves SLFM based flame calculation for bluff body flames like HM1 and HM3e. Similar case studies with SLFM are also performed for swirl based flames with SMH1 flame. Both the above flame configurations have similar fuel air composition. Therefore, the same set of flamelet solutions can be used for the two burners.

The steady flamelet profiles used in SLFM based calculations of the non-premixed Sydney bluff-body HM1 and HM3e flames and swirl stabilized SMH1 flame are shown in Fig. 7.1. For both the flames, the fuel stream is composed of a mixture of CH_4 and H_2 in 1:1 ratio by volume while the oxidizer stream consists of pure air. Both the streams are at a temperature of 300 K. For these strictly non-premixed conditions, extinction of a flamelet occurs at $\chi_{st,q}$ approximately equal to 55 s^{-1}. The steady flamelet solutions in Fig. 7.1 represent the GRI 2.11 mechanism calculations. A similar calculation is also performed with GRI 3.0 mechanism for CH_4-H_2 fueled burners which is not shown.

The flamelet in non-premixed conditions in the above figure consists of a thin diffusive-reaction zone characterised by a high temperature gradient around the stoichiometric mixture fraction f_{st}. The reactants are consumed within this reaction zone and species attain maximum value while density attains lowest due to the maximum heat release. As the stretch on the flamelet increases, the peak temperature drops due to the greater extent of heat loss to the outer regions of the reaction zone in comparison to the amount of heat released. The flamelet finally extinguishes when the stretch rate reaches quenching limit $\chi_{st} = \chi_{st,q}$ resulting in an inert mixing of the reactants. The flamelet profiles of the reactants are not shown in the above figure.

In each set of profiles shown in Fig 7.1 a discontinuity between the fully burning states and the extinguished (or quenched) state can be clearly seen which is due to the absence of partially extinguished intermediate states which cannot be accounted in SLFM. Present cases with SLFM have been mainly employed with fully burning turbulent flames alone and hence the absence of partially extinguished flame states resulted in the discontinuous region is the above figure.

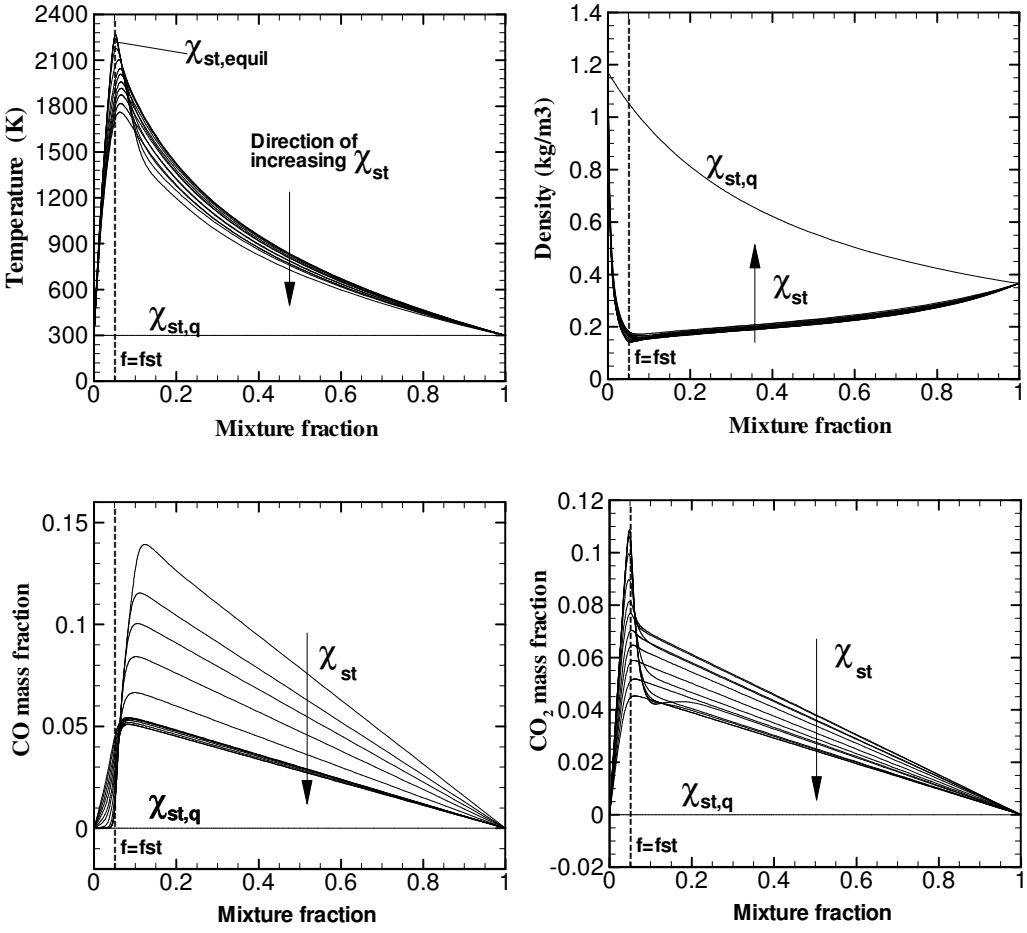

Figure 7.1: Steady flamelet solutions generated for HM1, HM3 and SMH1 diffusion flames. Profiles corresponding to fully burning state and extinguished state are represented with increasing value in scalar dissipation rate, $\chi_{st.}$

An interesting observation that can be made from the density profiles is that the influence of scalar dissipation rate on the density for the fully burning flamelets is very negligible. This indicates that when simulating turbulent non-premixed flames which are devoid of any local extinction, considering a single representative scalar dissipation rate should yield a mixing field prediction which is more or less similar to that obtained when considering the effect of scalar dissipation rate. This set of solution have proved advantageous for the work performed by Ranga Dinesh (2007) and Hossain (1999) where turbulent non-premixed flames operating far from blow-off have been simulated with a single flamelet approach using LES and RANS respectively. Employing a single scalar dissipation is particularly useful in LES where the modelled values of scalar dissipation rate fluctuate by large magnitudes often

leading to numerical instability. This has proved very advantageous in the present work of non-adiabatic flamelet model when coupling radiation with turbulence-chemistry. However, considering single flamelet alone is not sufficient for temperature and species predictions as the effect of stretch on peak temperatures and species mass fractions is more as shown in Fig. 7.1. In the present SLFM study, a total of 14 flamelet profiles (13 fully burning solutions + 1 fully extinguished inert mixing solution) have been provided as input to the pre-integration code which generates look-up-table of mean scalars for SLFM based turbulent flame calculations.

7.1.2Steady Non-Adiabatic Flamelets

The methodology used in the generation of non-adiabatic flamelets is taken from the studies conducted by Ravikanti *et al.* (2008). Steady non-adiabatic flamelet profiles are generated for varying levels of non-equilibrium conditions represented by χ_{st} and non-adiabatic conditions represented by the enthalpy defect (ζ). Fully burning and completely extinguished flamelets are only considered for the flamelet solution for every enthalpy defect shelf. The quenching value of scalar dissipation rate for the fuel and oxidiser composition for SMH1 flame is obtained as $55sec^{-1}$. As radiation is accounted in the form of enthalpy defect, flamelet equations are solved in its steady state for laminar adiabatic flamelet modelling. The technique which is based on the ideas of Hossain *et al.* (2001) has been developed and incorporated in the present work. Generating a steady non-adiabatic flamelet profile with the enthalpy defect concept requires a two step procedure, which is as follows:

1. The adiabatic flamelets are generated for all the scalar dissipation rates from equilibrium to extinction for each of the predefined enthalpy defect shelf. Adiabatic temperature profile for all the above flamelets is then treated with the enthalpy defect resulting in a downward shift of the temperature profile as shown in Fig. 7.2 which represents profiles at enthalpy defect of -90 kJ/kg. The resulting adiabatic flamelet temperature profile is treated at every point along the mixture fraction space with a temperature defect profile $\Delta T(f)$ which is computed from a pre-defined enthalpy defect using the formula:

$$\Delta T(f) = \frac{\zeta}{C_p(f)} \tag{7.3}$$

The profile after treatment is represented with $T(f)-|\Delta T(f)|$ for the non-adiabatic temperature profile. But this results in temperature of fuel and oxidizer at the boundaries to drop below 300 K. So in order to avoid this unrealistic situation, mixture fraction limits corresponding to the boundary value temperatures of fuel and oxidizer are considered and the values below and above the lower and upper limits of modified mixture fraction are truncated with richer oxidizer and leaner fuel at the ends. The effect of truncation has a very negligible effect on the overall solution procedure as discussed by Ravikanti *et al.* (2008).

2. Non-adiabatic flamelets are calculated by solving the flamelet equations with modified inlet conditions for mixture fraction whilst maintaining the same inlet temperatures as in the case of adiabatic condition. The calculated flamelets in the mixture fraction space have the truncated mixture fraction span ranging from $f_{oxidiser}$ to f_{fuel} instead of ranging from 0 to 1.

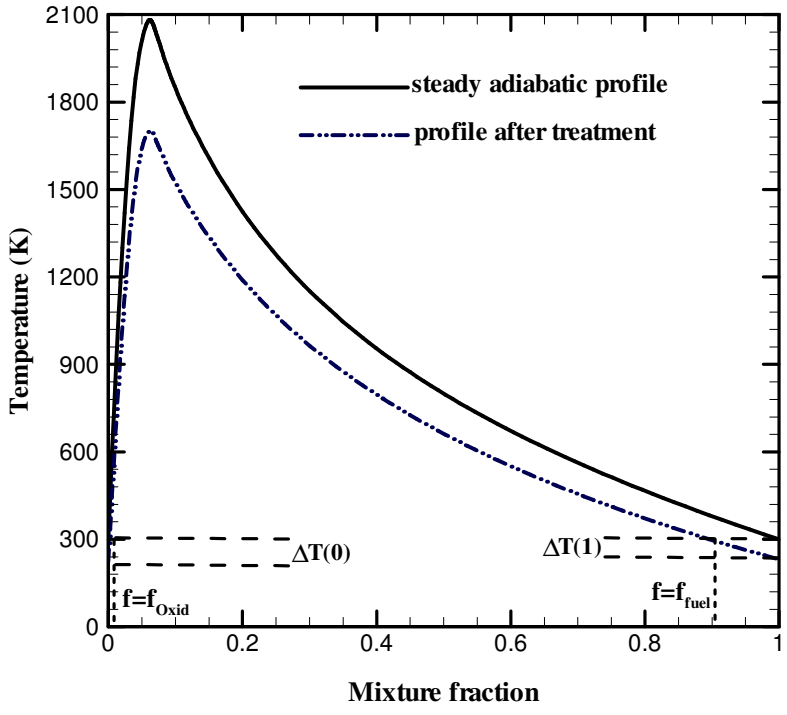

Fig. 7.2 Enthalpy defect implementation on temperature profile for SMH1/HM1 flame

Enthalpy defects of 0, -15, -45, -60, -75, -90, -105, -120, -150 and -180 kJ/kg has been considered to model adiabatic to extreme non-adiabatic conditions in the flame. Each enthalpy defect shelf has the flamelet profiles with scalar dissipation rate varying

from equilibrium to extinction limits. For each enthalpy defect, steady non-adiabatic flamelet profiles for $\chi_{st}(\zeta)$ varying from equilibrium to extinction condition have been generated. The series of enthalpy defects can thus be viewed as shelves with each shelf containing a set of fully burning non-adiabatic flamelet profiles. It is to be noted here that the extinction limit of a flamelet varies with enthalpy defect. An increase in enthalpy defect corresponds to an increased heat loss in comparison to the heat generation within a flamelet and hence extinction of a flamelet occurs at a lesser value of χ_{st}. This behavior can be observed in Fig. 7.3 for the flamelets generated for the CH_4-H_2 flame conditions where ζ_{max} is the maximum enthalpy defect = -180 kJ/kg in the present study for CH_4/H_2 flames. This set of data from each enthalpy defect is used for the generation of pre-integrated look up tables in mixture fraction, scalar dissipation rate and enthalpy defect space.

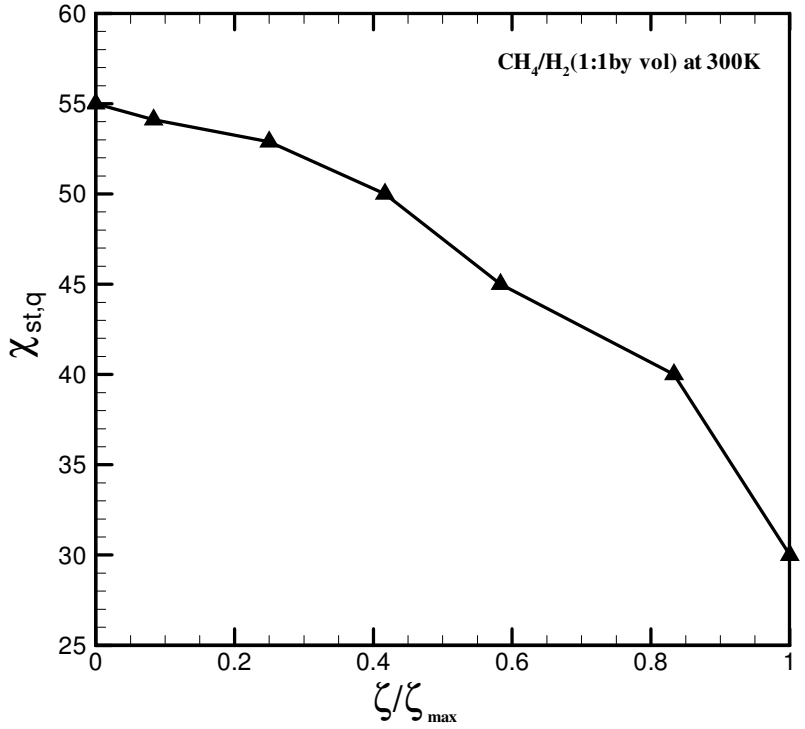

Figure 7.3: Variation of extinction limit with enthalpy defect for CH_4-H_2 conditions

7.1.3Unsteady Adiabatic Flamelets

Steady flamelet modelling has both advantages and as well as some demerits. It is easier to use and saves the computational cost and leads to good results when the assumptions are not violated when compared to fast chemistry. But the drawback of

using steady flamelet model is that it does not predict flame lift-off, which is typically a common feature in most of the combustion devices. The incorrect representation of flame lift can lead to large discrepancies in flow field predictions, as shown by Pierce and Moin (2004) and Pitsch *et al.* (1998) which would certainly translate into inaccuracies in the prediction of pollutants. Steady flamelets even could not predict local extinction and re-ignition effects appropriately. The reason is that the solution space used in the steady flamelet model is very restrictive.

Unsteady adiabatic flamelets are primarily utilized in the UFPV model which is modelled based on solving the flamelet equations containing the unsteady term as described in equations 4.5 and 4.6 in Chapter 4. Radiation is neglected and Lewis number is assumed to be unity with constant diffusivity for all species. Generation of unsteady flamelets involves time as the parameter that needs to be eliminated and solution domain has to be parameterized with a new variable called as flamelet parameter. For the UFPV model, the flamelet parameter replaces time and it facilitates unique identification of all the unsteady state solutions including the partially extinguished solutions. Thus, the discontinuity observed with the set of profiles used for SLFM can be bridged with the UFPV approach.

Berkeley flame operate under partially premixed conditions with the fuel consisting of a mixture of CH_4 and air in the ratio of 1:3 by volume and at a temperature of 323 K while the oxidizer consists of vitiated air at 1355 K. A similar experimental test case was also performed with H_2-N_2 fueled jet flame. The central nozzle for this case is 25% H_2 and 75% N_2. As the stretch rate is increased, the structure tends towards that of a single reaction zone and finally, quenching occurs at $\chi_{st,q} \approx 587\, s^{-1}$ for methane based flame and $\chi_{st,q} \approx 2649\, s^{-1}$ for hydrogen based fueled jet.

Figure 4.2 depicts the unsteady flamelet solutions which are represented by vertical dots at increasing scalar dissipation rate from equilibrium to extinction. At scalar dissipation rate of $0.1s^{-1}$ the flamelet profiles for temperature, density and other parameters are depicted in Fig. 7.4. A similar set of data is obtained for entire range of scalar dissipation rates from 0 to $587s^{-1}$. With variations in time, the flamelets are generated from equilibrium state to mixing limits in a smooth transition with uniform

change in time. In the present study, a total of 106 flamelet profiles have been considered at a single scalar dissipation rate to be converted into table format for the input for scalars in the LES simulation. These pre-PDF calculations are done with delta PDF for progress variable. Figure 7.4 gives an indication of variation in temperature, density, mass fraction of CO_2 and progress variable with mixture fraction.

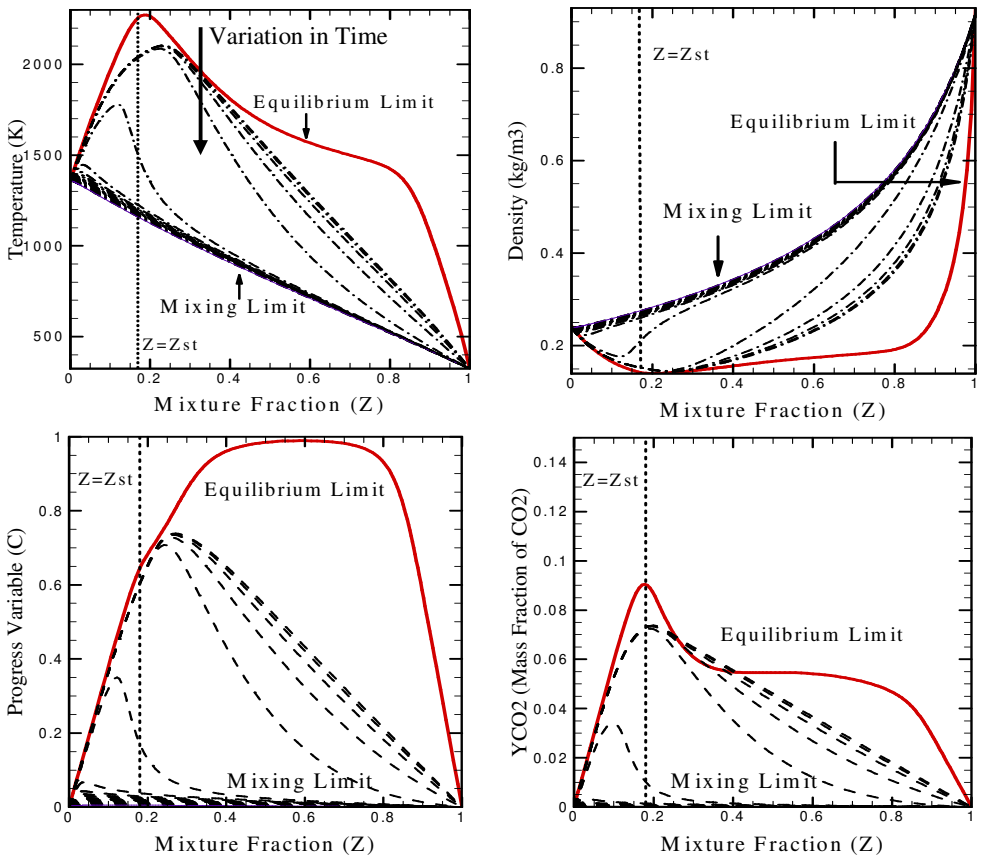

Figure 7.4: Unsteady flamelet solutions for fully burning, partially extinguished and fully extinguished states. Flamelets generated for the Berkeley CH_4-Air lifted jet flame conditions. These solutions are used for UFPV based turbulent flame calculations. (——) fully burning and fully extinguished states; (-------) partially extinguished state at 0.1 s^{-1}.

It is interesting to note that all the parameters especially density has notable change in its value from equilibrium to extinction along the increment in time. As specified before, time is eliminated by bringing progress variable as the element to parameterize. Therefore, density cannot be assumed to follow a single flamelet profile

in case of Berkeley flame related to CH_4-Air fueled burner. Hence the look-up tables for density, temperature and progress variable source term are defined in such a way that they are dependent on fluctuations in mixture fraction, scalar dissipation rate and progress variable. Progress variable varies from 0 to 1 in the present UFPV model. For H_2-N_2 fueled burner, flamelet equations are solved in the unsteady mode and Fig. 7.5 shows the flamelet solution domain under specified fuel-air composition.

Figure 7.6 shows the unsteady flamelet solutions for scalar dissipation rate of $0.0001 sec^{-1}$ based on H_2-N_2 fuel composition. These profiles have been generated at one particular scalar dissipation rate close to equilibrium. Similar set of data are generated for all the scalar dissipation rates till extinction. From Fig. 7.6 it is clear that density variations along the time are drastic and therefore cannot be neglected. Density look up table thus depends on mixture fraction variations, scalar dissipation rate and progress variable. Temperature, progress variable source and OH mass fraction look-up tables are the other elements that are considered in the present case. A total of 36 flamelets are selected for the scalar dissipation rate of 0.0001 sec^{-1}. The number of flamelets in each shelf of scalar dissipation rate varies. The dash dotted lines represent the unstable partial premixed flamelet solution.

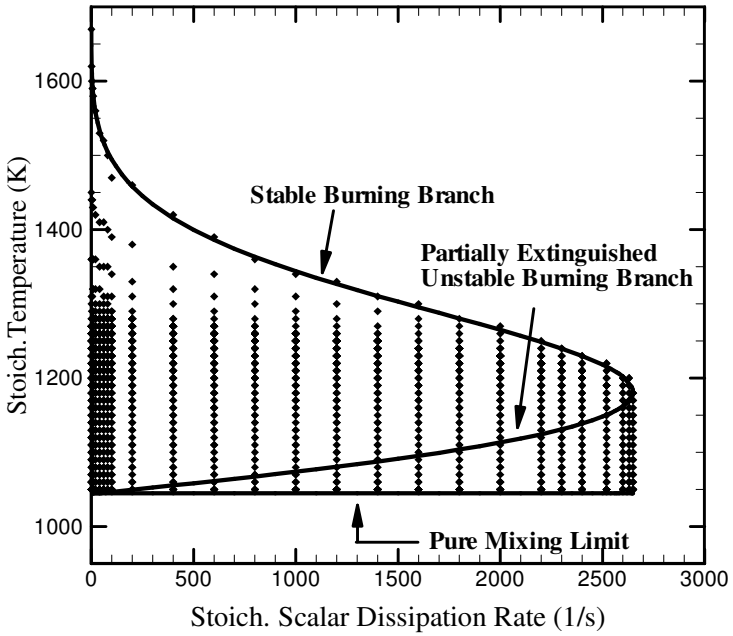

Figure 7.5 Unsteady flamelet solution space for H_2/N_2 flame. Dotted values resemble the unsteady flamelet solutions at various scalar dissipation rates

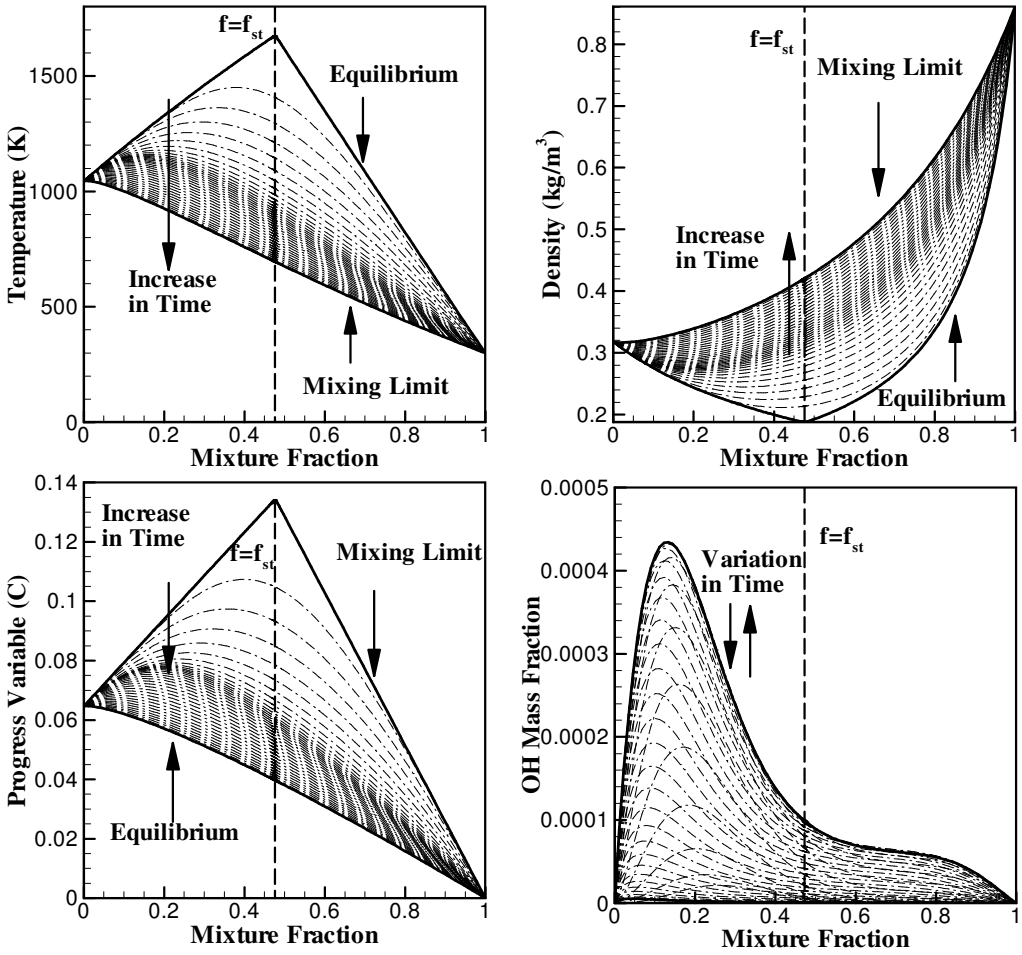

Figure 7.6: Unsteady flamelet solutions for fully burning, partially extinguished and fully extinguished states. Flamelets generated for the Berkeley H_2-N_2 lifted jet flame conditions. These solutions are used for UFPV based turbulent flame calculations. (–) fully burning and fully extinguished states; (-.-.-.-) partially extinguished state at $0.0001s^{-1}$.

The most interesting aspect regarding the progress variable in this case can be found from Fig. 7.6 where the range of progress variable goes from 0.0646 to 0 in its limits for mixture fraction from 0 to 1. The maximum value in the progress variable varies for each flamelet along the time and is not equal to 1. In order to implement a common scale to progress variable at all scalar dissipation rates, progress variable is normalized to vary from 0 to 1 for each of the scalar dissipation rates. The value of progress variable at mixture fraction equal to zero is changed from 0.0646 to 0 by

implementing the data correction in such a way that value of progress variable would be zero at both ends of the mixture fraction. Therefore, the new limits for progress variable are from 0 to 0 at the ends (mixture fraction equal to 0 and 1.0) and maximum value of progress variable is normalized to vary from 0 to 1. Corresponding values of scalars such as temperature and other species are changed to incorporate the changed progress variable limits. This data is then utilized for integration procedure for the generation of PDF look up tables. The definition of progress variable considered in this case is the mass fraction of H_2O.

7.2 PDF Look-up Tables for SLFM

Steady adiabatic laminar flamelets are needed for pre-processing to obtain integrated look-up-tables for Favre averaged or filtered thermo-chemical variables $\tilde{\phi}$ (density, temperature and species mass fraction) as a function of mean mixture fraction $\tilde{f}$, its normalized variance $\widetilde{f''^2_{norm}}$ and scalar dissipation rate $\tilde{\chi}$.

$$\tilde{\phi} = \tilde{\phi}\left(\tilde{f}, \widetilde{f''^2_{norm}}, \tilde{\chi}\right) \tag{7.4}$$

The in-house developed code is used to generate look-up-tables specific to SLFM. Steady adiabatic flamelets obtained from the flamelet calculations are fed into the tool along with ordered values of the look-up-table parameters $\tilde{f}$, $\widetilde{f''^2_{norm}}$ and $\tilde{\chi}$. Mean values for each thermo-chemical variable $\tilde{\phi}$ are then obtained at each combination of the three parameters by performing numerical integration of the steady adiabatic flamelets with presumed PDF for mixture fraction $\tilde{P}(f)$ and scalar dissipation rate $\tilde{P}(\chi_{st})$ thereby resulting in a 3D look-up-table. The double integral equation which is numerically evaluated is given by:

$$\tilde{\phi} = \int_0^{\infty}\int_0^{1} \phi(f;\chi_{st})\,\tilde{P}(f)\,\tilde{P}(\chi_{st})\,df\,d\chi \tag{7.5}$$

The conserved scalar mixture fraction is designed to vary from 0 to 1. For a given $\tilde{f}$, its variance $\widetilde{f''^2}$ can take values between 0 to a maximum of $\tilde{f}\left(1-\tilde{f}\right)$ in the turbulent flow field. A single range cannot be fixed if absolute variance is to be used as the

table parameter and therefore it needs to be normalized. In the present integration code, the absolute variance $\widetilde{f''^2}$ is normalized (Eq. 7.6) by its maximum value for each $\tilde{f}$ and the normalized variance $\widetilde{f''^2_{norm}}$ ranges between 0 to 1.

$$\widetilde{f''^2_{norm}} = \frac{\widetilde{f''^2}}{\tilde{f}\left(1-\tilde{f}\right)} \tag{7.6}$$

The distribution of grid points to cover the range of values for each of the table parameters is considered in such a manner that an optimum balance between computational cost and accuracy is achieved. For all the tables generated for SLFM calculations, size of 163 x 51 x 31 ($\tilde{f}$ x $\widetilde{f''^2_{norm}}$ x $\tilde{\chi}$) has been considered. This preferential allocation allows for accurate capturing of the variation of the mean scalar structure which is particularly steep along the $\tilde{f}$ axis of the look-up-table. The distribution of the discrete points along $\tilde{f}$ axis is directly obtained from the grid (Fig. 7.7) used for the flamelet calculations corresponding to equilibrium condition.

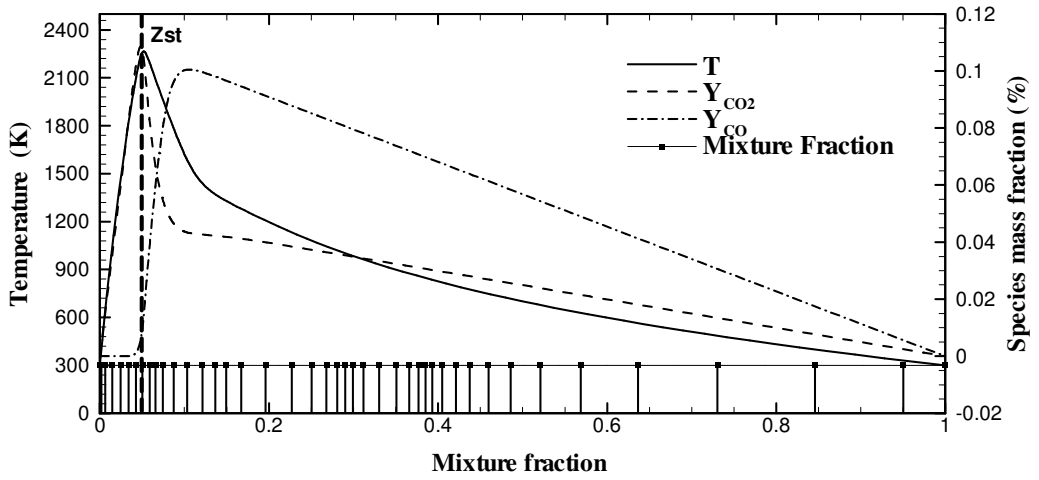

Figure 7.7: Steady adiabatic flamelet profiles at equilibrium condition generated for methane-hydrogen (SMH & HM) flames. Dots with vertical lines show alternative grid points along mixture fraction space.

While solving for the flamelet equations in the FlameMaster code, the grid on the mixture fraction space is refined automatically using an adaptive grid technique according to the steepness of the scalar gradient. The gradients in scalar structure at equilibrium condition are the steepest and hence the grid distribution along mixture

fraction is ideal to be imitated for the mean scalar structure. In Fig 7.7, the grid points can be observed to be densely populated around the stoichiometric mixture fraction where high gradients in scalars are observed.

Look-up table utilizes power law distribution with the profile as shown below for normalised mixture fraction variance and mean scalar dissipation rate.

$$\Psi(i) = exp(-a)(i-1)^{b} \tag{7.7}$$

Considering $\Psi = \widetilde{f''^2_{norm}}$ the grid count i varies from 1 to 51 and the constants a and b take the values of 5.0 and 2.95 respectively. Similarly for $\Psi = \tilde{\chi}$, the grid count i varies from 1 to 31 and the constants a and b take the values of 6.0 and 6.5 respectively.

Numerical integration is performed for every cell in the table and for every scalar of interest once the table properties are specified. Double integration of the above expression in Eq 7.5 is simplified by employing the approach followed by Lentini (1994) and Hossain (1999). A limited number of flamelet libraries (13 fully burning +1 fully extinguished) are considered with each represented by scalar dissipation rate χ_l. Integration range of χ is split into L sub-ranges [$\chi_{l-1/2}, \chi_{l+1/2}$] with l=1, 2 …L (in particular $\chi_{1/2}$=0), such that χ_l is a representative value for corresponding interval. The double integral is evaluated by means of the below approximation:

$$\tilde{\phi} = \sum_{l=1}^{L} \int_{\chi_{l-1/2}}^{\chi_{l+1/2}} \tilde{P}(\chi_{st})\, d\chi_{st} \int_{0}^{1} \phi(f, \chi_l)\, \tilde{P}(f)\, df \tag{7.8}$$

The above expression can be divided into two parts where the mixture fraction is solved separately from the scalar dissipation rate distribution. The shape of the mixture fraction equation is assumed to be β PDF and that of scalar dissipation rate χ is assumed to follow log-normal distribution.

Beta Probability Density Function (β-PDF)

The mixture fraction variable f is extracted from the above integral and can be shown as:

$$\int_0^1 \phi(f,\chi_l)P(f)df \tag{7.9}$$

The evaluation of the integral as shown below requires a presumed shape for *P(f)* and is assumed to be a β- function distribution. This distribution was described before from equations (4.14) to (4.16) in section 4.2.2. $\tilde{f}$ and $\tilde{f}''^2$ are obtained from the solution of their respective transport equations, where $\tilde{f}$ and $\tilde{f}''^2$ are the filtered mixture fraction and subgrid variance respectively.

In the present work, the subgrid variance term is modeled based on local equilibrium argument by Branley and Jones (2001) which can be summarized as:

$$\tilde{f}''^2 = C\Delta^2\left(\frac{\partial\tilde{f}}{\partial x_j}\frac{\partial\tilde{f}}{\partial x_j}\right) \tag{7.10}$$

where Δ being the local grid spacing with

$$\Delta = (\Delta x \Delta y \Delta z)^{1/3} \tag{7.11}$$

where Δx, Δy and Δz are the grid size for the *x, y* and *z* directions in the Cartesian coordinate system respectively. The value of C is obtained as 0.1 for most of the successful cases, Branley (1999). The integral in the Eq. 7.9 now becomes,

$$\int_0^1 \phi(f,\chi_l)P(f)df = \frac{\Gamma(a+b)}{\Gamma(a)\ \Gamma(b)}\int_0^1 \phi(f,\chi_l)f^{a-1}(1-f)^{b-1}df \tag{7.12}$$

Once we obtain the knowledge of *P(f)*, numerical integration of the above integral is carried out using ***Romberg's method*** with mid-point approximation (Press *et al*, 1996). There are a couple of numerical difficulties that are associated with calculation of the integral in Eq 7.9. Firstly at the limits of the integral i.e., at f=0 and f=1, a or b (Equations 4.15 and 4.16) can take a value less than unity which leads to singularity in the solution. This problem is solved by implementing the method suggested by Bray and Peters (1994) and Chen *et al* (1996) which takes the form:

$$\int_0^1 \phi(f,\chi_l)f^{a-1}(1-f)^{b-1}df \cong \frac{\xi^a}{a}\phi(0) + \int_\xi^{1-\xi}\phi(f,\chi_l)f^{a-1}(1-f)^{b-1}df + \frac{\xi^b}{b}\phi(1) \tag{7.13}$$

ξ here represents a very small number usually taken as 10^{-30}. Secondly, the overflow problem caused when the computed values of *a* and *b* reach several hundred thousands in magnitude during the iteration process. According to characteristic of *β*-function, the distribution will be close to delta function when *a* or *b* is adequately large. Hence this problem is tackled by approximating *P(f)* to be a delta function under such circumstances. A value of 500 has been set as the limit. Therefore,

$$P(f) = \delta\left(f - \tilde{f}\right) \tag{7.14}$$

Solving for Scalar Dissipation Rate

Evaluation of scalar dissipation rate distribution is done with the solution of the following integral:

$$\int_{\chi_{l-1/2}}^{\chi_{l+1/2}} P(\chi_{st}) d\chi_{st} \tag{7.15}$$

The scalar dissipation space is assumed to follow a presumed Pdf function namely Log-normal distribution for $P(\chi)$. This expression is given as:

$$P(\chi_{st}) = \frac{1}{\chi_{st}\sigma\sqrt{2\pi}} \exp\left[-\frac{1}{2\sigma^2}\left(\ln\chi_{st} - \mu\right)^2\right] \tag{7.16}$$

where μ and σ are related to the mean value of χ with the following:

$$\tilde{\chi} = \exp\left(\mu + \frac{\sigma^2}{2}\right) \tag{7.17}$$

with $\tilde{\chi}$ obtained from

$$\tilde{\chi} = C_\chi \frac{\tilde{\varepsilon}}{\tilde{k}} \tilde{f}''^2 \tag{7.18}$$

and

$$\tilde{\chi}''^2 = \tilde{\chi}^2\left(\exp\sigma^2 - 1\right) \tag{7.19}$$

Here C_χ and σ have the value of 2.0 each. With the introduction of variable $\theta = \left(ln\chi_{st} - \mu\right)/\sqrt{2}\sigma$ the above integral for χ becomes:

$$\int_{\chi_{l-1/2}}^{\chi_{l+1/2}} P(\chi)d\chi = \frac{1}{\sqrt{\pi}}\int_{\theta_{l-1/2}}^{\theta_{l+1/2}} e^{-\theta^2} d\theta \tag{7.20}$$

where $\theta_{l\mp 1/2} = (\ln \chi_{l\mp 1/2} - \mu)\sqrt{2\sigma}$ (7.21)

Equation 7.20 can be further reduced to

$$\frac{1}{\sqrt{\pi}}\int e^{-\theta^2} d\theta = \frac{1}{2}\left[erf(\theta_{l+1/2}) - erf(\theta_{l-1/2})\right] \tag{7.22}$$

where *erf* denotes the error function and its argument is given by:

$$\theta_{l\mp 1/2} = \frac{1}{\sqrt{2}\sigma} ln\left(\frac{\chi_{l\mp 1/2}}{\tilde{\chi}}\right) - \frac{\sigma}{2\sqrt{2}} \tag{7.23}$$

In the set of flamelet profiles considered for the calculation, one of them corresponds to inert mixing which represents post-quenching state. In order to accurately account for contribution of the inert state, the integration range is divided into subranges in such a way that $\chi_{L-1/2} = \chi_{st,q}$ (flamelet at quenching limit) and $\chi_{L+1/2} = \chi_{\infty}$ (post quenching).

The final forms of the approximated equations for filtered density and Favre averaged (or filtered) scalars $\tilde{\phi}$ are given by:

$$\bar{\rho} = \left[\sum_{l=1}^{L}\frac{1}{2}\left[erf\left(\theta_{l+1/2}\right) - erf\left(\theta_{l-1/2}\right)\right]\int_0^1 \frac{\tilde{P}(f)}{\rho(f,\chi_l)} df\right]^{-1} \tag{7.24}$$

$$\tilde{\phi} = \sum_{l=1}^{L}\frac{1}{2}\left[erf\left(\theta_{l+1/2}\right) - erf\left(\theta_{l-1/2}\right)\right]\int_0^1 \phi(f,\chi_l)\tilde{P}(f) df \tag{7.25}$$

The chosen number of *L*=14 flamelets have been found to provide adequate accuracy and a reasonably good turn around time. The computational time for generation of 3D, 163x51x31 size look-up-tables for $\bar{\rho}, \tilde{T}$ and 6 species is kept to less than a day on a 2GB RAM Intel Pentium 4, 3GHZ processor. In LES, the tables are read as filtered scalar values (Example, filtered temperature) as a function of filtered mixture fraction, subgrid normalized variance and filtered scalar dissipation rate.

7.3 PDF Look-up Tables for NAFM

In the non-adiabatic flamelet model, NAFM, which has been developed for LES in the present work, the turbulent mean values of the thermo-chemical variables $\tilde{\phi}$ are dependant on $\tilde{f}, \widetilde{f''^2}, \tilde{\chi}$ and additionally on the enthalpy defect $\tilde{\zeta}$. Hence for turbulent flame calculations based on this model, 4D look-up-tables of the form given in Eq. (7.26) need to be generated for each mean reactive scalar $\tilde{\phi}$ (density, temperature and species mass fraction). In order to develop the pre-integrated tables, the in-house built code for SLFM was extended to incorporate the fourth dimension in the integration process and thus every scalar would be represented as

$$\tilde{\phi} = \tilde{\phi}\left(\tilde{f}, \widetilde{f''^2}, \tilde{\chi}, \tilde{\zeta}\right) \tag{7.26}$$

The Pre-PDF NAFM integration code takes the steady non-adiabatic flamelets as input and conducts numerical integration for each reactive scalar of interest for each cell in a 4D table. As part of the specification of table properties, the range and distribution of enthalpy defect $\tilde{\zeta}$ points needs to be specified in addition to those for $\tilde{f}$, $\widetilde{f''^2_{norm}}$ and $\tilde{\chi}$ which take the same definitions as with SLFM as discussed earlier For methane-hydrogen flame conditions like HM and SMH flames, a range of 0 (adiabatic) to -180 kJ/kg is specified for the mean enthalpy defect $\tilde{\zeta}$ and this span has been covered by 10 uniformly spaced values. Therefore, the size of look-up-table for HM1 and SMH1 flames for NAFM model based calculations are 163x51x31x10 ($\tilde{f}, \widetilde{f''^2_{norm}}, \tilde{\chi}, \tilde{\zeta}$) respectively. The equation for evaluation of mean scalars with NAFM model is given by:

$$\tilde{\phi} = \int_0^\infty \int_0^1 \int_{\zeta_{min}}^{\zeta_{max}} \phi(f;\chi_{st};\zeta)\tilde{P}(f)\tilde{P}(\chi_{st})\tilde{P}(\zeta)\,d\zeta\,df\,d\chi_{st} \tag{7.27}$$

Since the flamelet structures are now a function of enthalpy defect as well, a limited number of enthalpy defect shelves are considered for the integrations and within each shelf, a limited number of flamelets corresponding to fully burning and extinguished states are considered. For calculating tables for HM1 and SMH1 flames, a total of 10 enthalpy defect shelves are considered with the total number of non-adiabatic flamelets equal to 100.

The approximations made in generation of look-up tables with regard to the integrations with respect to f and χ_{st} are enforced here as well. In addition to the above two mentioned PDF's we require to perform $\tilde{P}(\zeta)$ and this is assumed to follow δ function. Therefore, the third integral with respect to enthalpy defect can be eliminated and the task of interpolation is thereby reduced by bringing down the overall computational effort. However, 4D integrations still demand a turn around time of approximately 10 times higher than that of time required for generating 3D look-up-tables for SLFM. The final equations for mean density and scalars take the form:

$$\bar{\rho} = \delta(\zeta - \tilde{\zeta}) \left[\sum_{l=1}^{L(\zeta)} \frac{1}{2} \left[erf(\theta_{l+1/2}) - erf(\theta_{l-1/2}) \right] \int_0^1 \frac{\tilde{P}(f)}{\rho(f, \chi_l, \zeta)} df \right]^{-1} \tag{7.28}$$

$$\tilde{\phi} = \delta(\zeta - \tilde{\zeta}) \left[\sum_{l=1}^{L(\zeta)} \frac{1}{2} \left[erf(\theta_{l+1/2}) - erf(\theta_{l-1/2}) \right] \int_0^1 \phi(f, \chi_l, \zeta) \tilde{P}(f) df \right] \tag{7.29}$$

The number of sub-ranges into which the integration range of the scalar dissipation rate is split, is now a function of enthalpy defect $L = L(\zeta)$. As previously discussed, extinction limit of a non-adiabatic flamelet decreases with the increase in enthalpy defect. Hence the range of χ_{st} for fully burning states reduces. This is exploited to gain computational efficiency by considering a lesser number of flamelets in higher enthalpy defect shelves. This four dimensional integrated look-up table for each of the scalars like temperature and major species are calculated and stored for LES calculations. Density variations are found to be very minimal with change in scalar dissipation rate as depicted in Fig. 7.1. Therefore, except density all other scalars are selected to perform the 4D integration. Density is assumed to depend on mixture fraction alone in this case and therefore depends on mean mixture fraction and its variance. Hence a single flamelet close to equilibrium is considered for the calculation of density with the beta PDF performed on mixture fraction alone.

Effect of truncated flamelets on mean scalars

As mentioned earlier in section 7.1.2, due to modified inlet conditions, the non-adiabatic flamelets are subjected to truncation in mixture fraction space. Hence the usual limits of f which vary from $f = 0$ to1, are truncated to $f = f_{oxid}$ to f_{fuel}, where f_{oxid}=

$f(\zeta) > 0$ and $f_{fuel} = f(\zeta) < 1$. For the non-adiabatic flamelets, integration for mean scalars is split according to Eq. 7.30 and the first and third parts are neglected.

$$\tilde{\phi} = \int_0^{\infty} \int_{f=0}^{f=f_{oxid}} \phi(f;\chi_{st};\zeta) P(f) P(\chi_{st}) df d\chi_{st} + \int_0^{\infty} \int_{f=f_{oxid}}^{f=f_{fuel}} \phi(f;\chi_{st};\zeta) P(f) P(\chi_{st}) df d\chi_{st} +$$

$$\int_0^{\infty} \int_{f=f_{fuel}}^{f=1} \phi(f;\chi_{st};\zeta) P(f) P(\chi_{st}) df\, d\chi_{st} \qquad (7.30)$$

For low enthalpy defects, f_{oxid} and f_{fuel} are close to 0 and 1 respectively and hence neglecting the contribution of first and last terms does not affect the accuracy of numerical integration. However, for higher enthalpy defects there is a concern that the first and last terms might have sizeable contribution and hence neglecting the terms might result in errors in the mean quantities viz. the mean temperature and major species. A detailed study was performed by Ravikanti *et al.* (2008) with this regard on the effect of truncation at both ends of the mixture fraction in high enthalpy defect regions. Based on the mixture fraction PDF distribution at higher enthalpy defect areas, which showed minimal effect on the PDF shapes in the truncated regions, it was concluded that truncation in the non-adiabatic flamelets is expected to have minimal or no impact on the integrated mean density and reactive scalars for the entire range of enthalpy defects encountered in the computed flame. With this confidence, NAFM is utilized for the coupling of radiation with turbulence in LES with the additional equation of enthalpy

7.4 PDF Look-up Tables for UFPV- δ Model

Development of UFPV model to lifted flame category was motivated from the flamelet progress variable (FPV) approach. FPV model was applied in the past for improvement in the predictions of temperature and major species. But this was used for the first time in the recent past for lifted flame burners by Ravikanti (2008). Unsteady effects are neglected in the FPV approach and therefore found not predicting the flame extinction and re-ignition in turbulent lifted flames. In order to include the unsteady behavior in the flamelet modelling, UFPV model was developed particularly for predicting the transient unstable behavior of the flame. The Pre-PDF UFPV δ generates 4D look-up-tables for mean values of each thermo-chemical variable of interest, parameterized by $\tilde{f}, \widetilde{f''^2_{norm}}, \tilde{\chi}$ and $\tilde{C}$.

The flamelets are parameterized by the mixture fraction *f,* flamelet parameter λ and the stoichiometric scalar dissipation rate χ_{st}. Since the flamelet solutions depend only on time, mixture fraction and stoichiometric scalar dissipation rate, the parameterization eliminates the time as a parameter by introducing the flamelet parameter λ. The flamelet solutions for all scalar quantities is given as

$$\phi = \phi\left(f, \lambda, \chi_{st}\right) \tag{7.31}$$

The evaluation of the filtered quantities is performed by the joint PDF of the three parameters $\tilde{P}(f, \lambda, \chi_{st})$. The filtered scalar values is given as

$$\tilde{\phi} = \int_{\lambda^-}^{\lambda^+} \int_{0}^{\lambda_{\max}} \int_{0}^{1} \phi\left(f, \lambda, \chi_{st}\right) \tilde{P}(f, \lambda, \chi_{st}) \; df \; d\lambda \; d\chi_{st} \tag{7.32}$$

The flamelet parameter is defined in such a way that it is independent of the mixture fraction as per the flamelet assumption discussed in the previous section. The stoichiometric scalar dissipation rate is defined in the similar fashion by the relation

$$\chi = \chi_{st} \psi\left(f\right) \tag{7.33}$$

Where $\psi\left(f\right)$ describes the mixture fraction dependence of the dissipation rate. The assumption in the Equation (7.33) describes the mixture fraction dependence of the dissipation rate which implies that χ_{st} is independent of the mixture fraction. Therefore, the joint PDF can then be written as

$$\tilde{P}(f, \lambda, \chi_{st}) = \tilde{P}\left(f\right) \tilde{P}\left(\lambda, \chi_{st}\right) \tag{7.34}$$

The marginal PDF of the mixture fraction can be defined by a beta function, which is defined from mean and variance of the mixture fraction. Research is intense for using beta function PDF for both flamelet parameter λ and stoichiometric scalar dissipation rate χ_{st} but the extra dimension in the look-up table increases the cost of the simulation. Therefore, both the above parameters are described by delta function PDF, Pitsch and Ihme (2005). The joint PDF is then shown as

$$\tilde{P}(f, \lambda, \chi_{st}) = \beta\left(f; \tilde{f}, \widetilde{f''^2}\right) \delta\left(\lambda - \lambda^*\right) \delta\left(\chi_{st} - \chi_{st}^*\right) \tag{7.35}$$

The values of λ^* and χ_{st}^* can be determined from the filtered quantities by the inversion of the integrals, Pitsch and Ihme (2005), as depicted below

$$\tilde{C} = \int_0^{\infty} \int_{\lambda^-}^{\lambda^+} \int_0^1 C(f, \lambda, \chi_{st}) \, \beta\left(f; \tilde{f}, \widetilde{f''^2}\right) \delta\left(\lambda - \lambda^*\right) \delta\left(\chi_{st} - \chi_{st}^*\right) df \, d\lambda \, d\chi_{st} \qquad (7.36)$$

and

$$\tilde{\chi} = \int_0^1 \chi_{st}^* \psi(f) \beta\left(f; \tilde{f}, \widetilde{f''^2}\right) \, df \qquad (7.37)$$

The filtered values namely $\tilde{f}, \tilde{C}, \widetilde{f''^2}$ and $\tilde{\chi}$ are known from the solution of the filtered transport equations and models for the variance and dissipation rate. The filtered values of the scalars are tabulated from the Equation (7.32) as a function of $\tilde{f}, \tilde{\lambda}, \widetilde{f''^2}$ and χ_{st}. These include the filtered values for the reaction progress variable $\tilde{C}$ and the scalar dissipation rate $\tilde{\chi}$. The value of λ is replaced $\tilde{C}$ through a proper re-mapping technique which is discussed later in the section and χ_{st} is replaced by $\tilde{\chi}$ so that the flamelet library provides the filtered scalars as function of $\tilde{f}, \tilde{C}, \widetilde{f''^2}$ and $\tilde{\chi}$ thereby completely eliminating flamelet parameter and stoichiometric scalar dissipation rate. The same constraint equation as discussed in equation 4.33 from Chapter 4 where the progress variable from the steady laminar flamelet equations is made equal to the value of progress variable obtained from its transport equation from the LES. Solving the inverse integrals to obtain the values as depicted in equations (7.36) and (7.37) is eliminated by re-interpolation technique or remapping methodology from λ space to *C* space. Similar to the above constraint equation for progress variable, scalar dissipation rate fluctuations are also constrained to the equation where the value of χ_{st} is made equal to the mean scalar dissipation rate from the equation (4.20) from Chapter 4. Therefore, we eliminate the task of inverse of the integrals and thus making the preprocessing task simple.

$$\chi_{st} = \tilde{\chi} \qquad (7.38)$$

The re-interpolated look-up tables include the scalar values as function of the quantities like $\tilde{f}$, $\widetilde{f''^2}$, $\tilde{C}$ and $\tilde{\chi}$ for the input to LES calculations. The variables like

the density, temperature and other species will be a function of the above mentioned quantities and thus,

$$\tilde{\rho} = \tilde{\rho}\left(\tilde{f}, \widetilde{f''^2}, \widetilde{C}, \tilde{\chi}\right), \tilde{T} = \tilde{T}\left(\tilde{f}, \widetilde{f''^2}, \widetilde{C}, \tilde{\chi}\right), \tilde{Y}_i = \tilde{Y}_i\left(\tilde{f}, \widetilde{f''^2}, \widetilde{C}, \tilde{\chi}\right) \text{ and } \tilde{\omega}_c = \tilde{\omega}_c\left(\tilde{f}, \widetilde{f''^2}, \widetilde{C}, \tilde{\chi}\right) \tag{7.39}$$

Re-mapping Strategy

The look-up table with the flamelet parameter needs to be converted to progress variable space. The mixture fraction is a conserved scalar normalized ranging from 0 to 1. But the variance of mixture fraction $\widetilde{f''^2}$ should be normalized before reading the flamelet library from the lookup tables. $\widetilde{f''^2}$ is normalized as

$$\widetilde{f''^2_{norm}} = \frac{\widetilde{f''^2}}{\tilde{f}\left(1-\tilde{f}\right)} \tag{7.40}$$

Here the parameter $\widetilde{f''^2_{norm}}$ is the normalized variance ranging from 0 to 1. The lookup table is an ordered matrix with the correct distribution of the variables like $\widetilde{f}$, $\widetilde{f''^2_{norm}}$, $\widetilde{C}$ and $\tilde{\chi}$ as 163x51x151x49. The mean scalar dissipation rate $\tilde{\chi}$ is ranging from equilibrium limit to above quenching limit covering the entire solution space as discussed earlier from the inverted S-shaped curve. The distribution of the mixture fraction in the table is kept in the same pattern as of first flamelet near to equilibrium ranging from 0 to 1. The points along the normalised mixture fraction variance and mean scalar dissipation rate axes of the look-up-table are distributed using power-law fit.

$$\Psi(i) = exp(-a)(i-1)^b \tag{7.41}$$

The values of *a* and *b* are varied for the two variables to have a uniform distribution. Scalar dissipation rate have a distribution that ranges from 0.1 to 3999.0 covering all the flamelets from equilibrium to quenching. The distribution of flamelet parameter λ in the initial lookup table is considered equal to the C_{max} values of the flamelets for each scalar dissipation rate. For every χ_{st} there are the flamelets varying along the time (all the vertical dots from Fig. 4.2) are normalized from 0 to 1. Therefore, for

every χ_{st} the range of λ varies from 0 to 1. Similarly the range of mean progress variable $\tilde{C}$ is normalized to range from 0 to 1. The lookup table consists of a power law distribution for the variable $\tilde{C}$ as shown in equation 4.89. Thus the size of the final 4D look-up-table is 163x51x151x49 ($\tilde{f}, \widetilde{f''^2_{norm}}, \tilde{C}_{norm}, \tilde{\chi}$). The task of re-mapping makes the next step to build up the final lookup table.

In order to implement the re-mapping methodology from λ space to $\tilde{C}$ space the first step and assumption is to use the constraint equation for progress variable (equation 4.33, Chapter 4) where $\tilde{C}_{slfe}$ is normalized to get the values from 0 to 1 as $\tilde{C}_{norm}$. Therefore, the equation becomes as

$$\tilde{C}_{slfe} = \tilde{C}_{norm} \tag{7.42}$$

The next step in the re-mapping procedure is to interpolate the values of the variables from λ space to $\tilde{C}_{norm}$ space. For every $\tilde{C}_{norm}$, the corresponding value of $\tilde{\lambda}$ is obtained by interpolating the extracted data for $\tilde{C}_{slfe}$. Using the interpolated value of $\tilde{\lambda}$, corresponding values of each scalar is obtained by interpolating its extracted data. The variables like density, temperature and progress variable source term are produced from the re-mapping technique for the present LES calculation. Therefore, the set of data from equation (7.39) leads to

$$\tilde{\rho} = \tilde{\rho}\left(\tilde{f}, \widetilde{f''^2}, \widetilde{C_{norm}}, \tilde{\chi}\right)$$

$$\tilde{T} = \tilde{T}\left(\tilde{f}, \widetilde{f''^2}, \widetilde{C_{norm}}, \tilde{\chi}\right)$$

$$\tilde{Y}_i = \tilde{Y}_i\left(\tilde{f}, \widetilde{f''^2}, \widetilde{C_{norm}}, \tilde{\chi}\right)$$

$$\tilde{\dot{\omega}}_c = \tilde{\dot{\omega}}_c\left(\tilde{f}, \widetilde{f''^2}, \widetilde{C_{norm}}, \tilde{\chi}\right) \tag{7.43}$$

During the LES calculations, the variables are read from the lookup table for every time step. Density and progress variable source term $\tilde{\dot{\omega}}_c$ are read for all inner iterations in order to solve for the transport equation for progress variable from the

lookup table. This makes the computational time to increase but the solution occupies all the flamelets in order to capture the re-ignition and extinction phenomena.

7.5 Closure

This chapter dealt with the pre-processing manipulations for the generation of look-up tables that were required for various combustion models like SLFM, NAFM and UFPV. It dealt with the flamelet generation for steady adiabatic and non-adiabatic conditions based on enthalpy defect concept. It also discussed the procedure for unsteady adiabatic flamelet generation and theory behind for the UFPV combustion model. A detail description on the integration process for each combustion model is also presented.

Chapter 8

Modelling of Turbulent Non-premixed Bluff Body and Swirl Stabilized Flames

Turbulent non-premixed flames are targeted for the validation of the present combustion models SLFM and NAFM. Sydney experimental series on bluff body and swirl stabilized flames are selected for the computational code validation as the data existing with these flames present themselves an ideal model problems for studies on turbulence-chemistry interaction with the complexity of the flow characteristics found very close to that of practical combustors while maintaining the geometry very simple and providing well defined boundary conditions. The simplicity of the burner configuration with its simple geometric features makes it advantageous for modelling using the in-house LES code and suitable for testing NAFM for the effect of radiation coupled with turbulent flows. Fuel is based on the simplest of hydrocarbons thereby making modelling studies beneficial from the available chemical mechanisms. The experimental data is available for flow, mixing field and compositional structure including the pollutant NO and therefore facilitating a comprehensive validation of the present combustion models.

In the present chapter, a comprehensive study on the bluff body flames known as HM1, HM1e and HM3e are performed with SLFM. HM1 and HM1e flames resemble similar in many contexts. Table 8.1 shows the differences in these flames. Similarly, swirl stabilized flames known as SMH1 is tested for SLFM capabilities on the complex swirling flames. The radiating features of HM1 and SMH1 flames demand a detailed study for non-adiabatic flamelet combustion model. Therefore, NAFM calculations on coupled LES-Radiation cases are tested for HM1 and SMH1 flames. The two chemical mechanisms namely GRI 2.11 and GRI 3.0 are tested for their capability to predict the flame conditions of HM1 and SMH1. Effect of radiation on turbulence-chemistry for these two flames is tested by comparing the results involving

without radiation calculations. On the other end, HM3e flame which has the most complex flame structure in terms of extinction is tested with SLFM. It is to be noted that SLFM cases are involved with multiple flamelets solutions which are integrated in the form of look-up tables. This chapter for the sake of simplicity is divided into two sections. First section of results deal with SLFM and NAFM comparisons for bluff body flames HM1 followed by SLFM applied to HM3e flame. Second section of the chapter consists of SLFM and NAFM comparisons for swirl stabilized flame SMH1. A complete study on radiation coupled turbulence-combustion calculations are presented for both HM1 and SMH1 flames in their respective results.

8.1 Experimental Details of Bluff-body Stabilized Flames

The bluff-body burner used for experimental investigation of the flames by Dally *et al*. (1998a; 2003) has an outer diameter, D_B , of 50 mm and a concentric jet diameter D_J of 3.6mm. A wind tunnel with an exit cross section of 254 x 254 mm encloses the burner till the burner exit. Figure 8.1 shows schematic diagram of the bluff-body flame along with measurement locations. The distance of these locations from exit of the burner is normalized by bluff-body diameter D_B. Single point Raman/Rayleigh/LIF technique has been used by Dally *et al*. (1998a) to measure temperature and the concentration of stable species CO_2, CO, H_2O, H_2, O_2, N_2 as well as concentration of OH and NO.

With the intension for improving predictions using SLFM with LES, the present case study is conducted for bluff body flames. HM1 and HM1e flames were observed to be far away from blow off limits and therefore SLFM combustion model can be applied with confidence. However, SLFM is tested for its predicting capabilities when applied to HM3e flame because this flame is considered to involve high blow off limits. But with the view to investigate the failure with HM3e flame based on SLFM calculations, a multiple flamelet look up table is generated with flamelet solutions from fully burning branch and extinguished state and tested for capability issues related to SLFM for high blow off conditions. Both the flames, HM1 and HM3e are considered with density variation dependence on mixture fraction alone as per the discussion in chapter 7 where the density variations are very negligible with respect to

HM and SMH flames (section 7.1.1). The fuel used in these flames is a mixture of 50% of CH_4 and 50% of H_2 by volume. Table 8.1 shows the experimental conditions for these two flames.

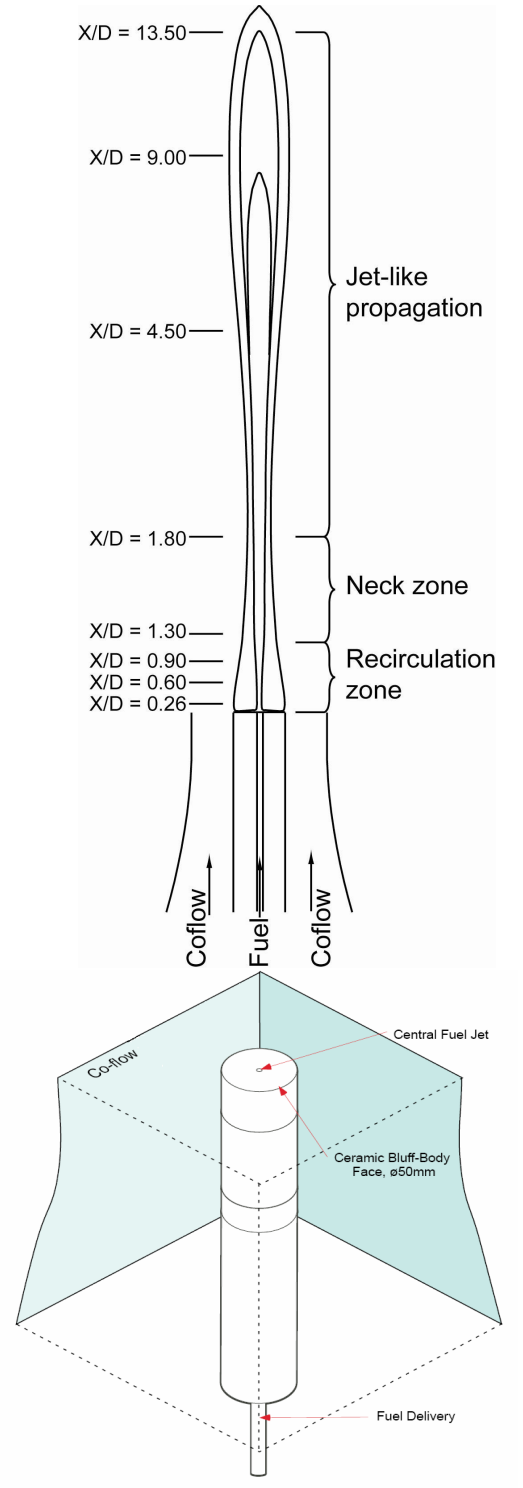

Figure 8.1: Schematic of bluff-body burner with measurement locations.
(Courtesy: www.aeromech.usyd.edu.au/thermofluids)

Table 8.1 Details of bluff body flames under study and their conditions

Fuel	Flame	U_j(m/s) / U_c(m/s)	Re_j	%Blow off	T_{in}(K)	f_{st}	T_{ad}(K)
CH_4/H_2 (1:1)	HM1	118/40	15800	50	298	0.05	2265
	HM1e	108/35	14461	50			
	HM3e	195/35	26110	90			

Experimental errors associated with mixture fraction was found to vary from 2.3 % to 5.7% (http://www.aeromech.usyd.edu.au/thermofluids/main_frame.htm).

The structure of a jet dominant bluff-body stabilized flame is shown in Fig. 8.1. It is characterized by three distinct zones. The first zone consists of recirculation created by flow separation due to presence of bluff body. This recirculation zone facilitates stabilization of the flame as the hot products of combustion are made to mix with the reactants. This zone has an outer vortex close to the co-flow air and inner vortex (not shown in the figure) close to central fuel jet. Position of inner vortex is dependent upon the fuel jet velocity. It shifts downstream on increasing the velocity and at sufficiently high velocities it becomes part of the jet. Also, the outer vortex becomes shorter and smaller. Downstream of the recirculation zone is the region of intense mixing where local extinction and blow-off could occur when the fuel jet velocity is increased. This is termed as neck zone and is a region of particular importance for testing a combustion model for its accuracy in predicting extreme non-equilibrium effects like local extinction. The third zone behaves like a jet and at sufficiently high velocities shows re-ignition.

8.2 LES Modelling of HM1 & HM3e Flames

Bluff body flames were studied in the past by various researchers using RANS and LES. Dally *et al.* (1998b) conducted numerical investigation of these flames to arrive at a modified k-ε model and Reynolds stress model which predict the spreading rate of the jet better than the standard models. Li *et al.* (2003) tested Reynolds stress model based turbulence closure on HM1e flame with different pressure-strain models. However, the above researchers concentrated on the improvement in turbulence models rather than on combustion modelling aspects. Apart from these research

findings there were researchers who developed combustion modelling like Liu *et al.* (2005) who employed the Joint PDF model with augmented reduced mechanism for the bluff-body flames with varying blow-off limits and found good agreement with experimental data for the flame far from extinction. In a different case study, Kuan and Lindstedt (2005) used a transported PDF approach closed at the joint scalar level for the bluff body stabilized turbulent diffusion flames HM1. Merci *et al.* (2006) studied the comparison of different micro-mixing models in scalar PDF simulations for bluff body flames HM1, HM1e and HM3e. A qualitative distinctive behavior was observed with these mixing models and quantitative comparison was performed with experiments. In their study, HM3 flame was showing large discrepancies in temperature and species predictions. Turbulence calculations were made with Reynolds stress model. Therefore, in order to judge the SLFM model predicting capabilities on HM3e, the present work attempts to simulate this highly fluctuating flame which has the maximum blow off criteria.

Although RANS based simulations have been carried out in the past, the present day computational power encourages carrying out LES based calculations and therefore forms the prime target for SLFM studies on bluff body stabilized flames. Apart from RANS based calculations, recently Kempf *et al.* (2006) have studied the performance of flamelet modelling approach on bluff body jet flames namely HM1 and HM1e using LES. The present study is closely related to the above work with the incorporation of multiple flamelets in the SLFM strategy and applied to HM1 and HM3e flames. Kempf *et al.* (2006) showed deviations in temperature and species predictions to some extent and significant errors in computed NO concentrations with their SLFM studies. However, the present work deals only with temperature and major species predictions like CO_2 and H_2O. Prior to this Raman and Pitsch (2005) used recursive filter refinement procedure for modelling bluff body flames using LES. Excellent results were reported with temperature and all other species predictions. Improved boundary conditions (co-flow boundary conditions) were specified to be sensitive on the LES technique used in their studies. However, OH predictions were showing significant differences from the experimental data. Based on the above research findings with SLFM based LES studies, an attempt is performed to refine the grid and utilize the SLFM with multiple flamelets to both medium and high blow-off conditions for the existing bluff body flames HM1 and HM3e. Kim and Huh (2002)

conducted the CMC model study of bluff body methane hydrogen diffusion flames with different chemical mechanisms and suggested that GRI 2.11 proved to be predicting well. Therefore, a comprehensive study on the effect of chemical mechanisms is studied in the present work using LES applied to both bluff body and swirl stabilized flames.

Parallel to SLFM studies, coupled calculations of radiation with turbulence using NAFM concepts were performed on HM1 flame. RANS based calculations using enthalpy defect concept for NAFM was studied in the past by Hossain *et al.* (2001) and later extended by Ravikanti (2008) with Reynolds stress model. Hossain *et al.* (2001) used single flamelet for every enthalpy defect shelf in their manipulation for library where as Ravikanti (2008) attempted to include multiple flamelets in each of the enthalpy defect shelf ranging from equilibrium to extinction. Both the above studies were found to predict minimum effect from radiation calculations tested on bluff body flames, HM1. Both the calculations were performed on RANS based studies. Present LES coupled radiation study is the first in its kind for application to flames like HM1 and SMH1 using the non-adiabatic combustion model, NAFM.

8.2.1Computational Details and Boundary Conditions

All the bluff body flame simulations in the current work include a computational domain of dimensions equal to 200 x 200 x 250 (all dimensions are in mm). The axial distance of approximately 70 jet diameters and the burner width of approximately 55 jet diameters is used in order to account the independency of flow entrainment from the surroundings. Wall boundary conditions are defined at the co-flow boundaries. The distance from the central jet is maintained at a sufficient distance in order to have negligible effect from flow entrainment from the surroundings. A detailed study on the location of the walls is performed on this type of flames and found that the flow entrainment has minimal effect at a distance of 100mm away from the central jet location. Therefore, the wall boundary conditions remain the same for simulations involving bluff body and swirl stabilized flames. However, free entrainment boundaries would be ideal for these kind of flame situations which can be implemented in the future research work. An inlet jet velocity profile is specified with a $1/7^{th}$ power law profile. Convective outlet boundary condition is used at the outlet

surface and all the walls and co-flow boundaries in the domain have been treated as adiabatic. No-slip boundary condition is used in the near wall flow using log-law wall functions.

The validation of the combustion model is performed by comparison of radial plots at different axial locations (normalized by bluff body diameter) for temperature and all other species mass fractions i.e., at z/D = 0.26, 0.6, 0.9, 1.3, 1.8 and 2.4. The results are discussed in detail later in this chapter. The average time to run the simulation on a 4GHz machine with single processor for each case with flames HM1 and HM3e takes around 20 days for HM1 and 35 days for HM3e for the flow to stabilize (t=30 ms) and thereafter 14 days (HM1) and 25 days (HM3e) for the collection of statistics (t=20ms) for post processing. An overall 50ms is run for each simulation for the two cases.

8.2.2Computational Grid

A Cartesian staggered non-uniform grid distribution of 100 x 100 x 120 in the X, Y and Z directions to discretize the domain has been used to optimize the simulation time. A detailed grid independence test was carried out by Ranga-Dinesh (2006) on a similar flame conditions and concluded that one million grid points as the optimum grid resolution. The computational geometry and grid details are depicted in the Fig 8.2. The radial grid distribution is maintained fine at the central jet region and gradually made coarser towards the wall boundaries. Similarly in the axial direction, uniform grid distribution is obtained in order to have sufficient grid points in both the central region of the flame and above the bluff body regions. Thus, it is ensured that the flame stabilization region where steep gradients in the flame are expected is well resolved.

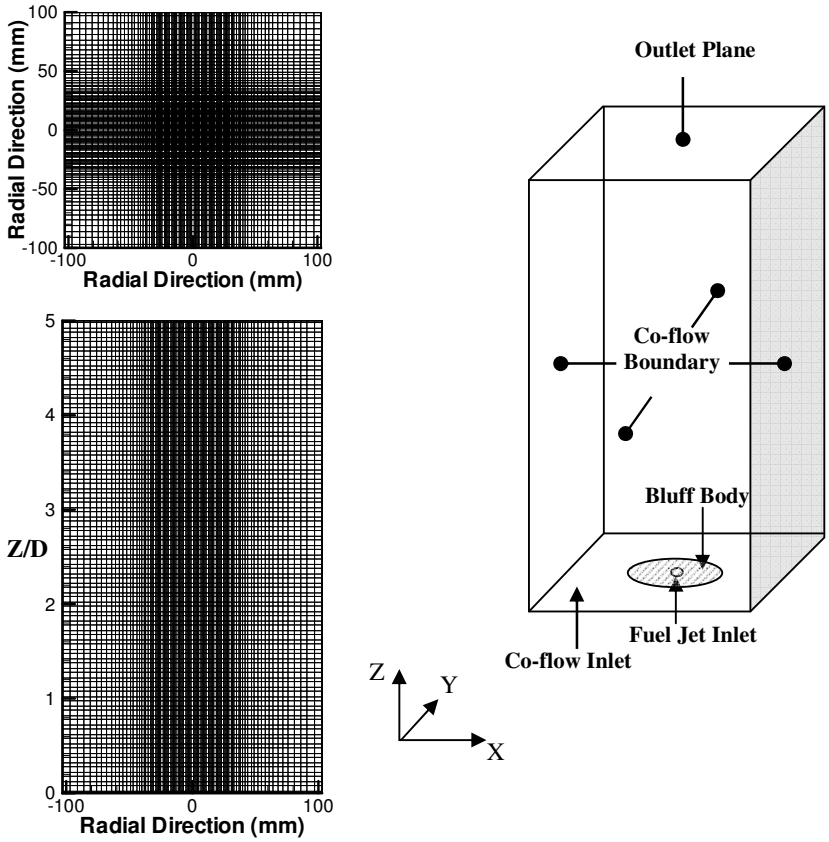

Figure 8.2 Details of computational grid and domain with boundary conditions specified.

8.3 Results and Discussion

Simulations of HM1 and HM3e flames have been conducted primarily to validate the accuracy with which flow field is predicted by SLFM when used in conjunction with LES. This section describes the results from both HM1 and HM3e flames. Initially the flow predictions for both the flames are compared using vector plots. Later the mixing and temperature predictions from HM1 flame are discussed followed by HM3e flame. Effect of chemical mechanism used is also discussed for HM1 flame alone. Finally, effect of inclusion of radiation and its comparison with LES without radiation is presented. Without radiation case means implementation of the SLFM combustion model alone (adiabatic conditions) for HM1 flame. Coupled radiation simulation using NAFM is performed only for HM1 flame due to computational time constraints. However, NAFM was successfully applied to swirl based SMH1 flame for the importance of radiation effects on turbulent swirling flows and discussed later in the chapter.

8.3.1Flow Field and Mixing Predictions

Figure 8.3 shows the streamlines of axial velocity imposed on averaged temperature contours near the bluff body. Firstly the different reaction regions of the system are identified. It can be clearly seen that there are two counter rotating vortices in the recirculation region. This double vortex comprises of an inner vortex close to the fuel jet and an outer vortex between the inner vortex and co-flow air. The main reaction zone where the preheated and partially reacted fuel and oxidizer meet which is located at the end of two vortices. These vortices transfer enthalpy from the primary reaction zone to the incoming fuel jet and the co-flow. The vortex structures result in three distinguishable shear layers. The inner shear layer is a manifestation of the contact between the high velocity fuel jet and the recirculating inner flow of inner vortex. Middle shear layer which occurs between the inner portion of the flow in the outer vortex and outer portion of flow in the inner vortex. The outer shear layer is found to occur between the co-flow stream and the outer part of outer vortex. The low stoichiometric mixture fraction of the fuel mixture helps to establish a thin reaction zone in the outer shear layer. The inner vortex is characterised by mixture fractions higher than the stoichiometric compositions and hence lead to lower temperatures and reaction rates. The large density gradient in the outer shear layer leads to some amount of vortex shedding.

As mentioned earlier, simulations were performed initially on the three different flames HM1, HM1e and HM3e. HM1 and HM1e resemble the same in many contexts and therefore only HM1 flame is considered for discussions in further sections. The above argument of three distinct zones in the flame applies for all the three different flames but it is noteworthy for the clear distinction between HM1 and HM3e flames with the inner vortex being destroyed in HM3e flame due to higher inlet fuel jet velocity leading to weak middle shear layer. The outer vortex gets stronger in intensity for the HM3e flame and therefore traps more air from the co-flow region and unburned gases to produce higher temperatures above the bluff body in the recirculation region.

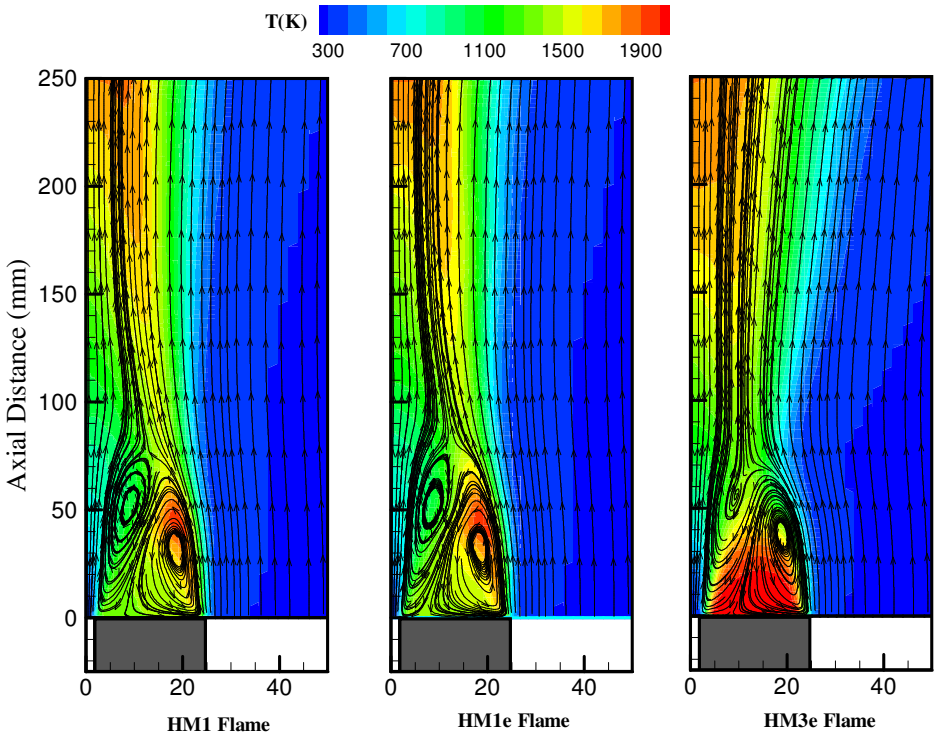

Figure 8.3: Streamlines of time averaged velocity fields from the simulation with temperature contours behind.

The comparisons for radial profiles of mixture fraction obtained from measurements and predictions are presented in Fig. 8.4. Predictions are obtained from SLFM based combustion simulations using LES for turbulence closure. Predictions show good agreement with data for the first two axial locations which fall within the recirculation zone. In the neck zone (z/D =0.9, 1.3) and jet-like flow region (z/D $\geq$ 1.8) the centerline mixture fraction is considerably under-predicted due to the over-prediction of decay rate of mixture fraction. However, the model captures the mixture fraction distribution in the neck region with much higher accuracy as we go along the radial direction. In the jet region, predictions are found to get improved with measurements. However, the discrepancy in the under-prediction at most of the downstream locations may be due to insufficient grid resolution and definition of boundary conditions. As specified by Raman and Pitsch (2005) about the improvement in mixing predictions with improved boundary conditions and higher grid resolution in the centerline region all along the downstream of the flame, it is recommended to implement the same in future. However, considering the computational cost and time restrictions, the present

predictions are found to be far better in agreement with the data when compared with the RANS calculations of Ravikanti (2008) with Reynolds stress model as turbulence closure.

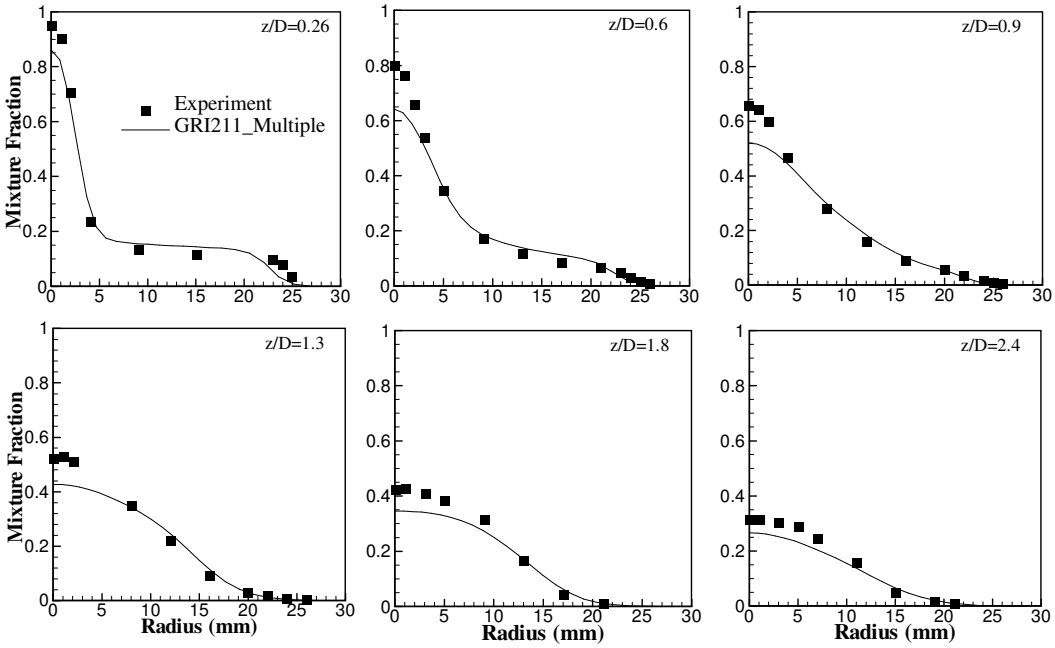

Figure 8.4 Radial profiles of mean mixture fraction at various axial lengths of HM1 flame. Predictions obtained from LES calculations with SLFM involving GRI 2.11 mechanism.

8.3.2Temperature and Major Species Predictions – HM1 Flame

The radial profiles of mean temperature at various axial locations along the flame are shown in Fig. 8.5. Numerically, the temperature profile shows a peak near the outer shear layer (between the radius ~ 20 to 25mm) at z/D=0.26. Even though the mean mixture fraction is predicted with reasonable accuracy, temperature profile indicates enhanced reactions at the interface of the recirculation and co-flow zones. This could indicate that the flamelet assumptions are not strictly valid in this zone. Centerline predictions are found to be in accurate match with experiments. At all the locations except z/D=0.26, temperature predictions are well captured with SLFM. The significant difference in the mean temperature in the radial direction may be due to possible deviation from flamelet regime. Predictions with both single and multiple flamelets are tested for this flame. At the locations z/D = {0.26 to 1.3} multiple

flamelets are better predicted compared to single flamelet solution. Inclusion of scalar dissipation rate with multiple flamelet solution proved to be advantageous.

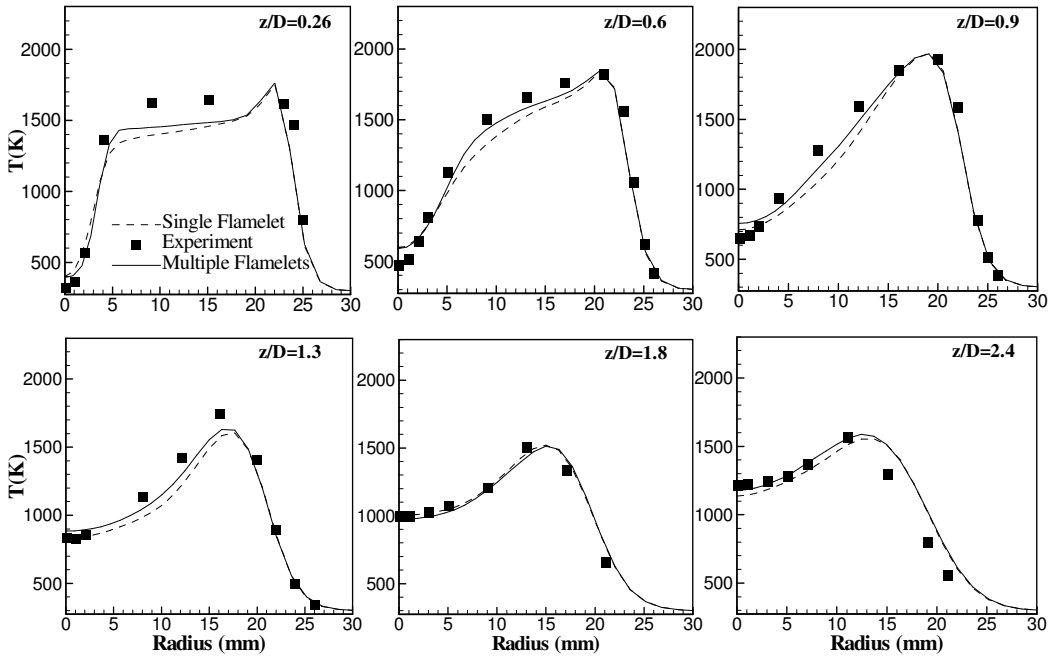

Figure 8.5: Radial profiles of mean temperature at various axial lengths of HM1 flame. Predictions obtained from LES calculations with SLFM.

Emission predictions such as mean mass fraction of CO_2 and H_2O are compared with experiments as depicted in Fig. 8.6.and 8.7 respectively. Mass fraction of CO_2 in general will follow temperature profile variations. However, with the SLFM, in the present HM1 case it is found to have large under prediction in the first two axial locations z/D = {0.26, 0.6}. Flamelet assumptions may not be strictly valid for CO_2 predictions in the region just above the bluff body (at the axial locations z/D=0.26 and z/D=0.6). Grid refinement in this region and advanced co-flow boundary conditions would be one of the options for improvement in CO_2 predictions. However, based on the present results, it is implied that large variations in CO_2 mass fractions just above the bluff body has extreme sensitivity to local sub-filter models. In the midst of this discrepancy the centerline values of the species CO_2 is very well captured. At the remaining locations the present combustion model predicts extremely well with the experiments. It is to be noted that flamelet solution with multiple flamelets performs well when compared with single flamelet solution. There is a significant difference between the two numerical solutions. The multiple flamelet solution with the

inclusion of scalar dissipation rate variations results in better predictions. This difference can be seen clearly at all the axial locations between radii equal to 0 to 20mm. In the region of co-flow, both numerical solutions are found to predict the same. This gives an indication that inclusion of scalar dissipation fluctuations through multiple flamelet solution has a definite influence in the highly turbulent recirculation region above bluff body specific to species mass fraction predictions.

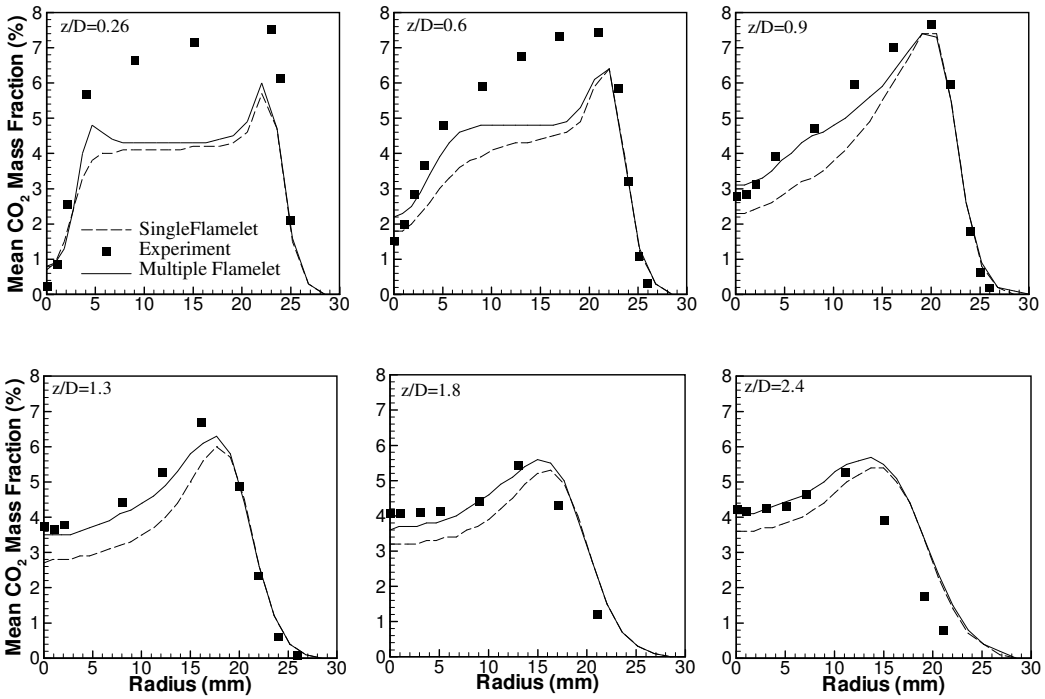

Figure 8.6: Radial profiles of mean mass fraction of CO_2 at various axial lengths of HM1 flame. Predictions obtained from LES calculations with SLFM.

A similar result close to temperature is predicted with H_2O mass fraction along the burner as depicted in Fig. 8.7. The under-prediction at the initial location z/D=0.26 as seen from temperature and CO_2 mass fraction predictions continues with H_2O mass fraction as well. Multiple flamelet solution for SLFM proved to be beneficial for the H_2O mass fraction predictions at most of the locations. However, the centerline values are better captured with single flamelet solution. Overall, SLFM with multiple flamelet solution is found to be the more suitable a combustion model with LES for HM1 flame as per the present conditions.

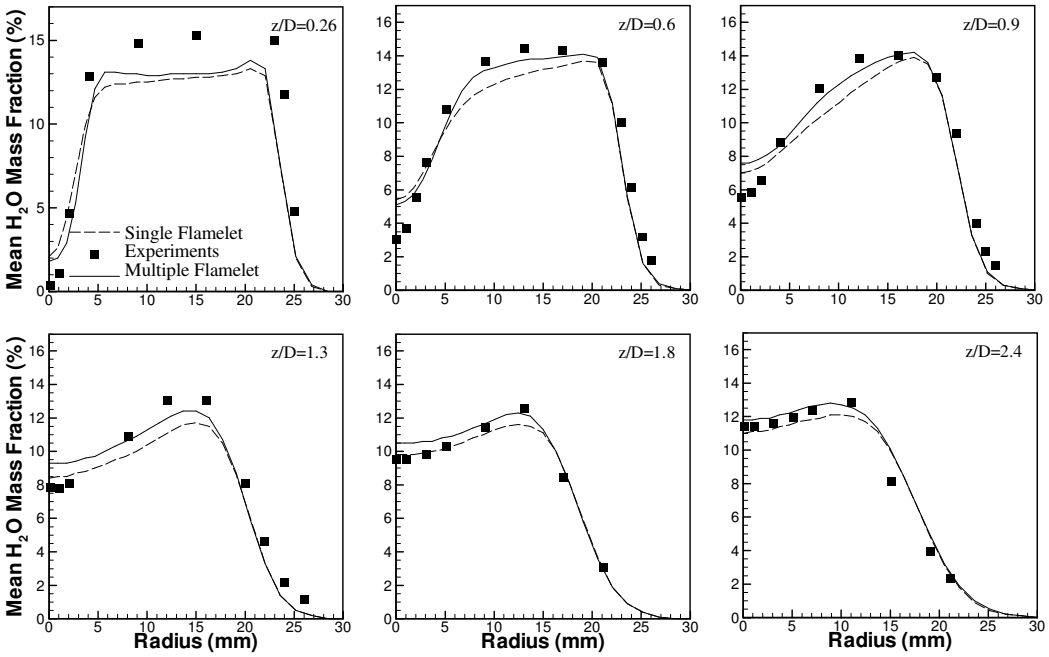

Figure 8.7: Radial profiles of mean mass fraction of H_2O at various axial lengths of HM1 flame. Predictions obtained from LES calculations with SLFM.

8.3.3Mixing, Temperature and Major Species Predictions – HM3e Flame

SLFM based combustion model is considered to be tested for its highest accuracy in predicting the capabilities for flame physics with the strongest turbulence-chemistry interaction involved with the well known Sydney flame series database. This present section attempts towards the predicting capabilities of SLFM for HM3e flame. This particular flame evolves toward global extinction and re-ignition in a limit cyclic process. This particular flame is tested with both single and multiple flamelet solution involved in combustion chemistry calculations. HM3e flame was of particular interest in the recent past because of its high blow off limits and found to be only partly successful with various combustion models involved (Merci *et al.,* 2006). But with the refined grid in the high shear region of the flame and present boundary conditions, SLFM combustion model is tested for HM3e for its extinction and re-ignition characteristics. This section of results highlights the mixing, temperature and species predictions at different axial locations along the flame. Figure 8.8 shows the mixture fraction profiles at various z/D locations. It is found that the centerline predictions in mixing are under-predicted by significant values. However, these predictions show a

good agreement along the radial direction after radius equal to 5mm. At the downstream locations z/D = {1.8, 2.4} numerical predictions crossover the experiments and suggests that SLFM is unable to reproduce the large fluctuations in the flame region at these locations where the flame tries to extinguish and re-ignite in cyclic operations. Scattered data should represent the flame extinction and re-ignition to most extent and therefore discussed later in this section for its flame diagnostics.

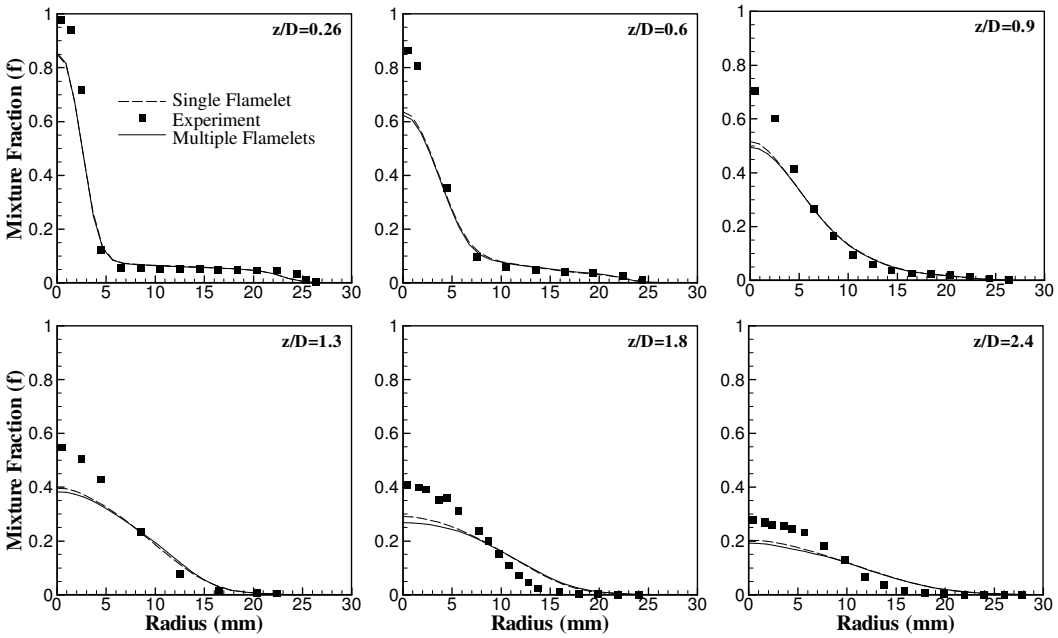

Figure 8.8 Radial profiles of mean mixture fraction at various axial lengths of HM3e flame. Predictions obtained from LES calculations with SLFM involving GRI 2.11 mechanism.

Any under-prediction in mixture fraction should reflect in over-prediction in temperature and therefore corresponding variations in species predictions. In the present simulation of HM3e, mixture fraction predictions are reasonably matched with experimental data at locations except in the last two locations. From Fig. 8.9 it can be seen that centreline values for temperature over-predict which is because of the marginal under-prediction in mixture fraction at these locations. Whereas at the remaining radial distances at the axial stations (z/D=0.26 to 1.3), temperature calculated numerically matches very well with experiments. Temperature at the last two locations (z/D=1.8, 2.4) is found to be over-predicting but observed to follow the trend with the experiments. Over-prediction in temperature at these two axial

locations is due to under-predicting nature of mixture fraction. Similar to HM1 flame, both single and multiple flamelet solution is utilized for combustion calculations for HM3e flame. Multiple flamelet solution is found to be advantageous for the bluff body flame predictions. At all the initial three locations (z/D=0.26 to 0.9) multiple flamelet lookup table strategy predicted well for temperature replication through numerical code. At the last two locations, single flamelet data resembles close to experiments. But however, based on the mixing patterns at these locations, we can depend only to a minimum for the predicting capability of SLFM under such highly fluctuating flame regions.

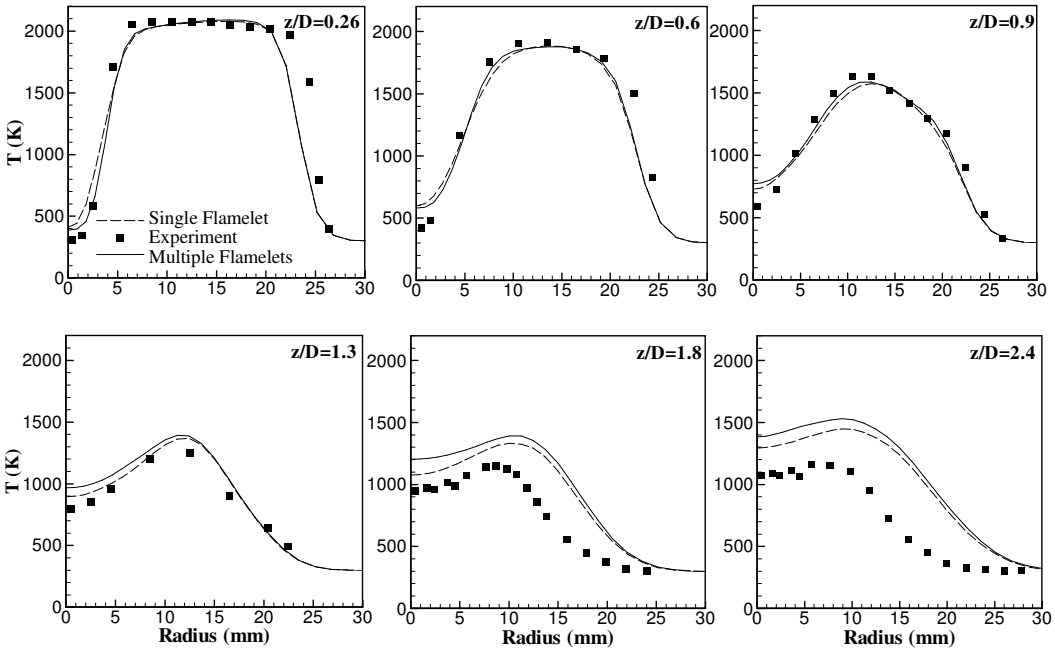

Figure 8.9: Radial profiles of mean temperature at various axial lengths of HM3e flame. Predictions obtained from LES calculations with SLFM.

Major product species CO_2 and H_2O can be expected to follow a similar trend like temperature in this regard. Figure 8.10 and 8.11 shows the CO_2 and H_2O mass fraction profiles at specified axial locations respectively. Both these species show an over-prediction in centerline values in their respective mass fractions. This is due to the above discussed reasons where mixture fraction under-predicts. At the axial locations z/D=0.26 to 1.3, at a radial distance from 5mm to outward direction, SLFM agrees well with the experiments similar to the statements that we prescribed for temperature

predictions. Last two axial locations are found to be problematic with species calculations as well.

But considering the accuracy of SLFM in reproducing the flame properties for HM1 and HM3e, it can be concluded that even though SLFM fails to predict to some degree with highly fluctuating flames as HM3e particularly in downstream regions of the flame, it can be used with confidence for bluff body flames. Mass fraction of CO is found to be over-predicting by huge margin with multiple flamelet solution in the combustion calculations at the last three axial locations (z/D=1.3 to 2.4) in Fig. 8.12. At these locations, single flamelet solution is found to predict closer to experimental data. But at the initial three axial locations (z/D=0.26 to 0.9) multiple flamelet solution proves to be beneficial. The centreline CO mass fraction values seem to over-predict at all the axial locations irrespective of the flamelet solution used. However, at the locations z/D = 0.6 and 1.3, multiple flamelets through lookup table strategy for SLFM predicts better when compared to single flamelet solution. While at location z/D=0.26 single flamelet solution for SLFM agrees well with experiments. SLFM with multiple flamelets again proved to be beneficial for species predictions but only at the axial locations in the upstream region of the flame.

Recently Liu *et al.* (2005) performed studies on bluff body flames with joint PDF model and HM3 was one of the flames in their research. A similar discrepancy was observed at the last two axial locations z/D = 1.8 and 2.4 in their calculations as well. When compared to their studies, the present SLFM combustion model predicts better and close to the experiments at most of the axial locations with regard to all scalars. However, the computations at last two axial locations seem to be in contradiction with the experiments for both the combustion models. Flame extinction and re-ignition properties are represented with respect to scattered data of temperature with mixture fraction at various axial locations along the burner. Experimental data collected at the same z/D locations are depicted in Fig. 8.13. At the initial three locations z/D=0.26 to 0.9, flame temperatures remain close towards the equilibrium. But at the last three axial locations (z/D=1.3 to 2.4) downstream of the burner, the flame temperature is found to fluctuate with extinction and re-attaching features which resulted in scattered temperature data all along from equilibrium to mixing limits.

Predicting scattered data through numerical code for close agreement with experimental data is a challenging task for any combustion model. Scattered data is used for the representation of flame extinction and re-ignition characteristics. Fig. 8.14 shows the scattered data computed numerically at different axial locations. The data is collected for a time of 10ms with collection interval of scattered values for every 0.2ms. At axial location z/D=0.26, the scattered data computed numerically shows distribution of data covering the entire solution space from mixing to equilibrium. But at this location, experiments show more towards the equilibrium values. At locations z/D=0.6 and 0.9, the data points are found near to equilibrium limits in good agreement with the experimental scattered data. The limits of temperature and mixture fraction are also well predicted with the numerical simulation at almost all the locations. At the last three axial locations, computational results show most of the data towards equilibrium whereas experimental data (Fig. 8.13) shows most of the data in between mixing and equilibrium limits. However, considering the past research failures with the studies involving HM3e flame, improvisation of the present SLFM combustion model with multiple flamelets proved to be beneficial and predicting well for flames involving with high blow off limits.

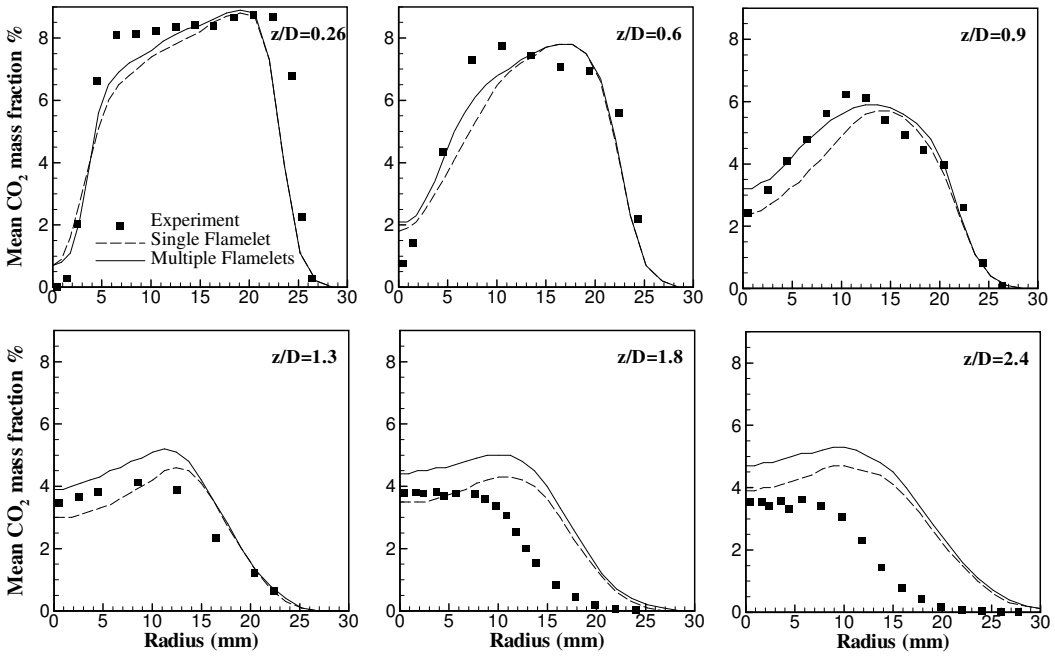

Figure 8.10: Radial profiles of mean mass fraction of CO_2 at various axial lengths of HM3e flame. Predictions obtained from LES calculations with SLFM.

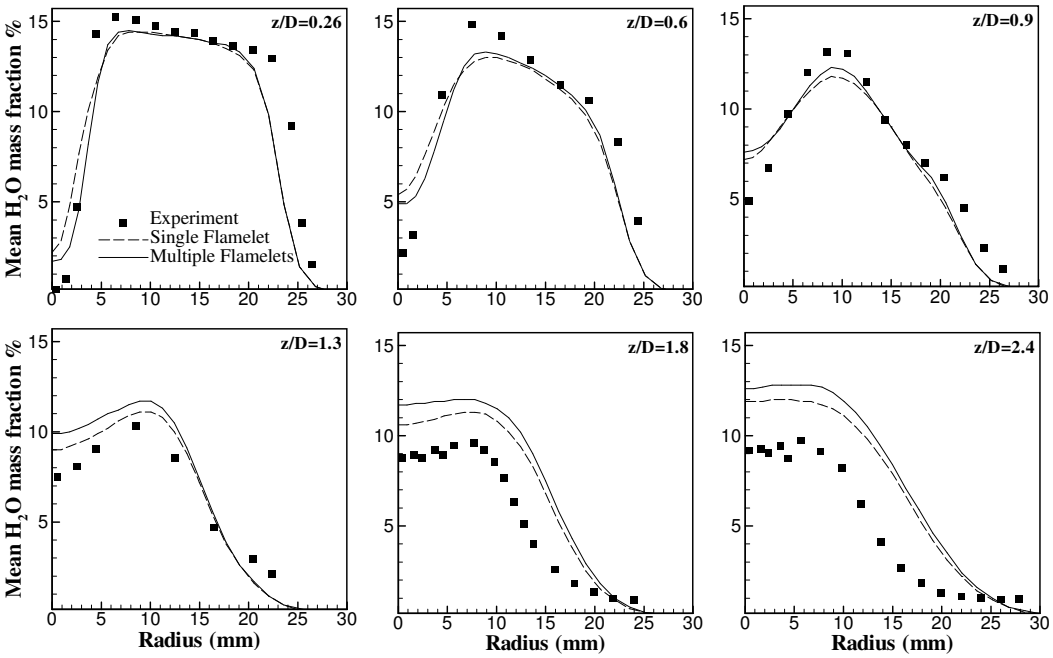

Figure 8.11: Radial profiles of mean mass fraction of H_2O at various axial lengths of HM3e flame. Predictions obtained from LES calculations with SLFM.

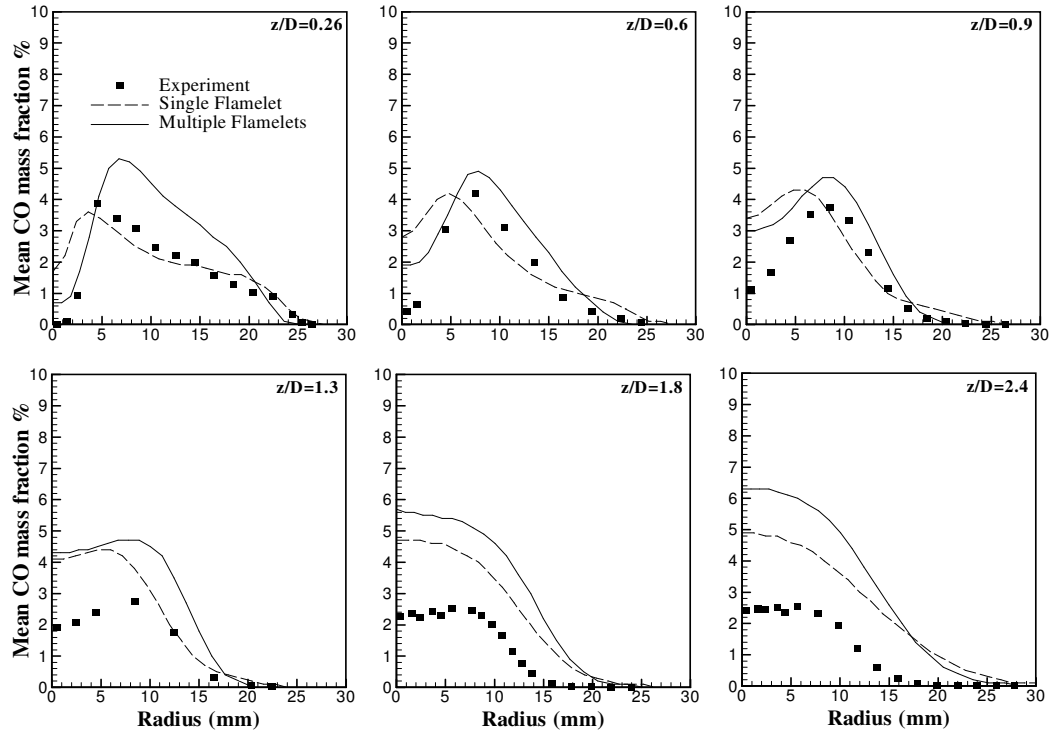

Figure 8.12: Radial profiles of mean mass fraction of CO at various axial lengths of HM3e flame. Predictions obtained from LES calculations with SLFM.

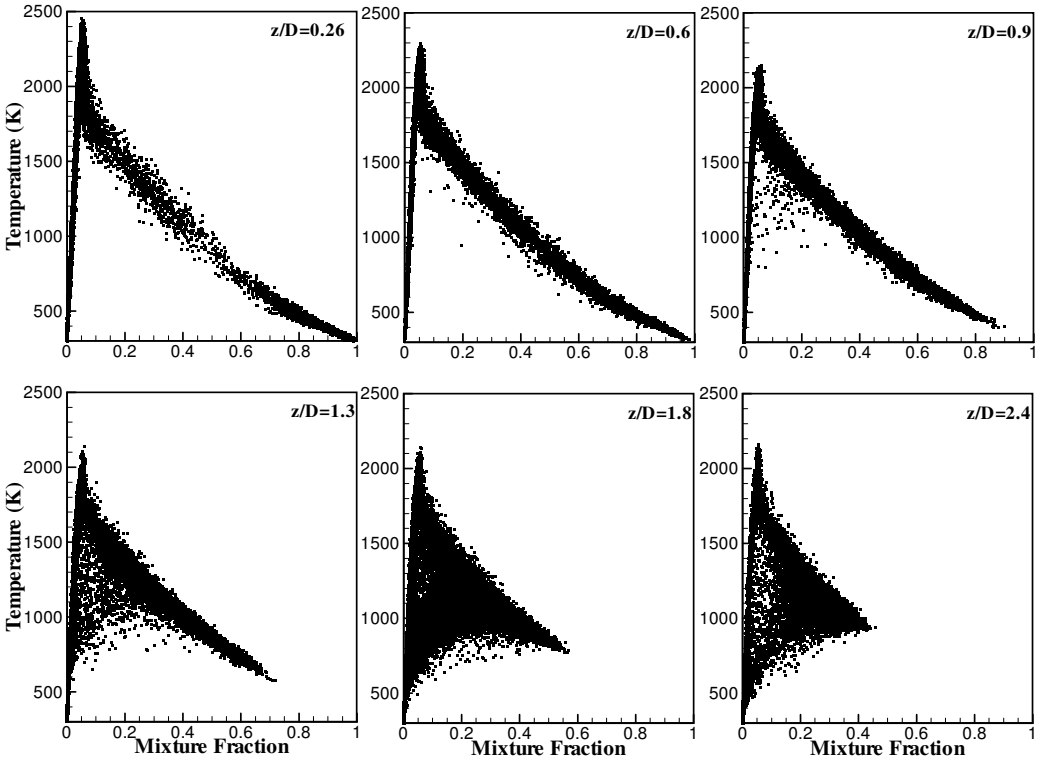

Figure 8.13: Experimental scattered data for temperature with mixture fraction at various axial locations along the HM3e flame.

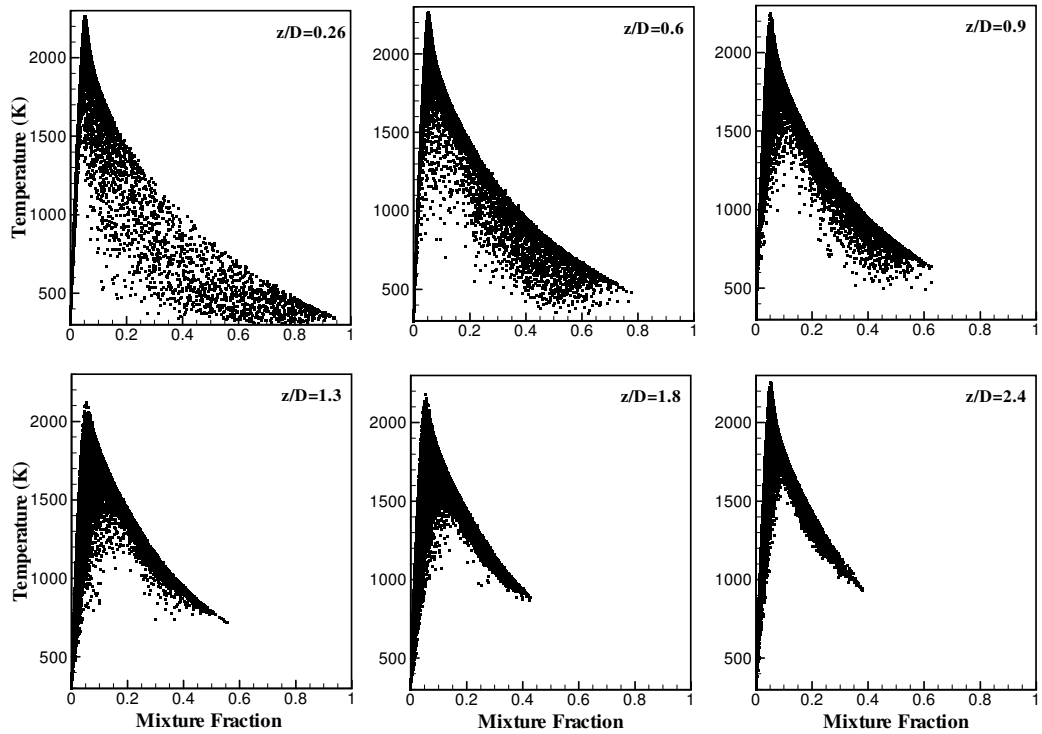

Figure 8.14: Computational scattered data for temperature with mixture fraction at various axial locations along the HM3e flame.

8.3.4Effect of Chemical Mechanism – HM1 Flame

In order to verify the effect of chemical mechanism on the numerical predictions, SLFM based HM1 flame simulations are conducted with detailed chemical mechanism of the GRI 3.0 (Smith *et al.* 2007) and GRI 2.11 (Bowman *et al.* 2007). The GRI 3.0 mechanism is a successor to the version 2.11 and comprises of 53 species with 325 elementary chemical reactions (hydrocarbon + nitrogen chemistry) in comparison to the 277 elementary reactions and 49 species with GRI 2.11. Notable modifications include changes in CH kinetics which are important to the Prompt NO formation. A previous study conducted by Kim and Huh (2002) on the HM1 flame has shown that the GRI 3.0 over-predicts NO twice as high as GRI 2.11 while the temperature and major species predictions are more or less similar to those from GRI 2.11. However, these findings are obtained from CMC model based combustion calculations and hence, whether or not they could be generalized was not certain. Hence, performance of GRI 3.0 has been re-investigated with the present SLFM based calculations. The mean temperature predictions of LES calculations of HM1flame with SLFM combustion model for the two different chemical mechanisms are compared to measurements in Fig. 8.15.

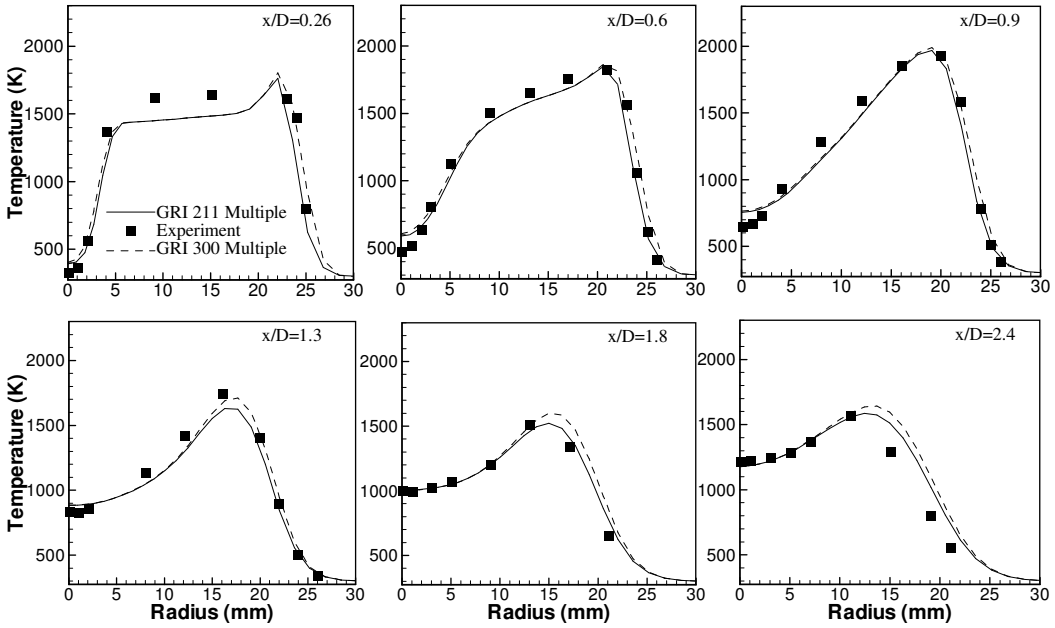

Figure 8.15: Radial profiles of mean temperature at various axial lengths of HM1 flame. Predictions obtained from LES calculations with SLFM for different chemical mechanisms used.

Similar to the findings of Kim and Huh (2002), no noticeable improvement in temperature predictions are observed with the GRI 3.0 mechanism. However, GRI 3.0 mechanism results in a predominantly over-prediction of mean CO_2 mass fraction at the interaction of recirculation zone and co-flow region as shown in Fig. 8.16. But at the remaining radial distances for all the axial locations, both the mechanisms are observed to result in similar manner for the mean CO_2 mass fraction. For the other major species investigated in the current study include H_2O where both the mechanisms have been found to result in similar pattern with very marginal over-prediction with GRI 3.0 (Fig. 8.17). Thus, from temperature and major species comparisons, the relatively new detailed GRI 3.0 mechanism seems to give no improvement in predictions when compared to GRI 2.11 for major species. Either of the detailed hydrocarbon chemistry GRI 2.11 or GRI 3.0 can be used for the present study where both temperature and compositional structure are of interest. However, both these mechanisms are again tested with swirl based SMH1 flame later in this chapter.

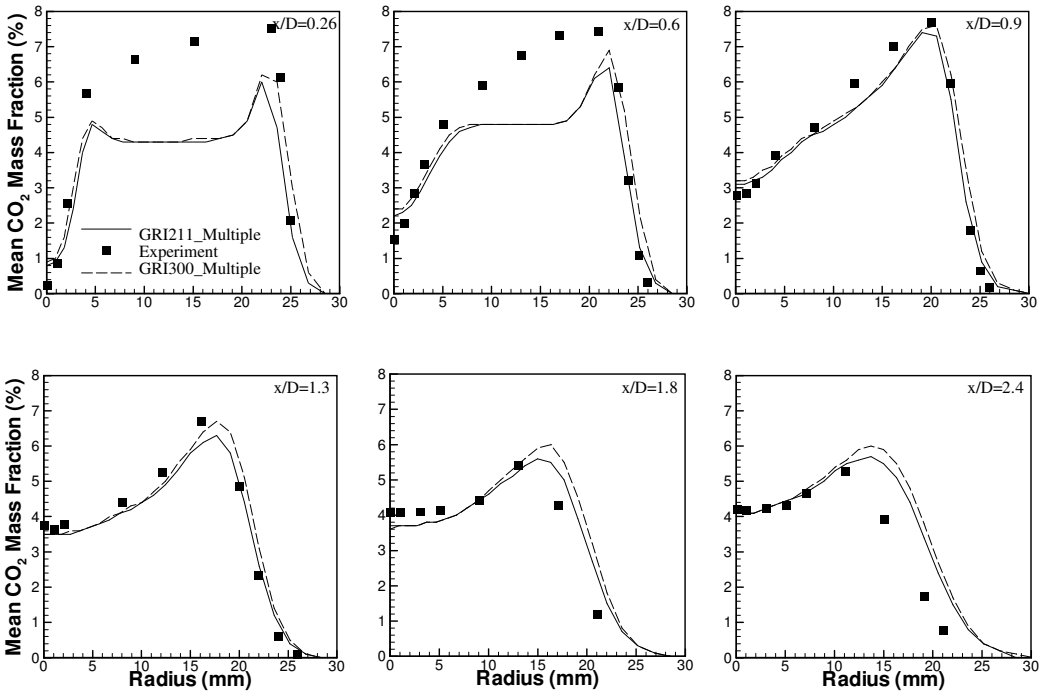

Figure 8.16: Radial profiles of mean mass fraction of CO_2 at various axial lengths of HM1 flame. Predictions obtained from LES calculations with SLFM for different chemical mechanisms used.

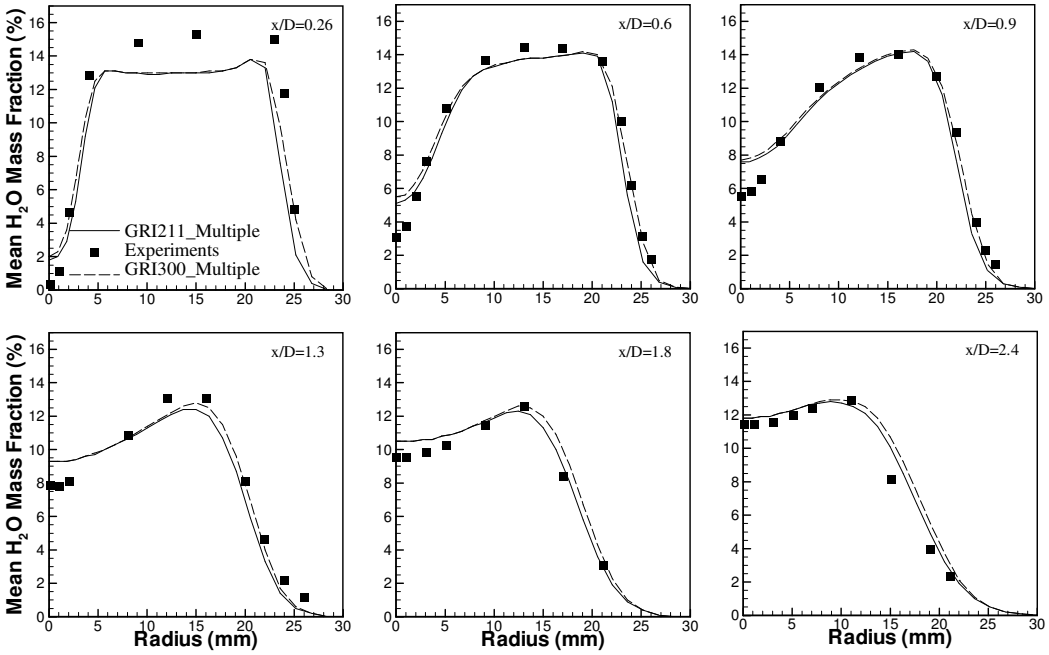

Figure 8.17: Radial profiles of mean mass fraction of H_2O at various axial lengths of HM1 flame. Predictions obtained from LES calculations with SLFM for different chemical mechanisms used.

8.3.5Non-adiabatic Flamelet Modelling – HM1 Flame

Consideration of radiation calculations in LES for the present flame HM1 involves solving for enthalpy equation with the implementation of the concept of enthalpy defect (Section 7.1.2) with NAFM combustion model. Using NAFM, we interpret the results and compare with SLFM case under similar boundary conditions. This section of results discuss the effect of radiation on turbulence-chemistry with comparison of mean mixture fraction, temperature and major species of products like CO_2 and H_2O by their radial plots at various axial locations along the burner.

Details of radiation calculations involved are discussed in chapter 5 which require ray tracing information to be stored in a file called RAY.dat and is recalled when ever radiation calculations are performed. But this ray file depends on the mesh size and therefore an increase in mesh size will increase the computational overhead to read the file and store in the memory for radiation calculations. Therefore, considering the computational memory issues, all the radiation calculations in the present work are performed with 16GHz machine with dual core processor and are limited to 1 million

grid nodal points. Hence in order to implement the NAFM with LES for HM1 flame, the grid originally used for the above SLFM studies has to be changed from 100x100x120 to 100x100x100. The grid refinement is changed only in z-direction from 120 to 100 keeping the uniformity of the mesh. This one million mesh is therefore used for the HM1 NAFM calculations and results are compared with one million mesh for SLFM case only. Therefore, both SLFM and NAFM cases are undertaken with one million in grid size each. However, in order to find the difference in the results with the change in the mesh, we first compare the effect of grid on mixture fraction and other scalars.

Figure 8.18 shows the mixture fraction radial plots for the two mesh configurations. Effect of mesh size on the mixing patterns remains the same till axial location of z/D=1.3. At the last two locations, 1.2 million grid provides a better solution close to the experiments. However, with both the grids, there is a significant under-prediction in the centerline values. Mixture fraction profiles thus convey that change in grid size has minimal effect on mixing.

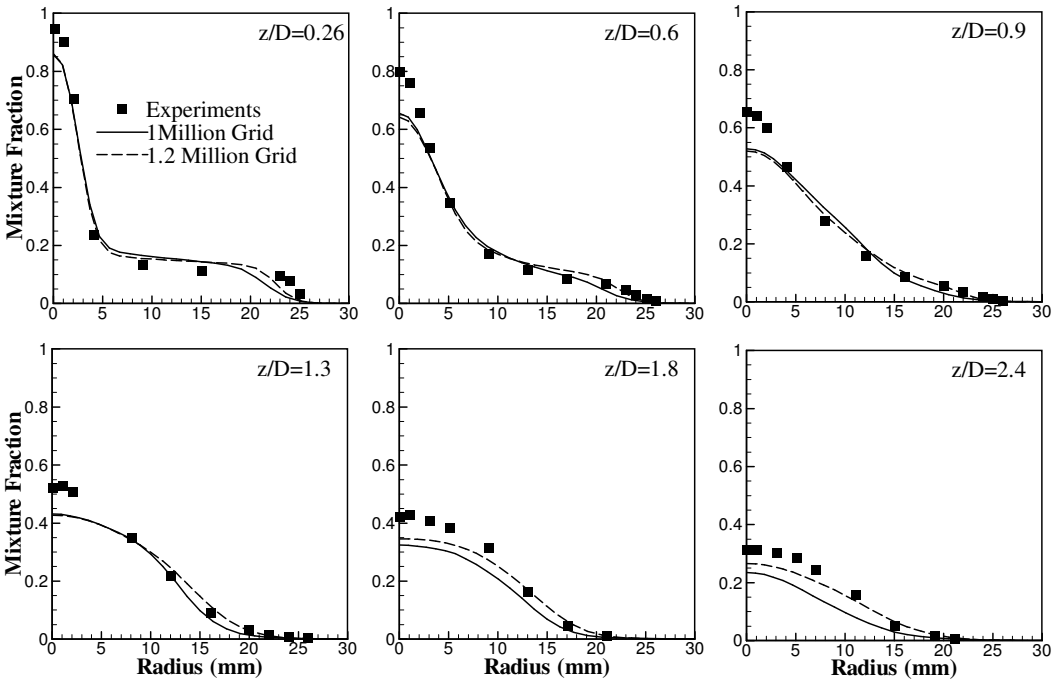

Figure 8.18 Radial profiles of mean mixture fraction at various axial distances for HM1 flame. Predictions obtained from LES calculations with SLFM involving GRI 2.11 mechanism.

Temperature profiles at the initial two axial locations show a good agreement for one million grid case which are found to predict close to the experiments as shown in Fig. 8.19. However, the profile that has a close trend towards experiments is 1.2 million. The peak rise in temperature at z/D=0.26 at the interface between co-flow and outer recirculation zone still persists irrelevant of the grid distribution. At the remaining axial locations, simulation with 1.2 million grid nodes predict close to the experiments. Considering the difference between the two cases, one million grid nodes can be used for studying radiation effects without loosing much information. Hence, keeping the computational difficulties in mind, one million grid distribution is considered for testing NAFM. Finally in order to check the predicting capabilities of NAFM, major species mass fractions are compared next in the section.

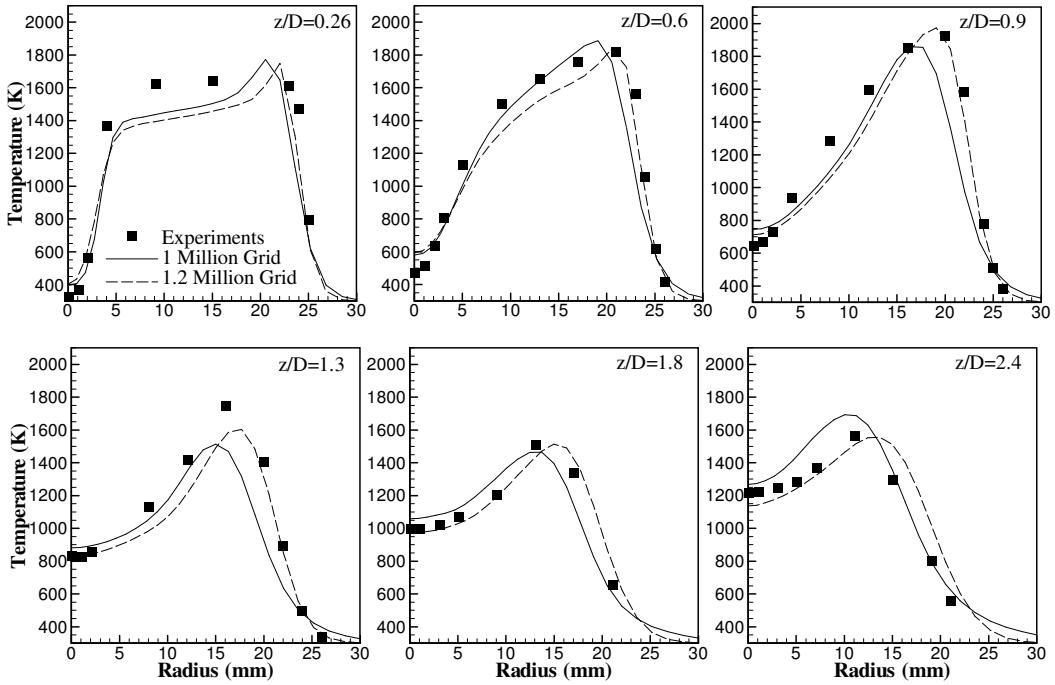

Figure 8.19 Radial profiles of mean temperature at various axial locations for HM1 flame. Predictions obtained from LES calculations with SLFM involving GRI 2.11 mechanism.

The mean mass fractions of CO_2 and H_2O are shown with the radial plots at various specified axial locations in Fig. 8.20 and 8.21 respectively. CO_2 mass fractions at the initial three locations indicate positive results for the one million grid while at the locations z/D=1.3 and 2.4, 1.2 million case results with its predictions close to experiments. At location z/D=1.8, one million mesh case gives closer agreement with

experiments. But with the predictions of mass fraction of H_2O which provides better results with 1.2 million grid case. However, considering the computational constraints in applying higher resolution mesh as discussed earlier, we undertake the detailed study of NAFM and compare with SLFM. The same scalars are considered for the prediction of NAFM and its effect on the medium to high luminous flames like HM1 when compared with SLFM.

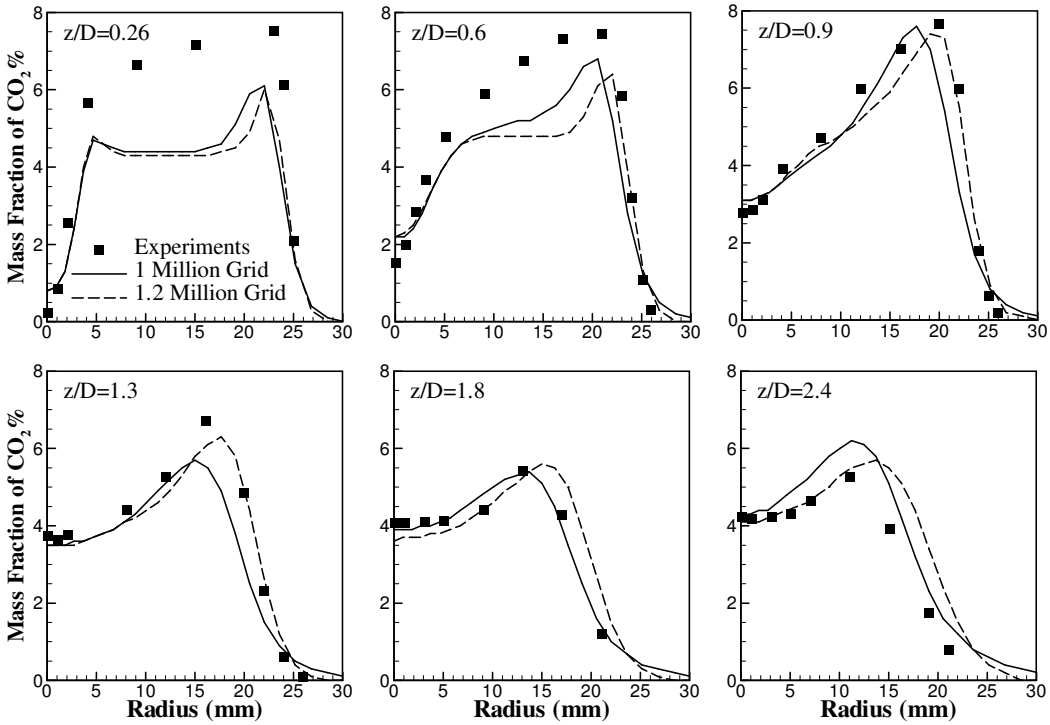

Figure 8.20 Radial profiles of mean mass fraction of CO_2 at various axial lengths of HM1 flame. LES with SLFM tested for two different grid configurations.

The effect of radiation on mixing, temperature and other species are discussed next. Figure 8.22 shows the mixture fraction profiles for NAFM and SLFM compared with experiments. At the first axial location z/D=0.26, both the cases predict in a similar way. At the remaining axial locations z/D = {0.6 to 1.8} radiation model, NAFM outperforms SLFM and predicts very close with experimental data. The under-prediction in the centreline values is less with NAFM at most of the axial locations. At z/D=1.3 and 1.8, NAFM proves to be beneficial with no under-prediction at the centreline values. However, at the last location, both the models behave in a similar pattern. Overall, the mixing profiles are found to improve with NAFM strategy and therefore effect of radiation cannot be neglected for such moderate to high luminous flames.

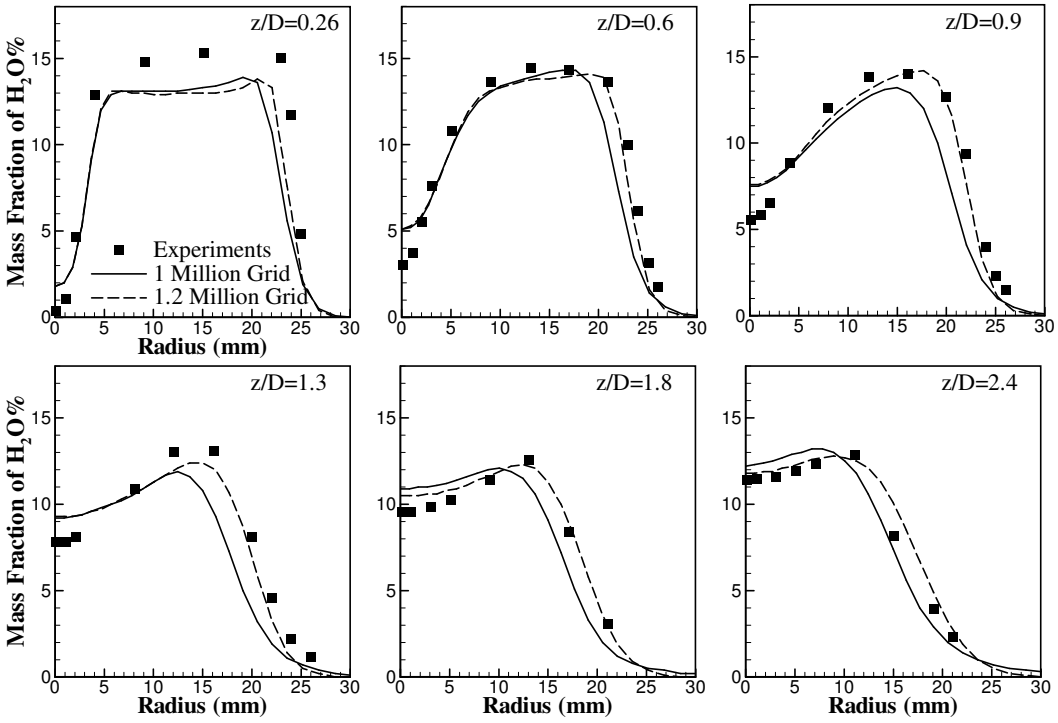

Figure 8.21 Radial profiles of mean mass fraction of H_2O at various axial lengths of HM1 flame. LES with SLFM tested for two different grid configurations.

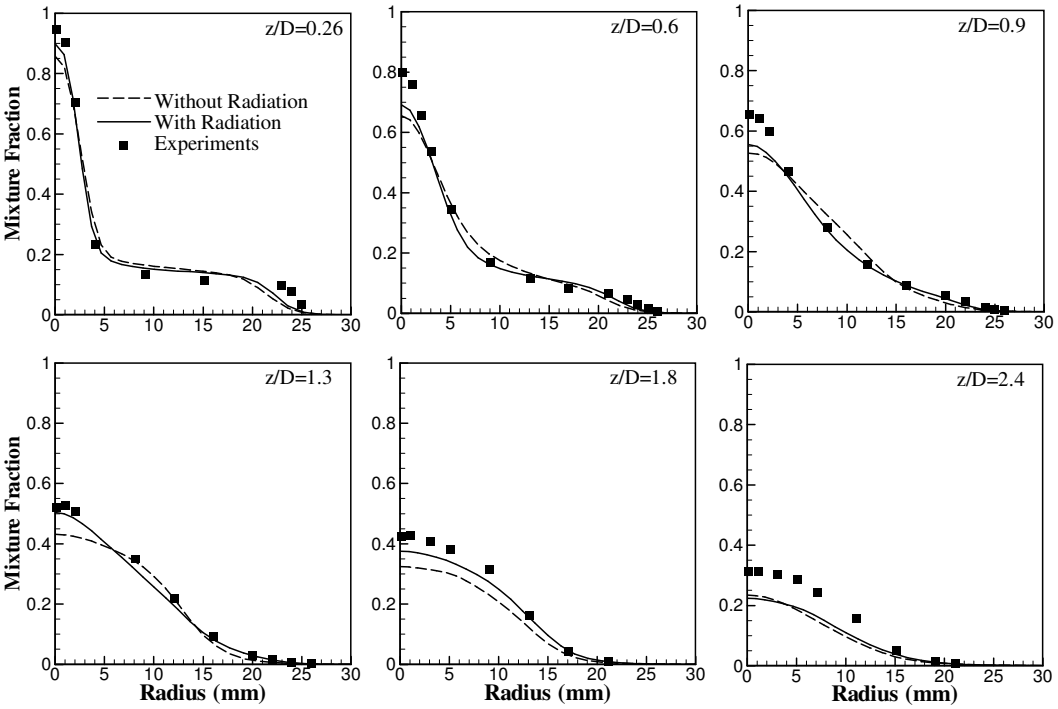

Figure 8.22 Radial profiles of mean temperature at various axial lengths of HM1 flame for comparison of SLFM and NAFM combustion models

Radial temperature profiles at various axial locations are depicted in Fig. 8.23 with and without radiation effects. Radiation definitely has an effect on the temperature profiles in the present case which is better explained as below. Results from adiabatic case with 1.2 million mesh is also shown for the effect of grid size on temperature pattern. However, the comparison is only discussed with respect to 1 million mesh case. At locations z/D = {0.26 to 0.9} temperature is found higher than the adiabatic case and shows a good agreement with the experiments. Locations z/D=0.26 and 0.6 fall very close to the jet base and bluff body, where NAFM have been observed to predict close with experiments. This particular region is considered more complex as the two contour rotating recirculation zones traps the mixture of fuel and air makes the flow complex in nature and is observed to predict high temperatures. Prediction of this high temperature pattern through NAFM combustion model is advantageous. At locations z/D = {0.9 and 1.3} radiation results proved to be closer with experiments. At the location z/D = 1.8, NAFM model matches very close with experiments from centreline to a radial distance of 10 mm while SLFM over-predicts. All three regions the recirculation zone, neck region and jet like region are well captured with NAFM than SLFM combustion model.

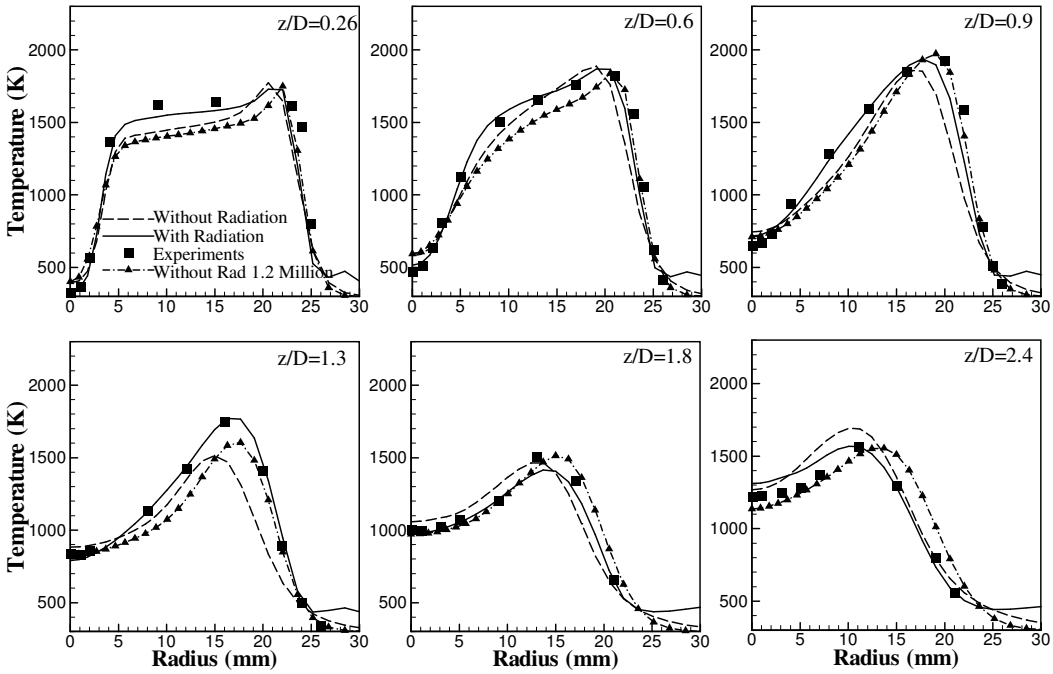

Figure 8.23 Radial profiles of mean temperature at various axial lengths of HM1 flame. LES with SLFM and NAFM tested for effect of radiation.

As temperature profiles are seen predicting well with NAFM, species predictions are also expected to be improved with NAFM rather than with SLFM. Radial plots of mass fraction of CO_2 are depicted in Fig. 8.24 for predicting the effect of radiation. The two extreme peaks in the mass fraction of CO_2 as seen at location z/D=0.26 is due to the two shear layers that are formed between inner recirculation, outer recirculation zone and co-flow velocity. These peaks are better reproduced with NAFM than SLFM. NAFM is found to capture the mass fraction from centerline till radius of 5mm in a good agreement with measurements both at initial two axial locations z/D=0.26 and 0.6. However, after radius equal to 5mm at these locations, a large under-prediction is found with both SLFM and NAFM. Out of these two models, NAFM predicts closer to experiments. At z/D=0.9 and 1.3, SLFM shows better predictions than NAFM in the radial locations from 0 to 15mm. But after this radial location, NAFM results are found to agree well with experiments. At the last two axial locations, which fall in the jet like region, there is no much difference found between the results from without and with radiation calculations.

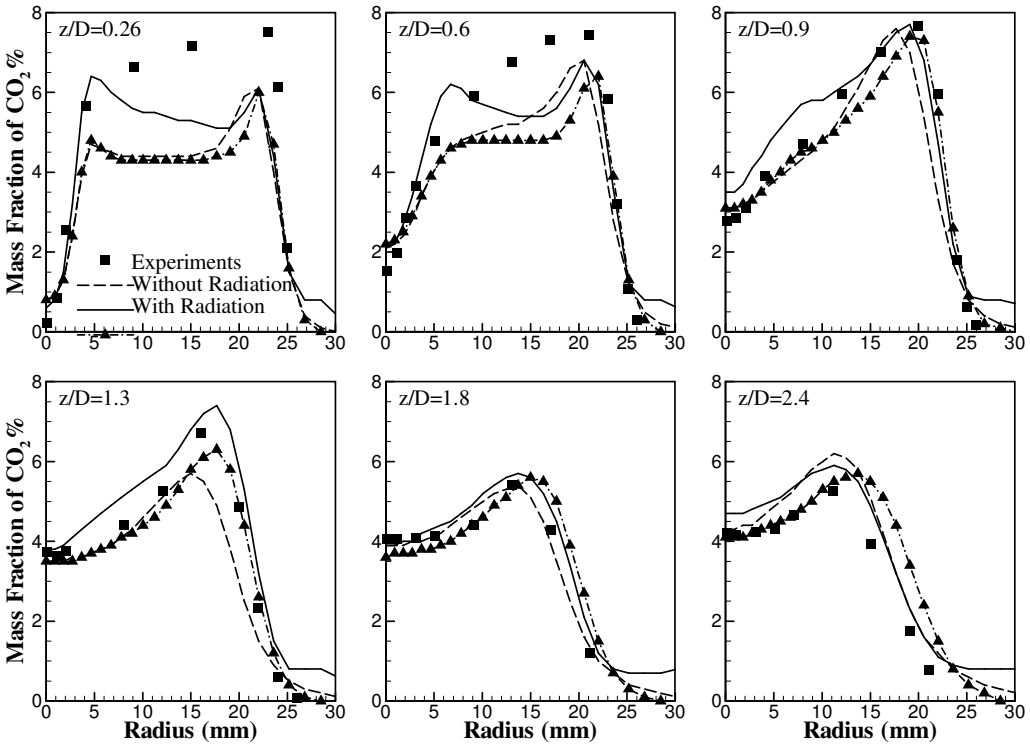

Figure 8.24 Radial profiles of mean mass fraction of CO_2 at various axial lengths of HM1 flame. LES with SLFM and NAFM tested for effect of radiation.

The under-prediction of CO_2 mass fraction at the initial two axial locations which are close to the bluff body base is most likely due to the incapability of the flamelet model at these highly recirculating regions. Overall, CO_2 mass fraction is observed to capture well with NAFM simulation. Mass fraction of H_2O at various axial locations is depicted in Fig. 8.25. At all the axial locations NAFM provides better results than SLFM. There is a little over-prediction in the centreline values with both the models. However, when compared to simulations without radiation effects, NAFM results are in closer agreement with the measurements. In NAFM calculations, it is considered that radiation losses are mainly due to H_2O and CO_2. Hence the energy dissipation and absorption are controlled by these two species which has a direct impact on temperature distribution. Therefore, turbulence with NAFM would ideally be more physical and should be closer with the measured data which has been observed with both species in Fig. 8.24 and 8.25. From the radial plots of temperature, mass fraction of H_2O, and mass fraction of CO_2 (Fig. 8.23 to 8.25) it is also seen that grid has an effect on the flow patterns for temperature and species concentrations. However, the percentage of effects from radiation and grid can be only judged when radiation calculations from 1.2 million case is performed.

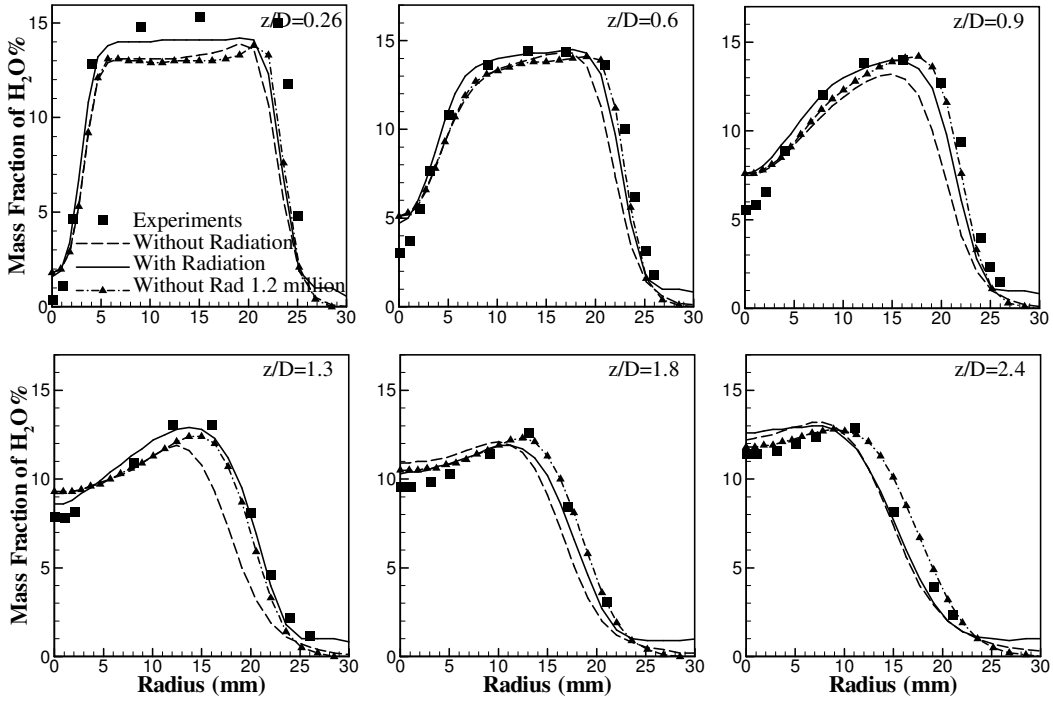

Figure 8.25 Radial profiles of mean mass fraction of H_2O at various axial lengths of HM1 flame. LES with SLFM and NAFM tested for effect of radiation.

The main observation from the above plots highlight higher predictions with NAFM than SLFM from axial locations z/D=0.26 to 1.3 for temperature and species mass fractions.. This under-prediction from adiabatic case (without radiation) when compared to NAFM in the high temperature recirculation zones may be due to the solution procedure for enthalpy equation in the NAFM which is not solved in SLFM. Involvement of enthalpy in the form of energy equation in NAFM results in difference in the temperature contours and higher in its value when compared to SLFM. The contour plot of Favre averaged temperature at the mid-plane for the two cases is depicted in Fig. 8.26 which clearly shows the difference in the patterns for temperature field all along the flame.

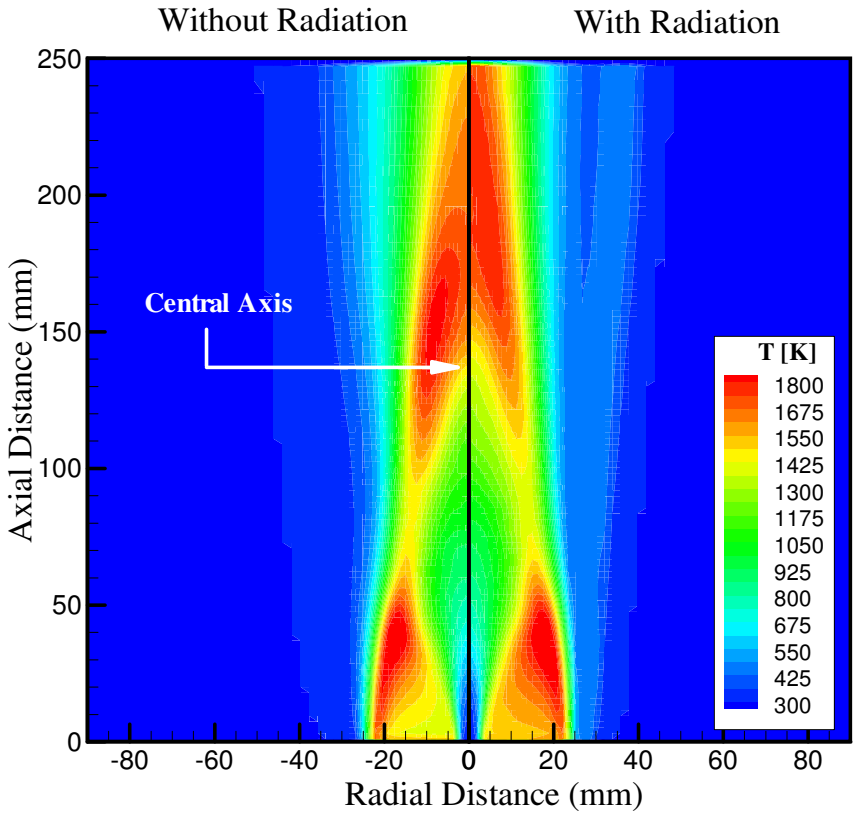

Figure 8.26 Contour plots of temperature highlighting the flame shapes with two different cases: (1) without radiation and (2) with radiation.

As discussed earlier, the mixing patterns were better captured with NAFM and can be seen from Fig. 8.26 which also shows the intensely high temperature regions above the bluff body region where the two contour rotating recirculating regions exist. With SLFM, the flame temperature is observed to be elongated rather than stabilized. The

necking zone is captured well with both the models. The temperature contours is clearly seen to be shifting in the downstream portion of the flame (near to jet like region) with the simulation results from NAFM with radiation (right hand side in Fig. 8.26) when compared with SLFM (without radiation) (left hand side in Fig. 8.26). At all the locations along the central axis (Fig. 8.26) inclusion of radiation (NAFM) resulted in lower temperature values when compared with SLFM. But the radiating characteristics of products of combustion makes the flame expand more in the radial direction and therefore the spread of temperature can be observed to be more on the right hand contours with radiation in the radial direction. This radial distribution of temperature all along the flame can be better explained with the instantaneous plot of temperature as shown in Fig. 8.27. It is very obvious that low to medium temperature patches can be seen all along the axial direction surrounding the flame which is due to the radiation heat sources generated from H_2O and CO_2 from high temperature regions.

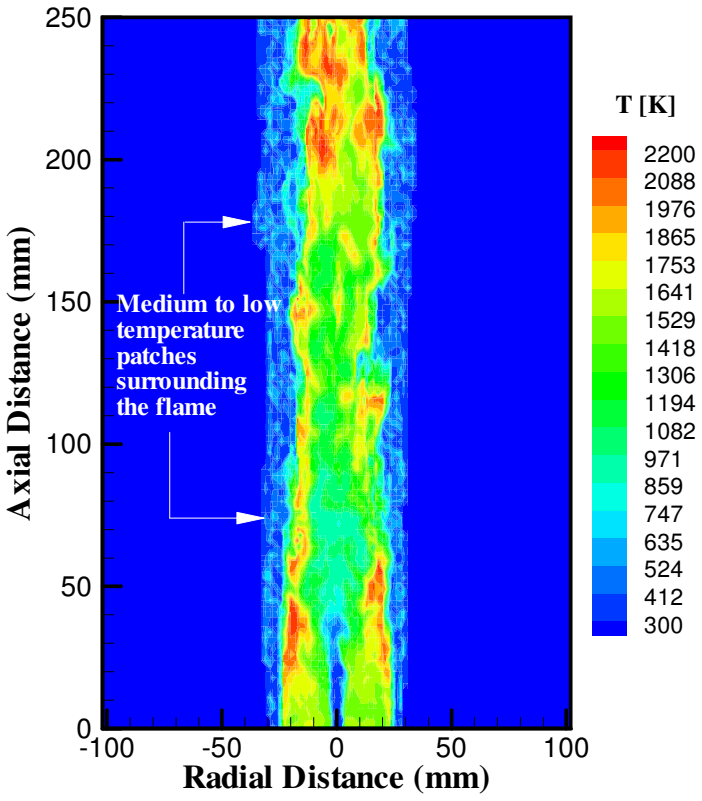

Figure 8.27 Instantaneous temperature contours at the mid-plane for the NAFM case.

8.4 Experimental Details of Swirl Stabilized Flames

Here combustion models SLFM and non-adiabatic flamelet model, NAFM are tested with CH_4:H_2 (1:1) fuelled swirl stabilized flame which was experimentally studied by Al-Abdeli *et al.* (2003) and Masri *et al* (2004). This flame is observed to be devoid of any flame extinction phenomena and therefore suitable for studies with laminar flamelet based models.

Swirl stabilization in flames is the most advanced technological flame control and stabilization process involved with any modern gas turbine engines. Sydney swirl flame experiments provide a high quality database for the validation of numerical codes. From this set of series the very well known SMH1 flame is selected for the present numerical validation. The details of the burner are depicted in Fig. 8.28. The burner has a central jet diameter of 3.6 mm with bluff body surrounding it with a diameter of 50 mm. The dimensions of the wind tunnel are 250mm x 250mm which covers the burner. Swirl is induced from three tangential ports to attain a swirl number of 0.32 at the swirl inlet located at the jet base. A central fuel jet consists of CH_4/H_2 (1:1) with an inlet velocity (U_j) of 140.8 m/s. The swirl annulus covers the bluff body with an outer diameter of 60 mm. The axial (U_s) and tangential (W_s) components of swirl velocity are 42.8 m/s and 13.8 m/s respectively. The ambient co-flow has an inlet velocity (U_e) of 20 m/s. The velocity field measurements showed a large recirculation zone just above the bluff body. This flame also found to exhibit a secondary vortex breakdown recirculation zone and a strong necking region. The upstream behavior of flow exhibited a highly rotating, downstream collar-like flow feature in region upstream of the second recirculation zone.

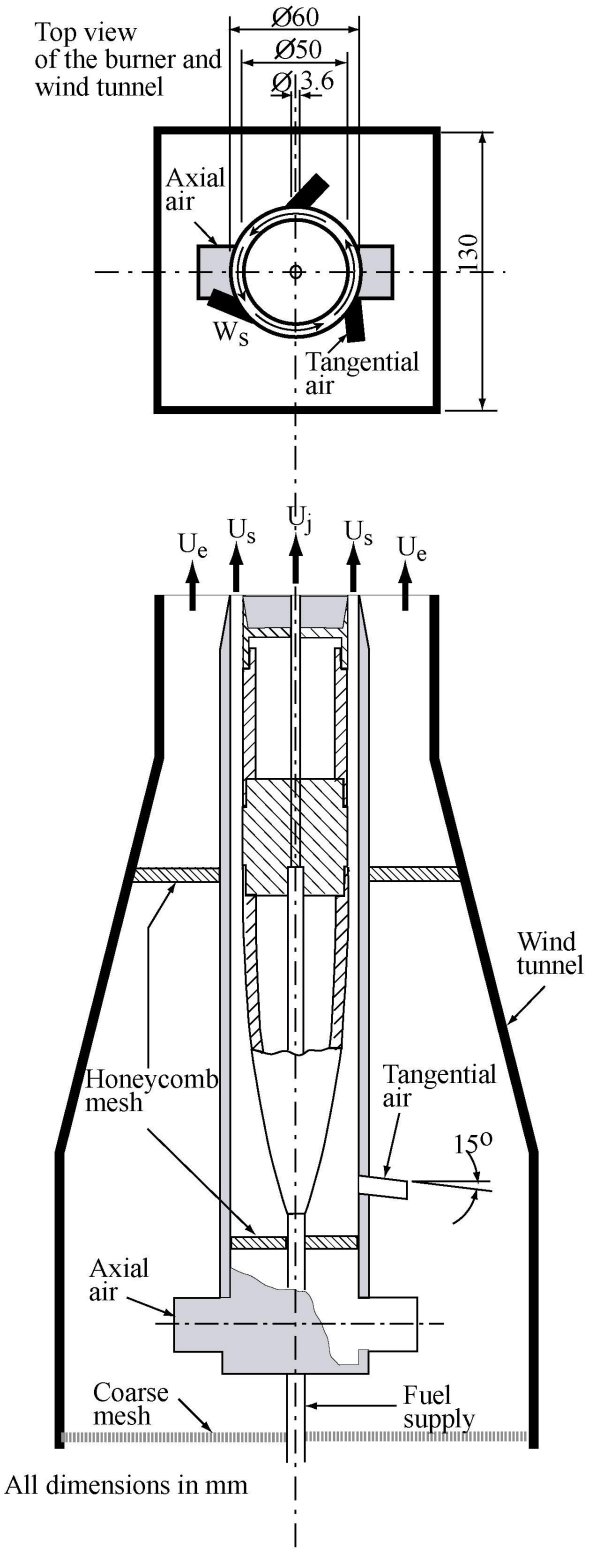

Figure 8.28 Schematic of experimental test facility for the SMH1 Flame.
(From: www.aeromech.usyd.edu.au/thermofluids)

8.5 LES Modelling of SMH1 Flame

8.5.1Computational Details and Boundary Conditions

The computational domain has dimensions of 200x200x250 (mm). The axial distance of approximately 70 jet diameters and the burner width of approximately 55 jet diameters is considered in order to account the independency of flow entrainment from the surroundings. An inlet jet velocity is specified at the inlet with a $1/7^{th}$ power law profile. Convective outlet boundary condition is used at the outlet plane and all walls and co-flow boundaries are treated as adiabatic. No-slip boundary condition is used in the near wall flow using log-law wall functions. For radiation calculations the boundaries are assumed to be black walls at 300 K. Temperature and species mole fractions of CO_2 and H_2O are read into the radiation code and absorption coefficient field is calculated. In order to check the effect of number of rays, two different LES-DTM coupled calculations are performed with number of rays equal to 100 and 256. The computational time for radiation calculations is reduced by providing the stored ray file (contain ray tracing information) as an input to the radiation code when ever it is required.

The validation of the combustion models are performed by comparison of radial plots at different axial locations (normalized by bluff body diameter) for temperature and all other species mass fractions i.e., at z/D = 0.2, 0.4, 0.5, 0.8, 1.2, 1.6, 2.5 and 3.5. The results are discussed in detail later in this chapter. All the SLFM cases are performed on a 4GHz memory machine while all NAFM cases involving radiation are performed on 16 GHz memory machine. The average time to run the SLFM simulation on a 4GHz machine with single processor for each case with flame SMH1 takes around 25 days for the flow to stabilize (t=30 ms) and thereafter approximately 15 days for the collection of statistics (t=20 ms) for post processing. A total of 50 ms for the entire simulation is performed for swirl stabilized flames considering sufficient flow stabilization. The time taken for NAFM on a 16 GHz memory machine for SMH1 flame takes around 45 days for the flow to stabilize (t=30 ms) and thereafter approximately 30 days for the collection of statistics (t=20 ms) for averaging the data for post-processing.

8.5.2Computational Grid

A Cartesian staggered non-uniform grid distribution of 100x100x100 in X, Y and Z directions are specified to discretize the computational domain with a total of one million grid points in order to optimize the simulation time. The computational geometry and grid details are depicted in the Fig 8.29.

The radial grid distribution is maintained fine at the central jet region and gradually made coarser towards the wall boundaries. Similarly in the axial direction, uniform grid distribution is obtained in order to have sufficient grid points in the central region of the flame and above the bluff body regions. Grid pattern is almost the same as maintained for HM1 and HM3e flames. Therefore, with the present swirl flame it is ensured that the flame stabilization region where steep gradients in the flame are expected is well resolved.

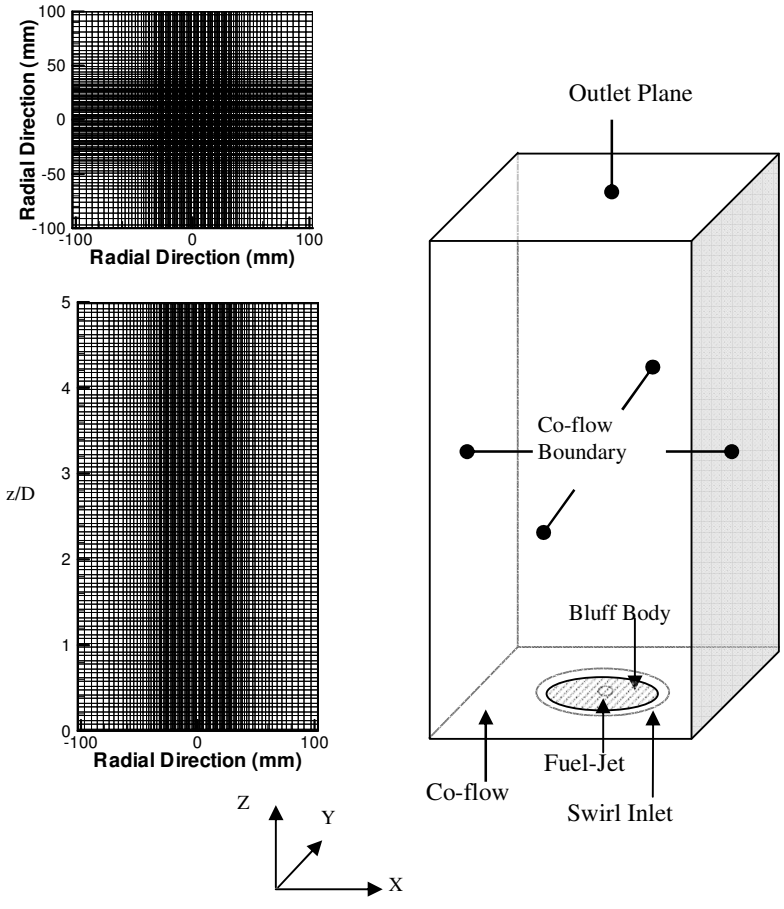

Figure 8.29 Computational details of SMH1 flame

8.6 Results and Discussion – NAFM

This section presents the results from various numerical simulations performed on SMH1 flame. The following cases are tested in the present work: (i) LES without radiation, (ii) LES coupled with radiation for 10x10 rays, (iii) LES coupled with radiation for 16x16 rays and (iv) LES coupled with radiation for 16x16 rays with radiation calculations operated for every 0.18 ms in the numerical procedure. All the above cases are compared with experimental data. LES calculations without radiation indicates combustion model with SLFM. Multiple flamelets are considered for SLFM case in order to have more precision with respect to flamelet solution. Flame stabilization is achieved by either introducing geometric features like the bluff body or by inducing swirl. Swirl involves the most complex flow structure which is generally used for flame stabilization. Numerical methods often find very difficult to capture the flow structure induced by swirl. Figure 8.30 shows the flow pattern with streamlines of axial velocity plotted on temperature contours.

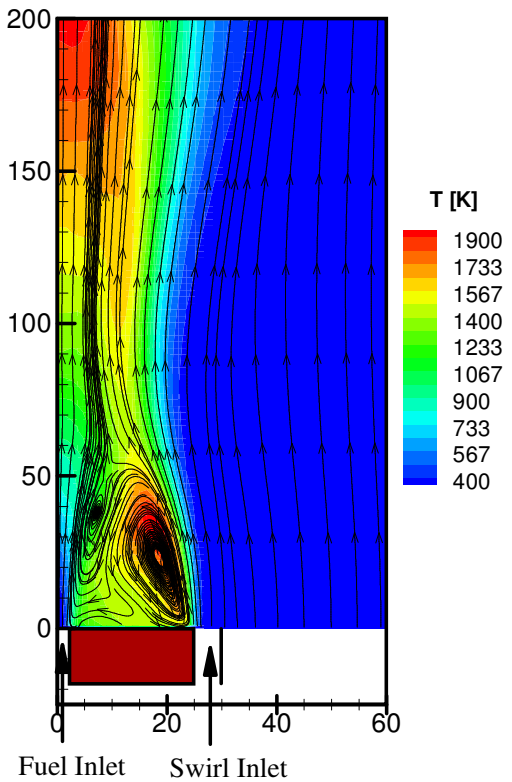

Figure 8.30 Streamlines of axial velocity plotted against temperature at the centre plane

The two recirculation zones which are responsible for the flame stabilization process above the bluff body are predicted very well by numerical simulation. The two counter rotating vortex zones lead to high temperature regions above the bluff body. Results are presented for velocity flow field and comparison with experiments. Temperature, mixture fraction and species mass fractions are compared with respective experimental data. Effect of radiation is highlighted in all the above results.

8.6.1Flow Field Predictions

The axial and swirl components of velocity are compared with the experimental data for their mean and fluctuating values at various axial locations. Figures 8.31-8.34 depict the velocity comparisons with measurements. The axial velocity <W> comparisons are found to be very well captured with numerical code when compared with experiments (Fig. 8.31). Except at one downstream location z/D=2.5, LES resolves the axial velocity component very well. Recently, Ranga-Dinesh (2007) studied for vortex breakdown in SMH1 flame and found similar discrepancy in the results with LES at the above axial location. Fluctuating component of axial velocity is found to predict reasonably close to the experimental data in Fig. 8.32. But predictions were found deviating from the measurements at the radial regions r/R = {0.9-1.2} for axial locations of z/D = {0.8-3.5}. Figure 8.33 shows the comparison of swirl component of velocity <U> at different axial locations. Swirl velocity has been provided with the axial and tangential velocity components in the LES numerical solution. The increase in the swirl velocity pattern at radial distance of r/R = {1.0-1.2} at the initial three axial locations are captured well enough with both the models (NAFM and SLFM). However, the discrepancy in the predictions can be found in the further downstream locations. The flame characteristics with combustion involved makes the flow structure very complex and therefore results in the fluctuations in numerical predictions. Figure 8.34 depicts the fluctuating component of swirl velocity with a reasonable agreement with the experiments. LES with radiation effects and without radiation, show a similar trend in the velocity profiles. Hence this concludes that radiation has minimal effect on flow structure with respect to velocity field. This also indicates that density fluctuations which depend on temperature, has very minimal effect with radiation calculations. However, predictions of temperature and other major species will provide an insight for the importance of radiation effects.

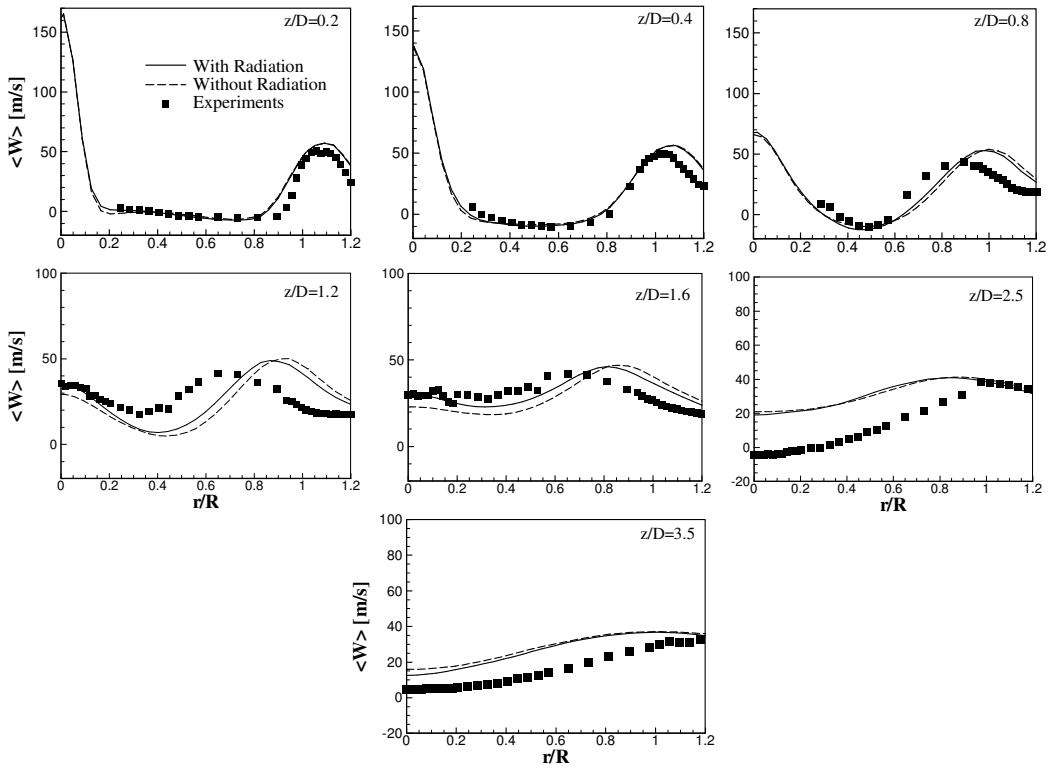

Figure 8.31 Radial plots for axial velocity at different axial locations

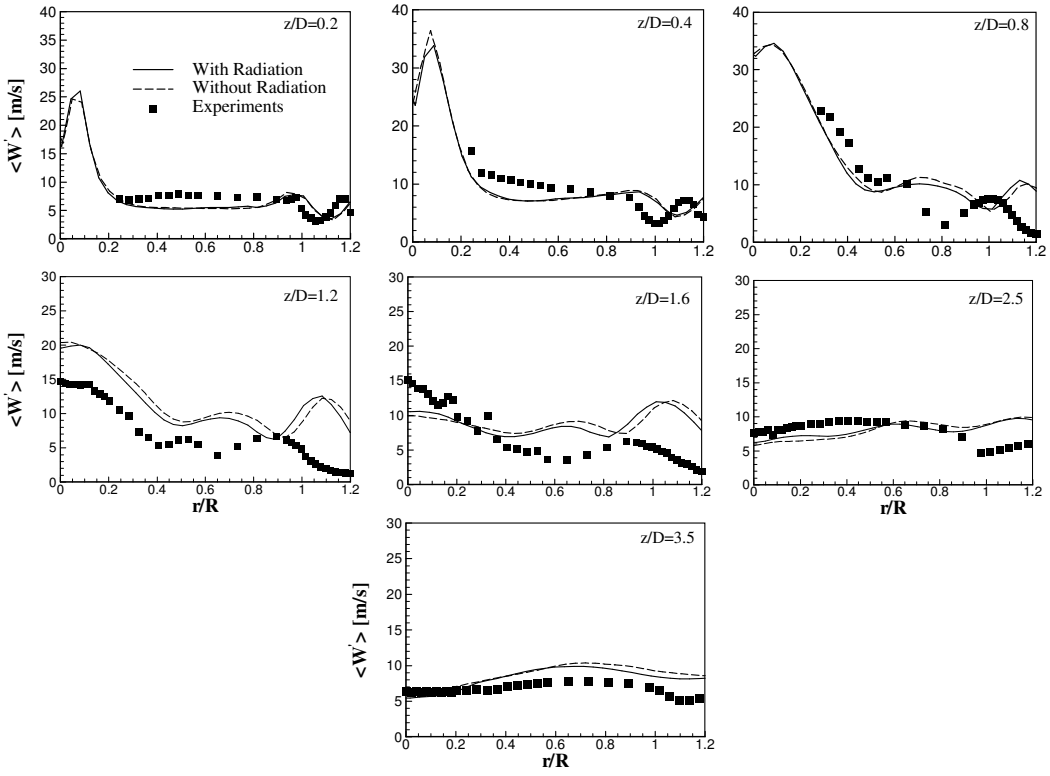

Figure 8.32 Radial plots for RMS of axial velocity at different axial locations

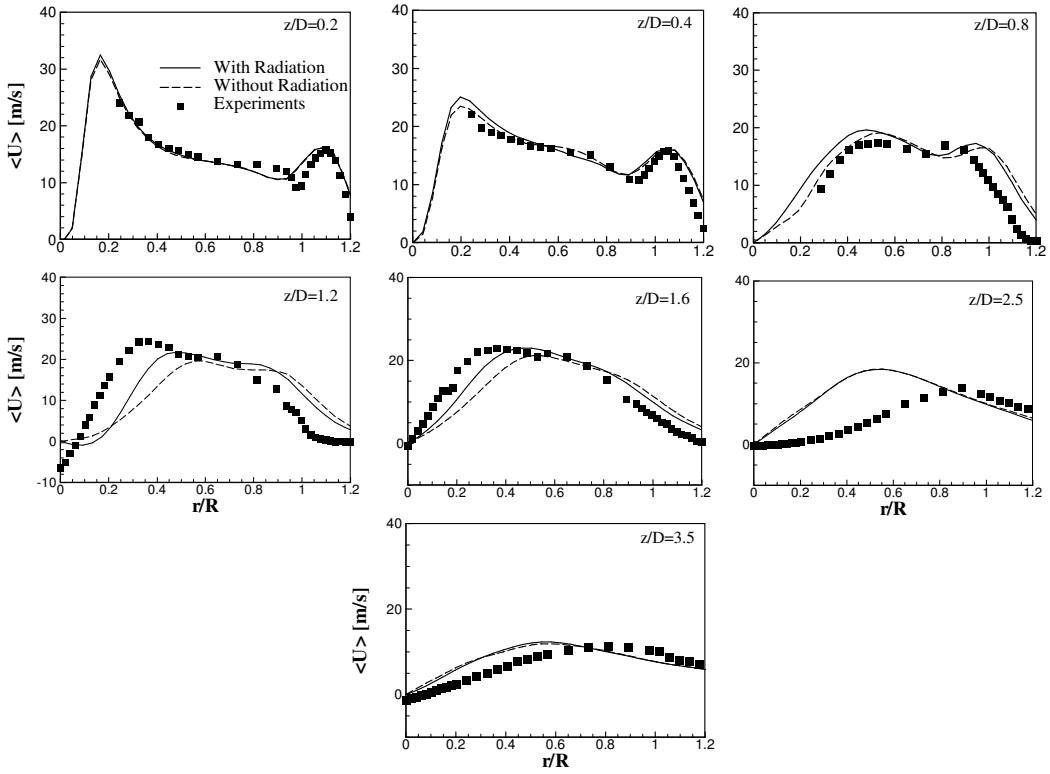

Figure 8.33 Radial plots for swirl velocity at different axial locations

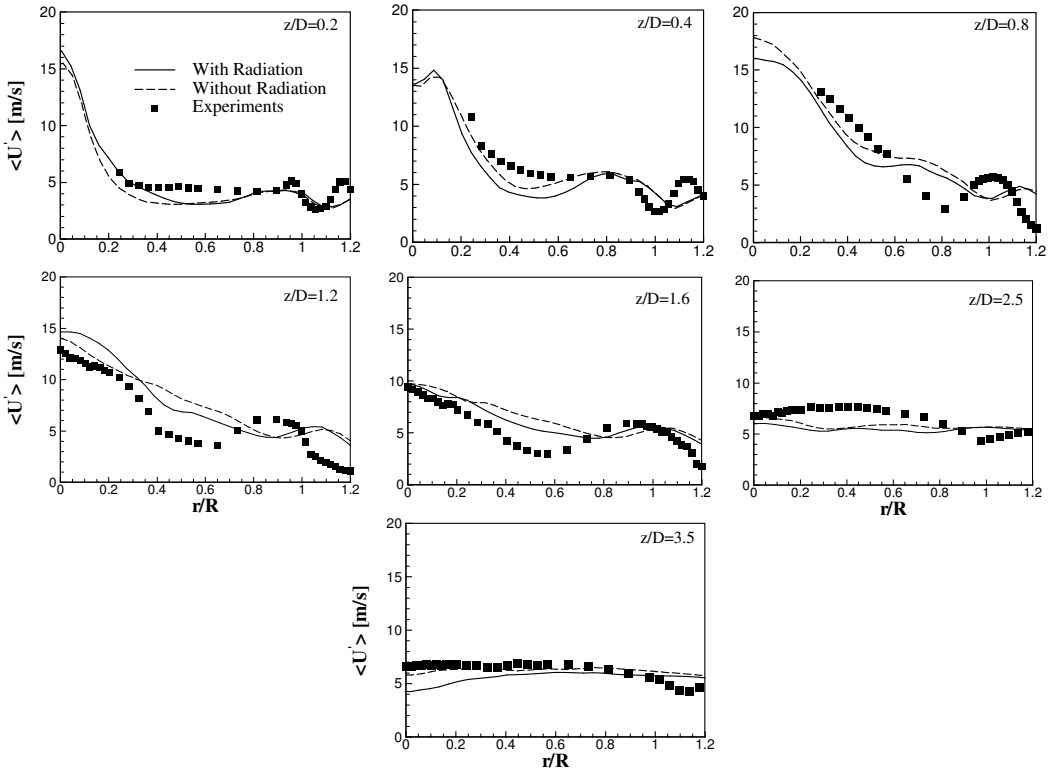

Figure 8.34 Radial plots for RMS of swirl velocity at different axial locations

8.6.2Mixing, Temperature and Major Species Predictions – SMH1 Flame

Performance of NAFM has been assessed through comparison between experiments and predictions from adiabatic flamelet model. Figure 8.35 shows the predictions of mean mixture fraction from NAFM and adiabatic model compared with measurements. The plots show very close agreement with the experiments and both the models show similar trend in mixing. Radiation results are highlighted with two set of rays i.e., 10x10 and 16x16 rays. Both show a similar trend at all the axial locations. However, mixture fraction variance is the parameter which determines the fluctuations in the mixing field and Fig. 8.36 shows the comparison of experiments with the predictions for the two models. A similar trend to mean mixture fraction is observed for its variance. Simulation with 16x16 rays alone is shown in Fig. 8.36 for comparison with SLFM adiabatic model. Inclusion of radiation calculations has significant influence on the mixture fraction variance.

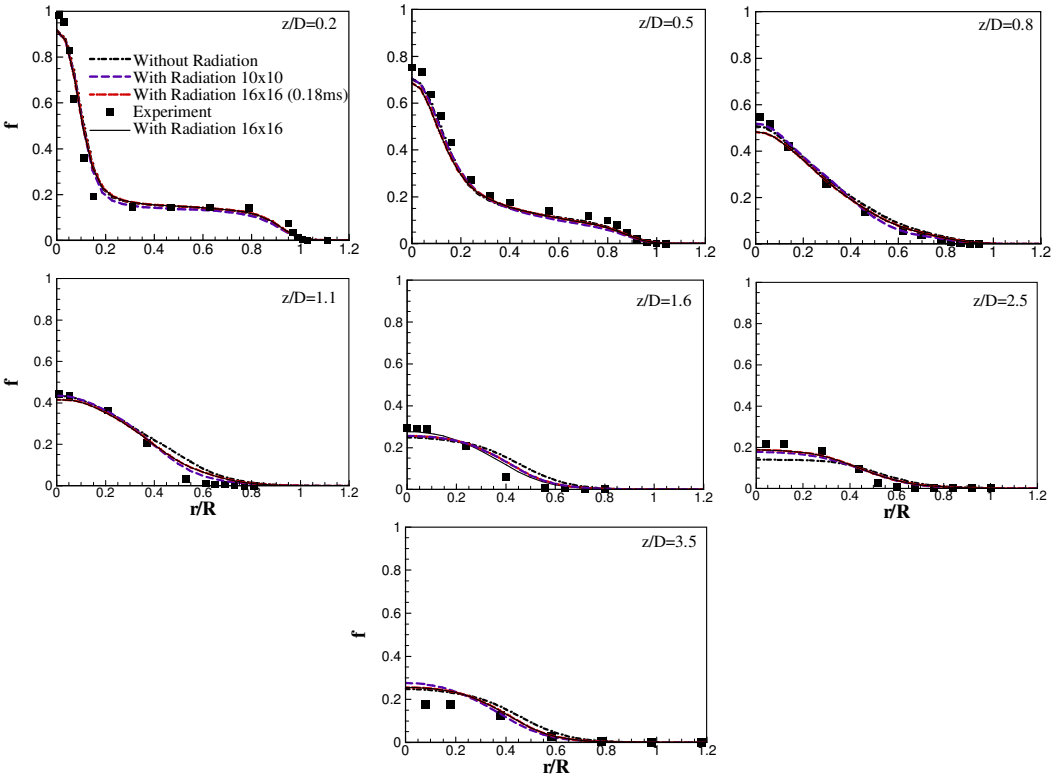

Figure 8.35 Radial plots for mixture fraction at different axial locations

Radial profiles of mean temperature at various axial locations are compared in Fig. 8.37 for predictions with experiments. NAFM with the inclusion of radiation effects

(both 10x10 rays and 16x16 rays) predicts better when compared with SLFM (without radiation) case. Radiation coupled with LES calculations gives a close agreement with the experiments for mean temperature and the difference in the mean values at most of the locations could be clearly seen from Fig. 8.37. SLFM over-predicts in all the downstream locations whereas NAFM with the radiation heat losses, predict close to the experiments. This gives an indication of the importance in the effects of radiation in a medium to high luminosity flames like SMH1. However, at the last location far away in the downstream portion, both the models are found to differ from measurements at the centerline locations. This resembles the incapability of the flamelet model in the highly fluctuating region like the downstream locations of z/D=2.5 and z/D=3.5. Radiation losses can be clearly depicted from the drop in temperatures when compared with adiabatic model at almost all the downstream locations from z/D = {0.8-3.5}. Therefore, the radiation heat loss can be categorized as strongly influencing on the temperature flow field in the present simulation.

Effect of radiation is found to be very negligible at the central axis from locations z/D=0.2 to 1.6. At the last two axial locations, effect of radiation is observed to have an influence because of the flame fluctuations due to temperature variations that are formed only after an axial distance of 125 mm (z/D=2.5). Below this axial location, the temperature variations are very minimal. This can be better depicted from Fig. 8.38 where the contour plots for temperatures with radiation and without radiation are shown. The turbulence generated due to vortex break down in the downstream portion of the flame generates high temperature variations which lead to large fluctuations in radiation intensities and thus the effect of radiation at the central axis is found only at the last two axial locations from Fig. 8.37. Along the central axis till the axial distance of z/D=1.6, the effect from radiation is negligible due to the lower temperature fluctuations which is mainly occupied by fuel and oxidizer mixture. Whereas, in the outer regions of the flame for these axial distances, flame temperature fluctuations are high and therefore the effect of radiation at these radial locations (r/R>0.2) are clearly seen in Fig. 8.37.

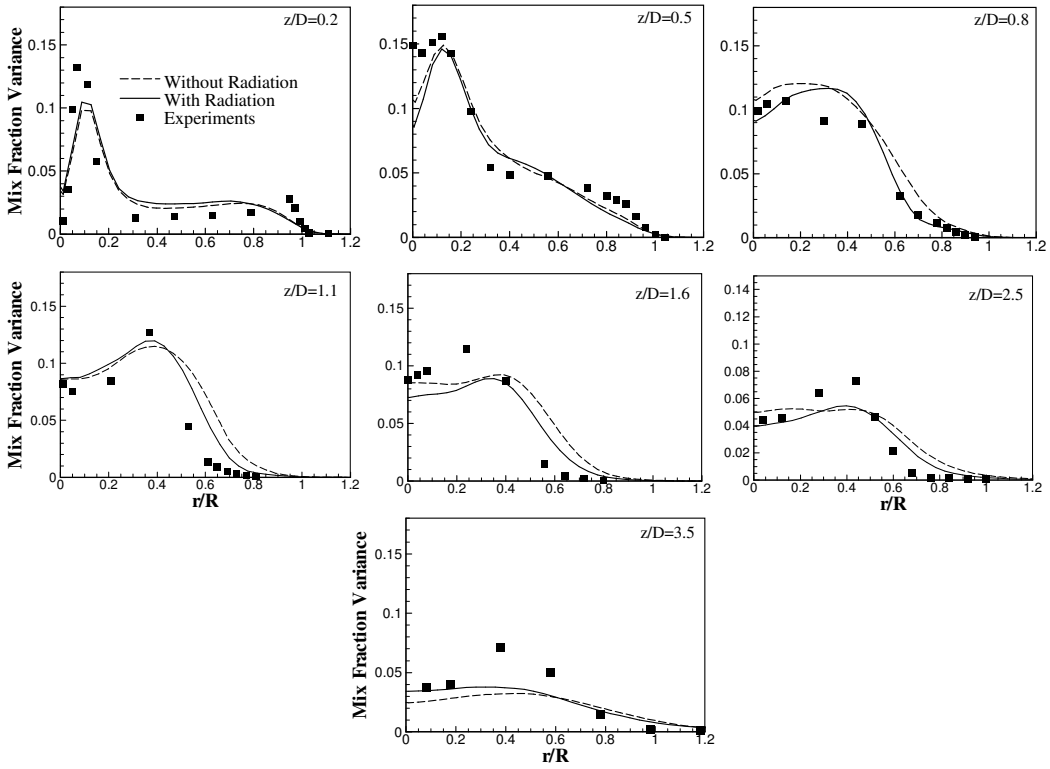

Fig. 8.36 Radial plots of mixture fraction variance at different axial locations

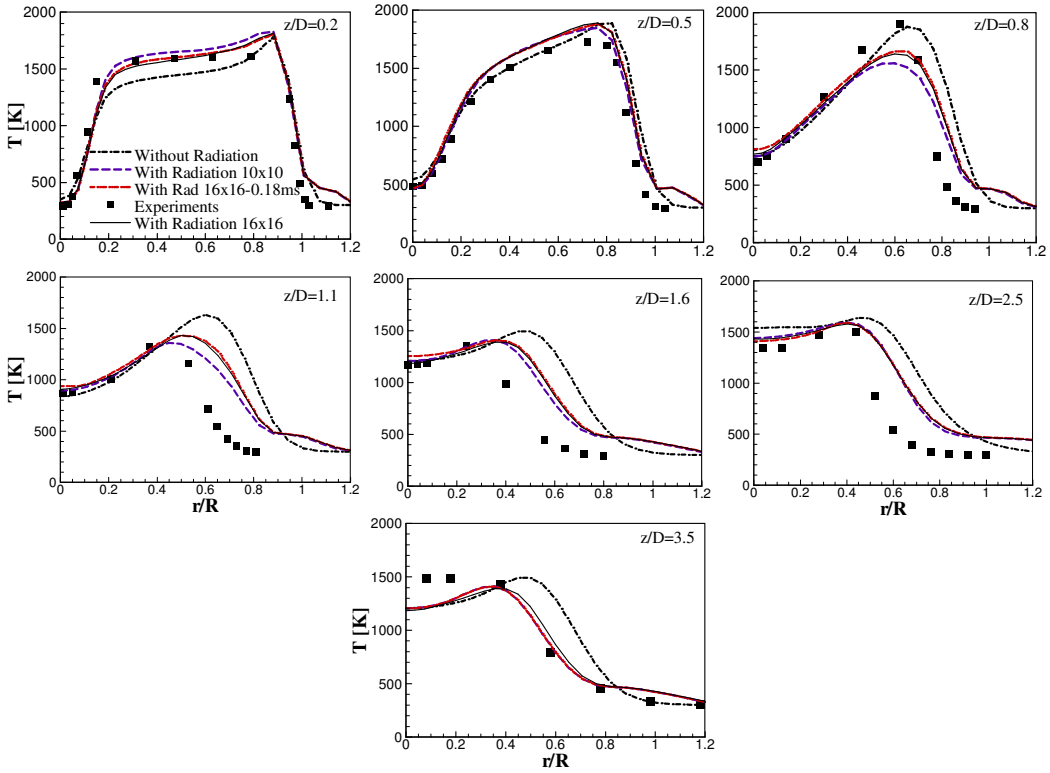

Figure 8.37 Radial plots of temperature at different axial locations

The contour plot of temperature provides a clear picture of the flame with respect to the high temperature zones. Figure 8.38 depicts the mean temperature contours at the centre plane for both the models. There are three recirculation zones as observed in the experiments, two above the bluff body region and one in the central vortex breakdown region in the downstream of the flame. Both the models (NAFM and adiabatic SLFM) predict these flow characteristics very well. A low velocity recirculation zone creates a high temperature region, which is shown in Fig. 8.38 with both SLFM and NAFM calculations. However, there is a change in the temperature contours for the two models as seen at the central plane (x=0) from Fig. 8.38. Considering the temperature values along the centerline of the burner, NAFM (with radiation included) predicts lower temperatures when compared with SLFM adiabatic model. Therefore, radiation effects cannot be neglected for swirl flames of this kind. The radiation losses due to emitted species like CO_2 and H_2O are the main source of temperature drop. The flow pattern above the bluff body governs the high temperature region. With radiation effects included in NAFM, this zone of temperature for flame stabilization is spread equally all over above the bluff body. But with the case of SLFM adiabatic model, the flame temperature above the bluff body (Fig. 8.38 - without radiation) is observed to elongate in the axial direction and therefore predicting lower temperatures compared to NAFM case. This gives an indication that radiation effects are controlling the temperature pattern in the re-circulation zones above the bluff body.

With NAFM simulation, the most important observation is that the flame diffuses more in the radial direction (Fig. 8.38). This is due to the strong emitting characteristics of the flame mainly from the products of combustion like CO_2 and H_2O. The amount of heat loss due to radiation to the surroundings is depicted through the spread of temperature in the radial direction all along the flame length as seen from NAFM case (with radiation). The above argument can be supported with the results of instantaneous temperature contour plots as shown in Fig. 8.39. The patches of medium to low temperature are seen around the flame in the entire region. This cluster of temperature zones are due to the radiation heat loss caused from highly emitting products to the surroundings. This results in the radial diffusion of mean temperature as shown in Fig. 8.38.

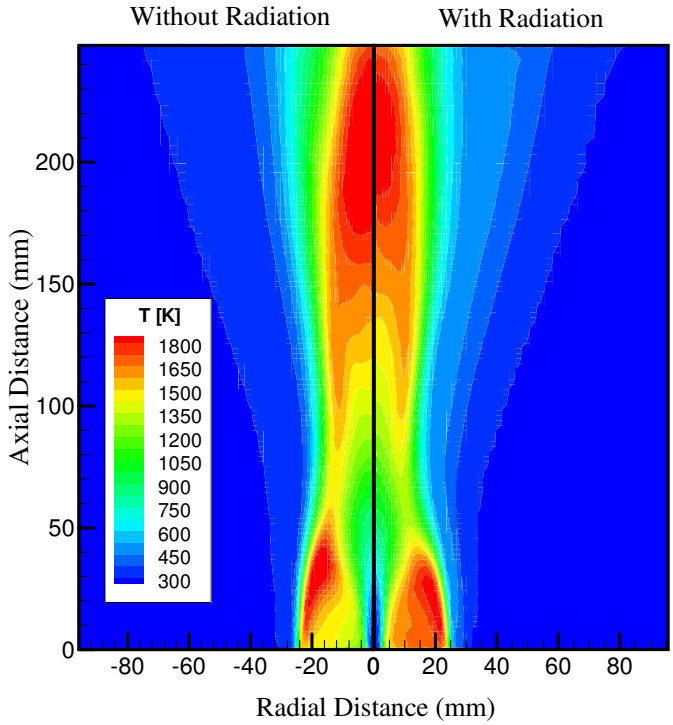

Figure 8.38 Comparison of mean temperature plot at centre plane (a) Without radiation (left) (b) With radiation (right)

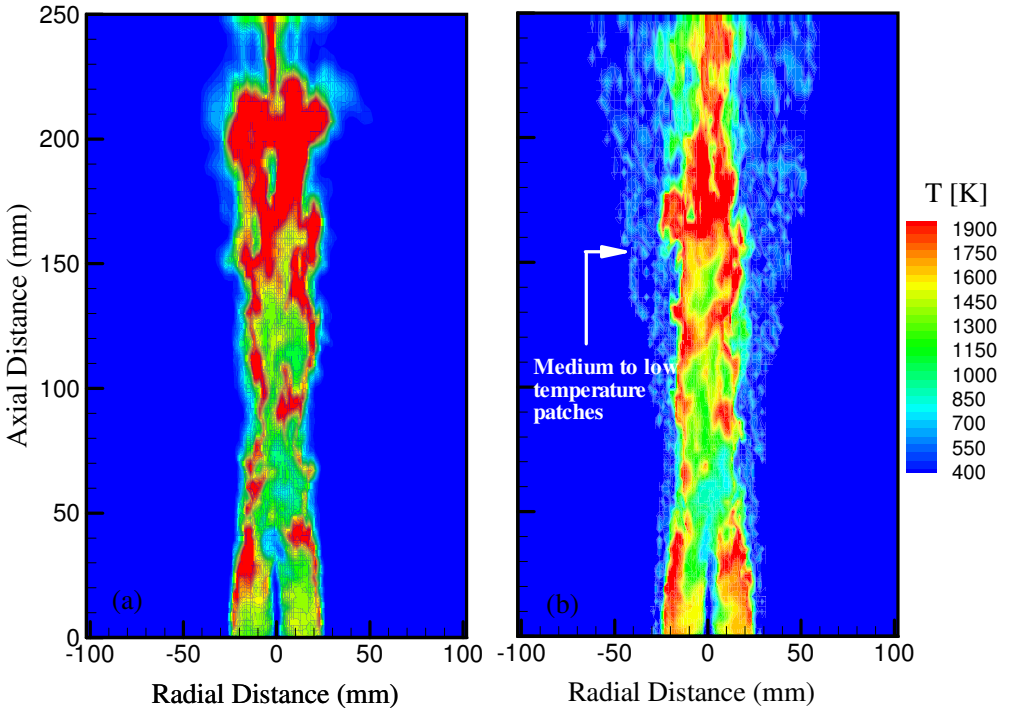

Figure 8.39 Instantaneous temperature comparisons at the centre plane (x=0) (a) Without radiation (b) With radiation

Products of combustion like H_2O and CO_2 are calculated for the present flame configuration. Figure 8.40 and 8.41 shows the predictions of mass fraction of H_2O and CO_2 respectively compared with experiments. H_2O predictions are better captured with simulations with radiation involved. At the initial three locations z/D = {0.2, 0.5, 0.8} simulations without radiation is under-predicted. Radiation calculations are found to predict well very close with the experimental data at these locations. At the remaining locations, downstream of the burner, inclusion of radiation effects seems to improve the results. Results with radiation case are found to be in close agreement with experiments in these downstream locations. The predictions from both numerical models are found to over-predict between r/R=0.4 and r/R=0.8. But results with radiation calculations are found to be in better agreement with experiments.

Temperature measured from experiments at all the axial locations for radial distance r/R = (0.4 to 0.8) from Fig. 8.37 shows lower values when compared with computational results, indicating that radiation losses are very significant in these locations. Mass fraction of CO_2 and H_2O is expected to behave in the similar trend. H_2O mass fraction predictions are observed to follow the similar profiles to that of temperature at almost all axial locations in Fig. 8.40. But with the predictions of mass fraction of CO_2, inclusion of radiation effects is found to over-predict and numerical simulations without radiation case is found to under-predict in the upstream portion of the flame. However, NAFM radiation case is clearly seen to follow similar trend of experimental data all along the radius. At the initial two axial locations, SLFM without radiation case is found to predict a sudden jump (peak) in mass fraction of CO_2 at radial location r/R~0.8. NAFM with radiation case is found to be predicting well with no sudden rise in its values at these radial distances similar to measured values. Based on the results discussed, it can be concluded that radiation plays a vital role in determining the flame characteristics and therefore cannot be neglected for any reacting flow simulation.

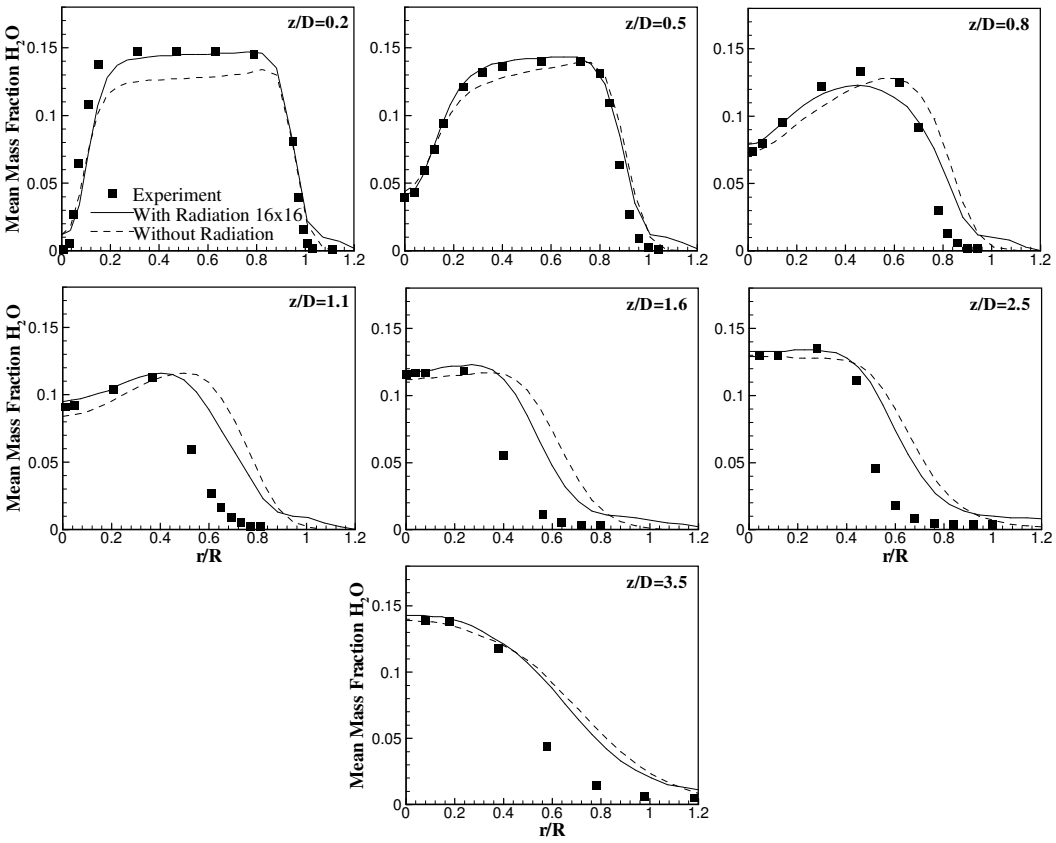

Figure 8.40 Radial plots for mean mass fraction of H_2O at different axial locations

The performance of NAFM is studied with radiation calculations performed for every 0.18 ms in the transient simulation of LES in order to reduce the computational time involved as discussed earlier. Figure 8.37 shows the temperature profiles with the difference between the radiation calculations operated for every time step (With Radiation 16x16) and with an interval of 0.18 ms (With Radiation 16x16-0.18 ms). There is not much difference found in the temperature profiles with the two radiation LES results. Similar results were observed with mixture fraction and other species (not shown). Therefore, it is highly recommended to implement the radiation calculations every 0.18 ms in order to save the computational time. However, the present research deals with radiation calculations every time step in order to attain the highest accuracy in the results. But considering the computational time involved, calculations performed every 0.18 ms would be ideal for inclusion of radiation effects in LES combustion for swirl flames of this category. The reason for under-prediction with SLFM for temperature and species compared to NAFM would be same as explained with HM1 radiation results (Section 8.3.5).

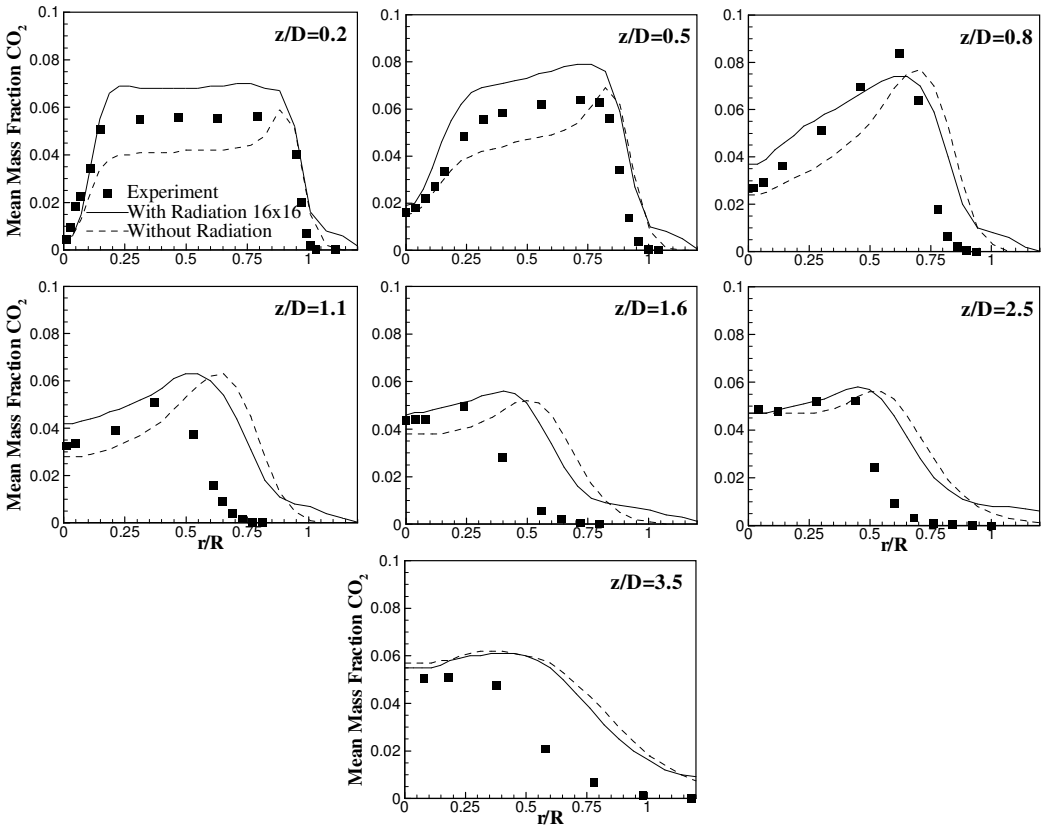

Figure 8.41 Radial plots for mean mass fraction of CO_2 at different axial locations

8.6.3Effect of Number of Rays Fired

A detailed study is conducted for a number of rays to be fired in the DTM code in order to attain the maximum possible accuracy in terms of radiation intensity and source. As specified earlier, considering the computational cost and time required, only two cases are considered in order to study the effect of number of rays fired. Radiative source is considered as the limiting parameter to obtain the optimized value of rays fired. A total of 16x16 and 10x10 rays are found to produce similar values for radiative source and therefore considered to be the best suitable values to test for the present flame configuration. The two different cases with a total of 10x10 and 16x16 rays are considered and their effect on the temperature alone is studied in the present work. Figure 8.37 shows the radial temperature profiles at different axial locations highlighting the difference between the two cases. The plots show a significant difference in the temperature for the number of rays fired. Simulation results with 16x16 shows a near match with the experiments when compared with 10x10 rays at the initial three axial locations z/D={0.2 to 0.8}. Based on the results as depicted in

Fig. 8.37 it is strongly recommended to implement higher order for number of rays to be fired. However, research shows that 16x16 would be ideal for testing the effect of radiation on medium to high luminous flames.

8.7 Effect of Chemical Mechanism

Effect of using different chemical mechanisms which was tested for bluff body flames as discussed earlier in this chapter revealed that there is hardly any influence of chemical mechanism on flame properties. A similar study is conducted for swirl stabilized flames with SMH1 and the results are shown below. Temperature variations with the two chemical mechanisms like GRI 2.11 and GRI 3.0 have been tested and shown in Fig. 8.42.

At all axial locations, there is very minimal effect of chemical mechanisms used. Both the mechanisms behave in the similar way but overall GRI 2.11 can be understood to predict more close with the experiments at the downstream locations. Even though GRI 2.11 over-predicts marginally when compared with GRI 3.0 in the axial locations z/D= {0.2 to 0.8}, GRI 2.11 is found to agree well with the experiments at the centreline locations. Similarly, the results are compared for the product species mass fraction of CO_2 and H_2O for studying the influence of chemical mechanism used and are depicted in Fig. 8.43 and Fig. 8.44 respectively.

Even with the CO_2 concentration plots, at the locations z/D=0.5 and 0.8 predictions at the centerline of the flame jet can be clearly seen in favour of GRI 2.11 mechanism. At the remaining locations, both the mechanisms behave in a similar way. H_2O mass fraction is also observed to predict in the same way as CO_2 concentration with very close agreement between the two mechanisms. Overall GRI 2.11 can be taken with confidence for all simulations to be carried out in future for any combustion simulation related to either swirl based or bluff body based flames. Ravikanti (2008) has experimented with RANS based calculations for various chemical mechanisms other than the GRI mechanisms and concluded with GRI 2.11 to be most favorable chemical mechanism applied to bluff body flames.

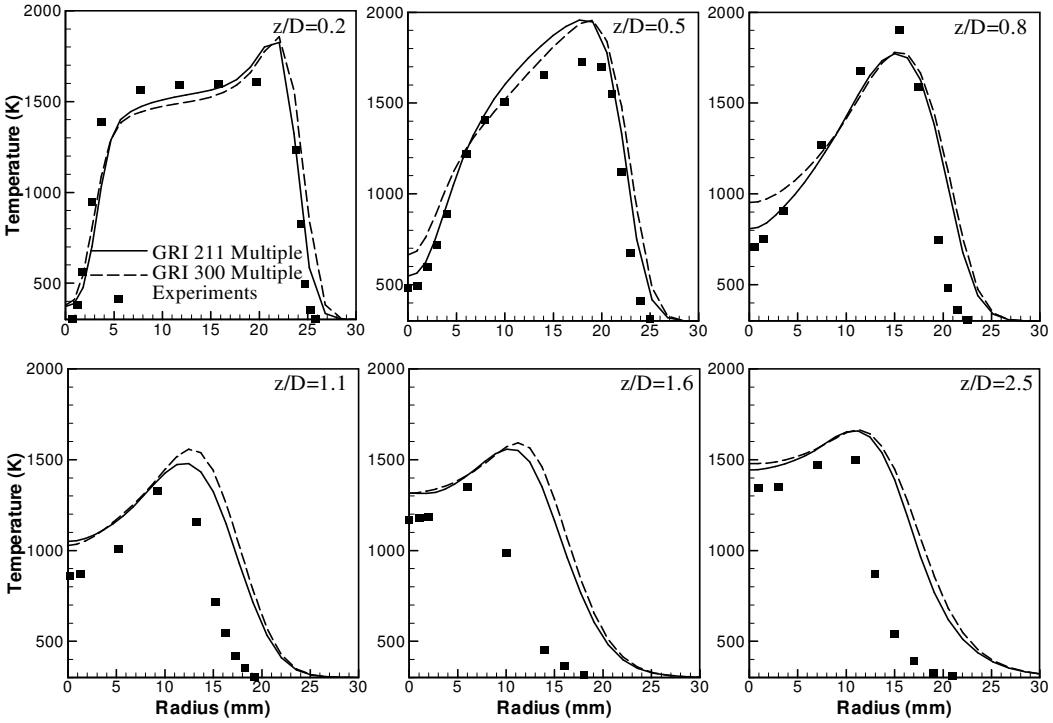

Figure 8.42 Radial plots for mean temperature at different axial locations – comparison for different chemical mechanisms.

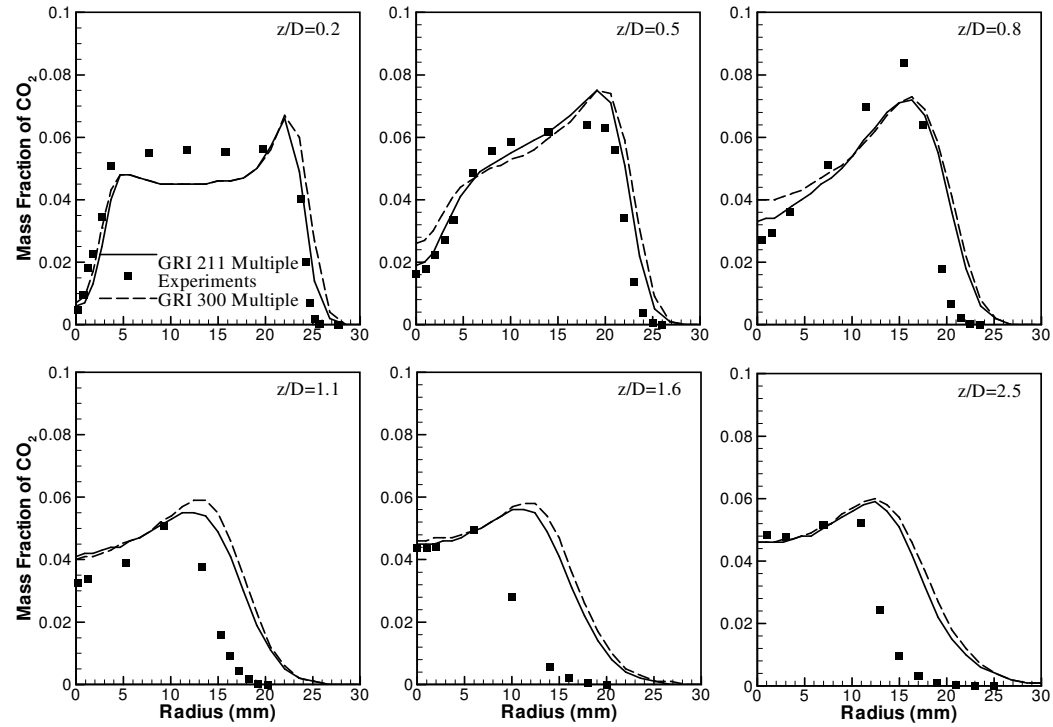

Figure 8.43 Radial plots for mean CO_2 mass fraction at different axial locations – comparison for different chemical mechanisms.

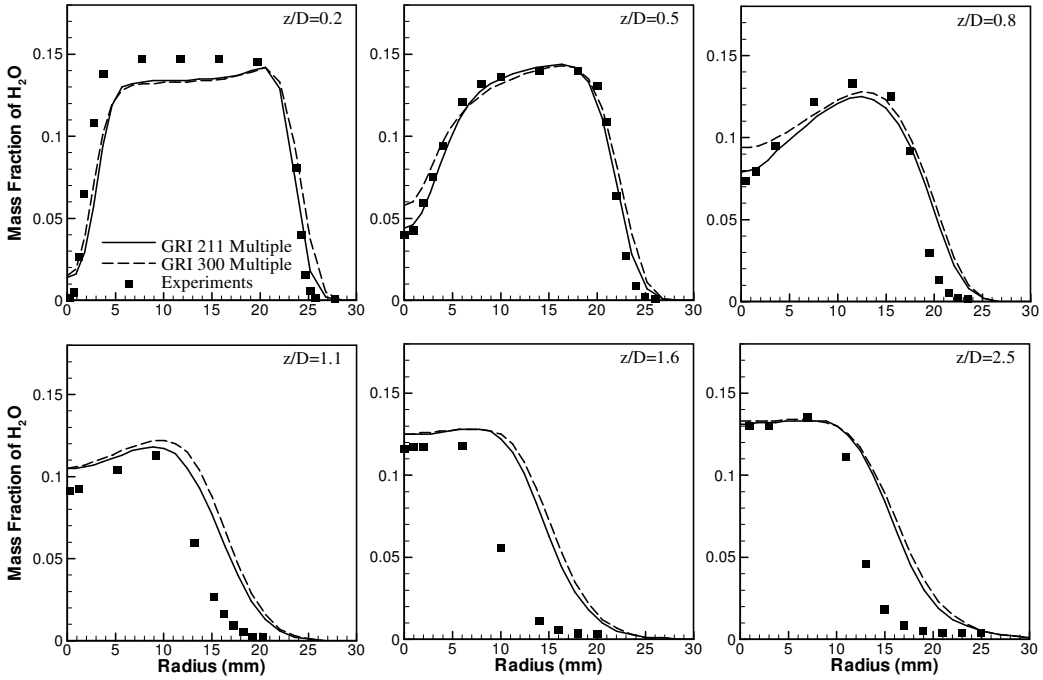

Figure 8.44 Radial plots for mean H_2O mass fraction at different axial locations – comparison for different chemical mechanisms.

8.8 Closure

This chapter provided results and discussion for both bluff body and swirl stabilized flames. SLFM was tested for both HM1 and HM3e bluff body flames and results showed very good agreement with the experimental data. Results obtained from combustion models SLFM and NAFM were discussed for the importance of radiation effects on the flame properties. Inclusion of radiation was shown to predict better for temperature and other major species for both the flames HM1 and SMH1. Influence of chemical mechanism used was also discussed. GRI 2.11 was found to be performing better when compared to GRI 3.0 mechanism for both the flames HM1 and SMH1.

Chapter 9

Partially Premixed Combustion – An UFPV Approach

This chapter presents the application of the combustion model called UFPV (Unsteady Flamelet Progress Variable) towards the numerical prediction of turbulent partially premixed lifted flames. This model is tested for the first time with partially premixed flame conditions for its capability to reproduce the lifted flame diagnostics. Additionally, LES based modelling has been carried out with SLFM to confirm its limitations and advantages. Testing this model needs a comprehensive detailed experimental data for its comparison. In this regard, the test case selected for modelling is the Berkeley CH_4/air and H_2/N_2 lifted jet flame in vitiated co-flow, experimentally studied by Cabra *et al.* (2005). The vitiated co-flow works in similar conditions to those encountered in real gas turbine combustors and furnaces when a partially premixed fuel interacts with recirculating hot combustion products. In addition, the vitiated co-flow introduces auto-ignition as a possible mechanism for flame stabilization in addition to premixed flamelet front propagation (Cabra *et al.*, 2005).

Validation of the current combustion model is performed by carrying out studies with two different fuel and co-flow inlet compositions. Both methane and hydrogen based fuels are tested for the strengths and weaknesses of UPFV approach to its application with lifted flames. Details of these two flames tested are discussed later in the chapter. Section 9.1 provides complete details of the burner configuration with boundary conditions for the test case. Computational description of the flame conditions is presented in section 9.2 applied for LES with domain under investigation and grid details required to ensure maximum possible resolution for the present test case. Results and discussion is divided into two major sections dealing with results from methane and hydrogen based flames separately. Pre-integrated lookup tables which are generated prior to LES calculations for two different fuel compositions are

utilized. SLFM calculations are performed on CH_4/Air flame alone and compared with UFPV in order to highlight the differences in their predicting capabilities towards partially premixed flame category.

9.1 Experimental Details of the Burner

A schematic of the burner used for the experimental investigation of the partially premixed lifted jet flame by Cabra *et al.* (2005) is shown in Fig. 9.1. The burner has two set of experimental data for different fuel compositions. The first set of data is for CH_4/Air as the fuel jet inlet with vitiated co-flow of H_2/Air and second set is for H_2/N_2 as fuel and H_2/Air as co-flow inlet. The present combustion model is tested for both these configurations and results are compared with experiments. The burner consists of a central nozzle with inner diameter (D) of 4.57 mm and outer diameter of 6.35 mm. A perforated plate of 210 mm diameter through which vitiated co-flow of air is issued surrounds the central nozzle. A flow blockage of 85% was reported with 2200 holes drilled in it. The vitiated co-flow consists of products of lean premixed H_2/Air flame with an equivalence ratio of 0.4. The entrainment of ambient air into the co-flow has been delayed by incorporating an exit collar which surrounds the perforated plate. The fuel jet consisting of a mixture of 33% CH_4 and 67% air is issued from the central nozzle for the first set of data and 25% H_2 and 75% N_2 for the second. Table 9.1 shows the details of the two fuel compositions and their inlet conditions. *Fuel jet varies for the two flame configurations: 1) CH_4/Air 2) H_2/N_2

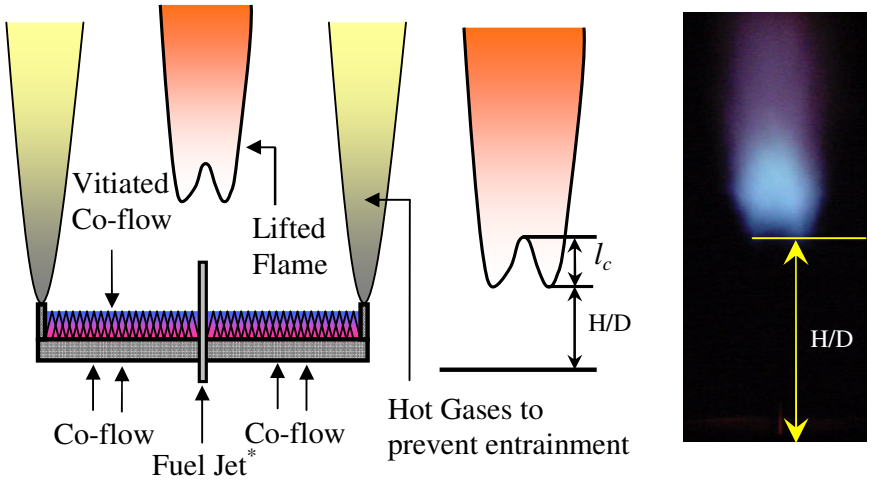

Figure 9.1: Schematic of the burner geometry
(From: http://www.me.berkeley.edu/cal/VCB/Data/)

Experimentally captured image of the lifted flame (right most picture in Fig. 9.1) is captured through the luminosity of the flame CH_4/Air. The lift-off height H/D technically corresponds to an average stabilization position of the flame. The absolute lift-off height H has been determined in the measurements by considering the lowest point where the luminosity of the flame has been detected. For the baseline conditions, the measured mean lift-off height normalized over fuel jet diameter has been reported to be H/D ~ 35 for CH_4/Air flame. It has also been observed in the experiments that the lifted flame base is highly unstable and fluctuates by several times the jet diameter thereby resulting in extinction and re-ignition for this flame conditions. The current lifted jet flame thus tests the capability of UFPV model to predict the extinction and re-ignition phenomena as well.

Table 9.1 Details of the two lifted flame configurations – Berkeley flames

	H_2/N_2 Flame		CH_4/Air Flame	
	Jet	Co-flow	Jet	Co-flow
Re	23,600	18,600	28,000	23,300
V (m/s)	107	3.5	100	5.4
T (K)	305	1045	300	1355
X_{O2}	0.0021	0.15	0.15	0.12
X_{N2}	0.74	0.75	0.52	0.73
X_{H2O}	0.0015	0.099	0.0029	0.15
X_{OH}(ppm)	<1	<1	<1	200
X_{H2}	0.25	5×10^{-4}	100	100
X_{CH4}	-	-	0.33	0.0003
f_{st}	0.47		0.17	

Cabra *et al.* (2005) performed numerical studies on the sensitivity of the flame lift off height with respect to jet and co-flow velocities. Studies also included detailed description on effect of co-flow temperature on lift off height using joint PDF calculations with modified-curl mixing model. A marginal drop in co-flow temperature was found to increase the lift-off height twice in its length. An important result from the parametric study was that auto-ignition of very lean mixtures which have the shortest ignition delay might be the controlling mechanism. This was based on the argument that the modified-curl mixing model which relies entirely on auto-ignition for initial flame stabilization was able to capture the measured sensitivity of lift-off height to co-flow temperature. However, the experimental scattered data although limited with respect to number of measured locations, did not show such a

preference for reactivity at very lean mixtures and hence the relative importance of auto-ignition and turbulent flame propagation in stabilizing these flames has to be understood in detail.

9.2 Computational Setup for LES

The computational domain has dimensions of 200 x 200 x 410 (all dimensions are in mm) in x, y and z directions respectively. The axial distance of approximately 90 jet diameters and the burner width of approximately 44 jet diameters is used in order to account the independency of flow entrainment from the surroundings. An inlet jet velocity is specified with a $1/7^{th}$ power law profile. Measured co-flow mean velocity profiles at the burner exit plane were found to be more or less uniform (Cabra *et al.*, 2005) and therefore plug flow has been specified along the co-flow inlet in the computations. Convective outlet boundary condition is used at the outlet surface and all the walls and co-flow boundaries in the domain have been treated as adiabatic. At both fuel and co-flow inlet, turbulent fluctuations have been superimposed on the mean velocity by scaling the measured RMS values of turbulent fluctuations with random numbers obtained from a Gaussian distribution. At the fuel inlet, filtered mixture fraction has been set to unity while it has been specified as zero at the co-flow inlet. For the UFPV model, the filtered progress variable is set to zero at both the inlets. Cartesian staggered non-uniform grid distribution of 85 x 85 x 150 in the x, y and z directions to discretize the domain is used. The grid details are depicted in the Fig. 9.2.

An ignition source is provided with a progress variable of 0.9 patched in the region of best mixed fuel air mixture. The average time to run the simulation on a 4GHz memory machine with single processor for each case with flames with different fuel compositions takes around 40 days for the flow to stabilize (t=40 ms) and thereafter 20 days for the collection of statistics (t=20ms) for post processing. A total time of 60ms is considered for each simulation. Adequate samples have been collected in the statistics collection phase of the run by allowing for a minimum of 7 flow passes. The calculations have been advanced in time with a time step such that the variation in Courant number was limited to the range, 0.2 to 0.8.

The validation of the combustion model is performed by comparison of radial plots at different axial locations (normalized by bluff body diameter) for temperature and all other species mass fractions i.e., at z/D = 1.0, 15.0, 30.0, 40.0, 50.0 and 70.0. The results are discussed in detail later in this chapter. For the simulation with SLFM model, the modeled scalar dissipation rate (Equation 4.20) has been found to result in instability in the beginning of the calculations due to significant fluctuations in density. To overcome this problem, LES calculation with SLFM has been carried out initially with a constant scalar dissipation rate corresponding to equilibrium conditions for a minimum of two flow-passes (~10 ms). The instantaneous solution at the end of this calculation has then been used as initial conditions for the main calculation where variation in scalar dissipation was accounted. For the simulations with UFPV models, no such instability issues have been observed.

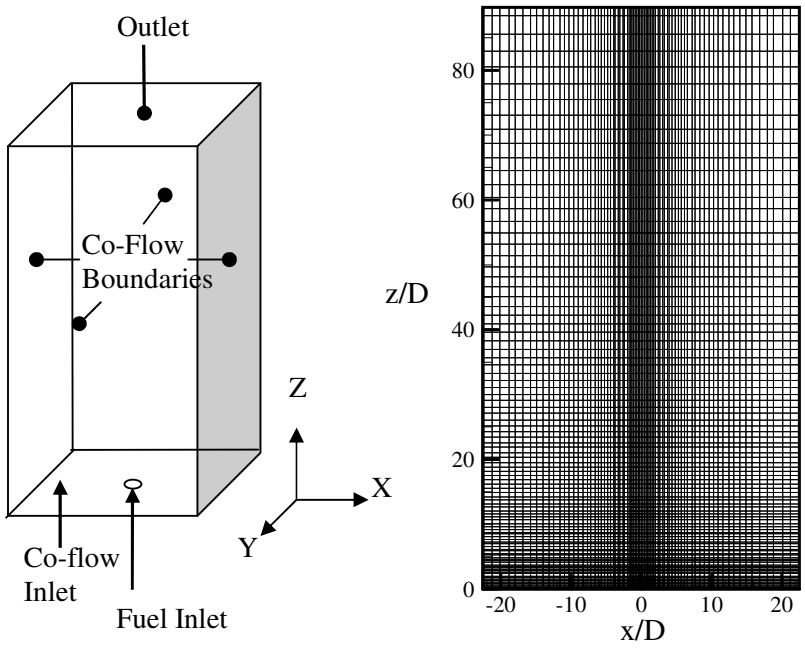

Figure 9.2 Details of computational grid and domain with boundary conditions specified – Berkeley Flame

9.3 Results and Discussion

This section is divided into two set of results. Initially, the predictions for CH_4/Air flame are discussed and later with H_2/N_2 flame. Results include the radial comparisons for mixture fraction, temperature and other major species at different axial locations along the burner. Scattered data is also compared at the locations of

interest for the prediction of flame extinction and re-ignition. The flame lift off is compared for both the flames with their corresponding experimental values with respect to the co-flow temperature. Also the definition of lift off height with mass fraction of OH is discussed for H_2/N_2 flame based on past research strategies.

9.3.1Performance of SLFM & UFPV Models – CH_4/Air Flame

Firstly, the predictions of mixture fraction distribution are presented for UFPV model compared with experiments. The predicting capabilities of using UFPV model compared with SLFM approach is also considered for the lifted flame category, followed by temperature and other species predictions. Finally the scattered data is compared for the flame instablity issues. Unsteady characteristics of the flame related to extinction and re-ignition is better understood with scattered data.

The radial mean mixture fraction at z/D locations of 1.0, 15.0, 30.0, 40.0, 50.0 and 70.0 are depicted in Fig. 9.3. The locations at z/D = 40.0, 50.0 and 70.0 on the downstream of the burner are the positions where predictions are difficult to capture numerically as the flame is expected to behave more dynamic and unstable in nature. Centreline mixture fraction is always found to under-predict at all the locations with SLFM. Whereas the predictions with UFPV is found to be in better agreement with the experiments. However, there is a little over-prediction in the radial direction at the first three axial locations. But compared to SLFM approach, UFPV model is found to predict better. Considering the effect of scalar dissipation rate coupled with unsteady flamelet progress variable concept proved to be beneficial for predictions of conserved scalar, mixture fraction when applied to lifted flames of the present kind.

The flame lift-off (Fig. 9.4) in the present work is considered as the height from the base where the temperature is equal to the co-flow temperature (1355K). Lift-off height is represented in terms of H/D where H is the axial distance from the base of the burner jet. Experimentally found value of H/D is 35 which was captured visually based on the flame luminosity. Here the numerical lift-off is found to be around 42 with the UFPV model. The discrepancy of the lift off height with experiments is about 20%. This over-prediction may be due to the highly fluctuating nature of the flame and also due to the co-flow temperature cutoff concept that has been chosen to obtain

this lift off height. Comparisons were also performed with SLFM. Figure 9.4 (b) shows the incapability of SLFM model to predict the lift off height. SLFM shows a flame attached to the burner base and therefore is not capable for predicting lifted flames of this category.

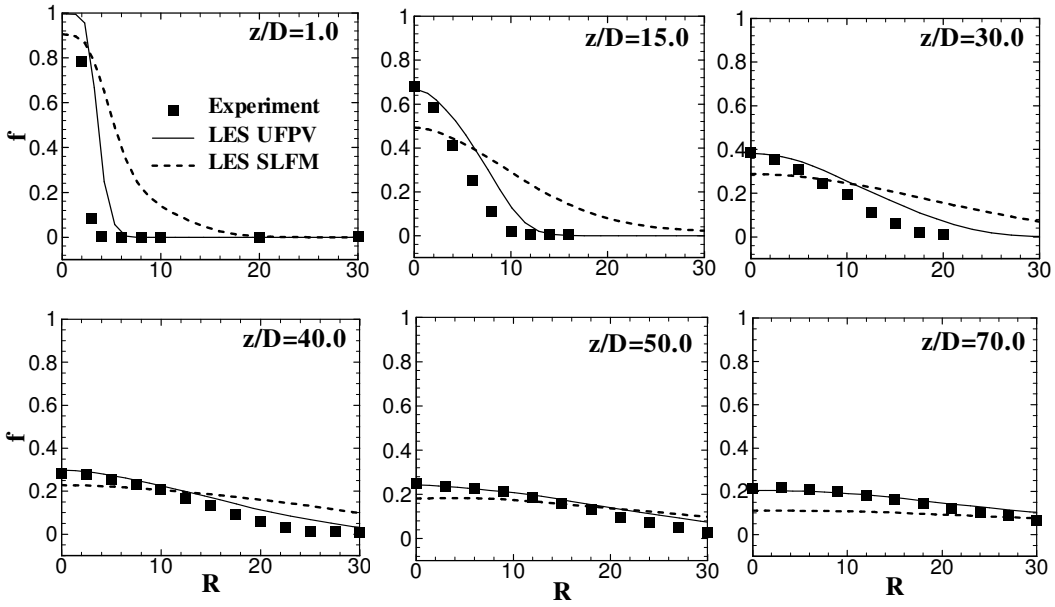

Figure 9.3 Radial plots of mixture fraction at various axial locations along the burner axis for CH_4/Air Flame

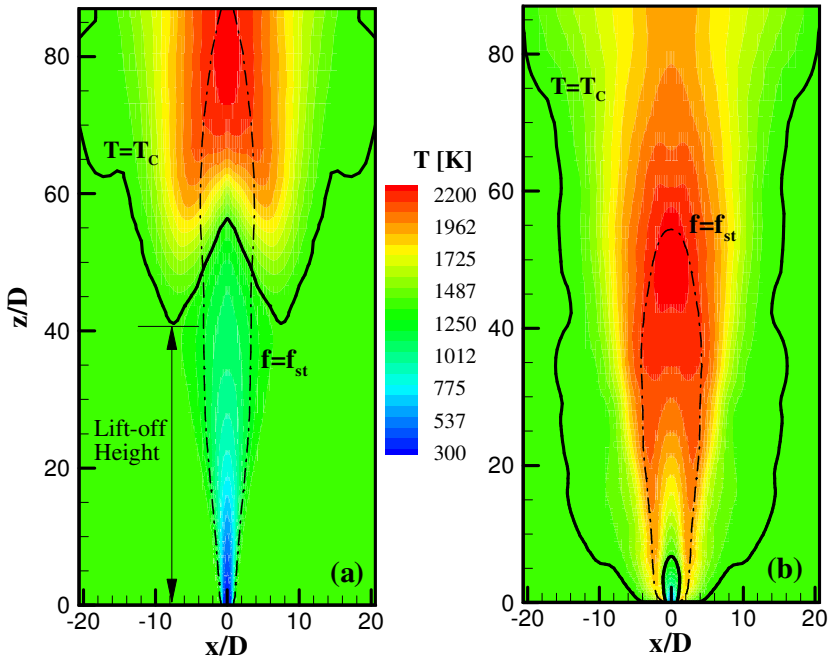

Figure 9.4 Temperature contours plot for comparison of SLFM and UFPV (a) UFPV (b) SLFM for CH_4/Air flame

Figure 9.5 shows the radial plots of temperature predictions which are found to be resonably good at the first three locations with UFPV, but under-predicted at locations z/D={40.0,50.0}. As mentioned earlier, this zone of the flame is considered as highly fluctuating and subjected to extintion and re-ignition. At the last location z/D=70.0, centreline temperature is found to be very close to the experiments. Overall, it can be concluded that except at the location z/D=50.0 predictions are reasonably good with UFPV. The UFPV model appears to be partially successful in capturing extinction and re-ignition effects.

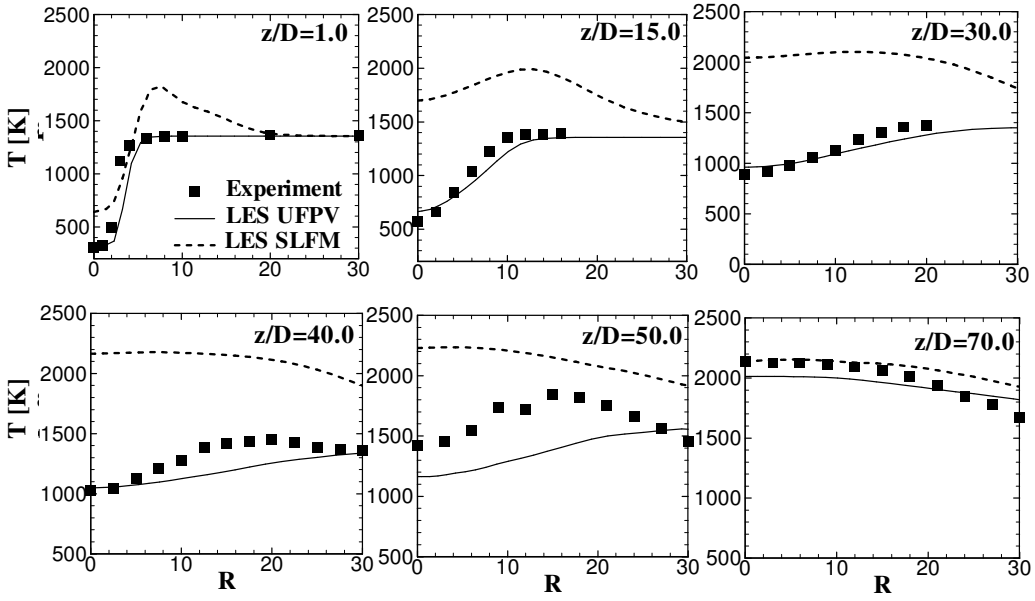

Figure 9.5 Radial plots of temperature at various axial locations along the burner axis for CH_4/Air Flame

Flame extinction and re-ignition can be represented with scattered data of temperature versus mixture fraction. Data is collected for all the axial location planes of interest and found that locations z/D={50.0,70.0} are prone to maximum flame instability where flame fluctuates with near blow-off and re-attaching features. Figure 9.6 shows scattered data for temperature at the last locations z/D=50.0 and 70.0. Left hand side figures (Fig 9.6(a) and Fig. 9.6(b)) represent experimental data and the right hand side plots (Fig 9.6(c) and Fig. 9.6(d)) shows the numerical calculations. At location z/D=70 flame conditions are almost close to equilibrium and UFPV is found to compare reasonably well with experiments with marginal under-prediction in peak temperatures close to equilibrium. Experimentally the temperatures vary from equilibrium to mixing as the flame tries to detach and re-ignite in the regions from

z/D~35 to 60. As the numerical simulation predicted a lift-off of around 42, it suggests that numerical predictions for scattered data at the location z/D=50.0 is most likely to show data biased towards mixing hence the observed discrepancy.

Scattered data is compared only at locations z/D={50.0,70.0}. Any location below z/D=50.0 should resemble only pure mixing limit. At the location plane z/D=50.0, the maximum temperature close to equilibrium is under-predicted but the mixture fraction limits agree well at all locations. Reasonably good agreement with the experiments for temperature for both radial and scattered plots at most locations except at z/D=50.0 shows the capability of the UFPV approach for the modelling of lifted flame physics.

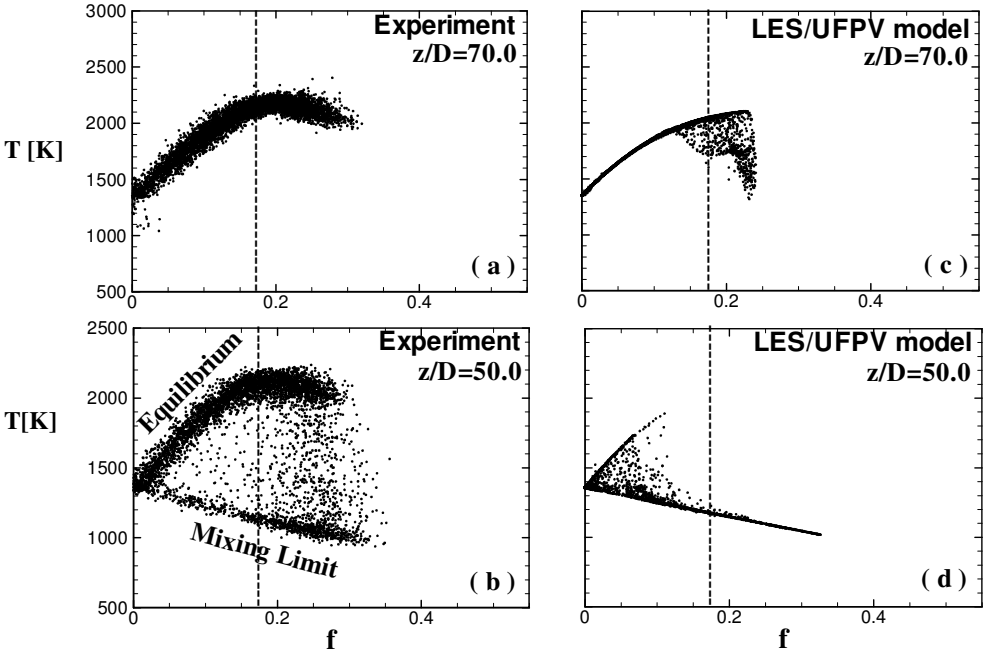

Figure 9.6 Scattered temperature data plotted against mixture fraction at specific axial locations

The definition of progress variable includes the summation of mass fractions of CO_2 and CO in the present simulation for UFPV of CH_4/Air flame. Therefore, species predictions like CO_2 and CO takes a similar form of the progress variable distribution rather than on their individual distributions and the definition of progress variable distinguishes the flame properties with burnt and unburnt mixture varying from 0 to 1. While the mass fraction of H_2O can be computed from the present simulations for the comparison with experiments as this scalar is not involved in the definition and solution of progress variable equation. Figure 9.7 shows the radial plots of mean mass

fraction of H_2O at the specified axial locations. Mass fraction of H_2O is found to follow a similar trend to that of temperature. It is observed to have a marginal under-prediction along the radial distance at the axial locations z/D={15.0 to 50.0} but predicts well when compared with SLFM. As mentioned earlier in temeprature predictions, at axial location of z/D=50.0, UFPV under-predicts to large extent. Highly fluctuating flame charactertics in this axial region might be the reason for this deviation. SLFM was not able to predict the flame lift off as discussed earlier. This lead to an over-prediction in temperature profile and therefore is the main cause for over-predictions in H_2O mass fraction as well at all the axial locations as shown in Fig. 9.7.

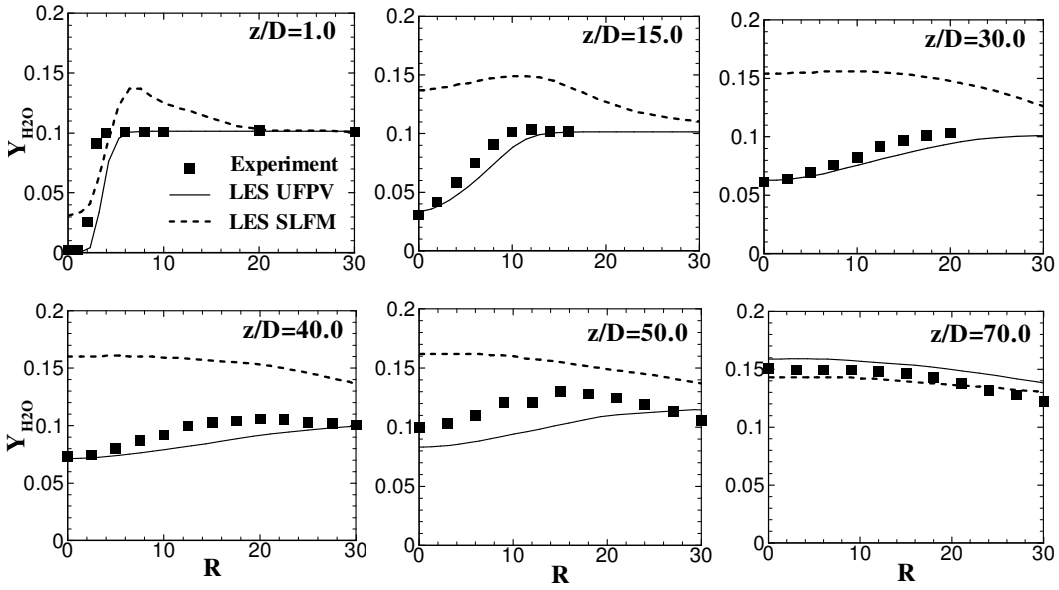

Figure 9.7 Radial plots of mean mass fraction of H_2O at various axial locations along the burner axis for CH_4/Air Flame

Production rate of CO_2 and CO are included in the calculation of source term for solving progress variable equation. Numerical results from these species would give little significance as the predictions would follow the same trend as of progress variable. However, the present work deals with the results and discussion of these two species for the complete analysis of species comparisons. The contours of mean mass fraction of CO_2 are shown in Fig. 9.8. The profiles replicate the temperature distribution pattern of the flame lift off and therefore any values below z/D=42 gives a value close to zero for CO_2 and CO mass fraction. Hence, we compare only at axial locations of z/D=50.0 and 70.0. SLFM shows an over-prediction in values as shown

in Fig. 9.9 while UFPV under-predicts. This pattern is similar to the trend followed by temperature and mass fraction of H_2O (Fig. 9.5 and Fig. 9.7) at these two locations. As the flame lift is found to be over-predicted with UFPV, H_2O and CO_2 mass fractions are found to be under-predicted with equal proportions. Flame fluctuations are found to be occuring more in the axial region of z/D=35 to 60 which can be a possible reason for descripancy in the results at z/D=50.0. But at location z/D=70.0, CO_2 mass fraction has a good agreement with the experiments for both the models.

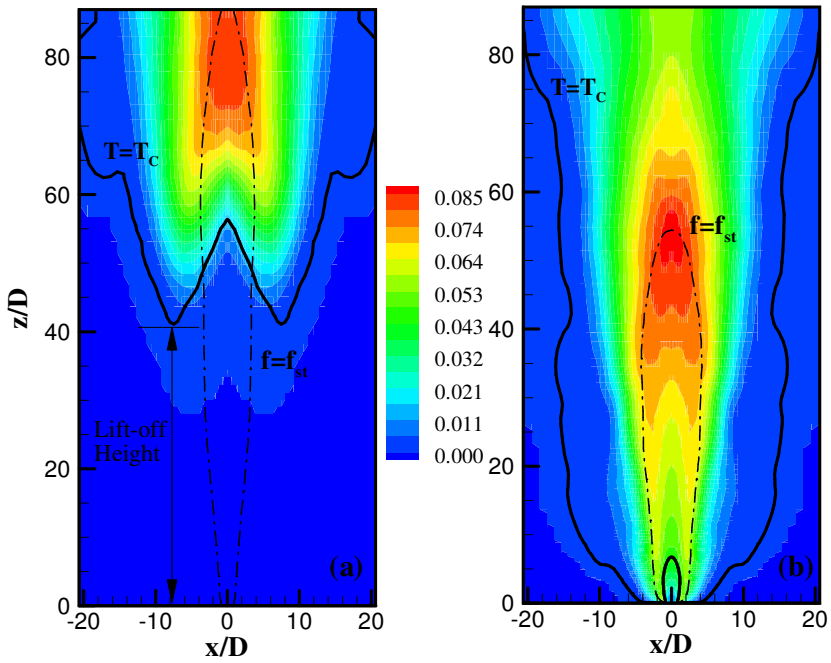

Figure 9.8 Mass fraction of CO_2 contours plot for comparison of SLFM and UFPV (a) UFPV (b) SLFM

The mean mass fraction of CO predictions are shown in Fig. 9.10 at the two aforementioned axial locations. UFPV is found to under-predict at z/D=50.0 while SLFM has a close agreement with the measurements. But at location z/D=70.0 UFPV performs better compared with SLFM. Therefore, the two contradicting arguments with CO mass fraction predictions indicates that definition of progress variable can be altered in future work in order to predict CO_2 and CO in a better way. However, considering the model contraints, the present simulation results with UFPV is favorable to recommend this combustion model for any partially premixed lifted flame. The predicting capabilities of UFPV is further tested with a different fuel configuration (H_2/N_2) and their results are presented next. Because SLFM failed to

predict the structure of lifted flames, results of H_2/N_2 flame deal only with UFPV approach and compared with measurements.

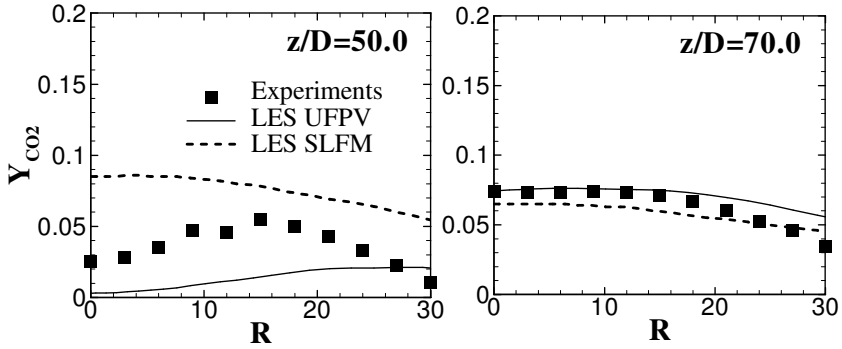

Figure 9.9 Radial plots of mean mass fraction of CO_2 at two axial locations along the burner axis for CH_4/Air Flame

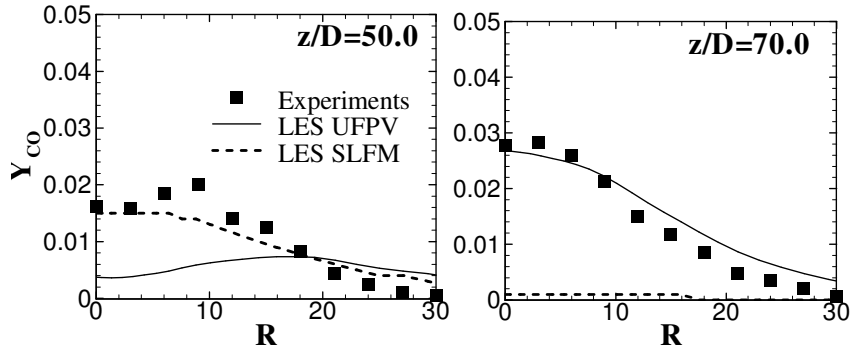

Figure 9.10 Radial plots of mean mass fraction of CO at two axial locations along the burner axis for CH_4/Air Flame

9.3.2Performance of UFPV Model – H_2/N_2 Flame

Similar to CH_4/Air flame, this section discusses the performance capabilities of UFPV model with mixture fraction, temperature and OH mass fraction plots for H_2/N_2 flame. The structure of the H_2/N_2 lifted turbulent flame is investigated by examing the comparisons at the axial locations z/D={1.0,8.0,9.0,10.0,11.0,14.0}. The mean mixture fraction at these locations is found to be very well predicted by UFPV as shown in Fig. 9.11. It is however clear that there is a very marginal over-prediction radially but the overall comparison with the experimental data is very encouraging. Jones and Navarro-Martinez (2007) studied this flame configuration with Eulerian stochastic field method to the solution of the subgrid joint PDF using LES. UFPV combustion model is found to be better in predicting the mixing field when compared with the results of Jones and Navarro-Martinez (2007).

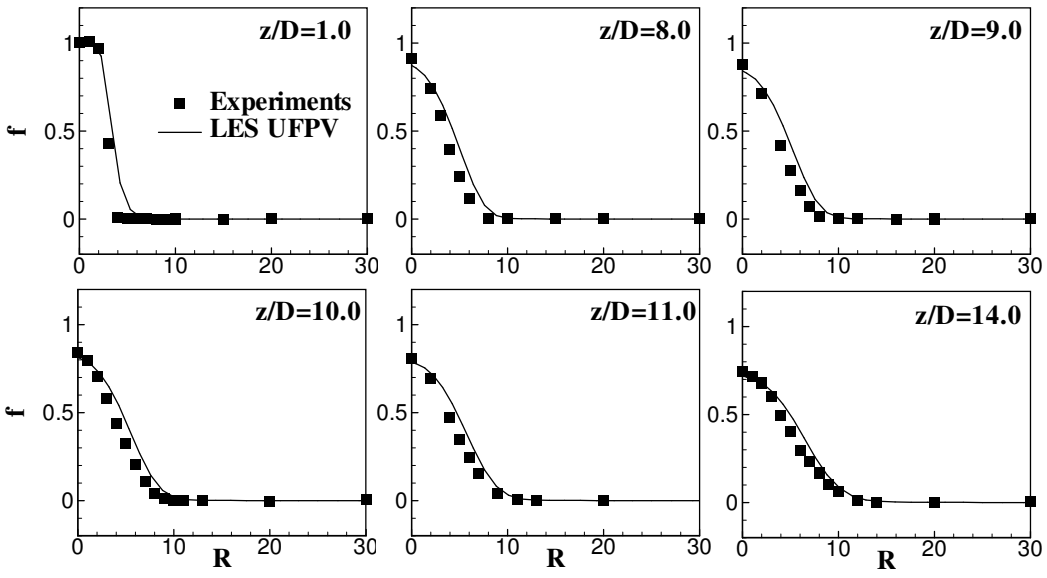

Figure 9.11 Radial plots of mixture fraction at various axial locations along the burner axis for H_2/N_2 Flame

Mixture fraction and temperature are closely related with the unsteady flamelet solution through the PDF look-up tables generated prior to the LES calculations. Therefore, any marginal discrepancy in the mixture fraction predictions should alter the mean radial temperatures. Figure 9.12 shows the radial plot comparisons for temperatures at different axial locations. Eventhough the radial mixture fraction predictions are good, temperature plots show an over-prediction at locations z/D={8.0 to 10.0} radially at around 6~9mm. The sudden rise in temperature at this radial location calculated numerically indicates that the flame base is not lifted. But at the same radial location experimental data does not show any sudden rise in the temperature. This is because experimentally observed lift-off height was found as H/D=10 which is higher than the axial locations z/D=1.0 to 10.0. Hence at the higher axial location z/D=11.0 the peak rise in temperature is numerically well predicted because this location falls well above the desired lift off height of experiments. As mentioned earlier the work of Jones and Navarro-Martinez (2007) the temperature predictions were found to over-predict by a large margin. Results from their studies showed that as the co-flow temperature was increased, the lift-off height decreased. For the co-flow temperature of 1045 K, their studies showed an over-prediction in the temperature profiles at the above mentioned axial locations. But the present UFPV model has the advantage of producing better and closer predictions compared to the

above. Figure 9.13 depicts the flame base with a flame lift based on the co-flow temperature boundary line (1045K) and numerically calculated lift off is found to be in the order of z/D~5.0. This is considerable under-prediction in lift-off height. The dotted line represents the stoichiometric mixture fraction locations (f=f_{st}=0.47). The temperature range from minimum to maximum is 1045 to 1413K (a very narrow range), therefore from a temperature contour alone it is difficult to judge the lift off height accurately.

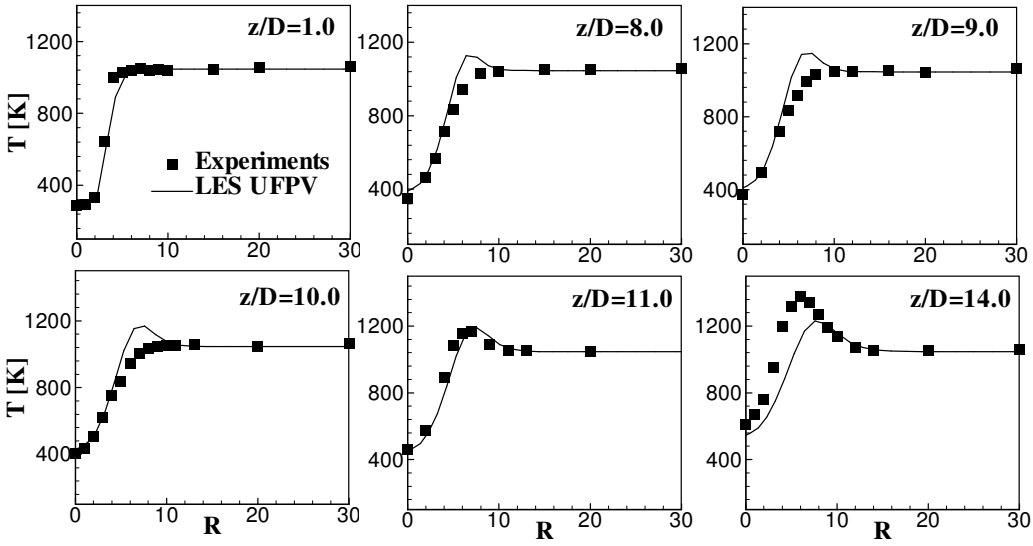

Figure 9.12 Radial plots of temperature at various axial locations along the burner axis for H_2/N_2 Flame

Cabra *et al.* (2002) conducted both experimental and numerical studies of the present flame. They defined lift off height in terms of OH mass fraction instead of using co-flow temperature as the demarcation line. The iso-contours of mass fraction of OH equal to 600ppm was considered for the determination of lift off height in their studies. But it is to be noted that the present simulation of UFPV utilises the value of OH mass fraction in the definition of progress variable and production rate of OH is used for the calculation of source term which is provided as an input source for progress variable equation. Therefore, OH mass fraction predictions from this UFPV model might deviate when compared with experiments as the OH mass fraction is expected to follow the progress variable distribution instead. The time averaged data of OH mass fraction has a maximum value of 573 ppm in the present simulation but instantaneous values give a maximum value of 1273 ppm at the centre plane (x=0). Figure 9.14 shows the mean mass fraction of OH contours. An isocontour of 600 ppm

OH mass fraction is not possible from this contour plot. An instantaneous contour plot of OH mass fraction as shown in Fig. 9.15, highlighted with the isocounters of OH mass fraction equal to 600 ppm with the solid lines. The minimum lift off limit for this mass fraction is around at z/D=7.0. This value is slightly better than the lift off height observed with temperature contours.

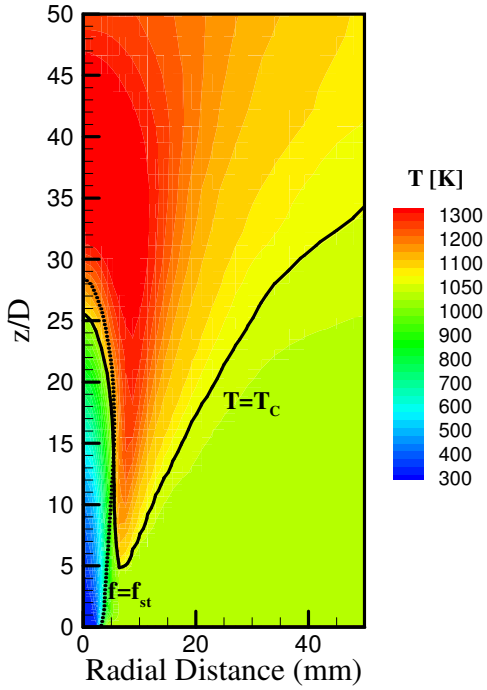

Figure 9.13 Temperature contour plot for the observation of lift-off at the centre plane for H_2-N_2 flame

Similar studies were conducted by Cao *et al.* (2005) on this flame to predict its flame characteristics. The lift off height in their studies based on the OH mass fraction where the iso-contour of Favre mean OH mass fraction equal to 200 ppm at any radius was considered. Therefore, based on this assumption, the current UFPV model predicts a lift off (H/D) equal to 5.5 as depicted in Fig. 9.16. Therefore, whatever may the the selection criteria for flame liftoff height, the present UFPV model results in H/D value close to 5.0. Eventhough the present UPFV model is underpredicting lift off height by 50 %, lifted flame of this kind is said to be partially successful to model and predict the flame lift off from the base.

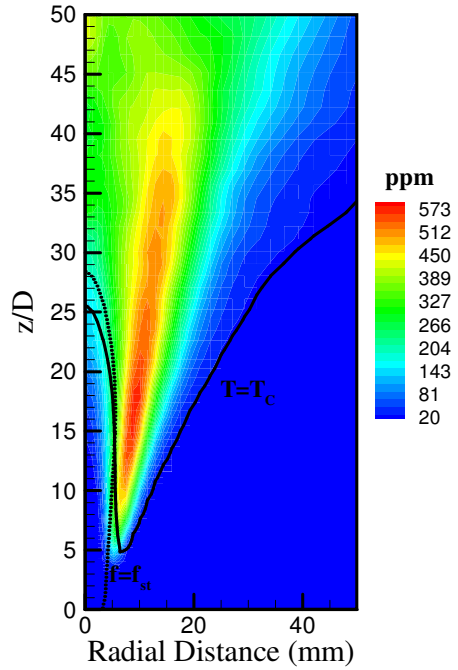

Figure 9.14 Contour plot of averaged OH mass fraction (ppm) for the observation of lift-off at the centre plane for H_2-N_2 flame

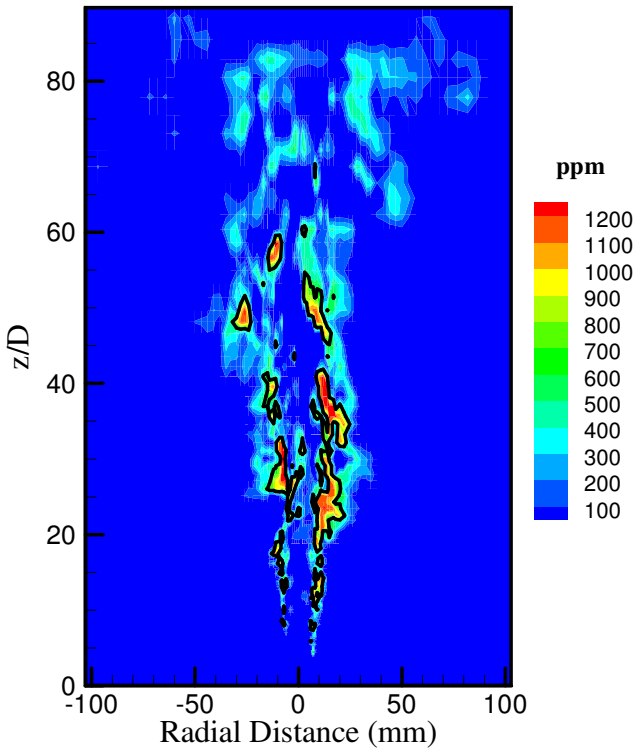

Figure 9.15 Contour plot of instantaneous OH mass fraction (ppm) for the observation of lift-off at the centre plane for H_2-N_2 flame

As discussed earlier, scattered data of temperature with respect to mixture fraction defines the instability associated with any flame. Figure 9.17 shows the experimental data at various axial locations while Fig. 9.18 depicts the computationally calculated data at the same specified locations. It is to be noted that computational scattered data is extracted for a particular time equal to 5ms in the present work. Mixing limits at the locations z/D={8,9,10,11} are observed more with experimental data. But numerical calculations does not show any sign of mixing characteristics. However, the burning region above the mixing is well captured with UFPV. The flame lift off height as found from the temperature coflow boundary line is under-predicted from simulations (H/D=5), pure mixing of fuel and oxidizer is minimised at all locations and hence the descrepency with the experiments as the experimental lift off is at H/D=10. Therefore, prediction of mixing limit depends very much on the flame lift. At the last two locations z/D={14,26}, UFPV model is found to predict well with the experimental data. Peak temperatures near equilibrium is also well captured at almost all locations.

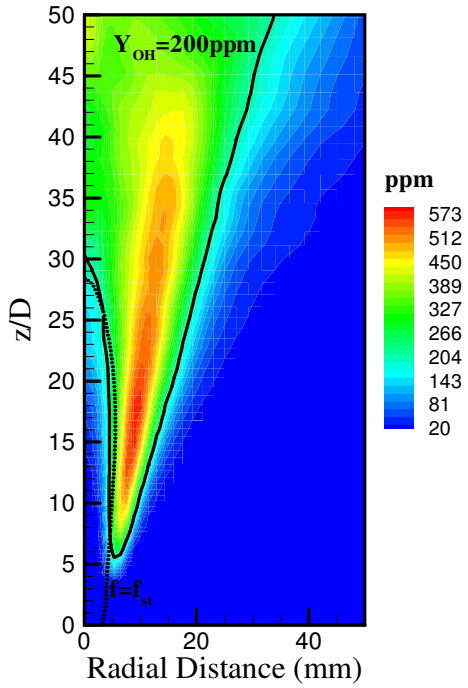

Figure 9.16 Contour plot of averaged OH mass fraction (ppm) for the observation of lift-off at the centre plane for H_2-N_2 flame with 200ppm iso-contour line

Therefore, relating to the above conclusions and results for lift off height, the definition of progress variable can be tested with some other parameter like the maximum temperature instead of using maximum value of OH mass fraction to

consider better predictions of OH for this particular flame. Based on overall observations and constraints involved, the present combustion model forms one of the best choice for application towards the simulation of lifted flames. Futher improvements to this model can be made (i) by the inclusion of radiation and (ii) by changing the definition of progress variable.

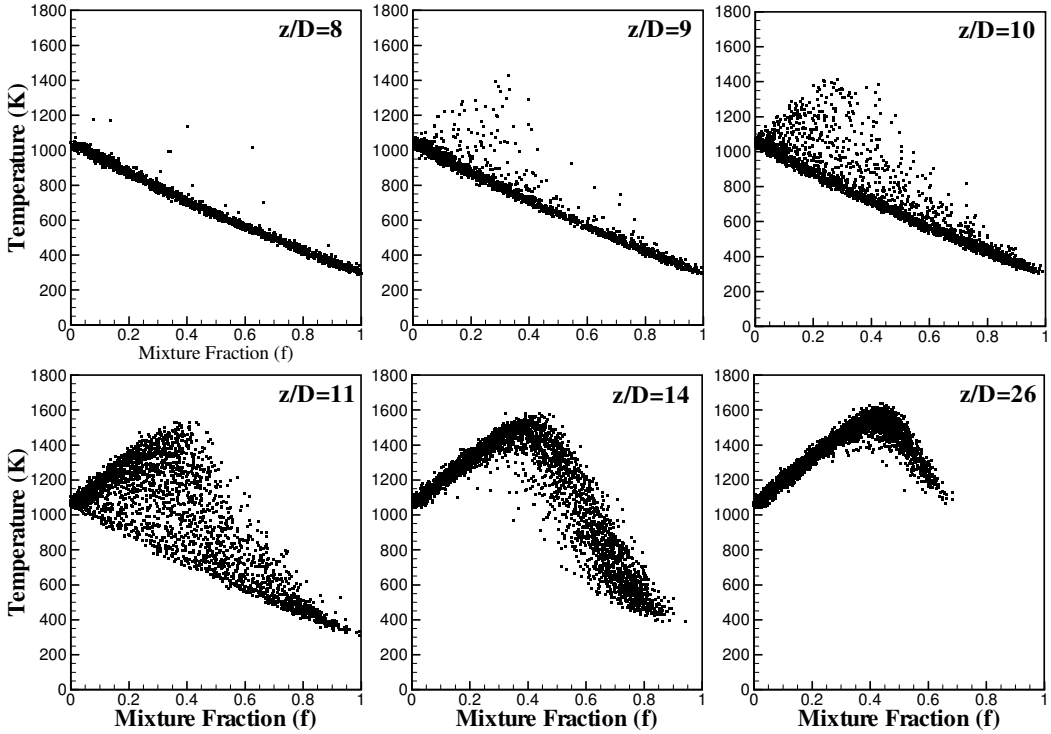

Figure 9.17 Experimental scattered data for temperature with mixture fraction at different axial locations along the burner

Other than the scattered data, instantaneous plots of temperature at mid-plane (x=0) would also give an indication of the flame instability issues. In Fig 9.19, the instantaneous filtered temperature distributions predicted by LES UFPV-δ function calculations have been shown for different times (time is indicated at the bottom right corner of every contour plot) at x=0 plane. In all the contour plots, the boundary T_c demarcates the inert mixing zone from the reaction occurring zone and hence serves as a guide for locating the flame base and consequently the fuel core region that it surrounds. The instantaneous shape of the flame base can be observed to be highly asymmetric and corrugated and varies significantly with respect to time. The snapshots of these instantaneous temperature plots are taken for every 1.25ms from 30ms till 51.25ms. The gradual increase in time helps to depict the flame shape

irregularities. It is clear that the flame front is highly fluctuating which can be seen from the inner fuel core region that tries to penetrate more in the axial direction as the time progresses.

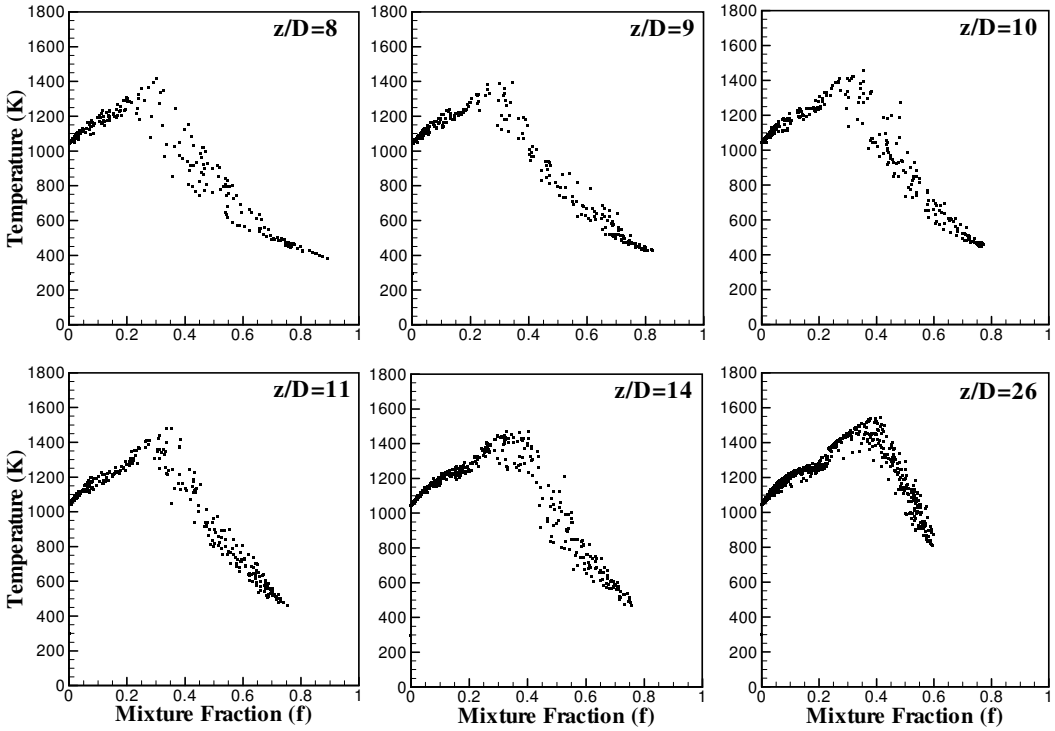

Figure 9.18 Numerical calculated scattered data for temperature with mixture fraction at different axial locations along the burner

At initial time of 30ms the fuel penetration depth reaches near to 120mm in the axial direction and till time t=50ms it fluctuates in between axial distance of 100mm to 120mm. At t=50ms, it reaches a distance of 150mm which is about 33% rise in the fuel jet penetration into the flame region. From 30ms to 50ms the flame has uniform fluctuating characteristics in the axial direction. But soon after, flame tries to extinguish with increase in its central fuel jet depth. It is evident that at time t=51.25 ms (Fig. 9.19), the core region depresses back indicating the flame stabilization process taking place. This fluctuating behavior was found to repeat. But it is interesting to note that the base of the flame front on either side of the fuel jet remains lifted from the base and found not to fluctuate as much as that of the central fuel core jet. The liftoff height of this flame base is found to stay around 20-30mm in the axial direction. Therefore, this explains that the flame stabilization persists irrespective of the extinguishing features of the flame.

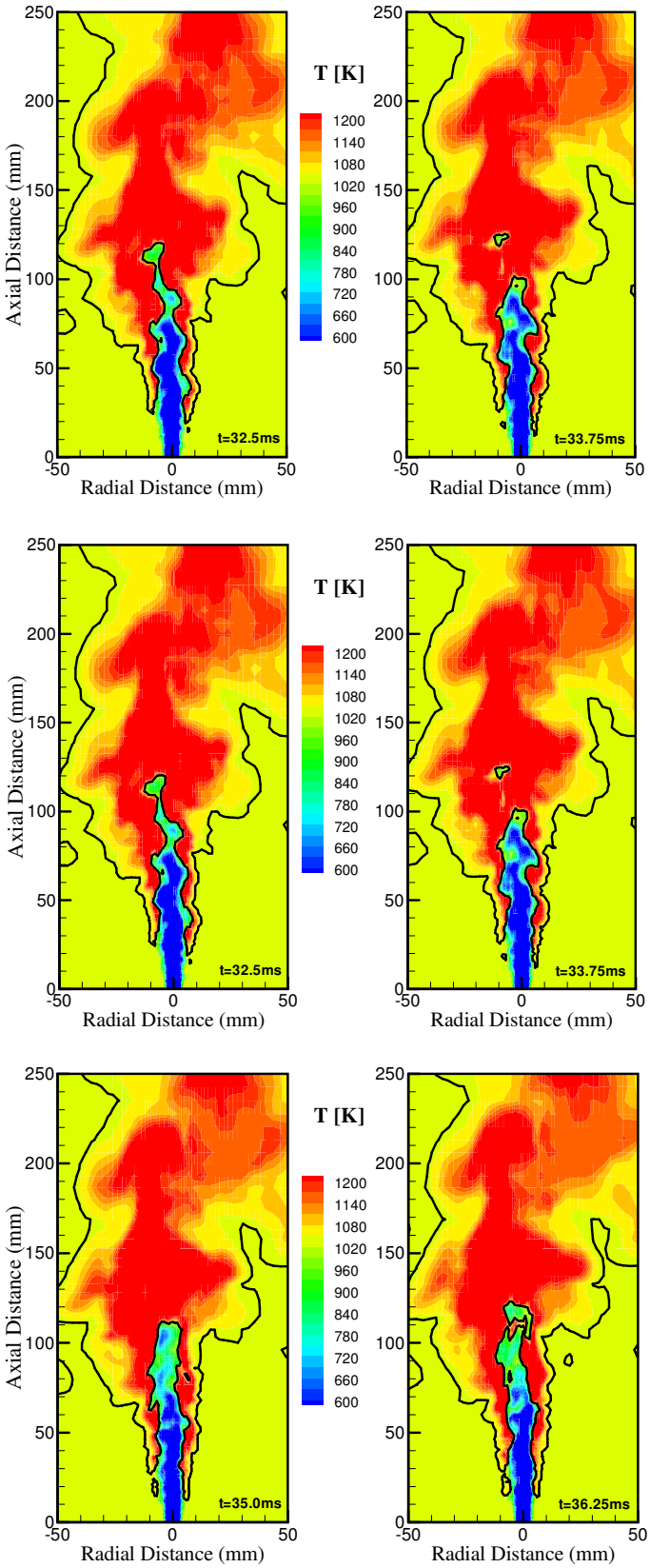
T [K]
1200
1140
1080
1020
960
900
840
780
720
660
600
Axial Distance (mm)
Radial Distance (mm)
t=32.5ms
t=33.75ms
t=32.5ms
t=33.75ms
t=35.0ms
t=36.25ms

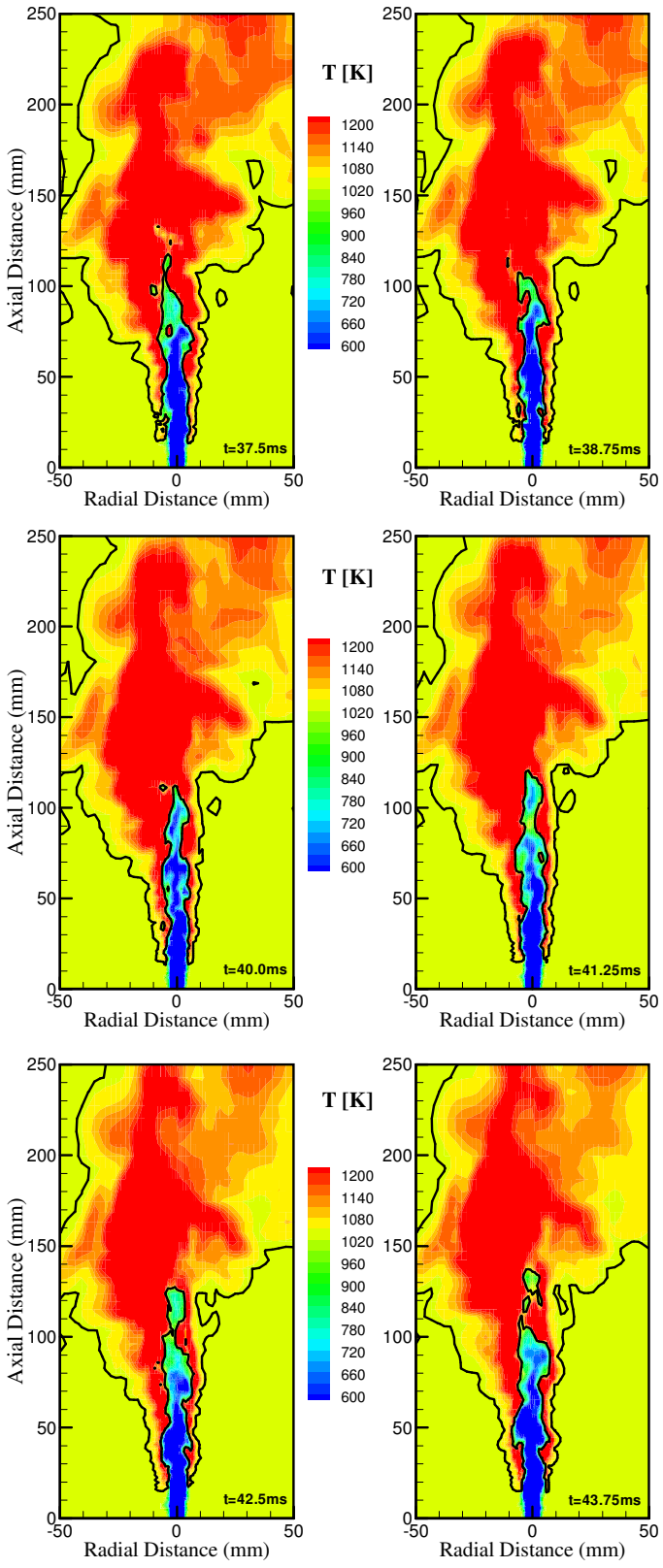
T [K]
1200
1140
1080
1020
960
900
840
780
720
660
600
Axial Distance (mm)
Radial Distance (mm)
t=37.5ms
t=38.75ms
t=40.0ms
t=41.25ms
t=42.5ms
t=43.75ms

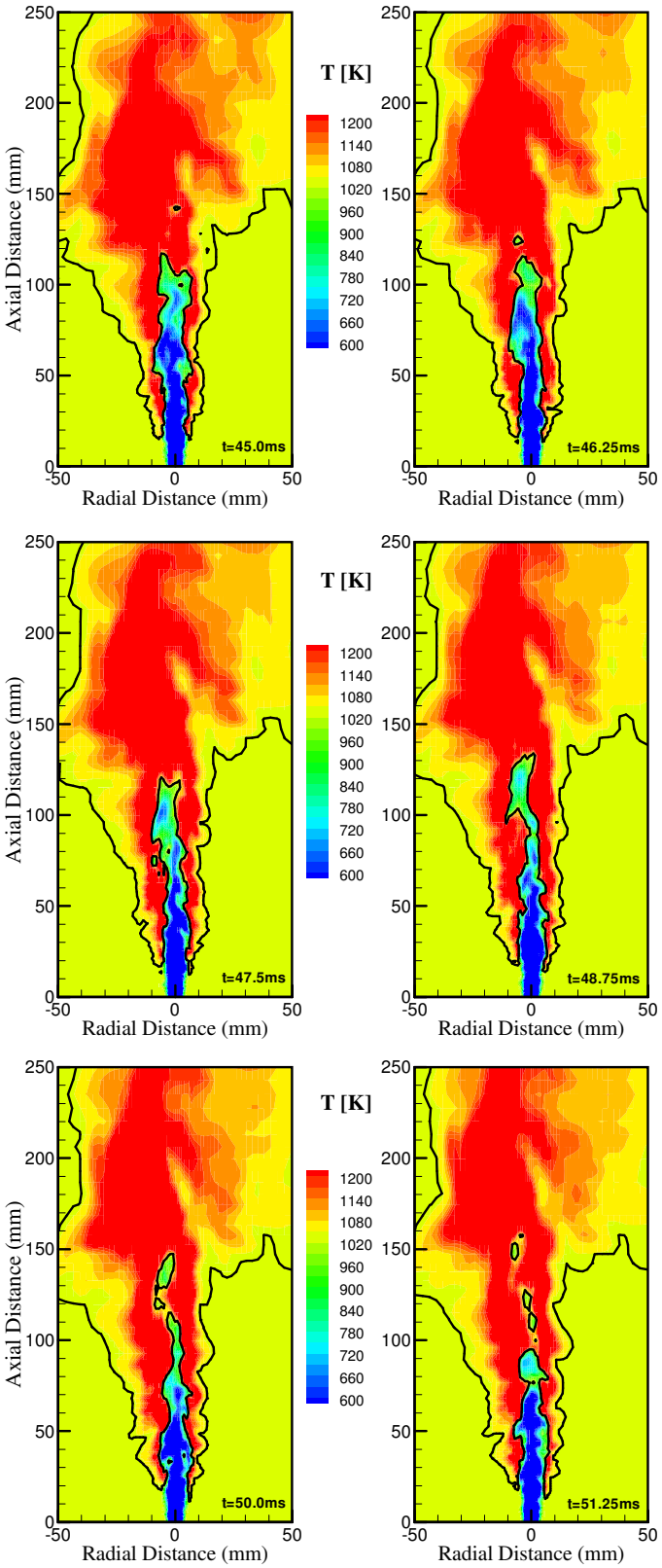

Figure 9.19: Variation in the instantaneous filtered temperature (K) distribution with respect to time – H_2/N_2 Flame.

9.4 Closure

Detailed discussion on the prediction capability with UFPV combustion model is depicted in this chapter. The model was applied on two different fuel compositions (CH_4/Air and H_2/N_2 flame) for the same burner configuration. A lift off height of H/D=42 was computed numerically when compared to H/D=35 from experiments for CH_4/Air flame. Lift off was also observed with H_2/N_2 flame but under predicted with 50% in its value. UFPV model was also compared with SLFM for its predicting capabilities. SLFM combustion model was found to predict as an attached flame. Results showed favorable numerical predictions from UFPV and encourages using this model for any lifted flame of this kind.

Chapter 10

Conclusions and Future Work

Application of classical steady laminar flamelet model, SLFM to non-premixed jet flames is the most popular choice among the different available combustion models. However, this model has its own drawbacks in predicting some of the vital features like extinction and re-ignition. Therefore, inclusion of flamelet solution covering from equilibrium to extinction and pre-integrating flamelet solution to develop a lookup table concept was intended as one of the solutions in order to optimize the computational time. SLFM was found to capture the flame characteristics well with the bluff body and swirl stabilized flames but could not succeed with flames related to lift and high blow-off limits. In order to predict the above features, FPV approach was developed for reproducing the flame properties which have medium to high percentage of blow off characteristics. Research was also performed to include the unsteady flamelet solution to capture the flame extinction and re-ignition. Therefore, one of the prime targets of the current research focused on building procedure for UFPV model mainly applicable to lifted flames which are considered to be partially premixed in nature. Along with the SLFM modelling, UFPV is also tested for lifted flames.

In the current research work, two major tasks were considered. Firstly, application of multiple flamelet solution through a lookup table concept of SLFM to bluff body and swirl stabilized flames. One of the complex flame structures, HM3e was tested with this SLFM strategy for prediction of its blow off characteristics. Secondly, an LES based turbulent non-premixed combustion modelling strategy, for the effects of radiation heat loss on detailed structure of the turbulent non-premixed flame, has been developed and its performance on turbulent bluff-body stabilized and swirl stabilized flames have been investigated. The combustion model developed in this regard is based on non-adiabatic flamelet model (NAFM). Discrete transfer method (DTM) was used for calculation of radiation parameters including the radiation source term which is required in order to solve for the enthalpy equation in LES.

Lastly, combustion models based on unsteady flamelet/progress variable (UFPV) approach, primarily developed by Ihme and Pitsch (2005) for turbulent non-premixed combustion, have been employed in LES framework and their capability to account for partially premixed combustion in lifted turbulent jet flames in vitiated co-flow has been investigated. Numerical investigations have been carried out using in-house finite volume based LES code into which the advanced models have been incorporated. Based on the above said combustion and radiation models, different flame configurations like HM1 and SMH1 are tested for non-premixed jet flames while the partially premixed Berkeley lifted jet flame series in vitiated co-flow is tested for UFPV model. The main conclusions and future recommendations from the present work are highlighted in the sections below.

10.1 Conclusions

The key conclusions from the current research work on LES based modelling of turbulent non-premixed flames are as follows:

- For the HM1 bluff-body stabilized flame, prediction of mixing field, temperature and major species with both SLFM and NAFM are in reasonably good agreement with measurements and NAFM showed better results when compared with SLFM. HM3e flame was tested with SLFM with multiple flamelet solution using lookup table method. Reasonable success was achieved for the most complex flame structure HM3e using SLFM combustion model with multiple flamelet solution.
- Similarly for the SMH1 swirl stabilized flame, prediction of mixing field, temperature and major species with both SLFM and NAFM are in reasonably good agreement with measurements and here too NAFM showed better results when compared with SLFM. SMH1 is found to be highly radiating when compared with HM1 flame. NAFM radiation calculations proved very vital for predictions of flame structure. The temperature field was found to vary significantly with the inclusion of radiation losses with NAFM for both the flames under consideration.
- Consideration of radiation heat loss when applied to both HM1 and SMH1 flames resulted in improved predictions for species mass fractions for CO_2 and H_2O.

- Influence of chemical mechanism used was tested and has been found to be negligible. Both GRI 2.11 and GRI 3.0 are found to behave very similarly for both HM1 and SMH1 flames. However, in some cases GRI 2.11 is found slightly closer towards the experiments when compared to predictions with GRI 3.0 mechanism.

The key conclusions from the LES based modelling of turbulent partially premixed lifted flames are as follows:

- From the UFPV modelling it has been found to successfully predict the lift-off phenomenon while the incapability of SLFM formulation is confirmed by its prediction with an attached flame with the jet base. This model was tested for two different flame configurations where the fuel and co-flow compositions varied. It was tested for CH_4/Air and H_2/N_2 flame under different experimental conditions.
- The lift-off height with UFPV- δ function model resulted in marginal over-prediction with CH_4/Air flame. However, the increase of 20% in lift-off height is reasonable based on the present circumstances where the definition of progress variable dictates the amount of lift to be predicted. Therefore, change in the definition of progress variable is very much needed in order to study the effect of definition of progress variable on flame structure.
- Lift-off height for H_2/N_2 flame was found to under-predict by a margin of 50% when compared with experiments. However, the radial distribution of mixing profiles and temperature are well in agreement with the measurements. Lift off height based on OH contours was tested and found to give almost the same results as of constant co-flow temperature iso-contour line.
- Numerical predictions of CO_2 and CO mass fraction were found to deviate from the experiments. This might be due to the inclusion of these mass fractions and their production rates in the definition of progress variable. Hence the mass fractions of CO and CO_2 are most likely to predict in a similar pattern to that of progress variable. The contour plots of these species were observed to follow a similar structure as progress variable. However, mean mass fraction of H_2O was found to predict well with UFPV as this was not involved in the progress variable definition.

- Fluctuation in the flame base is also captured by the UFPV model in LES. This is confirmed from comparisons of predicted and experimental scattered data. The scattered data shows excellent agreement with measurements at the downstream locations where the flame fluctuations are found to be high. The model is able to predict the broadening of the flame base associated with inert mixing as well as partially reacted samples, remarkably well. The model is as well able to predict the extinction and re-ignition phenomena occurring in fuel rich zone of the flame base (or downstream end). However, in conditions close to stoichiometric and fuel lean (upstream end of flame base), the model is unable to predict the extinction. However, the predicted levels of fluctuations with the UFPV model are closer to measurements than that with SLFM.
- Methane based CH_4/Air flame was found to extinguish and re-ignite very often with time and therefore resulted in higher mean lift off height. While hydrogen based H_2/N_2 flame was found to predict stabilized flame base with minimum fluctuations with an under-prediction in flame lift off height.
- Good predictions in mean lift-off height involving extinction and re-ignition prediction characteristics with the model show a significant improvement in mean temperature predictions. However, the inability of the UFPV model to capture the exact re-ignition in fuel lean conditions needs to be resolved. Consideration of scalar dissipation fluctuations has indeed resulted in over-prediction of lift-off height but gave reasonable statistics for the flame fluctuations with the scattered data.

10.2 Recommendations for Future Work

- Even though SLFM predicted well for HM1 and HM3e flame, it is worth testing the flame with UFPV or FPV approaches. FPV model was tested in the past for non-premixed flames and so can be used for bluff body flames as well. HM3e flame promises to predict well with FPV or UFPV approaches for its flame instabilities. As it is known that the blow off percentage is high for HM3e, it is highly recommended to test UFPV approach for HM3e flame.
- As it is well known that downstream vortex breakdown causes the complex swirl flame to stabilize, swirl stabilized flames can also be used for testing

UFPV model for predicting better in terms of its vortex breakdown characteristics.

- The causes for the discrepancies observed with the predicted levels of extinction with UFPV models in LES can be investigated with varying some of the below:
    1. Form of the PDF for reaction progress variable. Beta PDF for progress variable would increase the look up table dimensions but might result in more accurate flow field predictions and flame lift mechanisms.
    2. The definition of progress variable
    3. Numerical accuracy of the procedure adopted to remap the look-up-tables from flamelet parameter space to progress variable space.
- As the conclusions above state that radiation improves the temperature and other species predictions, it is sensible in implementing radiation through NAFM and enthalpy defect concepts for UFPV combustion model. However, the dimensions of the lookup table would definitely increase to a very high level which would be a serious concern for the computations to handle.

References

Adams, B. R., Smith, P. J., (1995), "Modelling Effects of Soot and Turbulence-Radiation Transfer in Turbulent Gaseous Combustion", *Combusiton Science and Technology, 109, Issue-1-6*, 121-140.

Al-Abdeli, Y. M., Masri, A. R., (2003), "Recirculation and Flowfield Regimes of Unconfined Non-reacting Swirling Flows", *Exp. Thermal Fluid Sci*., *27*, 655–665.

Armfield, S., Street, R. (2002), "An Analysis and Comparison of the Time Accuracy of Fractional-Step Methods for the Navier–Stokes Equations on Staggered Grids", *International Journal for Numerical Methods in Fluids* 38, 255–282.

Barlow, R.S., Fiechtner, G.J., Carter, C.D. and Chen, J.Y. (2000), "Experiments on the Scalar Structure of Turbulent CO/H2/N2 Jet Flames", *Combustion and Flame 120*,549-569.

Barths, H., Antoni, C., and Peters, N. (1998), "Three-Dimensional Simulation of Pollutant Formation in a DI Diesel Engines Using Multiple Interactive Flamelets", *SAE Paper* 982459.

Barths, H., Hasse, C. and Peters, N., (2000),"Computational Fluid Dynamics Modelling of Non-Premixed Combustion in Direct Injection Diesel Engines", *International Journal of Engine Research 1,* 249-267.

Barths, H., Peters, N., Brehm, N., Mack, A., Pfitzner, M., and Smiljanovski, V. (1998a), "Simulation of Pollutant Formation in a Gas-Turbine Combustor Using Unsteady Flamelets", *Twenty-seventh Symposium (International) on Combustion/The Combustion Institute*, 1841-1847.

Bell, J.B. and Colella, P. (1989), "A Second Order Projection Method for the Incompressible Navier-Stokes Equations", *Journal of Computational Physics 85*, 257–283.

Bilger, R.W. (1988), "The Structure of Turbulent NonPremixed flames", *Twenty-second Symposium (International) on Combustion/The Combustion Institute*, 475-488.

Bilger, R.W. (1993), "Conditional Moment Closure for Turbulent Reactive Flows", *Physics of Fluids A 52*, 436-444.

Bowman, C. T., Hanson, R. K., Davidson, D.F., Gardiner, W.C., Lassianski, V., Smith, G. P., Golden, D. M., Frenklach, M., Wang, H. and Goldenberg, M. (2007) in http://www.me.berkeley.edu/gri-mech/releases.html

Bradley, D., Gaskell, P.H. and Gu, X.J. (1998a), "The Modelling of Aerodynamic Strain Rate and Flame Curvature Effects in Premixed Turbulent Combustion", *Twenty Seventh Symposium (International) on Combustion/The Combustion Institute*, 849-856.

Bradley, D., Gaskell, P.H. and Gu, X.J. (1998b), "The Mathematical Modelling of Liftoff and Blowoff of Turbulent Non-premixed Methane jet Flames at High Strain Rates", *Twenty Seventh Symposium (International) on Combustion/The Combustion Institute*, 915-922.

Bradley, D., Gaskell, P.H. and Lau, A.K.C. (1990), "A Mixedness-Reactedness Flamelet Model for Turbulent Diffusion Flames", *Twenty Third Symposium (International) on Combustion/The Combustion Institute*, 685-692.

Branley, N., (1999), "Large eddy simulation of non-premixed turbulent flames", PhD Thesis, Imperial College, UK.

Branley, N. and Jones, W.P. (1999), "Large Eddy Simulation of a Nonpremixed Turbulent Swirling Flame", in W. Rodi and D.Laurence (Eds.), *Engineering Turbulence Modelling and Experiments 4*, pp.861-870, Amsterdam: Elsevier Science.

Branley, N. and Jones, W.P. (2001), "Large Eddy Simulation of a Turbulent Non-premixed Flame", *Combustion and Flame 127*, 1914–1934.

Bray, K.N.C., and Moss. J.B., (1977), "A Unified Statistical Model of the Premixed Turbulent Flame". *Acta Astronautica,* 4, 291-319.

Bray, K.N.C., and Peters, N. (1994), "Laminar Flamelets in Turbulent Flames", in P.A. Libby and F.A. Williams (Eds.), *Turbulent Reacting Flows*, Chapter 2,pp.63-94, London : Academic Press.

Broadwell, J.E., Dahm, W.J.A. and Mungal, M.G. (1984), "Blowout of Turbulent Diffusion Flames", *Twentieth Symposium (International) on Combustion/The Combustion Institute*, 303-310.

Bushe, W.K. and Steiner, H. (1999), "Conditional Moment Closure for Large Eddy Simulation of Nonpremixed Turbulent Reacting Flows", *Physics of Fluids 11*, 1896–1906.

Burke, S.P., Schumann, T.E.W., (1928), "Diffusion Flames," *Ind. Eng. Chem.*, *29*, 998–1004.

Cabra, R., Chen, J.-Y., Dibble, R.W., Karpetis, A.N. and Barlow, R.S. (2005), "Lifted Methane-Air Jet Flames in a Vitiated Coflow", *Combustion and Flame 143*, 491-506.

Cabra, R., Myhrvold, T., Chen, J.-Y., Dibble, R.W., Karpetis, A.N. and Barlow, R.S. (2002), "Simultaneous Laser Raman-Rayleigh-LIF Measurements and Numerical Modelling Results of a Lifted Turbulent H_2/N_2 Jet flame in a Vitiated Co-flow", *Proceedings of the Combustion Institute, 29*, 1881-1888.

Cao, R. R., Pope, S. B., Masri, A. R., (2005), "Turbulent Lifted Flames in a Vitiated Co-flow Investigated using Joint PDF Calculations", *Combustion and Flame, 142,* 438-453.

Castro, I. P., Jones, J. M., (1987), "Studies in Numerical Computations of Recirculating Flows", *International Journal of Numerical Methods Fluids, 7,* 793-823.

Chen, J.-Y., and Chang, W.C. (1996), "Flamelet and PDF Modelling of CO and NOx Emissions from a Turbulent, Methane Hydrogen Jet Nonpremixed Flame", *Twenty-sixth Symposium (International) on Combustion/The Combustion Institute*, 2207-2214.

Chen, C. S., Chang, K. C., Chen, J. Y., (1996), "Application of a Robustbeta PDF Treatment to Analysis of Thermal NO Formation in Nonpremixed Hydrogen-air Flame", *Combustion and Flame, 98*, 375-390.

Chen, M., Hermann, M. and Peters, N. (2000), "Flamelet Modelling of Lifted Turbulent Methane/Air and Propane/Air Jet Diffusion Flames", *Twenty Eigth Symposium (International) on Combustion/The Combustion Institute*, 167-174.

Chou, C-P., Chen, J-Y., Yam, C. G., Marx, K. D., (1998), "Numerical Modelling of NO Formation in Laminar Bunsen Flames-A Flamelet Approach", *Combustion and Flame, 114,* 420-435.

Chung, S.H., Lee, B. J., (1991), "On the Characteristics of Laminar Lifted Flames in a Non-premixed Jet", *Combustion and Flame, 86,* 62-72.

Claramunt, K., Consul, R., Carbonell, D., Perez-Segarra, C. D., (2006), "Analysis of the Laminar Flamelet Concept for Nonpremixed Laminar Flames", *Combustion and Flame, 145, Issue4,* 845-862.

Coelho, P.J., and Peters, N. (2001a), "Unsteady Modelling of Piloted Methane/Air Jet Flame Based on the Eulerian Particle Flamelet Model", *Combustion and Flame 124,* 444-465.

Coelho, P.J., and Peters, N. (2001b), "Numerical Simulation of a Mild Combustion Burner", *Combustion and Flame 124,* 503-518.

Coelho, P.J., Teerling, O.J., Roekaerts, D. (2003), "Spectral Radiative Effects and Turbulence/Radiation Interaction in a Non-Luminous Turbulent Jet Diffusion Flame", *Combustion and Flame 133,* 75-91.

Coelho, P., Teerling, O., Roekaerts, D., (2003), "Spectral Radiative Effects and Turbulence/Radiation Interaction in a Non-luminous Turbulent Jet Diffusion Flame", *Combustion and Flame 133 (1-2)* 75-91.

Coelho, P.J. (2004), "Detailed Numerical Simulation of Radiative Transfer in a Non-Luminous Turbulent Jet Diffusion Flame", *Combustion and Flame 136,* 481-492.

Coelho, P. J., (2007), "Numerical Simulation of the Interaction between Turbulence and Radiation in Reactive Flows", *Prog. Energy and Comb. Sci.*, *33,* 311-383.

Coelho, P. J., (2009), "Approximate Solutions of the Filtered Radiative Transfer Equation in Large Eddy Simulations of Turbulent Reactive Flows", *Combustion and Flame, 156*, 1099-1110

Cook, A.W. and Riley, J.J. (1994), "A Subgrid Model for Equilibrium Chemistry in Turbulent Flows", *Physics of Fluids 6*, 2868–2870.

Cook, A.W. and Riley, J.J. (1998), "Subgrid-Scale Modelling for Turbulent Reactive Flows", *Combustion and Flame 112*, 593–606.

Cook, A.W. and Riley, J.J. and Kosaly, G. (1997), "A Laminar Flamelet Approach to Subgrid Scale Chemistry in Turbulent Flows", *Combustion and Flame 109*, 332-341.

Cook, D. J., Pitsch, H., Chen, J. H., Hawkes, E. R., (2007), "Flamelet-based Modelling of Auto-ignition with Thermal Inhomogeneities for Application to HCCI Engines", *Proceedings of the Combustion Institute*, *31, Issue 2*, 2903-2911.

Correa, S.M., and Gulati, A. (1992), "Measurements and Modelling of a Bluff Body Stabilized Flame", *Combustion and Flame 89*,195-213.

Cox, G., (1977), "On radiant Heat Transfer in Turbulent Flames", *Combustion Science and Technology*, *17*, No 1-2, 75-78..

Dahm, W. J. A., Dibble, R. W., (1988), "Combustion Stability Limits of Coflowing Turbulent Jet Diffusion Flames", *26th Aerospace Sciences Meeting*, AIAA Paper no. 88-0538, p-8

Dally, B.B., Fletcher, D.F., Masri, A.R. (1998b), "Flow and Mixing Fields of Turbulent Bluff-Body Jets and Flames", *Combustion Theory and Modelling 2*, 193-219.

Dally, B.B., Masri, A.R., Barlow, R.S., Fiechtner, G.J. (1998a), "Instantaneous and Mean Compositional Structure of a Bluff-Body Stabilized Nonpremixed Flames", *Combustion and Flame 114*, 119-148.

Dally, B.B., Masri, A.R., Barlow, R.S., Fiechtner, G.J. (2003), "Two Photon Laser-Induced Fluorescence Measurement of CO in Turbulent Non-Premixed Bluff-Body Flames", *Combustion and Flame 132*, 272-274.

De Bruyn Kops, S.M., Riley, J.J., Kosaly, G., Cook, A.W. (1998), "Investigation of Modelling for Non-premixed Turbulent Combustion", *Flow Turbulence and Combustion 60*,105–122.

Deardorff, J.W. (1970), "A Numerical Study of Three-Dimensional Turbulent Channel Flow at Large Reynolds Numbers", *Journal of Fluid Mechanics 41*, 453-480.

Delhaye, S., Somers, L.M.T., Van Oijen, J.A., De Goey, L.P.H., (2008), "Incorporating Unsteady Flow-Effects in Flamelet-Generated Manifolds", *Combustion and Flame, 155(1-2),* 133-144.

Deshmukh, K. V., Modest, M. F., Haworth, D. C., (2008), "Direct Numerical Simulation of Turbulence–Radiation Interactions in a Statistically One-dimensional Nonpremixed System", *J. Quant. Spect. & Rad. Transfer, 109*, 2391–2400.

Domingo, P. and Vervisch, L. (1996), "Triple Flames and Partially-premixed Combustion in Auto-ignition of Non-premixed Turbulent Mixtures", *Twenty Sixth Symposium (International) on Combustion/The Combustion Institute*, 233-240.

Donnerhack, S., and Peters, N. (1984), "Stabilization Heights in Lifted Methane-Air Jet Diffusion Flames Diluted with Nitrogen", *Combustion Science and Technology*, *41*, 101-108.

Drake, C (1986), "Stretched Laminar Flamelet Analysis of Turbulent H_2 and $CO/H_2/N_2$ Diffusion Flames", *Twenty-first Symposium (International) on Combustion/The Combustion Institute*, 1579-1589.

Drake, M.C., and Blint, R.J. (1988), "Structure of Laminar Opposed-Flow Diffusion Flames with $CO/H_2/N_2$ Fuel", *Combustion Science and Technology 61*, 187-224.

Duchamp de Lageneste, L. and Pitsch, H. (2001), "Progress in Large-Eddy Simulation of Premixed and Partially-premixed Turbulent Combustion", *Annual Research Briefs*, Center for Turbulence Research, NASA Ames/Stanford University.97–107.

Edwards, D. K., Balakrishnan, A. (1973), "Thermal Radiation by Combustion Gases", 16, 25-40.

Effelsberg, E., and Peters, N. (1988), "Scalar Dissipation Rates in Turbulent Jets and Jet Diffusion Flames", *Twenty-second Symposium (International) on Combustion/The Combustion Institute*, 693-700.

Eickhoff, H., Lenze, B., Leuckel, W. (1986), "Experimental Investigation on the Stabilization Mechanism of Jet Diffusion Flames", *Twentieth Symposium (International) on Combustion/The Combustion Institute*, 311-318.

Faeth,. G. M., Gore. J. P., Chuech S. G., Jeng. S. M., (1989), "Radiation from Turbulent Diffusion Flames", *In: Annual review of numerical fluid mechanics and heat transfer*, 2,1–38.

Felsch, C., Gauding, M., Hasse, C., Vogel, S, Peters, N., (1996), "An Extended Flamelet Model for Multiple Injections in DI Diesel Engines", Proceedings of the Combustion Institute, 32, 2, 2775-2783.

Ferraris, S. A., Wen, J. X., (2008), "LES of the Sandia Flame D Using Laminar Flamelet Decomposition for Conditional Source-term Estimation", *Flow Turbulence and Combustion, 81,* 609-639.

Ferreira, J.C. (1996), "Flamelet Modelling of Stabilization in Turbulent Non-Premixed Combustion", PhD Thesis, ETH Nr.1184.

Ferreira, J.C. (2001), "Steady and Transient Flamelet Modelling of Turbulent Non-Premixed Combustion", *Progress in Computational Fluid Dynamics 1,* 29-42.

Ferziger, J. H., (1977), "Large Eddy Numerical Simulations of Turbulent Flows", *AIAA Journal*, *15*, No. 9, 1261–1267

Forkel, H., Janicka, J. (1999), "Large Eddy Simulation of a Turbulent Hydrogen Diffusion Flame", *Proceedings of the 1st International Symposium on Turbulence and Shear Flow Phenomena*, pp. 65-70.

Germano, M., Piomelli, U., Moin, P., and Cabot, W. H. (1991), "A Dynamic Sub-grid Scale Eddy Viscosity Model", *Physics of Fluids A (3)*, 1760-1765.

Giordano, P. and Lentini, D. (2001), "Combustion-Radiation-Turbulence Interaction Modelling in Absorbing/Emitting Nonpremixed flames", *Combustion Science and Technology 172*, 1-22.

Girimaji, S.S., Zhou, Y. (1996), "Analysis and Modelling of Subgrid Scalar Mixing using Numerical Data", *Physics of Fluids 8*, 1224-1236.

Goncalves dos Santos, R., Lecanu, M., Ducruix, S., Gicquel, O., Iacona, E., Veynante, D. (2008), "Coupled Large Eddy Simulations of Turbulent Combustion and Radiative Heat Transfer", *Combustion and Flame*, 152, 387-400.

Gore, J. P., Faeth, G. M., (1986), "Structure and Spectral Radiation Properties of Turbulent Ethylene/air Diffusion Flames", *21st Symposium. (International) on Combustion,*1521–1531.

Gore, J. P., Ip, U-S., Sivathanu, Y. R., (1992), "Coupled Structure and Radiation Analysis of Acetylene/Air Flame", *Journal of Heat Transfer, 114*, 487-493.

Hartick, J. W., Neuber, A. A., Fournier, R, Hassel, E.P., Janicka, J., (1995), "Modelling Turbulence-Radiation Interaction in Confined Diffusion Flames", *The 8th International Symp. on Transport Phenomena in Combustion, San Francisco.*

Hartick, J. W., Tacke, M., Fruchtel, G., Hassel, E. P., Janicka, J., (1996), "Interaction of Turbulence and Radiation in Confined Diffusion Flames", *26th Symposium (International) on Combustion/The Combustion Institute*, 75-82.

Haworth, D.C., Drake, M.C., and Blint, R.J. (1988a), "Stretched Laminar Flamelet Modelling of a Turbulent Jet Diffusion Flame", *Combustion Science and Technology 60,* 287-318.

Haworth, D.C., Drake, M.C., Pope, S.B., and Blint, R.J. (1988b), "The Importance of Time Dependent Flame Structure In Stretched Laminar Flamelet Models For Turbulent Jet Diffusion Flames", *Twenty-Second Symposium (International) on Combustion/The Combustion Institute*, 589-597.

Henson, J.C., Malalasekera, W., (1997), "Comparison of Discrete Transfer and Monte-Carlo Methods for Radiative Heat Transfer in Three-dimensional Non-Homogeneous Scattering Media", *Numerical. Heat Transfer Part A: Applications*, *32(1),* 19-36.

Henson, J.C., (1999), "Numerical Simulation of Spark Ignition Engines with Special Emphasis on Radiative Heat Transfer", Ph.D. thesis, Loughborough University, UK.

Heyl, A., and Bockhorn, H. (2001), "Flamelet Modelling of NO Formation in Laminar and Turbulent Diffusion Flames", *Chemosphere 42,* 449-462.

Hottel, H. C., Sarofim, A. F., (1967), "Radiative Transfer", New York: McCraw-Hill

Hossain, M. (1999), "CFD Modelling of Turbulent Non-Premixed Combustion", Ph.D Thesis, Loughborough University, UK.

Hossain, M., and Malalasekera, W. (2003), "Modelling of a Bluff Body Stabilized CH4/H2 Flame Based on a Laminar Flamelet Model with Emphasis on NO Prediction", *Journal of Power and Energy 217*, 201-210.

Hossain, M., Jones, J.C. and Malalasekera, W. (2001), "Modelling of a Bluff-Body Nonpremixed Flame Using a Coupled Radiation/Flamelet Combustion Model", *Flow Turbulence and Combustion 67*, 217-234.

Hossain, M., Malalasekera, W. (2005), "Modelling of a Bluff body Stabilised CH_4/H_2 Flame based on a Laminar Flamelet Model with Emphasis on NO Prediction", *Proc. Instn Mech. Engrs, Part A: J. Power and Energy*, *217,* 201-210.

Ihme, M. and Pitsch, H. (2005), "LES of a Non-premixed Flame using an Extended Flamelet/Progress Variable Model", *AIAA Paper* 2005-0558.

Ihme, M., Cha, C.M. and Pitsch, H. (2005), "Prediction of Local Extinction and Re-ignition Effects in Non-premixed Turbulent Combustion by a Flamelet/Progress Variable Approach", *Thirtieth Symposium (International) on Combustion/The Combustion Institute*, 793-800.

Ihme, M. and Pitsch, H. (2008), "Prediction of Extinction and Reignition in Nonpremixed Turbulent Flames Using a Flamelet/Progress Variable Model: 1. A Priori Study and Presumed PDF Closure", *Combustion and Flame 155*, 70-89.

Johannes, W. H., Andreas, A. N., Gerhard, F., Hassel, E. P., Janicka, J., (1995), "Turbulence-radiation Interaction in Confined Combustion Systems", *Engineering Research, B.d 61*, Nr3.

Jones, W.P., and Whitelaw, J.H. (1982), "Calculation Methods for Reacting Turbulent Flows: A Review", *Combustion and Flame 48*,1-26.

Jones, W. P., Navarro-Martinez, S., (2008), "Study of Hydrogen Auto-ignition in a Turbulent Air Co-flow using a Large Eddy Simulation Approach", *Computers and Fluids, 37*, 802-808.

Kabashnikov, V. P., Kmit, G. I., (1979), "Influence of Turbulent Fluctuations of Thermal Radiation", *Institute of Physics, 31, No2,* 226-231.

Kabashnikov, V. P., Myasnikova, G. I., (1985), "Thermal Radiation in Turbulent Flows- Temperature and Concentration Fluctuations", *Heat Transfer, Soviet Research, 17, Isuue6,* 116-125.

Kalghatgi, G.T. (1981), "Blow-out Stability of Gaseous Jet Diffusion Flames. Part I: In Still Air", *Combustion Science and Technology 26*, 233-239.

Kalghatgi, G.T. (1984), "Lift-off Heights and Visible Lengths of Vertical Turbulent Jet Diffusion Flames in Still Air", *Combustion Science and Technology 41*, 17-29.

Kempf, A. M., (2003), "Large Eddy Simulation of Non-premixed Turbulent Flames", PhD Thesis, TU-Darmstadt, Germany.

Kempf, A., Flemming, F. and Janicka, J. (2005), "Investigation of Lengthscales, Scalar Dissipation and Flame Orientation in a Piloted Diffusion Flame by LES", *Thirteeth Symposium (International) on Combustion/The Combustion Institute*, 557-565.

Kempf, A., Lindstedt, R.P. and Janicka, J. (2006), "Large-eddy Simulation of a Bluff-body Stabilized Non-premixed Flame", *Combustion and Flame 144*, 170-189.

Kempf, A., Malalasekera, W., Ranga-Dinesh, K. K. J., Stein, O., (2008), "Large Eddy Simulation of Swirling Non-premixed Flames with Flamelet Models: A Comparison of Numerical Methods", *Flow Turbulence and Combustion, 81,* 523-561.

Kerstein, A.R. (1992), "Linear Eddy Modelling of Turbulent Transport: part 4: structure of diffusion flames", *Combustion Science and Technology 81*, 75-86.

Kim, S-K., Kang, S-M., Kim, Y-M., (2001), "Flamelet Modelling for Combustion Processes and NO_x Formation in the Turbulent Non-premixed $CO/H_2/N_2$ Jet Flames", *Combustion Science and Technology, 168(1),* 47-83.

Kim, H.S., Huh, Y.K. (2002), "Use of the Conditional Moment Closure Model to Predict NO formation in a Turbulent CH4/H2 flame over a Bluff-Body", *Combustion and Flame 130*, 94-111.

Kim, S-K., Kim, Y., (2008), "Assessment of the Eulerian Particle Flamelet Model for Non-premixed Turbulent Jet Flames", *Combustion and Flame, 154, Issue 1-2,* 232-247.

Kirkpatrick, M.P. (2002), "A Large Eddy Simulation Code for Industrial and Enviromental Flows", *Ph.D. Thesis*, University of Sydney, Australia.

Kirkpatrick, M.P., Armfield, S.W. and Kent, J.H. (2003), "A Representation of Curved Boundaries for the Solution of the Navier-Stokes Equations on a Staggered Three Dimensional Cartesian Grid", *Journal of Computational Physics 184*, 1–36.

Klimenko, A.Y. (1990), "Multicomponent Diffusion of Various Admixtures in Turbulent Flows, *Fluid Dynamics 25*, 327-334.

Koch, R., Krebs, W., Jeckel, R., Ganz, B., Wittig, S., (1994), "Spectral and Time Resolved Radiation Measurements in a Model Gas Turbine Combustor", *Int. Gas Turbine and Aeroengine Congress and Exposition, The Hague, Netherlands,* no. 94-GT-403.

Kounalakis, M. E., Gore, J. P., Faeth, G. M., (1988), "Turbulence/Radiation Interactions in Non-premixed Hydrogen/Air Flames", *22nd Symposium (International) on Combustion, The Combustion Institute,* 1281-1290.

Kritzstein, F., Soufiani, A., (1993), "Infrared Gas Radiation from a Homogeneously Turbulent Medium", *International Journal of Heat and Mass Transfer 36(7),* 1749–1762.

Kuan, T. S., Lindstedt, R. P., (2005), "Transported Probability Density Function Modelling of Bluff Body Stabilized Turbulent Flame", *Proceedings of the Combustion Institute, 30,* 767-774.

Kuo, K.K. (1986), "*Principles of Combustion*", New York: Wiley International.

Launder, B.E. and Spalding, D.B. (1974), "The Numerical Computation of Turbulent Flows", *Computer Methods in Applied Mechanics and Engineering 3*, 269–289.

Lee, T. W., Fenton, M., Shankland, R., (1997), "Effects of variable partial premixing on turbulent jet flame structure", *Combustion and Flame, 109*, 536-548.

Lentini, D. (1994), "Assessment of the Stretched Laminar Flamelet Approach for NonPremixed Turbulent Combustion", *Combustion Science and Technology 100*, 95-122.

Lentini, D. and Puri, I.K. (1995), "Stretched Laminar Flamelet Modelling of Turbulent Chloromethane-Air Nonpremixed Jet Flames", *Combustion and Flame 103,* 328-338.

Leonard, B.P. (1979), "A Stable and Accurate Convective Modelling Procedure Based on Quadratic Upstream Interpolation", *Journal of Computational Methods in Applied Mechanical Engineering 19*,59-98.

Leonard, B.P. (1987), "SHARP Simulation of Discontinuities in Highly Convective Steady Flow", *NASA Technical Report* 100240.

Lesieur, M., Zétais, M., (1996), "New Trends in Large-eddy Simulations of Turbulence", *Annu. Rev. Fluid Mech, 28,* 45–82.

Li, G., Bertrand, N., Roakaerts, D. (2003), "Numerical Investigation of a Bluff-Body Stabilised Nonpremixed Flame with Differential Reynolds-Stress Models", Flow *Turbulence and Combustion 70*, 211-240.

Li, G., Modest, M. F. (2003), "Importance of Turbulent-Radiation Interactions in Turbulent Diffusion Jet Flames", *Journal of Heat Transfer*, 125, 831-838.

Libby, P.A., Bray, K. N. C., (1981), "Counter-Gradient Diffusion in Premixed Turbulent Flames". *AIAA Journal 19,* 205-213.

Liew, S.K, Bray, K.N.C., Moss, J.B. (1984), "A Stretched Laminar Flamelet Model of Turbulent Nonpremixed Combustion", *Combustion and Flame 56,*199-213.

Lilly, D. K. (1991), "A Proposed Modification of the Germano Subgrid-Scale Closure Method", *Physics of Fluids A (4)*, 633-635.

Lilly, D.K. (1967), "The Representation of Small Scale Turbulence in Numerical Simulation Experiments", *In proceedings of the IBM scientific computing symposium on Environmental Sciences,* 320-1951, 195-210

Liñán, A. (1994), "Ignition and Flame Spread in Laminar Mixing Layers", In J.Buckmaster, T.L. Jackson, and A. Kumar (Eds.), *Combustion in High-Speed Flows*, Dordrecht: Kluwer Academic, 461-476.

Liu, K., Pope, S.B., Caughey, D.A. (2005), "Calculations of Bluff-Body Stabilized Flames Using a Joint Probability Density Function Model with Detailed Chemistry", *Combustion and Flame 141*, 89-117.

Liu, F., Guo, H., Smallwood, G. J., (2005), "Evaluation of the Laminar Diffusion Flamelet Model in the Calculation of an Axisymmetric Coflow Laminar Ethylene-air Diffusion Flame", *Combustion and Flame*, *144,* 605-618.

Lockwood, F.C. and Shah, N.G. (1981), "A New Radiation Solution for Incorporation in General Combustion Prediction Procedures", *Eighteenth Symposium (International) on Combustion/The Combustion Institute*, 1405-1413.

Lyons, K. M. (2007), "Toward an Understanding of the Stabilization Mechanism of Lifted Turbulent Jet Flames: Experiments", *Progress in Energy and Combustion Science*, 33, 211-231.

Ma, C.Y., Mahmud, T., Fairweather, M., Hampartsoumian, E. and Gaskell, P.H. (2002), "Prediction of Lifted Non-premixed Turbulent Flames using a Mixedness-Reactedness Flamelet Model with Radiation Heat Loss", *Combustion and Flame 128*, 60-73.

Mahesh, K., Constantinescu, G. and Moin, P. (2004), "A Numerical Method for Large-Eddy Simulation in Complex Geometries", *Journal of Computational Physics 197*, 215–240.

Malalasekera, W., Ranga-Dinesh, K. K. J., Ibrahim, S. S., Masri, A. R. (2008), "LES of Recirculation and Vortex Breakdown of Swirling Flames", *Combustion Science and Technology*, 180(5), 809-832.

Malalasekera, W., James, E. H., (1996), "Radiative Heat Transfer Calculations in Three-dimensional Complex Geometries", *Journal of Heat Transfer, 118*, 225-228.

Malalasekera, W., Versteeg, H. K., Henson, J. C., Jones, J. C., (2002), "Calculation of Radiative Heat Transfer in Combustion Systems", C*lean Air, 3, No1*, 113-143.

Marracino, B. and Lentini, D. (1997), "Radiation Modelling in Non-Luminous NonPremixed Turbulent Flames", *Combustion Science and Technology 128*, 23-48.

Mason, P. J., (1994), "Large-eddy Simulation: A Critical Review of the Technique", *Quart. J. Royal Meteor. Soc., 120*, 1-26

Masri, A.R., Bilger, R.W., and Dibble, R.W. (1988), "Turbulent NonPremixed Flames of Methane Near Extinction: Probability Density Functions", *Combustion and Flame 73*,261-285.

Masri, A. R., Pope, S. B., Dally, B. B., (2000), "Probability Density Function Computation of a Strongly Swirling Nonpremixed Flame Stabilized on a New Burner", *Proceedings of Combustion Institute, 28*, 123-131.

Masri, A. R., Kalt, P. A. M., Barlow, R. S., (2004), "The Compositional Structure of Swirl Stabilised Turbulent Non-Premixed Flames", *Combustion and Flame, 137*, 1-37.

Mauss, F, Keller, D., and Peters, N. (1990), "A Lagrangian Simulation of Flamelet Extinction and Re-Ignition In Turbulent Jet Diffusion Flames", *Twenty-third Symposium (International) on Combustion/The Combustion Institute*, 693- 698.

Mazumder S, Modest M. F., (1999), "A PDF approach to Modelling Turbulence–Radiation Interactions in Nonluminous Flames", *International Journal of Heat Mass Transfer, 42*, 971–991.

Merci, B., Dirk, R., Naud, B., Pope, S. B., (2006), "Comparative Study of Micromixing Models in Transported Scalar PDF Simulations of Turbulent Nonpremixed Bluff Body Flames", *Combustion and Flame, 146*, 109-130.

Miake-Lye, R. C.; Hammer, J. A., (1988), "Lifted Turbulent Jet Flames: a Stability Criterion Based on the Jet Large-scale Structure", 22nd *Symposium (International) on combustion, The Combustion Institute,* 817–824.

Modest, M. F. (2003), "Fundamentals of thermal radiation", *Radiative Heat Transfer (Second Edition)*, 1-29

Müller, C. M., Breitbach, H. and Peters, N. (1994), "Partially Premixed Turbulent Flame Propagation in Jet Flames", *Twenty fifth Symposium (International) on Combustion/The Combustion Institute*, 1099-1106.

Nelson, D. A., (1989), "Band Radiation from a Fluctuating Medium", *Journal of Heat Transfer, 111(1),* 131–134.

Odedra, A., Malalasekera, W., (2007), "Eulerian Particle Flamelet Modelling of a Bluff-body CH_4/H_2 Flame", *Combustion and Flame, 151, Issue3*, 512-531.

Peters, N. (1983), "Local Quenching Due to Flame Stretch and Non-Premixed Turbulent Combustion", *Combustion Science and Technology 30,* 1-17.

Peters, N. (1984), "Laminar Diffusion Flamelet Models in Non-Premixed Turbulent Combustion", *Progress in Energy and Combustion Science 10*,319-339.

Peters, N. (1986), "Laminar Flamelet Concepts in Turbulent Combustion", *Twenty-first Symposium (International) on Combustion/The Combustion Institute*, 1231-1250.

Peters, N. (1999), "The Turbulent Burning Velocity for Large Scale and Small Scale Turbulence", *Journal of Fluid Mechanics 384*, 107-132.

Peters, N. and Williams, F.A. (1983), "Lift-off Characteristics of Turbulent Jet Diffusion Flames", *AIAA Journal 21*, 423-429.

Peters, N., Rogg, B., (1993), "Lecture Notes in Physics-Reduced Kinetic Mechanisms for Applications in Combustion Systems", Springer.

Pierce, C.D. (2001), "Progress-Variable Approach for Large-Eddy Simulation of Turbulent Combustion", *Ph.D Thesis*, Stanford University, USA.

Pierce, C.D. and Moin, P. (1998), "A Dynamic Model for Subgrid-Scale Variance and Dissipation Rate of a Conserved Scalar", *Physics of Fluids 10*, 3041–3044.

Pierce, C.D. and Moin, P. (2004), "Progress-Variable Approach for Large Eddy Simulation of Non-premixed Turbulent Combustion", *Journal of Fluid Mechanics 504*, 73-97.

Piomelli, U. and Liu, J. (1995), "Large Eddy Simulation of Rotating Channel Flows using a Localized Dynamic Model", *Physics of Fluids 7*, 839-848.

Piomelli, U., Yu, Y. and Adrian, R. J. (1996), "Subgrid-scale Energy Transfer and Near-Wall Turbulence Structure", *Physics of Fluids 8*, 215–224.

Piomelli, U. (1999) "Large Eddy Simulation: Achievements and Challenges", *Aeros Sci.*, 35, 335-362.

Piomelli, U., Chasnov, J. R., (1996), "Large Eddy Simulaitons: Theory and Applications", Kluwer, United Kingdom.

Pitsch, H. (1998), A C++ Computer Program for 0-D and 1-D Laminar Flame Calculations, RWTH Aachen.

Pitsch, H. (2000), "Unsteady Flamelet Modelling of Differential Diffusion in Turbulent Jet Diffusion Flames", *Combustion and Flame 123,* 358-374.

Pitsch, H. (2002), "Improved Pollutant Predictions in Large-Eddy Simulations of Turbulent Non-premixed Combustion by Considering Scalar Dissipation rate Fluctuations", *Twenty Ninth Symposium (International) on Combustion/The Combustion Institute*,1971–1978.

Pitsch, H. (2002), "Improved Pollutant Predictions in Large-Eddy Simulations of Turbulent Non-premixed Combustion by Considering Scalar Dissipation Rate Fluctuations", *Twenty Ninth Symposium (International) on Combustion/The Combustion Institute*, 1971-1978.

Pitsch, H. and Duchamp de Lageneste, L. (2001), "Large-Eddy Simulation of Premixed and Partially Premixed Turbulent Combustion Using a Level Set Method", *Fifty Fourth Annual Meeting of the Division of Fluid Dynamics, Session KP -Turbulent Reacting Flows II*, KP002.

Pitsch, H. and Ihme, M. (2005), "An Unsteady/Flamelet Progress Variable Method for LES of Nonpremixed Turbulent Combustion", *AIAA Paper* 2004-557.

Pitsch, H., and Peters, N. (1998), "A Consistent Flamelet Formulation for Non-Premixed Combustion Considering Differential Diffusion Effects", *Combustion and Flame 114*, 26-40.

Pitsch, H., Barths, H., and Peters, N. (1996), "Three Dimensional Modelling of NOx and Soot Formation in DI-Diesel Engines Using Detailed Chemistry Based on the Interactive Flamelet Approach", *SAE Paper* 962057.

Pitsch, H., Chen, M., and Peters, N. (1998), "Unsteady Flamelet Modelling of Turbulent Hydrogen-Air Diffusion Flames", *Twenty-Seventh Symposium (International) on Combustion/The Combustion Institute*, 1057-1064.

Pitsch, H., Steiner, H. (2000). "Large-Eddy Simulation of a Turbulent Piloted Methane/Air Diffusion flame (Sandia Flame D)", *Physics of Fluids 12*, 2541–2554.

Pitsch, H., Fedotov, S., (2001), "Investigation of Scalar Dissipation Rate Fluctuations in Non-Premixed Turbulent Combustion Using a Stochastic Approach", *Combustion Theory and Modelling, 5*, 41-57.

Pitsch, H., Cha, C. M., Fedotov, S., (2003), "Flamelet Modelling of Non-premixed Turbulent Combustion with Local Extinction and Re-ignition", *Combust. Theory Modelling, 7*, 317–332

Pitts, W. M., (1988), "Assessment of Theories for the Behavior and Blowout of Lifted Turbulent Jet Diffusion Flame" 22nd Symposium (International) on combustion, The Combustion Institute, 809–816.

Pitts, W. M., (1990), "Large-scale Turbulent Structures and the Stabilization of Lifted Turbulent Jet Diffusion Flames", *23rd Symposium (International) on combustion, The Combustion Institute,* 661–668.

Pope, S.B. (1985), "PDF methods for Turbulent Reactive Flows", *Progress in Energy and Combustion Science 11*,119-192.

Poinsot, T., Veynante, D. (2001), "Theoretical and Numerical Combustion", *In Theoretical and numerical combustion*, R. T. Edwards.

Porscht, R., (1974), "Studies on Characteristic Fluctuations of the Flame Radiation Emitted by Fires", *Combustion Science and Technology, 10*, 73-84.

Press, W.H., Flannery, B.P., Teukolsky, S.A., Vetterling, W.T. (1993), *Numerical Recipes in FORTRAN, The Art of Computing Science*. Cambridge: Cambridge University Press.

Raman, V., Pitsch, H. (2005), "Large-Eddy Simulation of a Bluff-body Stabilized Nonpremixed Flame using a Recursive-Refinement Procedure", *Combustion and Flame 142*, 329–347.

Ranga-Dinesh, K.K.J. (2007), "Large Eddy Simulation of Turbulent Swirling Flames", *Ph.D Thesis*, Loughborough University, UK.

Ranga-Dinesh, K.K.J., Malalasekera, W., Ibrahim, S.S., Kirkpatrick, M.P. (2006), "Large Eddy Simulation of Turbulent Non-Premixed Swirling Flames", *Proceedings of the 5th International Symposium on Turbulence, Heat and Mass Transfer*, pp 1-7.

Ravikanti, M., Malalasekera, W., Hossain, M., Mahmud, T., (2008), "Flamelet Based NO_x Radiation Integrated Modelling of Turbulent Non-premixed Flame using Reynolds-stress Model", *Flow Turbulence and Combustion, 81*, 301-319.

Ravikanti, M., (2008), "Advanced Flamelet Modelling of Turbulent Non-premixed and Partially Premixed Combustion", PhD Thesis, Loughborough University, UK.

Riesmeier, E., Honnet, S., and Peters, N. (2004), "Flamelet Modelling of Pollutant Formation in a Gas Turbine Combustion Chamber Using Detailed Chemistry for a Kerosene Model Fuel", *Journal of Engineering for Gas Turbines and Power 126,* 899-905.

Roberts, P.T and Moss, J.B. (1981), "A Wrinkled Flame Interpretation of The Open Turbulent Diffusion Flame", *Eighteenth Symposium (International) on Combustion/The Combustion Institute*, 941.

Rogallo, R. S., Moin, P., (1984), "Numerical Simulation of Turbulent Flows", *Annual Rev. Fluids Mech., 16,* 99-137.

Rogg, B., Behrendt, F., Warnatz, J., (1986), "Turbulent Non-premixed Combustion in Partially Premixed Diffusion Famelets with Detailed Chemistry", *Twenty-first Symposium (International) on Combustion. The Combustion Institute, Pittsburgh,* 1533–1541.

Sanders, J.P.H, Chen, J.-Y., and Gökalp (1997), "Flamelet based Modelling of NO formation in Turbulent Hydrogen Jet Diffusion Flames", *Combustion and Flame 111,* 1-15.

Sanders, J.P.H. and Lamers, A.P.G.G. (1994), "Modelling and Calculation of Turbulent Lifted Diffusion Flames", *Combustion and Flame 96*, 22-33.

Savas, O., Gollahalli, S. R., (1986), "Flame Structure in Near Nozzle Region of Gas Jet Flames", *AIAA Journal, 24*, 1137-1140

Schefer, R. W., Namazian, M., Kelly, J., (1990), "In: *Twenty-Third Symposium (International) on Combustion*, *The Combustion Institute, Pittsburgh*, 669.

Schlatter, M., Ferreira, J.C., Flury, M., and Gass, J. (1996) "Analysis of Turbulence-Chemistry Interaction With Respect to NO Formation in Turbulent Nonpremixed Hydrogen-Air Flames", *Twenty-sixth Symposium (International) on Combustion/The Combustion Institute*, 2215-2222.

Shah, N. G., (1979), "The Computation of Radiation Heat Transfer", PhD Thesis, Imperial College, London.

Siegel, R., Howell, J., (2001), "Thermal Radiation Heat Transfer", New York: Hemisphere.

Sivathanu, Y. R., Gore, J. P. Dolinar, J., (1990), "Transient Scalar Properties of Strongly Radiating Jet Flames", *ASME HTD, Heat and Mass Transfer in Fires and Combustion Systems*, Grosshandler, W. L. and Semerjian, H. G. (eds.), *148,* 45-56.

Sivathanu, Y. R., Gore, J. P. (1993), "A Discrete Probability Function Method for the Equation of Radiative Transfer", *Journal of Quant. Spectrose Radiative Transfer*, 49, 3, 269-280.

Smagorinsky, J. (1963), "General Circulation Experiments with the Primitive Equations, Part I: The Basic Experiment", *Monthly Weather Review 91*, 99-164.

Smith, P.G, Golden, D.M., Frenklach, M., Moriarty, N.W., Eiteneer, B., Goldenberg, M., Bowman, C.T., Hanson, R.K., Song, S., Gardiner, W.C., Lissianski, V. and Qin, Z. (2007), in http://www.me.berkeley.edu/gri-mech/releases.html

Song, T. H., Viskanta, R., (1987), "Interaction of Radiation with Turbulence : Application to a Combustion System", *Journal of Thermophysics, 1, No1*, 56-62

Sreenivasan, K. R., Antonia, R. A. and Danh, H. Q. (1977), "Temperature Dissipation Fluctuations in a Turbulent Boundary Layer", *Physics of Fluids 20*, 1238-1249.

Tan, E., Foster, P. J., (1978), "Radiation Through a Turbulent Medium", *Heat Transfer, Hemisphere Publishing Corp., Washington DC*, *3*, 403-408.

Tesse, L., Dupoirieux, F., Taine, J., (2004), "Monte Carlo Modelling of Radiative Transfer in a Turbulent Sooty Flame", *International Journal Heat and Mass Transfer, 47 (3),* 555-572.

Truelove, J. S., (1976), "A Mixed Grey Gas Model for Flame Radiation", AERE Harwell, Oxfordshire, UK.

VanKan, J. (1986), "A Second Order Accurate Pressure Correction Scheme for Viscous Incompressible Flow", *SIAM* Journal of Scientific and Statistical Computing 7*, 870-891.*

Vanquickenborne, L. and Van Tiggelen, A. (1966), "The stabilization Mechanism of Lifted Diffusion Flames", *Combustion and Flame 10*,pp. 59-69.

Versteeg, H.K., and Malalasekera, W. (2007), "*An Introduction to Computational Fluid Dynamics*: *The Finite Volume Method*", Harlow, England; New York: Pearson Education Ltd.

Veynante, D., Vervisch, L., Poinsot, T., Liñán, A., Ruetsch, G. (1994), "Triple Flame Structure and Diffusion Flame Stabilization". *Summer Proceedings of Center for Turbulence Research*, NASA Ames/Stanford University, 55-73.

Viskanta, R., Mengue, M. P., (1987), "Radiation Heat Transfer in Combustion Systems", *Progress in Energy Combustion Science, 13*, 97-160.

Vranos, A., Knight, B.A., Proscia, W.M., Chiappetta, L., and Smooke, M.D. (1992), "Nitric Oxide Formation and Differential Diffusion in a Turbulent Methane-Hydrogen Diffusion Flame", *Twenty Fourth Symposium (International) on Combustion/The Combustion Institute*, 377-384.

Wang, L., Haworth, D., Turns, S., Modest, M. F., (2005), "Interactions among Soot, Thermal Radiation, and NO_x Emissions in Oxygen-enriched Turbulent Nonpremixed Flames: a Computational Fluid Dynamics Modelling Study", *Combustion and Flame 141 (1-2),* 170-179.

Werner, H. and Wengle, H. (1991), "Large Eddy Simulation of Turbulent Flow Over and Around a Cube in a Plane channel", Eighth *Symposium on Turbulent Shear Flows*, 155-168.

Williams, F.A. (1975), "Recent Advances in Theoretical Descriptions of Turbulent Diffusion Flames", In S.N.B. Murthy (Ed.), *Turbulent Mixing in Nonreactive and Reactive Flows*, pp.189-208, New York: Plenum Press.

Williams, F.A., (1985), "*Combustion Theory*", Addison-Wesley, California.

Wu, Y., Haworth, D. C., Modest, M. F., Cuenot, B., (2007), "Direct Numerical Simulation of Turbulence/Radiation Interaction in Premixed Combustion Systems", *Proc of Combustion Institute, 30*, 639-646.

Wu, Y., Modest, M. F., Haworth, D. C., (2007), "A High-order,Photon Monte Carlo Method for Radiative Transfer in Direct Numerical Simulation", *Journal of Computational Physics, 223*, 898-922.

Xu, X., Chen, Y., Wang, H. (2006), "Detailed Numerical Simulation of Thermal Radiation Influence in Sandia flame D", *International Journal of Heat and Mass Transfer 49*, 2347-2335.